

Amplitude Analysis and Modeling of Regional Phases in PNE Profiles in Northern Eurasia and Seismic Regionalization

**Igor B. Morozov
Hongyan Li
Elena Morozova
Joel Duenow
Haishan Zheng
Scott B. Smithson**

**University of Wyoming
Department of Geology and Geophysics
P.O. Box 3006
Laramie, WY 82071-3006**

Final Report

30 June 2006

APPROVED FOR PUBLIC RELEASE; DISTRIBUTION UNLIMITED.



**AIR FORCE RESEARCH LABORATORY
Space Vehicles Directorate
29 Randolph Road
AIR FORCE MATERIEL COMMAND
Hanscom AFB, MA 01731-3010**

Using Government drawings, specifications, or other data included in this document for any purpose other than Government procurement does not in any way obligate the U.S. Government. The fact that the Government formulated or supplied the drawings, specifications, or other data does not license the holder or any other person or corporation; or convey any rights or permission to manufacture, use, or sell any patented invention that may relate to them.

This report was cleared for public release by the Electronic Systems Center Public Affairs Office and is available to the general public, including foreign nationals. Qualified requestors may obtain additional copies from the Defense Technical Information Center (DTIC) (<http://www.dtic.mil>). All others should apply to the National Technical Information Service.

AFRL-VS-HA-TR-2006-1070 HAS BEEN REVIEWED AND IS APPROVED FOR PUBLICATION IN ACCORDANCE WITH ASSIGNED DISTRIBUTION STATEMENT.

//Signature//

ROBERT RAISTRICK
Contract Manager

//Signature//

ROBERT BELAND, Chief
Battlespace Surveillance Innovation Center

This report is published in the interest of scientific and technical information exchange, and its publication does not constitute the Government's approval or disapproval of its ideas or findings.

REPORT DOCUMENTATION PAGE			Form Approved OMB No. 0704-0188	
<small>Public reporting burden for this collection of information is estimated to average 1 hour per response, including the time for reviewing instructions, searching existing data sources, gathering and maintaining the data needed, and completing and reviewing this collection of information. Send comments regarding this burden estimate or any other aspect of this collection of information, including suggestions for reducing this burden to Department of Defense, Washington Headquarters Services, Directorate for Information Operations and Reports (0704-0188), 1215 Jefferson Davis Highway, Suite 1204, Arlington, VA 22202-4302. Respondents should be aware that notwithstanding any other provision of law, no person shall be subject to any penalty for failing to comply with a collection of information if it does not display a currently valid OMB control number. PLEASE DO NOT RETURN YOUR FORM TO THE ABOVE ADDRESS.</small>				
1. REPORT DATE 30-Jun-06		2. REPORT TYPE Final Report		3. DATES COVERED (From - To) 25 Sep 01 - 30 Jun 06
4. TITLE AND SUBTITLE Amplitude Analysis and Modeling of Regional Phases in PNE Profiles in Northern Eurasia and Seismic Regionalization		5a. CONTRACT NUMBER DTRA01-01-C-0057		
		5b. GRANT NUMBER		
		5c. PROGRAM ELEMENT NUMBER		
6. AUTHOR(S) Igor B. Morozov ^{1,2} , Hongyan Li ² , Elena Morozova ² , Joel Duenow ² , Haishan Zheng ¹ , and Scott B. Smithson ²		5d. PROJECT NUMBER DTRA		
		5e. TASK NUMBER OT		
		5f. WORK UNIT NUMBER A1		
7. PERFORMING ORGANIZATION NAME(S) AND ADDRESS(ES) University of Wyoming Department of Geology and Geophysics P.O. Box 3006 Laramie, WY 82071-3006		8. PERFORMING ORGANIZATION REPORT NUMBER		
9. SPONSORING / MONITORING AGENCY NAME(S) AND ADDRESS(ES) Air Force Research Laboratory 29 Randolph Road Hanscom AFB, MA 01731-3010		10. SPONSOR/MONITOR'S ACRONYM(S) AFRL/VSBYE		
		11. SPONSOR/MONITOR'S REPORT NUMBER(S) AFRL-VS-HA-TR-2006-1070		
12. DISTRIBUTION / AVAILABILITY STATEMENT Approved for Public Release; Distribution Unlimited.				
13. SUPPLEMENTARY NOTES ¹ University of Saskatchewan ² University of Wyoming				
14. ABSTRACT <p>Seismological observations play an important role in detecting and locating all nuclear events, determining their yields and distinguishin them from earthquakes and other chemical explosions. Regional phases play a critical role for small-yield nuclear test monitoring. Regional phases travel in the crust and the upper mantle, which are very heterogeneous, therefore, calibration of phase propagation characteristics within different tectonic and geologic environments is necessary to use regional phases for nuclear test monitoring.</p> <p>Among all the regional phases (Pn, Pg, Sn, and Lg), the Lg-phase is usually the most prominent and robust in continental regions. It has been widely used to discriminate nuclear explosions from earthquakes and to determine nuclear-explosion yield. However, the Lg phase is very sensitive to the variations of crustal structure, and will be highly attenuated or even blocked in some tectonic areas. Therefore, calibration is crucial for Lg propagation characteristics in different tectonic areas for its use in nuclear test monitoring.</p> <p>Over the past decades, Russian scientists acquired a network of dense, linear, long range, three-component Deep Seismic Sounding (DSS) profiles using conventional and Peaceful Nuclear Explosions (PNEs) over a large area of Northern Eurasia. Seven PNE profiles and 19 PNE shots were used in this study. From west to east, the seven profiles mainly traverse the East-European Craton, the Timan Belt, the Timan-Pechora Basin, the Ural Mountains, the West-Siberian Basin, the West-Siberian Rift, the Yenisei-Khantanga Basin, the Siberian Craton, the Baikal Rift zone, and the Altay-Sayan-Baikal fold belt, covering a wide range of tectonic features. This report covers seismological investigations using this data.</p>				
15. SUBJECT TERMS Seismic attenuation, Seismic propagation, Seismic yield				
16. SECURITY CLASSIFICATION OF:			17. LIMITATION OF ABSTRACT	18. NUMBER OF PAGES
a. REPORT UNCLAS	b. ABSTRACT UNCLAS	c. THIS PAGE UNCLAS	SAR	151
			19a. NAME OF RESPONSIBLE PERSON Robert J. Raistrick	
			19b. TELEPHONE NUMBER (include area code)	

Table of contents

1	INTRODUCTION	1
1.1	DSS PNE datasets	1
1.2	Geologic and tectonic setting	2
1.3	Scope, structure, key findings, and recommendations of this study.....	5
2	CORRELATION OF LG AMPLITUDE RATIOS FROM THE PNES WITH THE CRUSTAL STRUCTURE	9
2.1	Summary	9
2.2	Introduction	9
2.3	Data analysis	12
2.3.1	Data selection.....	12
2.3.2	A model for the logarithm of amplitude ratios	12
2.3.3	Selection of calibration parameters	14
2.4	Correlation of the amplitude ratios with crustal structures	17
2.5	Discussion	21
2.6	Conclusions	25
3	LG Q DISTRIBUTION IN NORTHERN EURASIA FROM PNE DATA.....	28
3.1	Summary	28
3.2	Introduction	28
3.3	Data processing.....	29
3.3.1	Interstation average $Lg\ 1/Q$ from a two-station method,.....	31
3.3.2	Averaging $Lg\ Q$ along the different crustal segments	33
3.4	Results.....	33
3.5	Discussion	35
3.6	Conclusions	42

4	EMPIRICAL PNE SOURCE SCALING.....	47
4.1	Summary	47
4.2	Introduction	47
4.3	Analysis of yield- m_b relationship from PNE data	50
4.4	Spectral characteristics of PNE regional phases	51
4.5	P and S-wave source spectra	52
4.6	Discussion	56
4.6.1	Yield- m_b -medium-depth relationship	56
4.6.2	Spectral characteristics of the regional phases	57
4.6.3	f_c -yield- m_b relationship.....	58
4.7	Conclusions	59
5	EMPIRICAL MODEL FOR PNE REGIONAL PHASE CODAS.....	64
5.1	Summary	64
5.2	Introduction	64
5.3	Coda decay rate of the long-range PNE arrivals	67
5.4	Decomposition of PNE energy	70
5.5	Energy patterns of PNE wavefield	71
5.6	Discussion	73
5.7	Conclusions	76
6	ANOMALIES IN FREQUENCY-DEPENDENT LG CODA Q	78
6.1	Summary	78
6.2	Geometrical-spreading corrected or frequency-dependent coda Q ?	78
6.3	Conclusions	83
7	CONSTRAINTS ON THE CRUSTAL STRUCTURE FROM P/S CONVERSIONS IN THE FIRST-ARRIVAL PNE CODAS	84

7.1	Summary	84
7.2	Introduction	84
7.3	Short-period coda of PNE arrivals.....	86
7.4	Conclusions	91
8	EMPIRICAL CALIBRATION OF PNE CODA Q BY USING 1.5-D NUMERICAL MODELING	92
8.1	Summary	92
8.2	Introduction	93
8.3	Crustal and coda attenuation	94
8.4	Coda model.....	94
8.5	Synthetic PNE sections and Green's functions.....	96
8.6	Numerical modeling	96
8.7	Modeling results.....	98
8.8	Interpretation of observations from PNE Quartz-4	100
8.9	Discussion	101
8.10	Conclusions.....	103
8.11	Figures to this Chapter.....	105
9	3-D FIRST-ARRIVAL REGIONAL TRAVEL-TIME CALIBRATION MODEL OF NORTHERN EURASIA.....	116
9.1	Summary	116
9.2	Introduction	116
9.3	Method.....	120
9.3.1	τ -p transformation of travel times	121
9.3.2	Mapping of τ -p travel-times into depth.....	122
9.3.3	Spatial interpolation	123
9.3.4	Prediction of travel times	125

9.4	Discussion	127
9.5	Conclusions	131
	ACKNOWLEDGEMENTS.....	132
10	BIBLIOGRAPHY	132

1 Introduction

Seismological observations play an important role in detecting and locating all nuclear events, determining their yields, and distinguishing them from earthquakes and other chemical explosions. Regional phases play a critical role for small-yield nuclear test monitoring. Regional phases travel in the crust and the upper mantle, which are very heterogeneous; therefore, calibration of phase propagation characteristics within different tectonic and geologic environments is necessary to use regional phases for nuclear test monitoring.

Among all the regional phases (*Pn*, *Pg*, *Sn*, and *Lg*), the *Lg*-phase is usually the most prominent and robust in continental regions. It has been widely used to discriminate nuclear explosions from earthquakes and to determine nuclear-explosion yield. However, the *Lg* phase is very sensitive to the variations of crustal structure, and will be highly attenuated or even blocked in some tectonic areas. Therefore, calibration is crucial for *Lg* propagation characteristics in different tectonic areas for its use in nuclear test monitoring.

Over the past decades, Russian scientists acquired a network of dense, linear, long range, three-component Deep Seismic Sounding (DSS) profiles using conventional and Peaceful Nuclear Explosions (PNEs) over a large area of Northern Eurasia. Seven PNE profiles and 19 PNE shots were used in this study. From west to east, the seven profiles mainly traverse the East-European Craton, the Timan Belt, the Timan-Pechora Basin, the Ural Mountains, the West-Siberian Basin, the West-Siberian Rift, the Yenisei-Khantanga Basin, the Siberian Craton, the Baikal Rift zone, and the Altay-Sayan-Baikal fold belt, covering a wide range of tectonic features. This report covers seismological investigations using this data.

1.1 DSS PNE datasets

The Russian Deep Seismic Sounding (DSS) program carried out from 1960's to 1990's remains a unique source of seismic refraction/reflection data covering over a half of the territory of the former USSR (Figure 1-1). It included densely recorded at 100- 500 m spacing wide-angle refraction-reflection profiles using chemical explosions for detailed imaging of the entire crust and the upper mantle. Along with regional and teleseismic recordings of PNEs to over 3000-km distance, detailed DSS, industry seismic, and borehole data allowed correlation of the results with the structure of the crust (Yegorkin, 1992, and personal communication).

From 1971 to 1989, the DSS program grew to include 39 PNEs carried out over widely distributed regions of the USSR (Figure 1-1). These special PNEs, with yields up to 23 kilotons, were used to study crustal and upper mantle structure along linear profiles, some of which were

more than 4000 km in length. Recording ranges of PNEs exceeded 3200 km, allowing observations of seismic phases diving down 800 km into the mantle (Egorkin et al, 1987; Ryaboy, 1989; Kozlovsky, 1990). On a typical profile, 3-4 nuclear explosions were recorded (analog, on magnetic tape) at 200-400 of three-component seismograph stations with spacing around 10 to 15 km. Specially designed recording system "Taiga" (Ryaboy, 1989) was used in most of the profiles, with the natural three-component sensor frequency of 1 Hz, and the frequency response flat above 1 Hz. The data were recorded on analog magnetic tapes and later digitized at 20-ms sampling intervals for the PNEs and 10-ms intervals for the chemical explosions.

About 50 - 80 chemical explosions (typically, 3000 - 5000 kg, and sometimes up to 15 ton, as near the site of PNE Quartz-1 that was apparently missed) per profile were also recorded to enable interpretation of the crustal and uppermost mantle structures. Several nuclear explosions at the weapons test sites and natural sources were also recorded at hundreds of three-component DSS stations, providing data additional to PNE data. Detailed information about the program, including accurate PNE locations and times, became available in 1996-1998 (e.g., Sultanov et al., 1999).

As collections of numerous regional phases densely recorded along continental-scale profiles traversing largely aseismic areas of Northern Eurasia, DSS datasets provide the key information for seismic calibration of this vast area. Along with their use in CTBT monitoring, DSS data still contain great potential for revealing the detailed structure of the crust and uppermost mantle. An overview of earlier interpretations was given by Ryaboy (1989), and several recent re-interpretations of the major DSS profiles have been carried out (Cipar et al., 1993; Mechie et al., 1993, 1997; Benz et al., 1993; Priestley et al. 1994; Ryberg et al., 1995, 1996; Pavlenkova, 1996; Pavlenkova et al., 1996; Morozova et al., 1995, 1997, and in press; Schueller et al., 1997). Of the above authors, only Schueller et al. (1996) and Morozova et al. (1995, 1999) analyzed a crustal DSS data set. However, detailed crustal models are critical for the understanding of *Lg* propagation (e.g., Kennett, 1986).

In this study, we use three-component records from 19 PNEs that have recently become available through out cooperation with Center GEON and sponsored by the Air Force Research Laboratory (Contract DTRA01-01-C-0081) and the National Science Foundation (Grant EAR-0092744).

1.2 Geologic and tectonic setting

A variety of contrasting geological structures are present in the vast geographical expanse of northern Eurasia (Figure 1-1), and thus the seismic profiles crossing the different tectonic provinces provide a good data base to calibrate the effects of crustal structure on regional phase propagation. The seven PNE profiles of this study (QUARTZ, RUBY-1, RUBY-2, CRATON, KIMBERLITE, RIFT, and METEORITE) traverse (listed from west to east, Figure 1-1): the East-European Craton, Timan fold belt and Timan-Pechora Basin, Uralian fold belt, West

Siberian Basin, Western Siberian Rift (Pur-Gurden Basin), Altay-Sayan-Baikal folded region, Siberian Craton, and Baikal Rift Zone.

The East European Craton is about 3000 km across, with basement formed at ~1600 Ma (Zonenshain et al, 1990). The craton is mostly surrounded by fold belts with no young orogenic uplifts present. The crustal thickness is 36-48 km, and the surrounding areas have generally thinner crust than its inner part (Volkov, 1984; Pavlenkova, 1996). The northern part of the East European Craton includes the stable Baltic Shield, which lacks significant sedimentary cover (Gaal and Gorbatshev, 1987). Between the eastern margin of the Baltic Shield and the Timan belt, the basement is disrupted by narrow and deep (in excess of 3 km) graben-like troughs called aulacogens or failed rifts (Zonenshain et al., 1990).

The Timan-Pechora platform (Figure 1-1) is mainly composed of the Timan-Pechora fold belt and Timan-Pechora Basin. The Timan-Pechora fold belt is an uplift of the Riphean basement of the Timan-Pechora platform. The basement was formed in the Proterozoic and filled with mainly Devonian to Carboniferous and Permian sedimentary rocks (Lindquist,

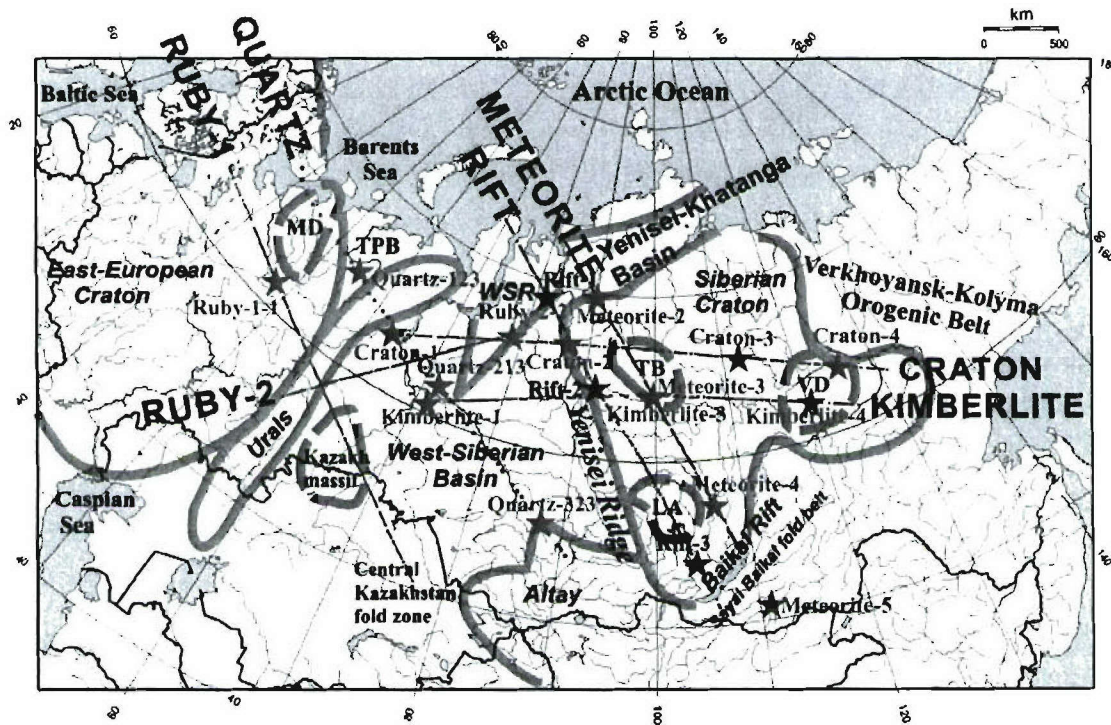


Figure 1-1. Location of PNE profiles and tectonic boundaries in northern Eurasia. Large labeled stars are the locations of PNEs of this study; uppercase labels indicate the PNE projects of this study. Thick solid lines show major tectonic features (WSR - West Siberian Rift; MD - Mezen' Depression; TPB - Timan-Pechora Basin; Zonenshain et al., 1990). The three major basins within the Siberian Craton are: Tunguss Basin (TB), Vilyui Depression (VD), and Low-Angara Basin (LA).

1999). The crustal thickness in this area is 36 to 40 km (Pavlenkova, 1996), and the sedimentary cover in the southern plain averages 3-7 km (Zonenshain et al., 1990).

The Uralian fold belt (Figure 1-1) represents a linear collisional fold belt formed at the end of the Paleozoic and the very beginning of the Mesozoic (310-220 Ma), extending 2500 km from north to south and separated from the Eastern-European and Timan-Pechora platform by the Uralian Foredeep (Zonenshain et al., 1990). The crustal thickness is about 40-53 km, with a ~14 km crustal root (Knapp et al., 1996; Pavlenkova, 1996; Morozova et al., 1999; Tryggvason et al., 2001).

The West Siberian Basin (Figure 1-1) is the largest known basin structure in the world and covers over 3.4 million km². The basement was formed of Paleozoic fold structures of various ages and older Precambrian blocks (Zonenshain et al., 1990) with subsidence from Triassic to Neogene (Khain, 1994). The subsidence was accompanied by extensive basaltic volcanism substantiated by drilling (Saunders et al., 2005). The basin is mainly covered by Mesozoic and Cenozoic sediments (Aplonov, 1995), averaging ~10 km in thickness in the north and ~3 km in the south (Aplonov, 1995; Ulmishek, 2003). The crustal thickness decreases from the edges (~42 km) to the central part of the platform (~34 km in the north along the West-Siberian Rift; Aplonov, 1995). The Kazakh massif is located southwest of the West-Siberian Basin and has a thick crust (40-45 km) with high average velocities (6.6 - 6.8 km/s), comparable to those of the Baltic shield (Pavlenkova, 1996). The sedimentary cover in the Kazakh massif is less than 2 km.

The Siberian Craton (Figure 1-1) extends for ~2500 km in the E-W direction and is mainly represented by its Achaean basement. Two shields (Aldan and Anabar) and three deep basins (Tunguss Basin, Low-Angara Basin, and Vilyui Depression) are identified within this craton. The western part of the Siberian Craton is generally covered by a 5-6 km sedimentary cover containing from 100-150 to 1400 m thick flood basalts of the Mesozoic Siberian Traps (Czamanske et al., 1998; Pavlenkova et al., 2002). Within the Tunguss and Low-Angara Basins, the sedimentary cover is up to 10 km (Egorkin et al., 1987; Pavlenkova, 1996; Pavlenkova et al., 2002). The Tunguss Basin is filled with a high-velocity (~6.0 km/s) Devonian sedimentary cover with a relatively flat Moho (~50 km) in the north (Egorkin et al., 1987; Pavlenkova, 1996), but with a Moho uplift (~3 km) in the south (Pavlenkova, 1996; GEON, personal communication). The Low-Angara Basin is filled with both Paleozoic and Mesozoic sedimentary rocks with somewhat lower velocities (~5.5 km/s), and the basement subsidence is compensated by a strong Moho uplift (~3-4 km; Pavlenkova, 1996). The Vilyui Depression is filled with 10-14 km of loose and low-velocity Mesozoic rocks (2.5-4.5 km/s), and the basement surface has steep dips with an up to 13-km anti-root Moho (Egorkin et al., 1987; Pavlenkova, 1996). The crustal thickness is 40 to 45 km on the average (Pavlenkova, 1996) increasing to 50 km below the Tunguss Basin and decreasing to ~35 km below the Vilyui Depression (Egorkin et al., 1987; Pavlenkova, 1996; Pavlenkova et al., 2002).

The Altay Mountains and Sayan-Baikal fold belt (Figure 1-1) are major fold belts surrounding the Siberian Craton and the West-Siberian Basin on the south. These fold belts are composed of a number of different units assembled by accretion of island arcs generally in the

Late Precambrian and Paleozoic (Volkov, 1984; Khain 1985). Under the Altai Mountains, the crust could be thicker than 50 km and even reach 60 km (Pavlenkova, 1996; Morozova et al., 1999; Dehandschutter, 2001). The crustal thickness beneath the Sayan-Baikal fold belt ranges from 36 to 55 km while staying between 40 and 45 km in most parts of the area (Beloussov et al., 1992).

The Western-Siberian Rift (Pur-Gurden Basin; Figure 1-1) is located on the northwest edge of the Siberian platform, a failed ocean of rift origin developed in the Triassic during the initial breakup of Pangea. Since the cessation of extension, the Western-Siberian Rift was filled by up to 13-km thick sediments (Cipar et al., 1993; Aplonov, 1995).

The Baikal Rift zone (BRZ; Figure 1-1) is superimposed on the Baikal fold belt and is composed of a branched chain of Late-Cenozoic half-grabens extending across ~1500 km along the S-shaped suture along the edge of the Siberian Craton (Logatchev and Zorin, 1992; Scholz and Hutchinson, 2000; Zorin et al., 2003). It is seismically active, still rifting, and represents one of the deepest rifts on the earth (Golmshtok et al., 2000). The Late-Cenozoic sediments are usually 2.5 - 3-km thick and even reach up to 7 km in thickness within the rift basins (Logatchev and Zorin, 1992; Hutchinson et al., 1992). The heat flow in the Baikal Rift is 60 - 75 mW/m², which is much lower than in other continental rifts (usually > 100 mW/m²). The thickness of the crust beneath the Baikal Rift Zone was inferred to be 35 - 45 km (Dehandschutter, 2001). Below the Moho, a layer of low mantle velocities (7.7 - 7.8 km/s, which is by 0.3 - 0.5 km/s lower than in the adjoining areas) was identified, pinching out toward the Siberian Craton (Beloussov et al., 1992; Zorin et al., 2003), which could be related to the relatively high heat flow.

1.3 Scope, structure, key findings, and recommendations of this study

The volumes of the DSS PNE datasets and their information contents in different seismological sub-disciplines greatly exceed what can be covered in a single study. In this project, we focused on the use of the datasets for empirical seismic calibration and nuclear test monitoring, which has not been examined previously. In addressing only the hitherto unexplored amplitude-, waveform- and spectral- and empirical travel-time-based approaches, we left aside development of detailed crustal and mantle models for which the PNE datasets are mostly known (and which, in our estimate, is also far from exhausting ~20% of its potential),

Application of the datasets to empirical seismic calibration also presents numerous opportunities, and we do not claim comprehensive coverage of this vast area. Instead, in this report, we focused on two main objectives:

- 1) to explore a broad range of new techniques that could contribute an empirical (including travel-time and wavefield amplitude information) model of the entire area of Northern

Eurasia by using the records from all seven PNE projects (Figure 1-1), and

- 2) to elaborate on some of these techniques and provide new measurements of crustal properties along selected profiles, such as Quartz (the highest-quality and best-studied PNE profile to date), Craton, and Kimberlite (Figure 1-1).

The ultimate goal of DSS PNE research would thus be to eventually merge these two lines of approach, to incorporate the chemical-explosion datasets, to include the results from detailed structural studies, and produce an integrated 3-D model of Northern Eurasia that could also be extended and merged with the surrounding regions. This model should incorporate both the structural features of the crust and upper mantle (e.g., it should predict the refraction and reflection travel times and possibly relative amplitudes), and also should also provide physically reasonable ways to incorporate empirical information (such as amplitude ratios of the regional phases and short-period $Lg Q$). The approaches 1) and 2) are thus among the first steps to constructing such a model.

The report below examines the different aspects of 1)-2) above and is organized as series of papers (Chapters) with only a limited cross-referencing. Each Chapter includes a *Summary*, *Introduction*, and *Conclusions*. The key findings and recommendations of this work are as follows.

In **Chapter 2**, we look for an empirical correlation of the observed regional phase amplitude ratios from 19 PNEs with the crustal structures. We find that a linear relationship of the slope of both logarithms of amplitude ratios with the corresponding Moho slopes and the average vertical travel times of Lg through the sedimentary cover can be determined. The observations suggest that abrupt variations of crustal thickness is the most important factor affecting Lg propagation.

From this study, we suggest that in northern Eurasia, the logarithms of Lg/S and $Lg/P coda$ amplitude ratios at frequencies of 0.5 – 3 Hz could be useful parameters to calibrate the effects of the variations in the crustal structure on Lg propagation. In an important implication for seismic calibration, it appears that the mapped crustal structure could be used to empirically predict the Lg/S and $Lg/P coda$ amplitude ratios.

In **Chapter 3**, we perform $Lg Q$ measurements along the seven PNE profiles. The resulting values are consistent for the reversed and intersecting profiles, and strong Q variations correlated with the geological features are detected. Similarly to Chapter 2, we propose a linear regression model relating $Lg Q$ to the crustal parameters. Such regression could also be incorporated in the future integrated calibration model for prediction of $Lg Q$.

Chapter 4 is an empirical PNE source scaling study, in which we examine the empirical yield- m_b relationships for the different PNE charge emplacement media and estimate the effective P - and S -wave source spectra from the regional phase recordings. From these spectra, we estimate the corner frequencies and correlate them with m_b . As above, these correlations could potentially be utilized in numerical models of seismic wave excitation within the area.

In **Chapter 5**, we develop a simple empirical model of the wavefield amplitude observed in all PNE records, and examine the model more closely using the records from profile QUARTZ. The fundamental observation here is that at PNE frequencies (0.5-20 Hz), crustal scattering is important, leading to extended event codas observed for 150-200 s following the primary arrivals. As a result, the amplitudes of the later phases (e.g., *S* and *Lg*) become significantly enhanced by the earlier phases (*P* and *Pg*). We propose a method for “deconvolving” these overlapping amplitude patterns. Most importantly for the resulting calibration model, we show how the crustal properties (*S*-wave *Q*) can be estimated from the coda observations.

In **Chapter 6**, we continue the study of the coda decay rates from DSS PNE, and point out a striking difference of *Lg* coda decay characters across the study area. Within the East European Platform and south-west West Siberian Basin (profile QUARTZ) *Lg* coda amplitude decays exhibit clear frequency dependence that was previously described (Chapter 5) by frequency-dependent coda quality factor *Q*, but within the Siberian Craton (profile KIMBERLITE), the coda shows a constant decay rate at all frequencies. We argue that this observation could be due to non-frequency dependent coda attenuation associated with geometric spreading and leakage of the energy from the crust. This also suggests that the broadly accepted frequency-dependent attenuation model *Q(f)* might not be optimal, and a modified coda amplitude decay relation could be more suitable for calibration studies:

$$\frac{d \log A}{dt} \approx -\gamma - \frac{\pi f}{Q},$$

where the geometric spreading parameter γ appears to be a stable parameters across the entire area.

Chapter 7 describes the first study of its kind attempting constraining the shallow crustal structures by applying the Receiver Function technique to refraction (PNE) records. He results show good correlation with the depth to the basement and provide a horizontal resolution level close to recording station spacing (10-15 km) and also suggest high (~0.35-0.4) average Poisson’s ratios within the sediments. Thus, deconvolving of the three-component recordings of early P-wave coda could help constraining the shallow structures (from sedimentary thickness to the Moho depth) where direct measurements are not available.

In **Chapter 8**, we apply “heuristic” Born-integral-type modeling to derive $Q_S(Q_{\text{coda}})$ relationships that could be used for to transform the observed Q_{coda} values (Chapters 5 and 6) into crustal Q_S . The inverted frequency-dependent Q_S appears to be somewhat surprisingly low; apparently this could be caused by the thick sedimentary cover in the area of measurements or by strong leaking of the energy into the mantle, as suggested by the results of Chapter 6. Note that all the Figures to this Chapter are given at its end.

In **Chapter 9**, we develop a completely empirical, 3-D, first-arrival travel-time calibration model of the area covered by the DSS PNE profiles. The model employs an innovative and physically better justified (compared to the currently accepted) travel-time interpolation

technique, does not require the use of any reference (e.g., IASP91) model, and lends itself to refinement by using additional data and kriging. The model accurately predicts the first P -wave arrivals from all PNEs and naturally allows interpolation between any source and receiver locations within the area. For its application in CTBT monitoring, Source-Specific Station Corrections for station BRVK in Kazakhstan are computed and correlated with the existing calibration dataset.

2 Correlation of Lg amplitude ratios from the PNEs with the crustal structure

2.1 Summary

Because the Lg phase is strongly affected by the variations of crustal structure, understanding of these factors is important for nuclear test monitoring. This study examines the effects of regional tectonic structure on Lg propagation using the Peaceful Nuclear Explosion (PNE) profiles in Russia. The logarithms of Lg/S and $Lg/Pcoda$ PNE-amplitude ratios at 0.5-3 Hz are measured and correlated with the regional crustal structure. Both of these ratios are found to decrease within the areas with thick sedimentary cover and across tectonic boundaries with abrupt variations of crustal thickness. A linear relationship between the offset derivative of the logarithms of amplitude ratios, the slope of the Moho, and the vertical travel time within the sedimentary cover is:

$$\frac{d \log(A_{Lg}/A_{Ph})}{d(x)} = 5 \cdot 10^{-4} - 7.6 \cdot 10^{-2} \cdot \text{abs}\left(\frac{d(H_M)}{d(x)} - 6 \cdot 10^{-4} \frac{H_s}{V_{ss}}\right),$$

where A_{Lg} is the Lg amplitude, and A_{Ph} is the amplitude of S or $Pcoda$; x is offset; H_M and H_s are the crustal and sedimentary thicknesses respectively, and V_{ss} is the S -wave velocity within the sedimentary cover. The error of this linear regression is estimated as $5 \cdot 10^{-4}$. Although the decrease in this derivative is similar in the areas of crustal thinning and crustal thickening, the abrupt crustal thickening decreases Lg energy much less than crustal thinning due to focusing energy from the Moho ramp, followed by an increase in slope ($\sim 0.003 \text{ km}^{-1}$ from the Vilyui Depression to the Mirninsk-Aihalsk High and $\sim 0.004 \text{ km}^{-1}$ across the Ural Mountains). The log-amplitude regression above could be useful for predicting Lg behavior in areas where amplitude measurements are not available.

2.2 Introduction

Because the Lg phase is strongly affected by the variations of crustal structure in some areas, understanding of these factors is important for nuclear test monitoring. The Lg phase is interpreted as consisting of multiple supercritical S -wave reflections or a superposition of higher-mode surface waves trapped within the crust (Knopoff et al., 1973; Campillo, 1987), or near-source scattering of explosion-generated Rg into S is the primary contributor to the low-frequency Lg from nuclear explosions (Gupta et al., 1992, 1997; He et al., 2005). Because of its short wavelength and an entire propagation path confined within the crust, the Lg phase is

highly sensitive to the variations of crustal structure, and *Lg* was observed to be totally or partially blocked in some areas (Baumgardt, 2001; McNamara and Walter, 2001; Sandvol et al., 2001). Therefore, studying the regional variability of *Lg* phase propagation, and particularly the relation of its amplitude to the regional crustal structure, is critical for nuclear test monitoring.

The *Lg* phase amplitudes measured within selected frequency bands are often used to describe *Lg* propagation characteristics in different tectonic areas. Rapine and Ni (2003) compared the *Lg* amplitude and pre-phase noise to measure the efficiency of *Lg* propagation. Several phase amplitude ratios: *Pg/Lg* (Phillips et al., 2001), *Lg/Pg* (Sandvol et al., 2001), and *Lg/Pcoda* (Rapine et al., 1997; McNamara and Walter, 2001) were used to calibrate *Lg* phase propagation across different crustal structure. In most studies (Rapine et al., 1997; Baumgardt, 2001; McNamara and Walter, 2001; Sandvol et al., 2001; Phillips et al., 2001; Rapine and Ni, 2003), the *Lg* propagation characteristics were derived from earthquake data. Since these data typically have relatively sparse coverage and the stations are rarely deployed in-line with the sources, such approaches provide general characterizations of the area yet do not allow us to study the detailed evolution of *Lg* phase amplitude during its propagation away from the source and across geologic and tectonic boundaries and of course, *Lg* generated from a nuclear-bomb source is ideal for test calibration..

Fortunately for seismic calibration of propagation in northern Eurasia and despite the paucity of its natural seismicity, extensive and unusually detailed recordings of short-period *Lg* and other regional phases are available in this region. From the 1970's to late 1980's, Russian scientists acquired a network of dense, linear, 2000-4000-km long, three-component Deep Seismic Sounding (DSS) profiles using chemical and Peaceful Nuclear Explosions (PNEs). Seven of these profiles including 19 PNEs were used in this study (Figure 1-1). These long-offset, dense, three-component data with known locations and origin times allow measurement of *Lg* phase propagation parameters at 10-15 km station spacing in one of the largest land mass on Earth in order to test the available models and relate these parameters to crustal structure. Importantly, many of these segments of profiles are reversed which provides even more unique data to analyze.

By comparing the logarithms of amplitude ratios of the *Lg* phase over *P*, *Pg*, *S*, *Pcoda*, and pre-phase noise (Figure 2-1) within different frequency bands, the present study uses $\log(A_{Lg}/A_{Sn})$ and $\log(A_{Lg}/A_{Pcoda})$ within a frequency band of 0.3-0.5-3-4 Hz to correlate the slopes of the logarithm of amplitude ratios with the variations of crustal structure and to determine the main factors affecting *Lg* propagation. From the observations of the variations of the slopes in different tectonic areas, a two-parameter linear regression model is proposed to calibrate the variations of *Lg* amplitude. The resulting two parameters are: 1) the Moho slope and 2) the vertical *S*-wave travel time within the sedimentary basins. From the strongest anomalies in the slopes of the log-amplitude ratios, the main tectonic areas affecting *Lg* propagation in northern Eurasia are: the Vilyui Depression, Ural Mountains, Yenisei Ridge (the boundary between the West-Siberian Basin and the Siberian Craton), the boundary between the

Kazakh massif and the West-Siberian Basin, the Mezen' depression, the West-Siberian Rift, and the West-Siberian Basin.

With the 19 PNE records, the *Lg* propagation characteristics in northern Eurasia is analyzed by using the logarithms of *Lg/Sn* and *Lg/Pcoda* amplitude ratios to determine the main factors that affect *Lg* propagation. *Lg Q* is calculated along the seven profiles by a two-station spectral ratio method to quantitatively describe the attenuation characteristics in different tectonic areas.

Source yield is commonly obtained through yield- m_b linear relationship. However, the relationship is affected by the source conditions including source medium and source depth. From 95 well-coupled nuclear explosions in former Soviet Union (FSU; Sultanov et al., 1999),

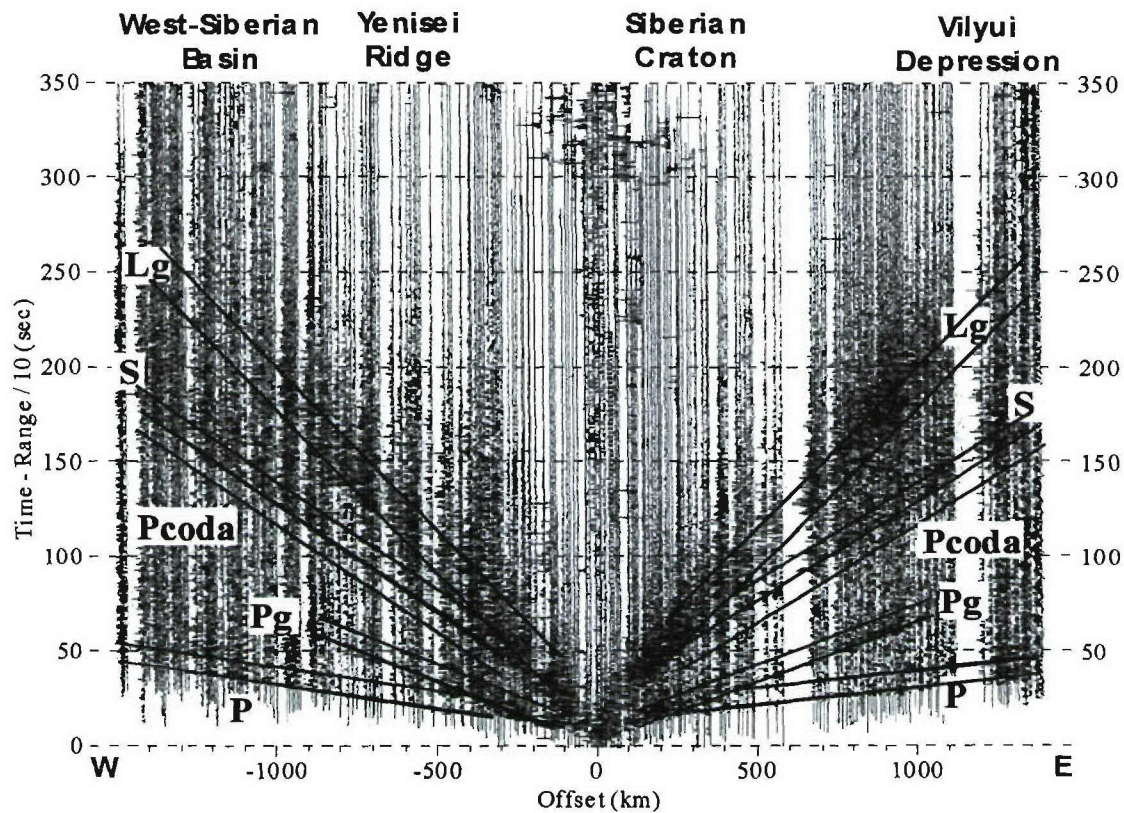


Figure 2-1. Vertical-component record of PNE Kimberlite-3, filtered within frequency band 0.5-8 Hz. The regional phases (*P*, *Pg*, *S*, and *Lg*) are clear and are observed to far offsets. *Lg* in the western branch is significantly weaker than the eastern one. Within the eastern branch, *Lg* becomes weak within the Vilyui Depression. Solid lines show the time window of *P*, *Pg*, *Pcoda*, *S*, and *Lg* used for computing the amplitude ratios.

the coupling effects in different media (clay, salt, sandstone/shale, and limestone/dolomite) and in different shot depths are compared, and then a general linear relationship is established for all the “hard” rocks except clay.

The source spectral characteristics should be different for nuclear explosions and earthquakes according to the different source models (Xie, 1999). The source spectrum of both *P*- and *S*-phases is determined for 19 PNEs by a modified Muller-Murphy explosion-source model (Serenio et al., 1988; Muller and Murphy, 1971) from *Pn* and *Sn* regional phases after attenuation compensation. Thereafter, an m_b - f_c linear relationship is resolved to obtain better constraint on m_b from f_c or estimate f_c from m_b to be used for nuclear discrimination (Xie 1999, 2002).

2.3 Data analysis

2.3.1 Data selection

In order to compute the amplitude ratios (Lg/Pn , Lg/Pg , Lg/Sn , and Lg/P_{coda}), a constant window length was used to measure the phase amplitudes. The phases were identified by correlating the record sections (Figure 2-1), and their onset times were picked interactively. The *Lg* and *S* (*Sn*) phases could usually be distinguished beyond offsets of ~300 km (Figure 2-1), and therefore, the amplitude ratios were computed at offsets exceeding that distance. The observed durations of the *P*, *Pg* and *S* wave trains were typically 10 to 20 s, whereas the duration of *Lg* was longer, usually > 20 s (Figure 2-1). Therefore, the phase window length was chosen equal 10 s for the *P*, *S*, and *Pg* waves and 20 s for the *Lg*. The window of the *P*-wave coda, referred to as *Pcoda*, was taken to be 10 s immediately preceding the *S*-wave onset times. For the *P*-wave window, if the time interval between its onset and the *Pg* was less than 10 s, the window was truncated at the picked onset of the *Pg* phase. For the *S*-wave window, if the time interval between its onset and the *Lg* was less than 10 s, the window was truncated at the picked onset of the *Lg* phase. The time windows were checked for spikes, data dropouts, and clipped amplitudes, and the amplitude ratios were computed with only the good traces.

As an example of a PNE seismic section, Figure 2-1 shows a record from PNE Kimberlite-3 detonated within the western part of the Siberian Craton. All of the regional phases (*P*, *Pg*, *S*, and *Lg*) are strong in the regional offset range. The *P* and *S* are strong at far offsets (> 1000 km) in both directions. The western branch of *Lg*, which travels into the West-Siberian Basin, is significantly weaker than the eastern one, traveling within the Siberian Craton. The *Lg* becomes very weak at ~1100 km offsets from the shotpoint, where it enters the Vilyui Depression. Similarly to the *Lg*, the *Pg* is visible to ~700 km to the west and ~1000 km to the east, where it appears to become quickly attenuated within the Vilyui Depression.

2.3.2 A model for the logarithm of amplitude ratios

Assume the amplitude of *Lg* is A_{Lg1} at position x_1 and A_{Lg2} at position x_2 , then for a given

frequency band, according to the attenuation equation:

$$A_{Lg2} = A_{Lg1} \left(\frac{x_2}{x_1} \right)^{-\gamma_{Lg}} e^{-\eta_{Lg}(x_2-x_1)}, \quad (2.1)$$

where γ_{Lg} is geometrical spreading parameter of Lg and η_{Lg} is the average attenuation factor of Lg between offsets x_1 and x_2 . Similarly, for the body-wave phases:

$$A_{Ph2} = A_{Ph1} \left(\frac{x_2}{x_1} \right)^{-\gamma_{Ph}} e^{-\eta_{Ph}(x_2-x_1)}, \quad (2.2)$$

where Ph represents the P or S phase, A_{Ph1} and A_{Ph2} are the corresponding amplitudes at x_1 and x_2 , respectively, γ_{Ph} is the geometrical spreading parameter, and η_{Ph} is the attenuation factor of between x_1 and x_2 .

By taking logarithm of the ratio of the amplitudes in equations (2.1) and (2.2), we obtain:

$$\log\left(\frac{A_{Lg2}}{A_{Ph2}}\right) - \log\left(\frac{A_{Lg1}}{A_{Ph1}}\right) = (\gamma_{Ph} - \gamma_{Lg})(\log(x_2) - \log(x_1)) + (\eta_{Ph} - \eta_{Lg})(x_2 - x_1). \quad (2.3)$$

Therefore, the difference of $\log(A_{Lg}/A_{Ph})$ between distances x_1 and x_2 is the differences of geometrical spreading and attenuation of the two phases between distances x_1 and x_2 .

Although a notable controversy in their interpretation can be noted (Ryberg et al., 1995), codas of the “fast” PNE phases (regional to teleseismic P and S) propagating through the mantle were interpreted as consisting of predominantly crustal S - and P waves generated in the vicinity of the receivers, and possibly partly near the source (Morozov et al., 2002). These coda waves sample large areas around the receivers, and they should be less affected by the variations of the crustal structure compared to Pg and Lg phases (Morozov et al., 2002). Therefore, the $Lg/Pcoda$ amplitude ratios could be expected to be a more stable parameter to measure the effects of the variations of crustal structure on Lg propagation.

For $Pcoda$ immediately before the S -wave onset at distances x_1 and x_2 :

$$A_{Pcoda1} = A_{P1} (t_1 - t_{01})^{-\gamma_{Pcoda}} e^{-\omega(t_1-t_{01})/Q_c} = A_{P1} \left(\frac{x_1}{V_S} - t_{Pcoda} - \frac{x_1}{V_P} \right)^{-\gamma_{Pcoda}} e^{-\omega(\frac{x_1}{V_S} - t_{Pcoda} - \frac{x_1}{V_P})/Q_c}, \quad (2.4)$$

$$A_{Pcoda2} = A_{P2} \left(\frac{x_2}{V_S} - t_{Pcoda} - \frac{x_2}{V_P} \right)^{-\gamma_{Pcoda}} e^{-\omega(\frac{x_2}{V_S} - t_{Pcoda} - \frac{x_2}{V_P})/Q_c}, \quad (2.5)$$

where A_{Pcoda1} and A_{Pcoda2} are $Pcoda$ amplitudes at distances x_1 and x_2 before the S phase; A_{P1} and A_{P2} are P phase amplitudes at distances x_1 and x_2 ; γ_{Pcoda} is the geometrical spreading parameter of $Pcoda$ and η_{Pcoda} is the attenuation parameter of $Pcoda$; ω is the angular frequency; V_P and V_S

are P and S phase velocities respectively; t_1 and t_{01} are the start time of $Pcoda$ and P phase at distance x_1 , and t_2 and t_{02} are the start time of $Pcoda$ and P phase at distance x_2 .

Because the time length of $Pcoda$ (t_{Pcoda} , taken as 10 s in this study) is small compared to the start times of S phase at far offsets: $\frac{x_1}{V_S} - t_{Pcoda} \approx \frac{x_1}{V_S}$, and therefore,

$$A_{Pcoda1} \approx A_{P1} \left(\frac{x_1}{V_S} - \frac{x_1}{V_P} \right)^{-\gamma_{Pcoda}} e^{-\eta_{Pcoda} x_1} \quad (2.6)$$

$$A_{Pcoda2} \approx A_{P2} \left(\frac{x_2}{V_S} - \frac{x_2}{V_P} \right)^{-\gamma_{Pcoda}} e^{-\eta_{Pcoda} x_2} \quad (2.7)$$

According to equation (2):

$$A_{Pcoda2} = A_{P1} \left(\frac{x_2}{x_1} \right)^{-\gamma_P} e^{-\eta_P (x_2 - x_1)} \left(\frac{x_2}{V_S} - \frac{x_2}{V_P} \right)^{-\gamma_{Pcoda}} e^{-\eta_{Pcoda} x_2}. \quad (2.8)$$

From equations (1), (6), and (8),

$$\log\left(\frac{A_{Lg2}}{A_{Pcoda2}}\right) - \log\left(\frac{A_{Lg1}}{A_{Pcoda1}}\right) = (\gamma_P + \gamma_{Pcoda} - \gamma_{Lg})(\log(x_2) - \log(x_1)) + (\eta_P + \eta_{Pcoda} - \eta_{Lg})(x_2 - x_1) \quad (2.9)$$

Therefore, the difference of $\log(A_{Lg}/A_{Pcoda})$ between distances x_1 and x_2 is the difference of geometrical spreading of P and $Pcoda$ with Lg and the difference in attenuation of P and $Pcoda$ with Lg between distances x_1 and x_2 .

2.3.3 Selection of calibration parameters

In interpreting the equation (2.9), our fundamental assumption is that the geometrical spreading parameters (γ) and most likely η_P are relatively smoothly varying with offsets (x), while crustal attenuation parameters η_{Lg} and η_{Coda} should be most sensitive to crustal heterogeneity. Subtraction of the regional offset trend from the logarithms of the amplitude ratios should thus remove the effects of geometrical spreading and average attenuation, and the residual variations of the log-amplitude ratios should only be mostly due to the attenuation along different crustal paths.

A general trend of $\log(A_{Lg}/A_P)$, $\log(A_{Lg}/A_S)$, and $\log(A_{Lg}/A_{Pcoda})$ (Figure 2-2) was first computed by averaging the logarithms of the amplitude ratios from PNEs Craton-2, 3, 4, and Kimberlite-3, 4 (Figure 1-1) along the travel paths within the Siberian Craton (excluding the Vilyui Depression, where the Lg behavior is anomalous). $\log(A_{Lg}/A_P)$ generally decreases with offset, and $\log(A_{Lg}/A_S)$ and $\log(A_{Lg}/A_{Pcoda})$ generally increase with offsets, with the slope of the former slightly smaller than the latter. According to equations (2.3) and (2.9), the attenuation parameter (η) affects the amplitude ratios stronger than geometrical spreading parameter (γ) because the range of variation in x is by about 10 times while the corresponding range of $\log(x)$

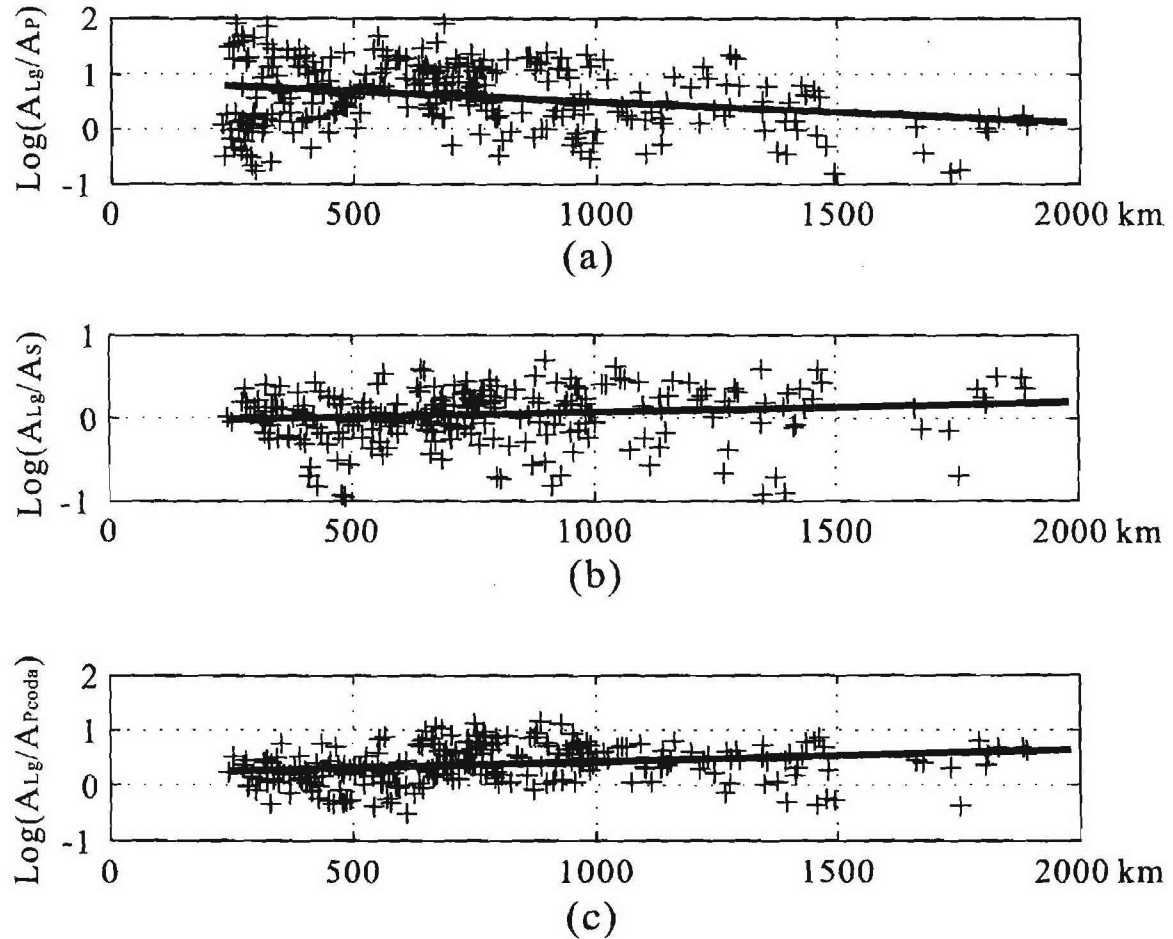


Figure 2-2. The average trends with offset of $\log(A_{Lg}/A_P)$, $\log(A_{Lg}/A_S)$, and $\log(A_{Lg}/A_{Pcoda})$ from PNEs Craton-2, Craton-3, Craton-4, Kimberlite-3, and Kimberlite-4 within the travel paths in the Siberian Craton (the segments within the Vilyui Depression are excluded). The $\log(A_{Lg}/A_P)$ ratios decrease with offset, while $\log(A_{Lg}/A_S)$ and $\log(A_{Lg}/A_{Pcoda})$ generally increase with offset. The scatter in the values of $\log(A_{Lg}/A_P)$ (upper plot) is much stronger than that of $\log(A_{Lg}/A_S)$ and $\log(A_{Lg}/A_{Pcoda})$.

is only ~ 1.0 (Figure 2-3). Accordingly, the attenuation parameters in equations (2.1) and (2.2) are difficult to separate from the geometrical spreading unless stringent assumptions about either the geometrical spreading or frequency dependence of attenuation are made. Therefore, we disregarded the $\log(x)$ terms in eq. (9) and determined a linear trend of the average logarithms of amplitude ratios (Figure 2-2) and subtracted them from the data.

Because of the variability of the P -wave amplitudes, the scatter in the observed values of $\log(A_{Lg}/A_P)$ is much larger than that of $\log(A_{Lg}/A_S)$ and $\log(A_{Lg}/A_{Pcoda})$, which are similar in magnitudes. Consequently, this paper uses the more stable $\log(A_{Lg}/A_S)$ and $\log(A_{Lg}/A_{Pcoda})$ to correlate the variations of amplitude ratios with the crustal structure.

Comparison of the logarithms of amplitude ratios measured within different frequency bands (Figure 2-3) shows that both ratios decrease with frequency, indicating that the Lg phase energy is concentrated at lower frequencies compared to S and $Pcoda$. Moreover, the variations of the log-amplitude ratios at low frequencies correlate with the variations of crustal structure better than those at higher frequencies. At low frequencies, both ratios remain constant or

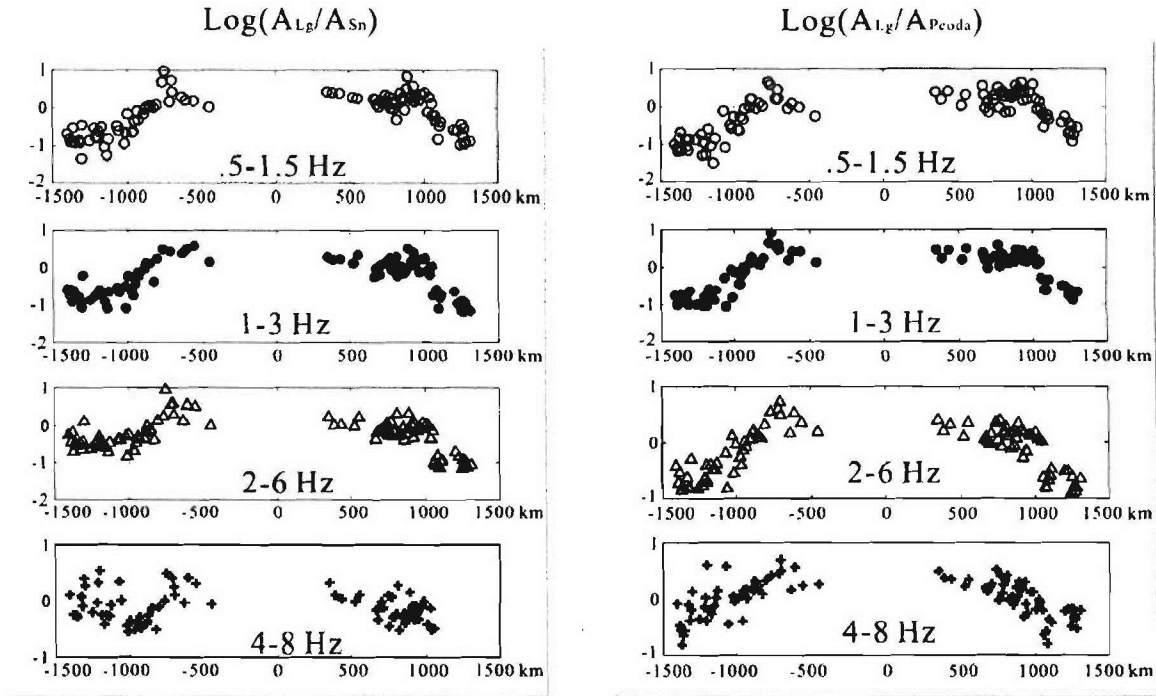


Figure 2-3. Logarithms of Lg/S and $Lg/Pcoda$ vector amplitude ratios from PNE Kimberlite-3 along KIMBERLITE profile (Fig. 1) within different frequency bands. The variation range of the amplitude ratios decreases with the increase of frequencies. For the frequency band 4-8 Hz, both amplitude ratios generally decrease with offset until background level, unrelated to the variations of crustal structure.

increase with offset within the Siberian Craton (except in the Vilyui Depression) while they decrease quickly with the travel paths in the Vilyui Depression and the West-Siberian Basin (Figure 2-3). By contrast, within the frequency band of 4 - 8 Hz, both amplitude ratios generally decrease with offsets until background level. Moreover, the variation range of the data is small with high frequencies. Therefore, a 0.5-3 Hz frequency band was used in this study.

The amplitude ratios were computed using single-component and vector measures, and also using different methods (RMS, peak, and median values) to compare the stability of these measures. The ratios determined from the first two methods were close, whereas the ratios of peak amplitudes showed large outliers and higher scatter. Vector measures provide consistently more stable estimates, apparently due to partial compensation of the effects of scattering (Kennett, 1993). In the following, we present the amplitude ratios computed using the RMS vector measure.

For both $\log(A_{Lg}/A_S)$ and $\log(A_{Lg}/A_{Pcoda})$, amplitude uncertainties due to discrete time sampling were estimated using a bootstrapping method (Figure 2-4; Mooney and Duval, 1993). The small errors demonstrated that the amplitude ratios are not significantly related to the lengths of the phase windows. Variations of the ratios among the adjacent stations represent a much stronger scatter and should be due to recording site effects and multipathing.

Because the *P*- and often *S*-wave phases are strong in PNE records, their codas contribute to the amplitudes of the later phases resulting in amplitude build-up competing with coda decay (Morozov et al., 2002). In this study, we do not attempt to remove the effects of the preceding coda contributions from the *Lg*. Instead, as is commonly done in observational seismology, we simply associate the average (RMS) amplitude within the corresponding phase windows. For example, the amplitude measured within the *Lg* time window as labeled as the *Lg* amplitude, A_{Lg} , and similarly for other phases (Figure 2-1).

2.4 Correlation of the amplitude ratios with crustal structures

After removal for the average offset trends, both $\log(A_{Lg}/A_S)$ and $\log(A_{Lg}/A_{Pcoda})$ exhibit local variations that appear to correlate with local structures. As an example, the CRATON profile (Figure 2-5) starts from the Pre-Ural High in the West-Siberian Basin, crosses the Ob-Tasovsk Depression in the West-Siberian Basin, traverses the Yenisei Ridge, the boundary between the West-Siberian Basin and the Siberian Craton, and passes the Tunguss Depression, the Mirninsk-Aihalsk High, the Vilyui Depression, and ends in the Aldan shield (Egorkin et al., 1987; Pavlenkova, 1996). The slopes of both ratios from the PNEs along the CRATON profile are $\sim -0.0017 \pm 0.0005 \text{ km}^{-1}$ within the Ob-Tasovsk Depression (profile distances 0-1000 km). This area is characterized by a thick ($\sim 8 \text{ km}$) and low-velocity ($V_P \sim 4 \text{ km/s}$) sedimentary cover and a rugged Moho (Figure 2-5). The slopes of both ratios change to $\sim -0.005 \pm 0.001 \text{ km}^{-1}$ near $\text{km} \sim 1000\text{-}1200$, where the crustal thickness increases by $\sim 10 \text{ km}$ from the West-Siberian Basin to the Yenisei Ridge. The slopes are small ($\sim 0 \text{ km}^{-1}$) from $\text{km} \sim 1300$ to 2500, corresponding to

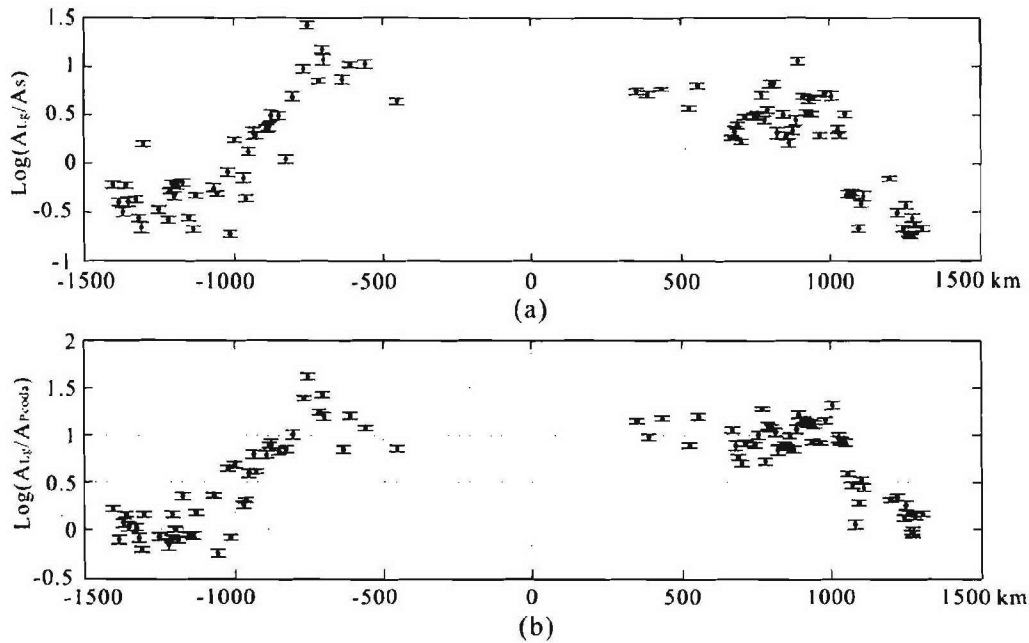


Figure 2-4. Vector amplitude ratios of (a) Lg/S , and (b) $Lg/Pcoda$, from PNE Kimberlite-3. The window length for Lg phase is 20 s, starting from the picked Lg start time. The window length of S phase is 10 s, starting from the picked S start time. The window length of the $Pcoda$ is selected as 10 s, ending at the picked S phase start time. The error bars indicate the measurement errors computed using 4000 samples of bootstrapped means of random samples taken from the data windows (Mooney and Dual, 1993).

the ~8-km-thick, but high-velocity ($V_P \sim 6$ km/s) Tunguss Basin, and the Mirninsk-Aihalsk High with a thin sedimentary cover and small Moho variation (< 5 km). The slopes of both ratios then become negative ($\sim -0.0045 \pm 0.001$ km $^{-1}$) within the Vilyui Depression (from km 2500-3000). In this area, an abrupt variation of crustal thickness (> 10 km) is combined with a thick (up to 13 km) low-velocity ($V_P \sim 4$ km/s) sedimentary cover.

At profile distances from km 2400 to 2700, the variations of both ratios from Craton-2 differ from those of Craton-4. For Craton-2, the ratios vary gently and then drop quickly to background level near km ~3000 (Figure 2-5). For PNE Craton-4, both ratios decrease quickly from km ~2700 to 2500, followed by an increase with offset until a profile distance of km ~2300. Between km 1000 and 1200 of the profile, the variations of both ratios from Craton-1 are also very different from Craton-3 and Craton-4. For Craton-3 and Craton-4, both ratios gradually increase with offsets until km ~1000 and then drop quickly in the area west of km 1000. For Craton-1, the ratios drop quickly from km 1000 to 1200 of the profile (Figure 2-5). The amplitude ratios from the two segments demonstrate that the effect of the variation of crustal thickness on the amplitude ratios; i.e., Lg propagation, depends on propagation direction. The effects of crustal thickening are different from crustal thinning.

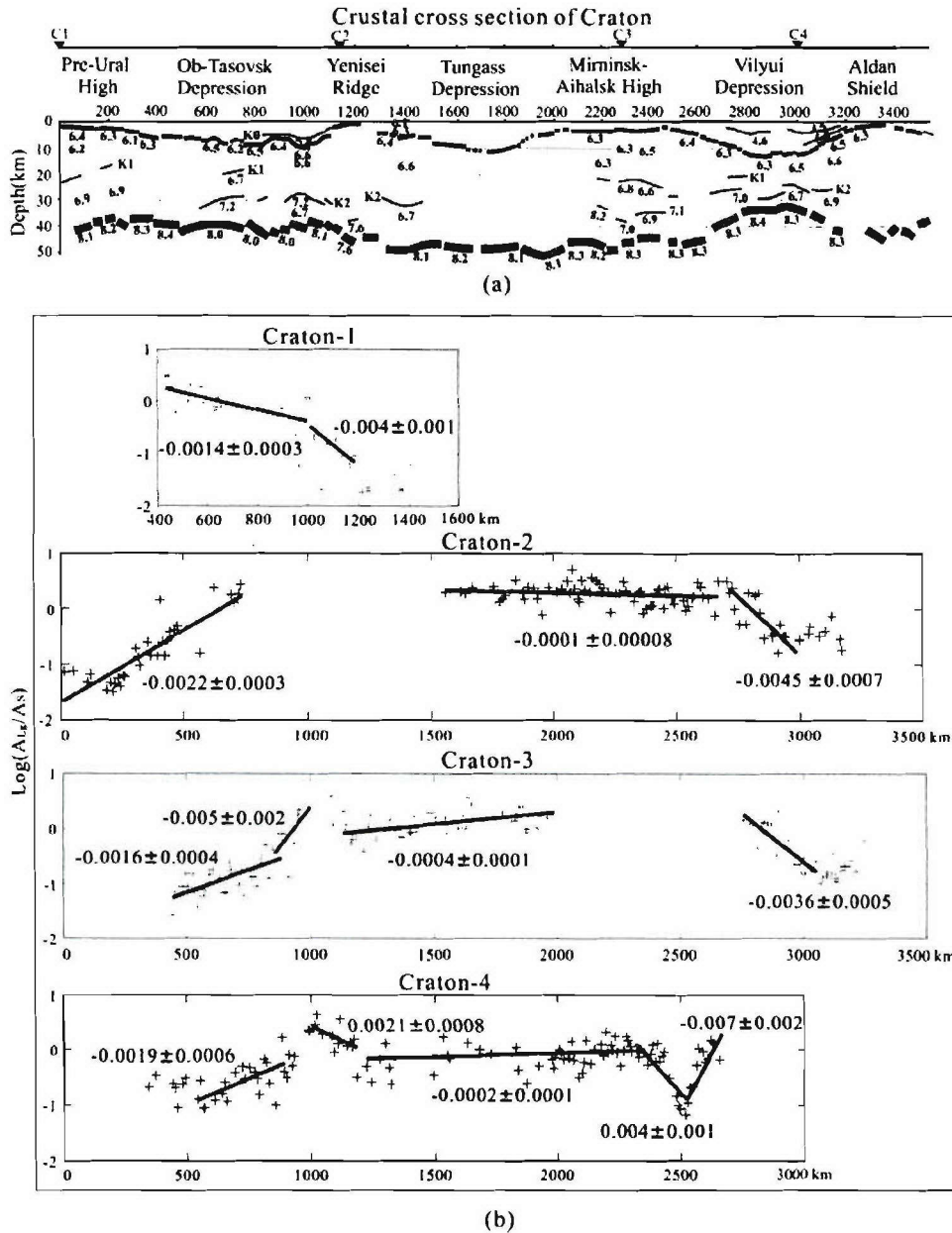


Figure 2-5. (a) Crustal cross section along the Craton profile (Egorkin et al., 1987), (b) $\log(A_{Lg}/A_S)$, and (c) $\log(A_{Lg}/A_{Pcoda})$ vector amplitude ratios from Craton-1, Craton-2, Craton-3, and Craton-4. Three basins along the profile are the Ob'-Tasovsk Depression, Tunguss Depression, and Vilyui Depression. The slopes of both ratios are $\sim 0.0018 \text{ km}^{-1}$ in the Ob-Tasovsk Depression; $\sim 0.005 \text{ km}^{-1}$ across the Yenisei Ridge; ~ 0 in the Tunguss Depression and the Mirninsk-Aihalsk High; and $\sim 0.0045 \text{ km}^{-1}$ in the Vilyui Depression.

Comparison of the slopes of both $\log(A_{Lg}/A_S)$ and $\log(A_{Lg}/A_{Pcoda})$ within the different segments along the seven PNE profiles to the corresponding Moho slopes, the velocities (V_P and V_S) and thickness of the sedimentary covers (Table 1) shows that the slopes of both ratios are close for all the similar structural segments along. Steeper slopes of $\log(A_{Lg}/A_S)$ and

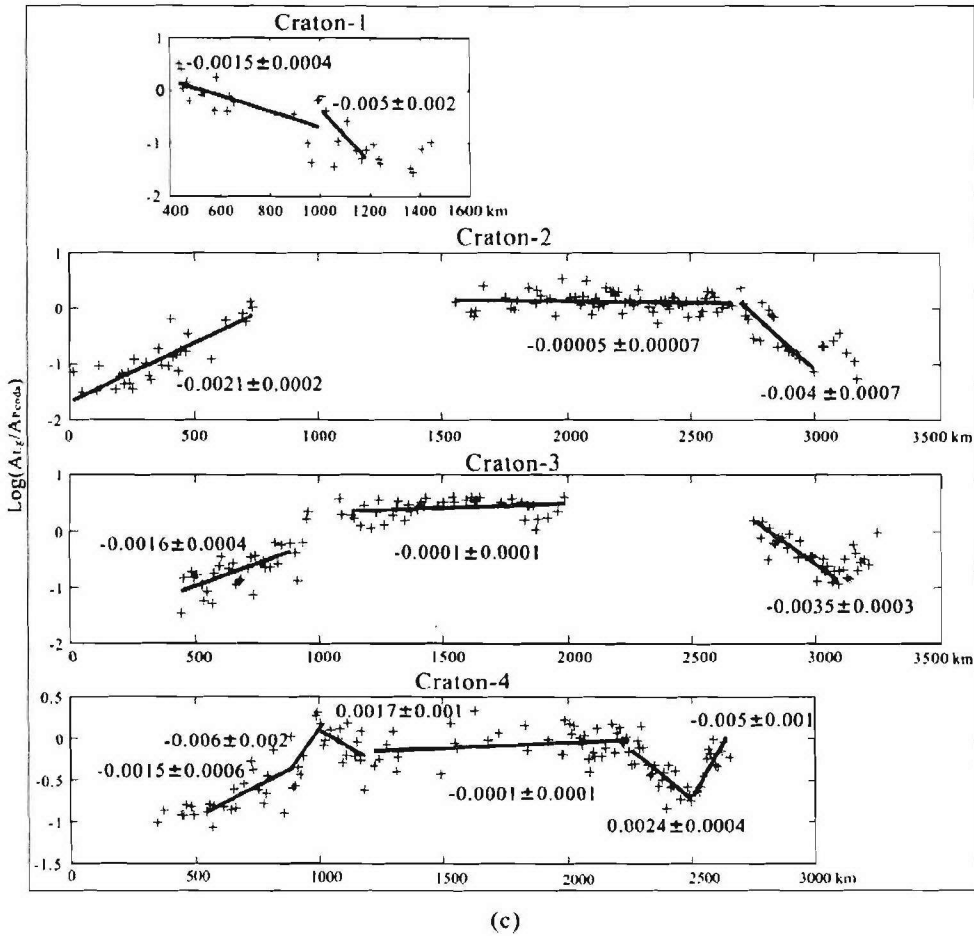


Figure 2-5, continued.

$\text{log}(A_{Lg}/A_{Pcoda})$ ($\leq -0.003 \text{ km}^{-1}$) are constrained within the Vilyui Depression, the Ural Mountains, across the Yenisei Ridge, the boundary between the Kazakh Massif and the West-Siberian Basin, and the Mezen' Depression. All of these locations correspond to abrupt crustal thinning or thickening. Moderate slopes ($-0.001 \sim -0.003 \text{ km}^{-1}$) correspond to thick low-velocity sedimentary cover and/or moderate crustal variations, the West-Siberian Basin, the Angara-Lena Terrace, and the southern part of the Siberian Craton. Low slopes ($> -0.001 \text{ km}^{-1}$) correspond to cratons with thin sedimentary covers (the Siberian Craton, the East-European Craton, and the Kazakh massif) or in sedimentary basins with thin (the Timan-Pechora Basin) or thick but high-velocity (the Tunguss Basin and the low-Angara Basin) sedimentary covers and small Moho variations. The shear velocity of the sedimentary basins is determined by comparing the P-wave velocity from the available velocity profiles and the global Crustal Model CRUST 2.0 for V_P , V_S , density, and thickness of all the crustal layers (Bassin et al., 2000).

2.5 Discussion

From the amplitude ratios of $\log(A_{Lg}/A_{Sn})$ and $\log(A_{Lg}/A_{P coda})$ at different frequency bands (Figure 2-3), the energy of the Lg phase is mainly concentrated at low frequencies, similar to the observations by Gupta et al. (1992). Moreover, both amplitude ratios within low-frequency bands correlate more clearly with the variations of crustal structure than do the high frequency band (4-8 Hz) since the Lg phase is mainly concentrated at low frequencies. Along the seven PNE profiles, the range of variation, the general trend, and the slopes (Figure 2-2, Table 1) of both $\log(A_{Lg}/A_{Sn})$ and $\log(A_{Lg}/A_{P coda})$ are always close to each other; this paper used both ratios to study Lg propagation in order to improve data reliability.

The slopes of $\log(A_{Lg}/A_{Sn})$ and $\log(A_{Lg}/A_{P coda})$ from all the 19 PNE seismic records along the seven profiles in northern Eurasia are summarized in Figure 2-6. Strong negative slopes ($< -0.003 \text{ km}^{-1}$) occur in the areas of abrupt crustal-thickness variations: the Ural Mountains ($\sim -0.007 \text{ km}^{-1}$), the Vilyui Depression (~ -0.005 to 0.004 km^{-1}), the Yenisei Ridge (~ -0.005 to -0.004 km^{-1}), the boundary between the Kazakh massif and the West-Siberian Basin ($\sim -0.004 \text{ km}^{-1}$), and the Mezen' Depression ($\sim -0.003 \text{ km}^{-1}$). Moderate negative slopes (< -0.001 and $> -0.003 \text{ km}^{-1}$) are found in the West-Siberian Rift (Ob-Tasovsk Depression) (-0.0022 to -0.0015 km^{-1}), within the West-Siberian Basin (-0.0015 km^{-1} to -0.0013 km^{-1}), and near the Baikal Rift Zone ($\sim -0.0014 \text{ km}^{-1}$). These values are interpreted as mainly corresponding to thick, low-velocity (V_P : $\sim 4 \text{ km/s}$) sedimentary cover and/or moderate Moho variations. Low negative slopes ($> -0.001 \text{ km}^{-1}$) usually correspond to thin (Timan belt and Timan-Pechora Basin) or thick but high-velocity sedimentary basins (Tunguss Basin and Low-Angara Basin) with gentle Moho variations. From PNE lines CRATON, KIMBERLTE, and METEORITE, the negative slopes of both ratios are stronger ($< -0.001 \text{ km}^{-1}$) in the south of Tunguss Basin compared to its northern part (~ 0) (Figure 2-6). According to the crustal cross section from KIMBERLTE and METEORITE, a $\sim 5\text{-km}$ Moho uplift is found in the south of the Tunguss Basin (Pavlenkova, 1996; GEON, personal communication). The residual slopes are flat $0 \pm 0.0006 \text{ km}^{-1}$ along the travel paths in cratons with thin sedimentary cover and slow Moho variations (part of the East-European Craton, the Siberian Craton, and the Kazakh massif).

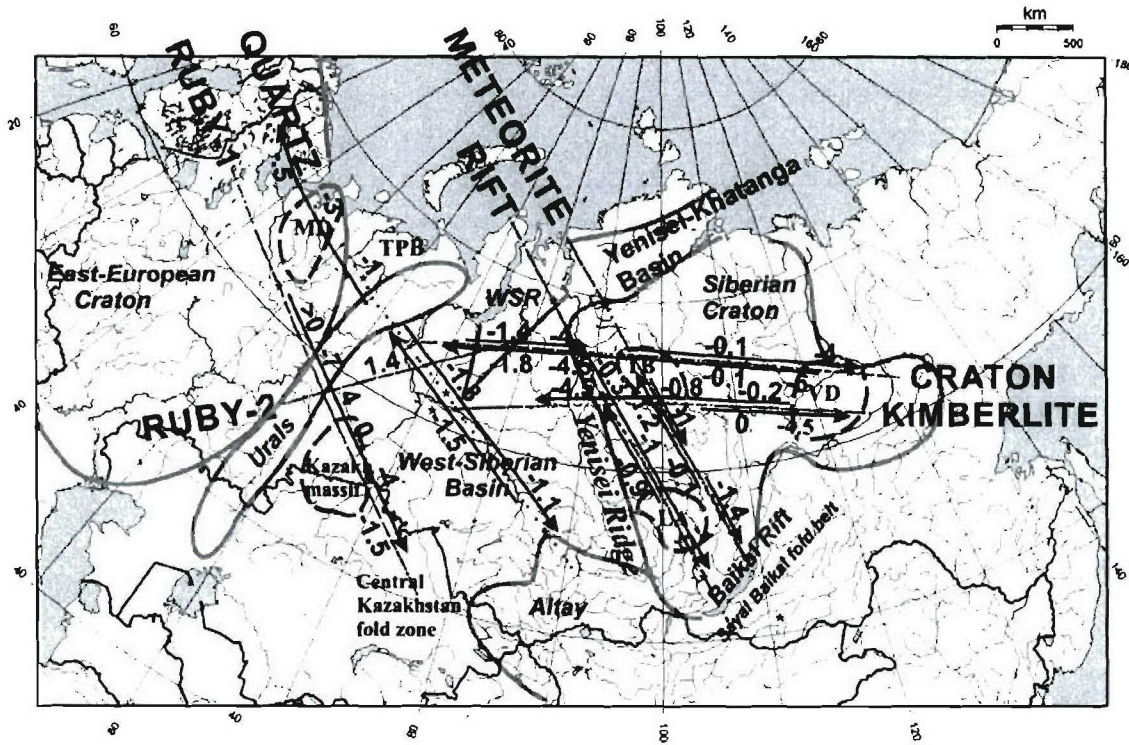


Figure 2-6. Sketch of tectonic boundaries of northern Eurasia and the PNE profiles. Labels indicate the observed residual slopes of the log-amplitude ratios along the profiles, in units of 0.001 km^{-1} . Abbreviations: WSR- West Siberian Rift; TB – Tunguss Basin; LA - Low-Angara Depression; VD - Vilyui Depression; MD – Mezen' Depression.

Along the seven PNE profiles, the variations of the slopes of both $\log(A_{Lg}/A_S)$ and $\log(A_{Lg}/A_{P coda})$ correlate with the variations of the corresponding crustal structure, mainly the Moho slope and the velocity and thickness of the sedimentary cover. Since the values of log-amplitude slopes of both $\log(A_{Lg}/A_S)$ and $\log(A_{Lg}/A_{P coda})$ are close to each other for all the profiles (Table 2-1), one linear relationship is simultaneously determined for both of them, as a function of the corresponding Moho depth gradient and the thickness of the sedimentary cover (H_S) divided by the shear velocity V_{SS} (Bassin et al., 2000). The selection of these parameter is dictated by a conjecture that the two most significant crustal properties ratios should be the corresponding Moho depth gradient (responsible for local focusing/defocusing of Lg waves) and the average S -wave travel time through a sedimentary cover (primarily responsible for attenuation).

According to Table 2-1, increased slopes of $\log(A_{Lg}/A_S)$ and $\log(A_{Lg}/A_{P coda})$ ($\leq -0.003 \text{ km}^{-1}$) are observed in the Vilyui Depression, the Ural Mountains, across the Yenisei Ridge, the boundary between the Kazakh massif and the West-Siberian Basin, and the Mezen' Depression. All of these locations correspond to abrupt crustal thinning or thickening. The moderate slopes ($-0.001 \sim -0.003 \text{ km}^{-1}$) correspond to thick low-velocity sedimentary cover and/or moderate

crustal variations, the West-Siberian Basin, the Angara-Lena Terrace, and the southern part of the Siberian Craton. The low slopes ($> -0.001 \text{ km}^{-1}$) are located in cratons with thin sedimentary cover (the Siberian Craton, the East-European Craton, and the Kazakh massif) or in sedimentary basins with thin (the Timan-Pechora Basin) or thick but high-velocity (the Tunguss Basin and the Low-Angara Basin) sedimentary cover and small Moho variations. The shear velocity of the sedimentary basins is determined by comparing the P -wave velocity from the available velocity profiles and the Global Crustal Model CRUST 2.0 for V_P , V_S , density, and thickness of all the crustal layers (Bassin et al., 2000).

Considering only the areas of crustal thinning (Table 2-1), the best-fit regression for log-amplitude ratios becomes:

$$\frac{d \log(A_{Lg}/A_{Ph})}{d(x)} = 5 \cdot 10^{-4} + 8.0 \cdot 10^{-2} \cdot \frac{d(H_M)}{d(x)} - 6 \cdot 10^{-4} \frac{H_S}{V_{SS}},$$

and in the areas of crustal thickening:

$$\frac{d \log(A_{Lg}/A_{Ph})}{d(x)} = 5 \cdot 10^{-4} - 7.5 \cdot 10^{-2} \cdot \frac{d(H_M)}{d(x)} - 6 \cdot 10^{-4} \frac{H_S}{V_{SS}}.$$

Since the regressions coefficients for crustal thinning and crustal thickening are close, a common linear regression was also determined:

$$\frac{d \log(A_{Lg}/A_{Ph})}{d(x)} = 5 \cdot 10^{-4} - 7.6 \cdot 10^{-2} \cdot \text{abs}\left(\frac{d(H_M)}{d(x)}\right) - 6 \cdot 10^{-4} \frac{H_S}{V_{SS}}.$$

Across the Ural Mountains with a $\sim 14 \text{ km}$ crustal root (Knapp et al., 1996; Pavlenkova, 1996; Morozova et al., 1999; Tryggvason et al., 2001; Table 2-1), both ratios show a decrease ($-0.007 \pm 0.001 \text{ km}^{-1}$ from RUBY-1) for $\sim 150 \text{ km}$ of offset, followed by an increase within another $\sim 150 \text{ km}$ ($0.004 \pm 0.001 \text{ km}^{-1}$ from RUBY-1).

Across the Vilyui Depression, in the crustal thinning direction, both ratios remain constant within the crustal thinning segment (from $\text{km } 2500$ to 2750 of Craton-2, Figure 2-5b,c; from $\text{km } 2400$ to 2500 of Kimberlite-3, Table 2-1), and then decrease sharply ($-0.0045 \pm 0.001 \text{ km}^{-1}$) to the noise level at further offsets. In the direction of crustal thickening, in the same area, both ratios decrease with offset ($-0.006 \pm 0.002 \text{ km}^{-1}$ from $\text{km } 2700$ to 2500 of Craton-4, Figure 2-5b,c), after which the amplitudes rebound back ($0.003 \pm 0.001 \text{ km}^{-1}$) from $\text{km } 2500$ to 2300 (Figure 2-5c).

Across the Yenisei Ridge, both ratios from PNEs Craton-3 and Craton-4 (Figure 2-5b,c) increase or remain constant within the crustal thinning segment from $\text{km } 1200$ to 1000 , and

decrease sharply at further offsets ($-0.005 \pm 0.002 \text{ km}^{-1}$) from km 1000 to 900. From PNE Craton-1, both ratios decrease (decay rates $-0.005 \pm 0.002 \text{ km}^{-1}$) from km 1000 to 1200 toward the Yenisei Ridge characterized by crustal thickening (Figure 2-5b,c).

By comparing both amplitude ratios across the Ural Mountains, the Vilyui Depression, and the Yenisei Ridge in both propagation directions, the decreases in slopes across crustal thinning and crustal thickening segments are similar, the decrease in slopes appears at farther offsets across the crustal thinning, while appears at the crustal thickening ramp across the crustal thickening (Figure 2-5). Moreover, there is a positive slope after crustal thickening (Figure 2-5), i.e., the *Lg* energy partially recovers after crustal thickening; therefore, the crustal thickening is observed to affect *Lg* propagation much less seriously than crustal thinning. For example, the effective slope of both ratios across the Vilyui Depression in the crustal thickening direction is $-0.006 \pm 0.003 = -0.003 \text{ km}^{-1}$; the effective slope across the Ural Mountains is $-0.007 \pm 0.004 = -0.003 \text{ km}^{-1}$. These observations on the different effects of crustal thinning and crustal thickening on *Lg* propagation should be addressed in a further study.

To explain the difference of *Lg* propagation characteristics in different directions across a same structure, consider two crustal models (Figure 2-7, Regan and Harkrider, 1989; Cao and

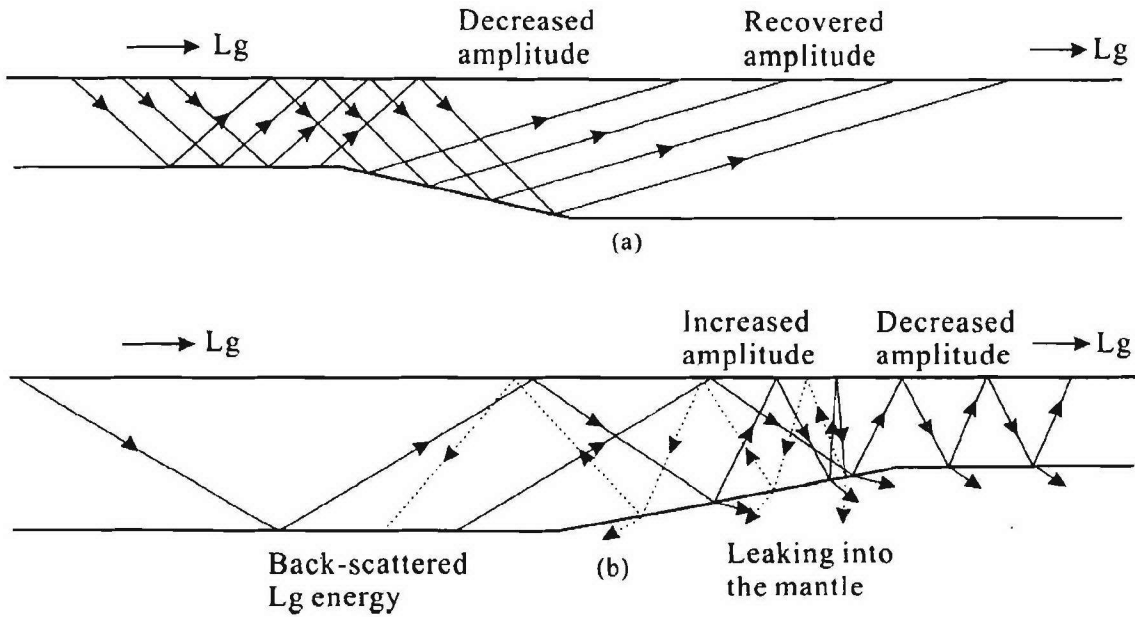


Figure 2-7. Comparison of the effects of (a) crustal thickening and (b) crustal thinning on *Lg* propagation in based on a ray-summing model. Across a crustal thickening segment, the *Lg* amplitude is expected to drop abruptly at the crust-thickening ramp due to de-focusing, but the amplitude will partially recover after passing the segment. Across a crustal thinning segment, the *Lg* amplitude increases at the upward Moho ramp due to ray focusing but drops quickly at farther offsets in the thin crust because of *Lg* energy leaking into the mantle or being backscattered (Regan and Harkrider, 1989; Cao and Muirhead, 1993).

Murihead, 1993). For crustal thickening; the Lg energy, and therefore the A_{Lg}/A_S and A_{Lg}/A_{Pcoda} amplitude ratios, decreases within the crustal thickening segment, which could be due to defocusing, and then increases after the crustal thickening segment. For crustal thinning: the Lg energy is redistributed within the crustal thinning segment where the energy could be converted to waves propagating into the mantle (Regan and Harkrider, 1989; Wu et al., 2000a, b) or backscattered to form waves propagating in the opposite direction (Cao and Muirhead, 1993). The Lg energy drops quickly at farther offsets within a thinner crust because a larger number of reflections are involved in formation of the Lg , as a result of which the energy could leak into the mantle or become backscattered into the opposite direction. Lg energy may increase along the crustal thinning ramp, which could be due to focusing and the backscattered Lg energy (Regan and Harkrider, 1989; Cao and Muirhead, 1993). Modeling of Lg propagation across a crustal anti-root and a crustal root (Wu et al, 2000a, b) showed that a crustal anti-root affects the Lg propagation stronger than a crustal root. In the latter case, although the wave fronts are also complicated due to scattering at the edges, more energy is trapped in the crust than the case of crustal anti-root in which a large percentage of Lg energy leaks into the mantle.

2.6 Conclusions

In northern Eurasia, the logarithms of Lg/Sn and $Lg/Pcoda$ amplitude ratios at frequencies of 0.5 – 3 Hz could be useful parameters to calibrate the effects of the variations in the crustal structure on Lg propagation. Records from seven ultra-long profiles sourced by 19 Peaceful Nuclear Explosions (PNEs) were used to correlate these amplitude ratios with the crustal structures. After removing the average trends with offsets measured for travel paths in the Siberian Craton, both ratios show increases with offsets or near-constant levels in cratonic areas with thin sedimentary cover and small Moho variations. The ratios decrease within sedimentary basins and near tectonic boundaries with abrupt variations of crustal thickness. A linear relationship of the slope of both logarithms of amplitude ratios with the corresponding Moho slope $d(H_M)/d(x)$ and the average vertical travel times of Lg through the sedimentary cover (H_s/V_{ss}) was determined:

$$\frac{d \log(A_{Lg}/A_{Ph})}{d(x)} = 5 \cdot 10^{-4} - 7.65 \cdot 10^{-2} \cdot \text{abs}\left(\frac{d(H_M)}{d(x)}\right) - 6 \cdot 10^{-4} \frac{H_s}{V_{ss}}.$$

Anomalous decreases in slopes were identified in tectonic areas with abrupt Moho variations, such as the Ural Mountains, the Vilyui Depression, the Yenisei Ridge, the boundary between the Kazakh massif and the West-Siberian Basin, and the Mezen' Depression. The observations suggest that abrupt variations of crustal thickness is the most important factor to affect Lg propagation. During propagation in the direction of crustal thickening, an increase in slope follows an abrupt decrease in slope, i.e., the Lg energy partially recovers at further offsets. Overall, from the PNE data, crustal thinning appears to be the most serious factor that affects Lg propagation.

Table 2-1 – Slopes of $\log(A_{Lg}/A_S)$ and $\log(A_{Lg}/A_{P coda})$ with source-receiver offset, the corresponding Moho slopes, and products of shear-wave slownesses with thicknesses of the sedimentary cover from the PNEs of this study

Profile	Distance (km)	location	$\log(A_{Lg}/A_S)$		$\log(A_{Lg}/A_{P coda})$		Slope of the Moho ($\Delta\text{Moho}/\Delta x$)	Vel. of the sedimentary cover		Shear Slowness \times thickness of the sedimentary cover (s/km \times km)
			slope	error	slope	error		V_p km/s	V_s km/s	
Craton	400-1000	West-Siberian Rift	-0.0018	0.0004	0.0017	0.0004	-5/800 = -0.006	3.8	1.9	1/1.9 \times 7 = 3.7
	1000-1200	Yenisei Ridge	-0.004	0.001	-0.005	0.002	10/200 = 0.05	3.7	1.9	1/1.9 \times 5 = 2.6
	1200-1000	Yenisei Ridge	-0.005	0.002	-0.006	0.002	-10/200 = -0.05	3.7	1.9	1/1.9 \times 5 = 2.6
	1300-1900	Siberian Craton	-0.0003	0.0001	-0.0001	0.0001	0	5.5	3.2	1/3.2 \times 7 = 2.2
	1900-2500	Siberian Craton	-0.0001	0.0001	-0.0008	0.00007	-5/1200 = -0.004	5.5	3.2	1/3.2 \times 3 = 0.93
	2800-2500	Vilyui Depression	-0.007	0.001	-0.005	0.001	13/300 = 0.043	4.1	2.6	1/2.6 \times 8 = 3.1
	2500-2800	Vilyui Depression	-0.004	0.0005	-0.0038	0.0005	-13/300 = -0.043	4.1	2.6	1/2.6 \times 8 = 3.1
Me Kimberlite	800-500	West-Siberian Basin	-0.0047	0.0008	-0.0045	0.0007	-8/300 = -0.027	3.8	1.9	1/1.9 \times 6 = 3.1
	1900-1100	Siberian Craton	-0.0006	0.0008	-0.0005	0.0006	-6/800 = -0.007	5.5	3.2	1/3.2 \times 6 = 1.9
	1800-2400	Siberian Craton	-0.0004	0.0002	-0.0002	0.0002	0	5.5	3.2	1/3.2 \times 3 = 0.9
Me	2400-2600	Vilyui Depression	-0.0051	0.0008	-0.0039	0.0008	-10/200 = -0.05	4.1	2.6	1/2.6 \times 7 = 2.7
	1000-1400	Siberian Craton	-0.0015	0.0002	-0.0011	0.0002	-5/400 = -0.012	5.5	3.2	1/3.2 \times 7 = 2.2

Quartz	1500-1900	Siberian Craton	0.0001	0.0002	0.0001	0.0002	0	5.2	3.0	$1/3.0 \times 4 = 1.3$
	2000-2400	Angara-Lena Terrace	-0.0014	0.0004	-0.0012	0.0003	-8/400 = -0.015	5.2	3.0	$1/3.0 \times 3 = 1.0$
	700-0	Baltic Shield	-0.0006	0.0003	-0.0004	0.0003	4/500 = 0.008	6	3.5	$1/6 \times 0 = 0$
	900-700	Mezen' Depression	-0.004	0.0015	-0.003	0.001	-6/200 = -0.03	3.6	1.8	$1/1.8 \times 3 = 1.7$
	1400-900	Timan Belt and Timan-Pechora Basin	-0.0009	0.0001	-0.0008	0.0001	2/400 = 0.005	4.0	2.4	$1/2.4 \times 2 = 0.83$
	3000-1700	West-Siberian Basin	-0.0015	0.0003	-0.0014	0.0003	5/1300 = 0.004	3.8	1.9	$1/1.9 \times 6 = 3.2$
	700-1000	Yenisei Ridge	-0.0002	0.0005	-0.0004	0.0004	0	5.5	3.2	$1/3.2 \times 1 = 0.31$
	1000-2400	Tungass Basin, Low-Angara Basin	-0.001	0.0001	-0.0009	0.0001	10/1400 = -0.007	5.2	3.0	$1/3.0 \times 6 = 2$
	350-600	East-European Craton	0.0017	0.0005	0.0012	0.0008	0	5.5	3.2	$1/3.2 \times 1 = 0.31$
	600-750	Ural Mountains	-0.007	0.001	-0.006	0.001	14/150 = 0.09	4.2	2.4	$1/2.4 \times 2 = 0.83$
Ruby-1	750-900	Ural Mountains	0.004	0.001	0.003	0.001	-14/150 = 0.09	4.2	2.4	$1/2.4 \times 2 = 0.83$
	800-1150	Kazakh massif	0.0003	0.0006	0.0001	0.0005	0	5.5	3.2	$1/3.2 \times 2 = 0.32$
	1150-1250	West-Siberian Basin	-0.0038	0.0009	-0.0031	0.0005	-7/100 = -0.07	3.8	1.8	$1/1.8 \times 2 = 1.1$
	1250-1800	West-Siberian Basin	-0.0013	0.0007	-0.0012	0.0004	3/550 = 0.005	3.8	1.8	$1/1.8 \times 4 = 2.2$
	300~1000	West-Siberian Basin	-0.0014	0.00017	-0.0014	0.00016	8/1000 = 0.008	3.9	2.0	$1/2 \times 5 = 2.5$
Ruby-2										

3 *Lg Q* distribution in Northern Eurasia from PNE data

3.1 Summary

Frequency-independent *Lg Q* is studied in northern Eurasia along the seven PNE profiles of this study using a two-station spectral ratio method. The frequency range is selected by hand based on the linear segment of the difference of the logarithms of spectra, mainly from 1 to 3 Hz. After determining the *Lg Q* between station pairs, an average *Lg Q* values are derived for the different regional crustal structures. The results show that *Lg Q* is the highest (800 and above) within the East-European Craton, the Kazakh massif, and the Siberian Craton with thin sedimentary covers. The lowest values of *Lg Q* (~300-400) are found within the Yenisei-Khatanga Basin, the West-Siberian Rift, the West-Siberian Basin, the Vilyui Depression, and the Mezen' Depression, where thick sedimentary covers and/or abrupt crustal thinning are also present. Low *Lg Q* is also found in the Ural Mountains with strong crustal thickening (up to 14 km). From the *Lg Q* computed in the areas with gentle Moho variations, a linear relationship between *Lg 1/Q* and the vertical travel time within the sedimentary cover is suggested: $1/Q = 10^{-3}[(0.57 \pm 0.05) + (0.59 \pm 0.02) \cdot H_s/V_{ss}]$. After removing the attenuation due to the sedimentary cover, a linear relationship is also determined for $1/Q$ as a function of crustal thinning, $1/Q = 10^{-3}[(0.9 \pm 0.1) - (17 \pm 3) \cdot d(H_M)/dx]$, and with crustal thickening: $1/Q = 10^{-3}[(0.9 \pm 0.1) + (25 \pm 2) \cdot d(H_M)/dx]$. The thick, low-velocity sedimentary cover and abrupt variations of crustal thickness appear to be the main factors affecting *Lg* propagation.

3.2 Introduction

Among the regional phases (*Pn*, *Pg*, *Sn*, and *Lg*), *Lg* is usually the strongest and most stable phase over a continental travel path and is widely used for source calibration ((Nuttli, 1986) and nuclear test discrimination (Knopoff et al., 1974; Walter et al, 1995; Xie, 2002). The *Lg* phase is interpreted as consisting of multiple supercritical *S*-wave reflections, or a superposition of higher-mode surface waves trapped within the crust (Knopoff et al., 1973), or near-source scattering of explosion-generated *Rg* into *S* is the primary contributor to the low-frequency *Lg* from nuclear explosions (Gupta et al., 1992; He et al., 2005). Because of its short wavelength and the entire propagation path confined within the crust, the *Lg* phase is highly sensitive to variations of crustal structure (Baumgardt, 2001; Li et al., submitted). Determining the distribution of inefficient *Lg* propagation is very important for yield

estimation, source calibration, and nuclear test monitoring.

From the wave propagation model

$$A(f, x) = S(f)G(x)R(f)e^{\frac{-\pi f x}{VQ}}, \quad (3.1)$$

where $S(f)$ is the source spectrum, $A(f, x)$ is the phase spectrum at offset x ; $G(x)$ is the geometrical spreading; $R(f)$ is the instrument response; Q is the average frequency-independent quality factor; and V is the phase velocity. In (1), Q is the only factor that affects the phase spectrum at an offset x ; therefore, by determining the Q distribution in different tectonic areas, Lg propagation characteristics in different areas can be understood and predicted.

Northern Eurasia, the largest landmass on Earth, includes different tectonic structures from old, stable shield to young, tectonic rift and orogenic belts. Therefore, determining the Lg Q distribution is significant for nuclear test monitoring, source yield or magnitude estimation. From the 1960s and 1980s, Russian scientists acquired a network of dense, linear, long-range (2000–4000 km), three-component Deep Seismic Sounding (DSS) profiles using chemical and Peaceful Nuclear Explosions (PNEs) over a large area of northern Eurasia. This historic data set provides a unique opportunity to study the seismic attenuation properties in northern Eurasia. Seven of these profiles including 19 PNEs were used in this study (Figure 1-1). The Lg phase is usually the strongest on the 19 seismic records and travels to far offsets (> 1000 km).

Lg Q was computed by different methods depending on the data set: frequency dependent Q by determining the Lg amplitude attenuation with distance within different frequency bands (Dwyer et al., 1983), frequency-dependent Q by determining the spectral difference between station pairs (Chun et al., 1987), frequency-independent Lg Q by determining the decrease in slope of the logarithm of Lg spectra, assuming a constant- Q model for a narrow frequency band near 1 Hz (Reese et al., 1999). Since the PNE data set is two-dimensional, with dense spacing but no true amplitude information which was lost during recording, a two-station spectral ratio method was applied to compute frequency-independent Lg Q within a narrow frequency band (~ 0.5 –3 Hz). After computing the average Lg Q between a pair of stations, an average Lg Q value is determined for each crustal segment along all the profiles.

3.3 Data processing

Frequency-independent Lg Q were measured from 19 PNEs along the seven reversed long-offset profiles with three-component seismic recorders spaced at about 10 km (Figure 1-1).

Before applying a two-station method to compute Lg Q , several processing steps were carried out to pick good traces with strong and unclipped Lg phase:

- 1) Trace editing. Since a number of spikes, data dropouts, clipping, and high noise occur, all the traces from all the PNEs are identified as good or bad for each regional phase (P_n , P_g , S_n and L_g) by looking at each trace, and only the traces marked with good for the L_g phase are used to compute $L_g Q$.
- 2) Estimation of L_g /pre- L_g amplitude ratios. Due to the strong pre- L_g P and S_n coda (Figure 3-1), L_g /pre- L_g amplitude ratio is calculated to determine if a trace will be used for $L_g Q$ calculation. The traces with the L_g /pre- L_g amplitude ratios less than 1.1 were discarded.
- 3) Measurement of the L_g and pre- L_g spectra. Due to the strong pre- L_g P and S_n coda energy, the L_g spectrum is compared with the pre- L_g spectrum to determine the frequency range for $L_g Q$ calculation. A 20-s window length is used for calculating $L_g Q$ and a 10-s window for pre- L_g noise.

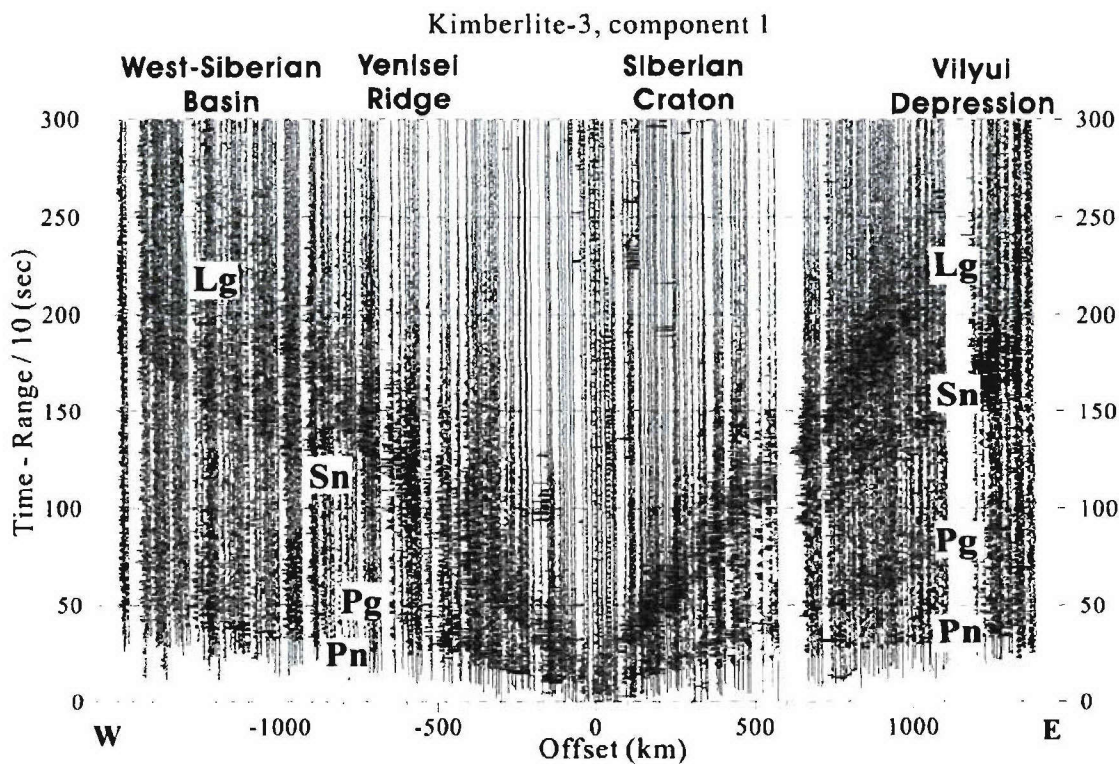


Figure 3-1. Vertical-component record from PNE Kimberlite-3, transverse component, filtered within a frequency band 0.5-8 Hz (the same as in Figure 2-1). The regional phases (P , P_g , S , and L_g) are clear and are observed to far offsets. Note that L_g in the western branch is significantly weaker than the eastern one. Within the eastern branch, L_g becomes very weak within the Vilyui Depression.

3.3.1 Interstation average Lg 1/ Q from a two-station method,

For a PNE source, denoting $A_1(f)$ and $A_2(f)$ the Lg amplitudes collected from two aligned stations at offsets x_1 and $x_1 + x_{12}$ respectively (Figure 3-2)

$$A_1(f) = S(f)G(x_1)R_1(f)\exp\left(\frac{-\pi f x_1}{Q_1 V_{Lg}}\right), \quad (3.2)$$

$$A_2(f) = S(f)G(x_2)R_2(f)\exp\left[\frac{-\pi f}{V_{Lg}}\left(\frac{x_1}{Q_1} + \frac{x_{12}}{Q_{12}}\right)\right], \quad (3.3)$$

where $S(f)$ is the source spectrum, $G(x_1)$ and $G(x_2)$ are the amplitude attenuation due to geometrical spreading within offsets x_1 and x_2 ; $R_1(f)$ and $R_2(f)$ are respectively the instrument responses at x_1 and x_2 and they are the same for all the stations (Ryaboy, 1989); V_{Lg} is the Lg group velocity (3.5 km/s); x_{12} is the distance between x_1 and x_2 ; Q_1 is the average quality factor within offset x_1 , and Q_{12} is the average quality factor between offsets x_1 and x_2 .

(2/3) and taking the logarithm,

$$\log\left(\frac{A_1(f)}{A_2(f)}\right) = \log\left(\frac{G(x_1)}{G(x_2)}\right) + \frac{\pi f x_{12}}{Q_{12} V_{Lg}}, \quad (3.4)$$

For frequencies f_1 and f_2 ,

$$\log\left(\frac{A_1(f_1)}{A_2(f_1)}\right) = \log\left(\frac{G(x_1)}{G(x_2)}\right) + \frac{\pi f_1 x_{12}}{Q_{12} V_{Lg}}, \quad (3.5)$$

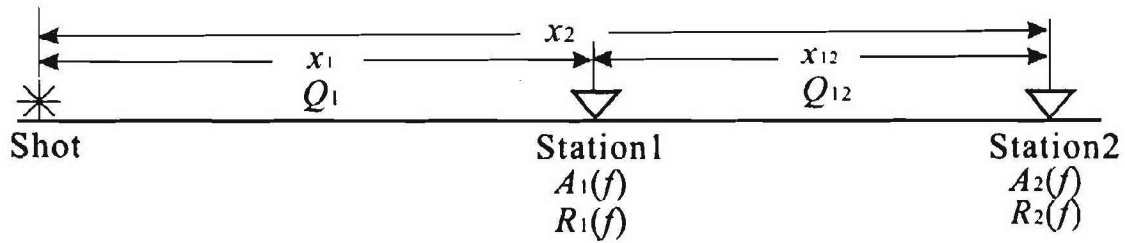


Figure 3-2. Schematic plot to show a two-station method to compute the average Lg Q between a pair of stations. x_1 and x_2 are respectively the offsets at station1 and station2, and x_{12} is the offset between x_1 and x_2 . Q_1 and Q_{12} are respectively the average Q within offset x_1 and between offsets x_1 and x_2 . $A_1(f)$ and $A_2(f)$ are the amplitude spectra at offsets x_1 and x_2 ; $R_1(f)$ and $R_2(f)$ are the station response at offsets x_1 and x_2 .

$$\log\left(\frac{A_1(f_2)}{A_2(f_2)}\right) = \log\left(\frac{G(x_1)}{G(x_2)}\right) + \frac{\pi f_2 x_{12}}{Q_{12} V_{Lg}}, \quad (3.6)$$

eq. (2.6)-(2.5),

$$\log\left(\frac{A_1(f_2)}{A_2(f_2)}\right) - \log\left(\frac{A_1(f_1)}{A_2(f_1)}\right) = \frac{\pi x_{12}(f_2 - f_1)}{Q_{12} V_{Lg}}, \quad (3.7)$$

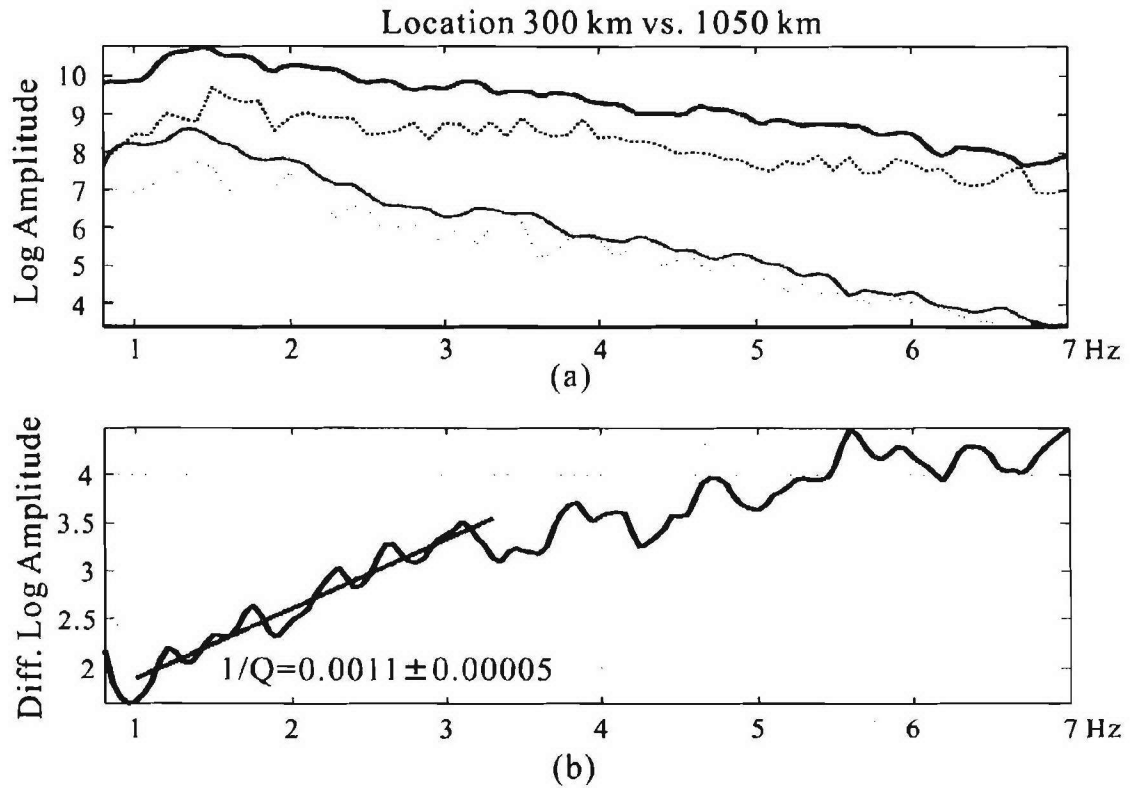


Figure 3-3. (a) Logarithms of Lg amplitudes of Kimberlite-3 at offsets 300 and 1050 km, and (b) the Lg $1/Q$ determined from the difference between the two logarithms of amplitudes. In plot (a), the black and gray thick lines are the Lg amplitude at offsets 300 and 1050 km respectively, and the dashed black and gray lines are the amplitude of the pre- Lg noise at the two locations. In (b), $1/Q$ is determined from the slope of the difference of the logarithms of amplitudes, and the error of $1/Q$ is determined from the error of the slope.

$$\frac{1}{Q_{12}} = \frac{\log\left(\frac{A_1(f_2)}{A_2(f_2)}\right) - \log\left(\frac{A_1(f_1)}{A_2(f_1)}\right)}{(f_2 - f_1)} \times \frac{V_{Lg}}{\pi\alpha_{12}}. \quad (3.8)$$

Therefore, by determining the slope of the difference of the logarithms of spectra between two stations (**Figure 3-3**), the interstation average $1/Q$ can be determined. The error of $1/Q$ is also determined from the error of the slope.

If we compare the Lg and the pre- Lg spectra (**Figure 3-3**), the Lg energy is mainly concentrated at low frequencies, and the Lg phase is highly contaminated by P and S coda at higher frequencies, the same observation obtained by Shin and Herrmann (1987). In this study, Lg $1/Q$ is calculated in a narrow low-frequency band (~ 1 -3 Hz). The principle of choosing a two-station combination is that: the offset of both stations is large enough to observe the Lg phase, and the distance between a station pair should be large enough to reduce measurement error of the interstation Q (> 200 -300 km in this study).

3.3.2 Averaging Lg Q along the different crustal segments

In order to determine the Lg Q along different crustal segments, only the station pairs where both stations are located in the same structure are used to calculate the average Lg $1/Q$ of that segment. After calculating Lg $1/Q$ and the corresponding error for all the station pairs that are located in a same structure, an average Lg Q is determined by the mean of the Q values from different station pairs and a standard error of the Q is also provided.

In addition, the site response is important and highly depends on local geology. In this study, the site response is assumed as constant over a narrow frequency band (~ 1 -3 Hz), which is used to calculate Lg Q . Moreover, by averaging the Lg Q determined from different station pairs and from the mostly reversed profiles, the effect of site response is minimized.

3.4 Results

The frequency-independent Lg Q distribution along the seven PNE profiles (**Figure 1-1**) was determined using the two-station spectral ratio method.

The Craton profile (**Figure 1-1**) starts from the Pre-Ural High, traverses the Ob-Tasovsk Depression in the West-Siberian Basin, the Yenisei Ridge, the Tungass Basin, the Mirninsk-Aihalsk High, the Vilyui Depression, and ends in the Aldan Shield (**Figure 3-4a**). In the Ob-Tasovsk Depression, Lg Q is 401 ± 43 (**Figure 3-4b**), corresponding to the thick (up to 8 km) and low-velocity (V_P 2.5-5.5 km/s) sedimentary cover with gradual Moho variations. Lg Q is 273 ± 24 across the Yenisei Ridge, where the Moho increases from ~ 40 km in the West-Siberian Basin to ~ 50 below the Tungass Basin and the sedimentary cover is up to 10 km. Lg Q is 634 ± 93 in the Tungass Basin, the thick (up to 10 km) but high-velocity ($V_P \sim 5.5$ km/s) sedimentary cover with a flat Moho. Lg Q is the highest (1077 ± 196) in the

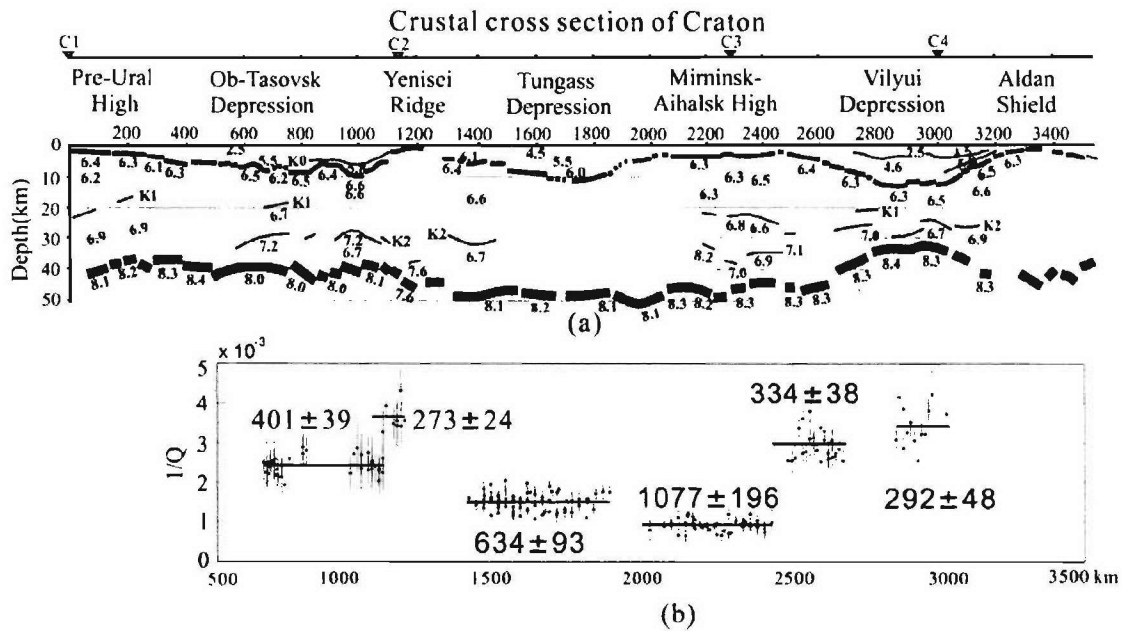


Figure 3-4. (a) Crustal cross section of CRATON (Egorkin et al, 1987), and (b) $Lg Q$ distribution along the profile determined from the PNEs Craton-1 (C1), Craton-2 (C2), Craton-3 (C3), and Craton-4 (C4). $Lg Q$ is ~400 in the West-Siberian Basin, and ~300 across the Yenisei Ridge. $Lg Q$ is ~650 in the Tunguss Basin and ~1000 in the Mirninsk-Aihalsk High, and decreases to ~300 in the Vilyui Depression. The calculated $Lg 1/Q$ with the two-station method is put in the middle of the two locations with error bars. The determined $Lg Q$ is the average of the inverted $1/Q$ along each segment.

Mirninsk-Aihalsk High with thin sedimentary cover (< 3 km) and a flat Moho. $Lg Q$ decreases to 292 ± 48 in the Vilyui Depression, a thick (more than 10 km) and low-velocity (V_P 2.5-4.5 km/s) sedimentary cover with an abrupt crustal thinning (up to 13 km).

Similarly, $Lg Q$ was computed within different crustal segments along other PNE profiles: KIMBERLTE (Figure 3-5), METEORITE (Figure 3-6), RIFT (Figure 3-7), QUARTZ (Figure 3-8), and RUBY-1, RUBY-2 (Figure 3-9). The $Lg Q$ of different crustal segments along all the seven PNE profiles with the corresponding Moho slope, the velocity (V_P and V_S) and thickness of the sedimentary cover is listed in Table 3-1.

From Table 3-1, the highest $Lg Q$ (800 and above) is found within the East-European Craton, the Kazakh massif, and the Siberian Craton with thin sedimentary cover and gently varying Moho. The high $Lg Q$ (~500-700) is located in the Tunguss Basin and the Low-Angara Basin with thick but high-velocity sedimentary cover and gently varying Moho, and the Angara-Lena Terrace with gradual crustal thinning toward the BRZ. The $Lg Q$ is ~360-420 in the West-Siberian Basin with thick (up to 8 km) and low-velocity sedimentary cover. The lowest $Lg Q$ (~300) is located in the Vilyui Depression, the Ural Mountains, the

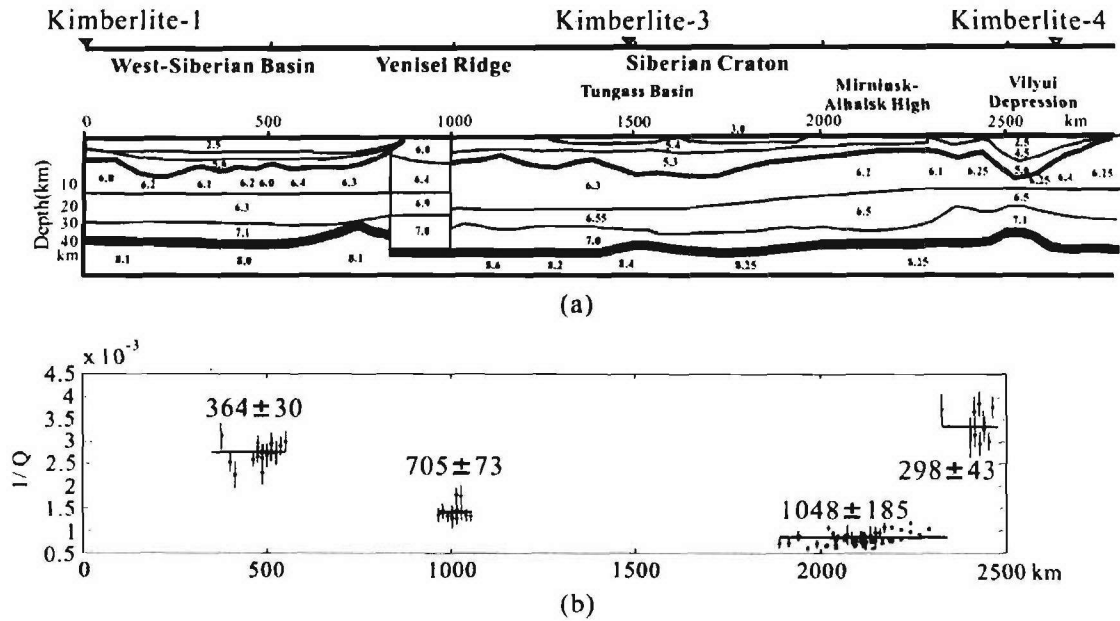


Figure 3-5. (a) Crustal cross section of KIMBERLITE profile (Pavlenkova, 1996), and (b) $Lg Q$ distribution along this profile determined from Kimberlite-1, Kimberlite-3, and Kimberlite-4. $Lg Q$ is ~ 360 in the West-Siberian Basin, ~ 700 between the Yenisei Ridge and the Tunguss Basin, and ~ 1050 in the Mirninsk-Aldansk High. $Lg Q$ is the lowest (~ 300) in the thick, low-velocity Vilyui Depression.

Mezen' Depression, and across the Yenisei Ridge, the boundary between the West-Siberian Basin and the Siberian Craton, with thick or thin sedimentary cover but abrupt crustal thickening or thinning. The shear velocity of the sedimentary basins is determined by comparing the P -wave velocity from the available velocity profiles and the Global Crustal Model CRUST 2.0 for V_P , V_S , density, and thickness of all the crustal layers (Bassin et al., 2000).

3.5 Discussion

After $Lg Q$ is calculated along different crustal segments of the seven PNE profiles, the $Lg Q$ distribution in northern Eurasia is determined to range between ~ 1000 and ~ 300 (Figure 3-11).

$Lg Q$ is ~ 1000 in the East-European Craton (Figure 3-8, Figure 3-9 and Figure 3-11) with thin sedimentary cover and gentle Moho (Belousov et al., 1992; Pavlenkova, 1996; Morozova et al., 1999). To the east of the Baltic shield, $Lg Q$ is 392 ± 39 below the Mezen' Depression, a ~ 3 -km-thick ($V_P \sim 4.0$ km/s) sedimentary basin with an abrupt crustal thinning (~ 35 km thick with an anti-root up to 6 km; Belousov et al., 1992; Morozova et al., 1999).

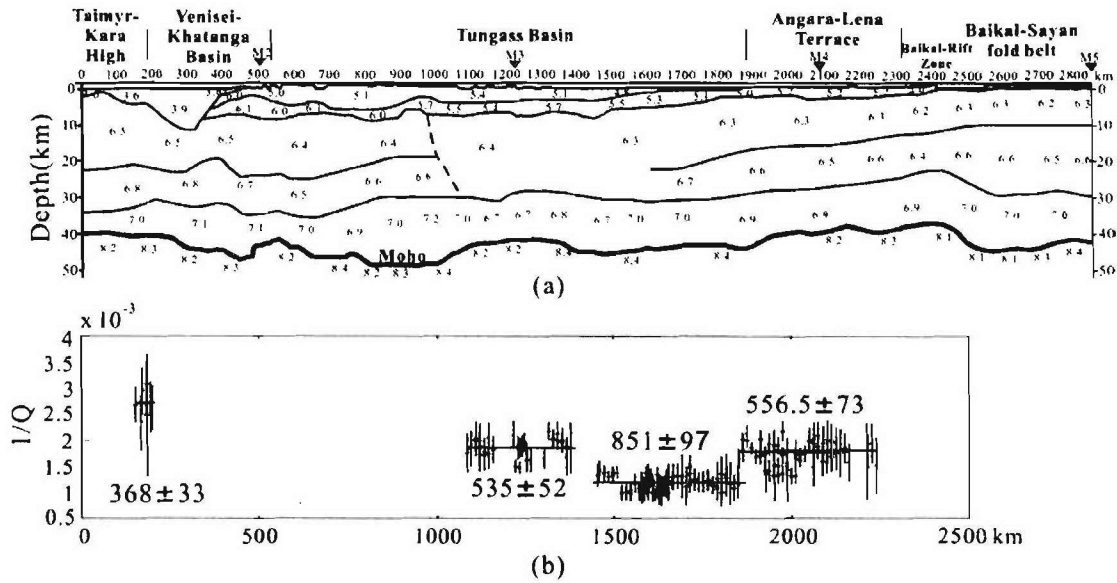


Figure 3-6. (a) Crustal cross section of METEORITE profile (GEON, personal communication; Pavlenkova, 1996), and (b) $L_g Q$ distribution along the profile determined from Meteorite-2 (M2), Meteorite-3 (M3), Meteorite-4 (M4), and Meteorite-5 (M5). $L_g Q$ is ~ 370 in the Yenisei-Khatanga Basin, and ~ 550 in the Tunguss Basin with ~ 4 -km Moho uplift. $L_g Q$ is ~ 850 between the Tunguss Basin and the Angara-Lena Terrace with thin sedimentary cover and a flat Moho. $L_g Q$ is ~ 550 in the Angara-Lena Terrace, which could be due to the crustal thinning and the decreasing crustal and upper mantle velocities toward the BRZ.

Across the Ural Mountains, $L_g Q$ is determined as ~ 320 by QUARTZ (Figure 3-8) and RUBY-1 (Figure 3-9a) profiles, corresponding to the abrupt crustal thickening (up to ~ 14 km; Morozova et al., 1999; Tryggvason et al., 2001).

The West-Siberian Basin was traversed by CRATON (Figure 3-4), KIMBERLITE (Figure 3-5), QUARTZ (Figure 3-8), and RUBY-2 (Figure 3-9b) profiles, and the $L_g Q$ is averaged as 394 ± 40 , corresponding to the thick (up to 8 km) and low-velocity (~ 2.5 - 5.5 km/s) sedimentary cover and gradual Moho variations. $L_g Q$ could be lower in the West-Siberian Rift with thick sediments (up to 13 km) according to the determined Q of ~ 300 along RUBY-2 profile (Figure 3-9b).

$L_g Q$ is determined as 273 ± 24 across the Yenisei Ridge (Figure 3-4) from east to west along the Craton profile, where the sedimentary cover is up to 10 km and the crustal thickness changes abruptly from ~ 50 km in the Siberian Craton to ~ 40 km in the West-Siberian Basin in a complicated way (Egorkin et al., 1987). Moreover, the high attenuation could also be due to the probable higher temperature in the crust and the upper mantle inferred from the P -wave velocities lower than other regions (Figure 3-4; Egorkin et al., 1987).

$Lg Q$ is determined as 368 ± 33 in the Yenisei-Khatanga Basin (Figure 3-6) with thick (up to more than 10 km) and low-velocity ($V_P \sim 3.8$ km/s) sedimentary cover but a gently varying Moho.

$Lg Q$ varies greatly in the different areas of the Siberian Craton: high (>800 , Figure 3-4 through Figure 3-7, and Figure 3-11) in the areas with thin sedimentary cover and gentle Moho variations, ~ 600 -700 in the Tunguss Basin and the Low-Angara Basin (Figure 3-4 through Figure 3-7, and Figure 3-11)) with thick (up to 10 km) but high-velocity ($V_P \sim 5.3$ -5.5 km/s) sedimentary cover and a gradually varying Moho. $Lg Q$ is 556 ± 73 in the Angara-Lena Terrace, corresponding to the ~ 3 km sedimentary cover and ~ 8 km crustal thinning toward the BRZ, and 307 ± 45 in the Vilyui Depression filled with loose (V_P 2.5-4.5 km/s) rocks up to more than 10 km thick and with an uplift of Moho up to 13 km.

In summary, the determined $Lg Q$ is the highest in stable tectonic areas with thin sedimentary cover and gentle Moho variations, and the lowest in the areas with thick and low-velocity sedimentary cover, or abrupt variations of crustal thickness, or both. The $Lg Q$ distribution in different tectonic areas in northern Eurasia determined in this study compares to the 1-Hz Lg coda Q determined by Mitchell et al (1997) in a tomographic method ($3^\circ \times 3^\circ$ resolution), but the resolution is greatly improved. From Mitchell et al, Lg coda Q is > 800 in the East-European Craton and the Siberian Craton, and ~ 400 -500 in the West-Siberian Basin. However, the low $Lg Q$ across the Ural Mountains and the Vilyui Depression is not resolved due to the low resolution. Similarly, Phillips et al (2000) determined the 1-Hz Lg Q distribution in central Asia by a tomographic method in $2^\circ \times 2^\circ$ resolution. $Lg Q$ is 800 or

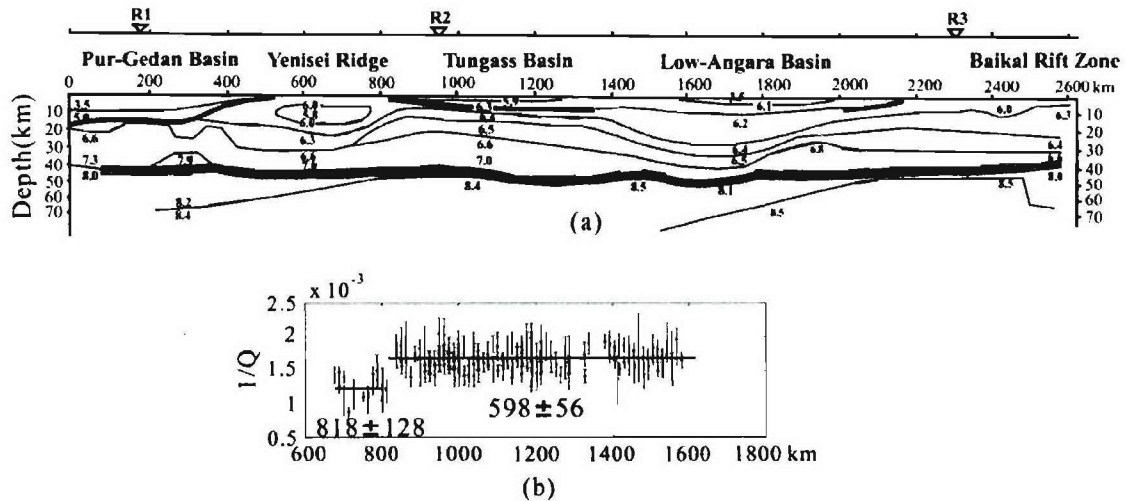


Figure 3-7. (a) Crustal cross section of RIFT profile (Pavlenkova et al., 2002), and (b) $Lg Q$ distribution along the profile determined from Rift-1 (R1), Rift-2 (R2), and Rift-3 (R3). $Lg Q$ is ~ 800 between the Yenisei Ridge and the north of the Tunguss Basin, and decreases to ~ 600 in the Tunguss Basin and the Low-Angara Basin.

above for platforms and older crust, ~ 500 in basins (Tarim Basin), and the lowest (200-400) in mountains (Tian Shan and the Pamir Range).

The distribution of $Lg Q$ in northern Eurasia determined from the seven PNE profiles corresponds to the slopes of the logarithms of Lg/Sn and $Lg/P coda$ amplitude ratios (Li et al., submitted). In the East-European Craton, the Kazakh massif, the Siberian Craton with thin sedimentary cover, $Lg Q$ is the highest (>800), and the residual slope of both ratios is ~ 0 . In the Vilyui Depression and the Ural Mountains, $Lg Q$ is the lowest (~ 300), and the decrease slope of the ratios is the highest (~ -0.004 to -0.005 km^{-1} in the Vilyui Depression; $\sim -0.007 \text{ km}^{-1}$ along the crustal thickening segment followed by an increase in slope $\sim 0.003 \text{ km}^{-1}$ at further offsets in the Urals). In the West-Siberian Basin and the Yenisei-Khantanga Basin with thick, low-velocity sedimentary cover and a gently varying Moho, $Lg Q$ is ~ 400 , and the slope is ~ -0.0015 to -0.002 km^{-1} . The medium $Lg Q$ (~ 500 -700) is determined in the Tunguss Basin and the Low-Angara Basin with thick (6-8 km) but high-velocity sedimentary cover and gentle Moho variations, and the Angara-Lena Terrane with moderate crustal thinning toward the BRZ, where the slope of the ratios is $\sim -0.001 \text{ km}^{-1}$.

According to the crustal cross sections (Figure 3-4 to Figure 3-8), the average velocity in the crystalline crust along all the seven profiles does not vary much, ~ 6.5 - 6.7 km/s (Pavlenkova 1996). Therefore, the Lg attenuation due to the crystalline crust is probably the

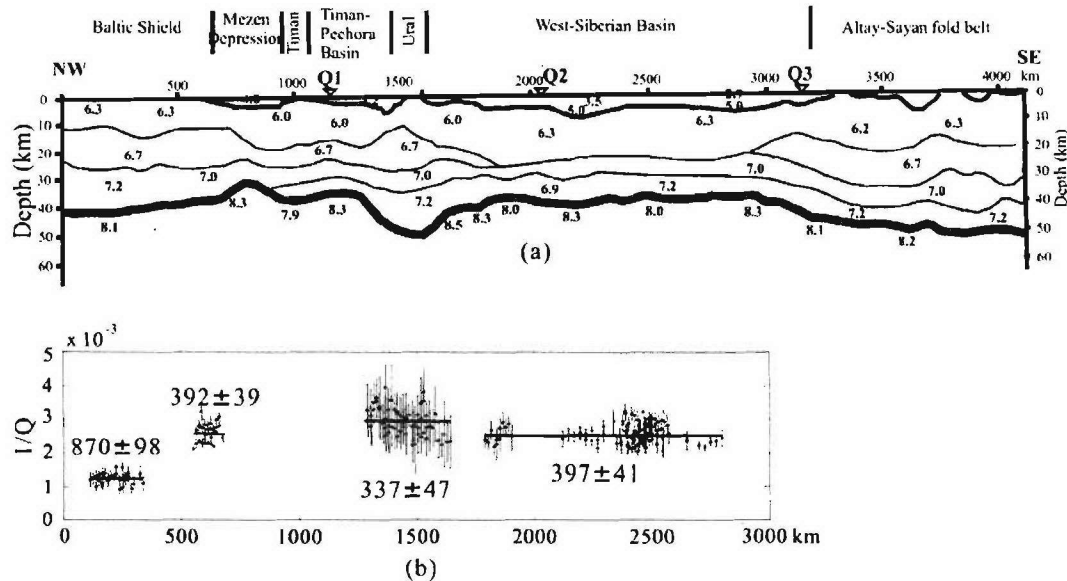


Figure 3-8. (a) Crustal cross section of QUARTZ profile (Belousov et al., 1992; Morozova et al., 1999), and (b) $Lg Q$ distribution along the profile determined from Quartz-123 (Q1), Quartz-213 (Q2), and Quartz-323 (Q3). $Lg Q$ is ~ 900 in the East-European Craton, ~ 400 in the Mezen' Depression corresponding to an abrupt uplift of the Moho, and is ~ 340 across the Ural Mountains due to abrupt crustal thickening. $Lg Q$ is ~ 400 in the West-Siberian Basin with thick sediments and gently varying Moho.

same for all the profiles. If we compare the $Lg Q$ variations with the variations of the crustal structure, not only the velocity and the thickness of the sedimentary cover, but the abrupt variations of the crustal thickness, affect the Lg attenuation. For the crustal segments with gentle Moho variations (the absolute Moho slope ≤ 0.01 , Table 1), a linear relationship between $Lg 1/Q$ and the vertical travel time in the sedimentary cover is determined,

$$1/Q = 10^{-3} [(0.57 \pm 0.05) + (0.59 \pm 0.02) \cdot H_s / V_{ss}], \quad (3.9)$$

where H_s and V_{ss} are respectively the thickness and shear velocity (Bassin et al., 2000) of the sedimentary cover. After removing the effect of the sedimentary cover on $1/Q$ with eq. (3.9), a linear relationship is also determined for $1/Q$ with crustal thinning

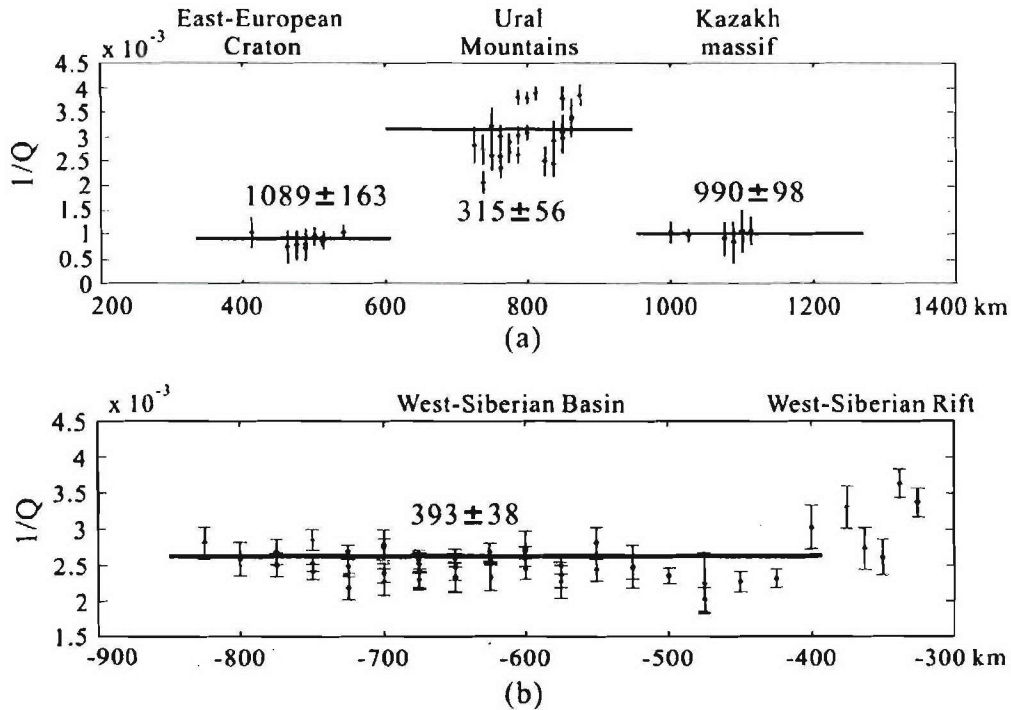


Figure 3-9. (a) $Lg Q$ distribution along (a) RUBY-1 and (b) RUBY-2 profiles. Along the RUBY-1 profile, $Lg Q$ is ~ 1100 in the East-European Craton with thin sedimentary cover and gently varying Moho (Pavlenkova, 1996). $Lg Q$ is ~ 300 across the Ural Mountains due to the abrupt crustal thickening. $Lg Q$ is ~ 1000 in the Kazakh massif, a stable crustal block with thin sedimentary cover and a flat Moho (Pavlenkova, 1996). From RUBY-2 profile, $Lg Q$ is determined as ~ 400 in the West-Siberian Basin, and shows a trend decreasing toward the West-Siberian Rift with a decreasing Moho and increasing sedimentary cover (Aplonov, 1995; Pavlenkova, 1996).

$$1/Q = 10^{-3} [(0.9 \pm 0.1) - (17 \pm 3) \cdot d(H_M)/dx], \quad (3.10)$$

and with crustal thickening

$$1/Q = 10^{-3} [(0.9 \pm 0.1) + (25 \pm 2) \cdot d(H_M)/dx], \quad (3.11)$$

where H_M is the Moho depth and x is offset. Because not enough Lg Q values were determined for crustal thinning and crustal thickening, the linear relationship of $1/Q$ with both the vertical travel time and the Moho slope was not determined simultaneously. From

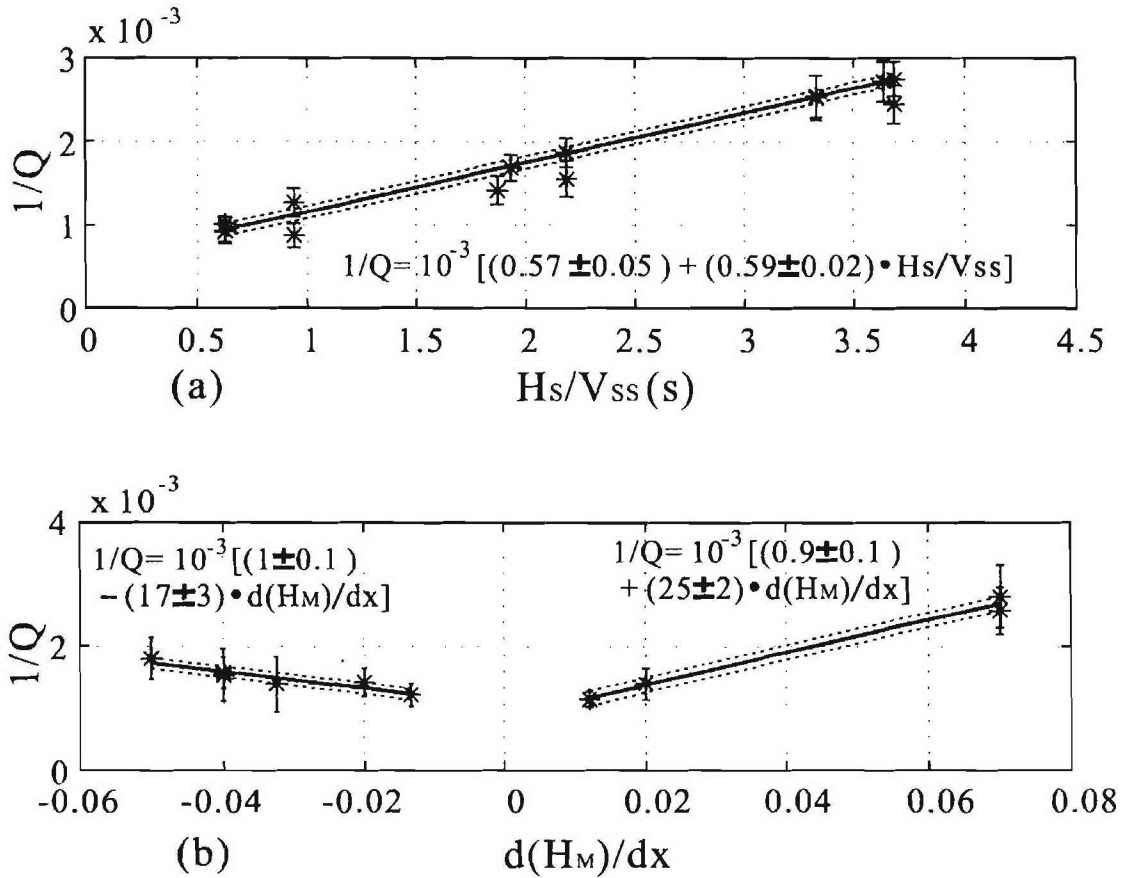


Figure 3-10. (a) the linear relationship between Lg $1/Q$ and the vertical travel time through the sedimentary cover from the crustal segments with gentle Moho variations; (b) the linear relationship of Lg $1/Q$ with crustal thinning and crustal thickening after removing the attenuation due to the sedimentary cover using the equation determined in (a). From the crustal segments with gently varying Moho, the linear relationship between $1/Q$ and the vertical travel time through the sedimentary cover is quite obvious. In (b), with the limited data points, the Lg attenuation due to crustal thickening is more important than crustal thinning.

the above equations, $Lg Q$ is ~ 1000 or above in the areas with no sediments and no Moho variations, consistent with the observations in stable shields and platforms (Mitchell et al., 1997; Phillips et al., 2000).

From eq. (3.10) and (3.11), the Lg attenuation due to crustal thickening could be more important than crustal thinning. The reason could be that: 1) across a crustal thickening segment, the Lg wave propagates longer distances, and therefore, suffers more attenuation due to the heterogeneities (Wu et al., 2000) and inelastic properties of the crust. 2) if we regard the Lg phase as guided waves, the low frequencies are blocked while higher frequencies are passed across a crustal thinning segment (Dresen and Rüter, 1994); therefore, the high-frequency energy is comparably richer across a crustal thinning segment than a crustal thickening segment, i.e., constant $Lg Q$ determined by the spectral ratio method is higher across a crustal thinning segment.

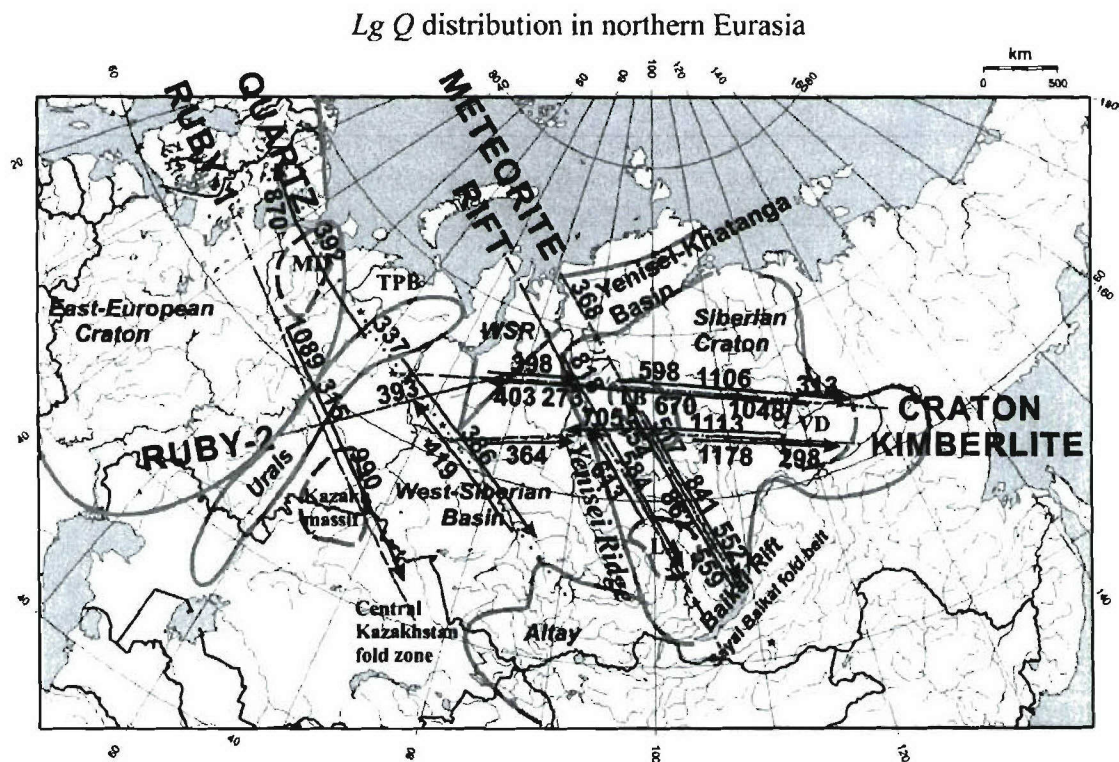


Figure 3-11. Distribution of PNE $Lg Q$ in northern Eurasia. The highest $Lg Q$ (800 and above) is found in the East-European Craton, the Kazakh massif, and the north and central part of the Siberian Craton. The medium $Lg Q$ (500-700) is located in the western part of the Siberian Craton, mainly the Tunguss Basin and the Low-Angara Basin. The low $Lg Q$ (~ 400) is determined in the West-Siberian Basin, the Yenisei-Khantanga Basin, and the Mezen' Depression. The lowest $Lg Q$ (~ 300) is determined in the Vilyui Depression, across the Yenisei Ridge, and across the Ural Mountains. (MD – Mezen' Depression; TB – Tunguss Basin; LA – Low-Angara Basin; VD – Vilyui Depression; WSR – West-Siberian Rift)

On the contrary, from the decreased slope of the logarithm of Lg/Sn and $Lg/P coda$ amplitude ratios (Chapter 2), the attenuation caused by crustal thinning appears to be more significant than from crustal thickening. The two apparently opposite observations can be reconciled by the different mechanisms of the observed phenomena. The constant $Lg Q$ determines the decrease slope of the Lg spectrum with offset due to the inelastic properties of the crust. However, the amplitude ratios compute the Lg amplitude within a narrow frequency band, and the decrease of the amplitude is due to both the inelastic properties of the crust and the scattering due to the heterogeneities in the crust, and the latter is much more frequency-dependent (Toksoz and Johnston, 1981) and therefore, does not affect the Lg spectrum as much as the former factor.

3.6 Conclusions

The frequency-independent $Lg Q$ is determined along seven PNE profiles using a two-station spectral ratio method. The highest Q (>800) is obtained in the East-European Craton, the Kazakh massif, and the Siberian Craton. The medium Q ($\sim 500-700$) is determined in the Tunguss Basin, the Low-Angara Basin and the Angara-Lena Terrace near the BRZ. $Lg Q$ is ~ 400 in the West-Siberian Basin, the Yenisei-Khatanga Basin and the Mezen' Depression. $Lg Q$ is the lowest (~ 300) in the Vilyui Depression, the Ural Mountains and across the Yenisei Ridge.

By comparing $Lg 1/Q$ with the corresponding crustal structure, the sedimentary basin and the abrupt variations of crustal structure are determined as the most important factors that affect Lg propagation. From the $1/Q$ determined along the crustal segments with gentle Moho variations (the absolute slope < 0.01), a linear relationship between $1/Q$ and the vertical travel time through the sedimentary cover is determined as

$$1/Q = 10^{-3}[(0.57 \pm 0.05) + (0.59 \pm 0.02) \cdot H_s / V_{ss}]$$

with high confidence (std error = 7.6×10^{-5}). After removing the attenuation due to the sedimentary cover, a linear relationship is also determined for $1/Q$ with crustal thinning

$$1/Q = 10^{-3}[(0.9 \pm 0.1) - (17 \pm 3) \cdot d(H_M)/dx],$$

and with crustal thickening,

$$1/Q = 10^{-3}[(0.9 \pm 0.1) + (25 \pm 2) \cdot d(H_M)/dx].$$

The frequency-independent Lg attenuation due to the abrupt crustal thickening could be more important than abrupt crustal thinning, which could be attributed to the longer travel path through a crustal thickening segment and the guided wave characteristics of the Lg -phase where low-frequency energy is blocked but high-frequency energy passes across a

crustal thinning segment. In conclusion, both low-velocity sedimentary cover and abrupt variations of crustal thickness are the principle factors that affect Lg attenuation in northern Eurasia.

Table 3-1 –The $Lg Q$, the corresponding Moho slope, and the corresponding product of shear slowness with thickness of the sedimentary cover from all the PNEs along different segments

Profile	Distance (km)	Location	Lg Q		Slope of the Moho ($\Delta \text{Moho}/\Delta x$)	Sedimentary cover		Vertical travel time of Lg in sedimen tary cover (s)
			Value	Error		Vp km/s	Vs km/s	
Craton	400-1000	West-Siberian Rift	398	35	-4/800 = -0.005	3.8	1.9	7 3.7
	1000-500	West-Siberian Rift	403	43	4/800 = -0.005	3.8	1.9	7 3.7
	1200-1000	Yenisei Ridge	273	24	-10/200 = -0.005	3.8	1.9	5 2.6
	1400-2000	Tunguss Basin	598	79	0	5.5	3.2	7 2.2
	2000-1200	Tunguss Basin	670	107	0	5.5	3.2	7 2.2
	2000-2500	Mirinsk-Aihalsk High	1106	207	-2/500 = -0.004	5.5	3.2	2 0.63
	2500-2000	Mirinsk-Aihalsk High	1048	185	2/500 = -0.004	5.5	3.2	2 0.63
	2500-3000	Vilyui Depression	316	48	-13/400 =	4.1	2.6	10 3.8

Kimberlite	300-800	West-Siberian Basin	364	30	0	3.8	1.9	6	3.2
					0.033				
	1800-900	Tunguss Basin	705	73	-3/300 = -0.01	5.5	3.2	6	1.9
	1800-2400	Miminsk-Aihalsk High	1178	244	-3/600 = -0.005	5.5	3.2	3	0.93
	2400-1800	Miminsk-Aihalsk High	1113	126	3/600 = 0.005	5.5	3.2	3	0.93
	2400-2800	Vilyui Depression	298	43	-10/250 = -0.04	4.1	2.6	8	3.1
	300-0	Taimyr-Kara High	368	33	-3/300 = -0.01	3.8	1.9	8	4.2
	1000-1400	Tunguss Basin (center)	517	48	-4/400 = -0.01	5.4	3.1	7	2.3
	1400-1000	Tunguss Basin (center)	554	56	-4/400 = -0.01	5.4	3.1	7	2.3
	1400-1900	Tunguss Basin (south)	841	89	0	5.2	3.0	3	1
Meteorite	1900-1400	Tunguss Basin (south)	862	105	0	5.2	3.0	3	1
	1800-2400	Angara-Lena Terrace	552	78	-8/400 = -0.02	5.0	2.9	3	1.03
	2400-1800	Angara-Lena Terrace	559	68	8/400 = 0.02	5.0	2.9	3	1.03

600-0	Baltic Shield	870	98	5/600 = 0.009	5.5	3.2	0	0
1000-500	Mezen' Depression	392	39	-6/200 = -0.03	3.6	1.8	3	1.7
1800-1300	Ural Mountains	337	47	14/200 = 0.07	4.2	2.4	2	0.83
1800-3000	West-Siberian Basin	386	44	0	3.8	1.8	6	3.3
3000-2000	West-Siberian Basin	419	38	0	3.8	1.8	6	3.3
600-1000	Yenisei Ridge	818	128	-3/600 = -0.005	5.5	3.2	1	0.31
1000-2000	Tungass Basin, Low-Angara Basin	584	56	-10/1000 = -0.01	5.2	3.0	6	2
1500-1000	Tungass Basin, Low-Angara Basin	613	58	10/1000 = 0.01	5.2	3.0	6	2
350-600	East-European Craton	1089	163	0	5.5	3.2	1	0.31
600-900	Ural Mountains	315	56	14/200 = 0.07	4.2	2.4	2	0.83
800-1150	Kazakh massif	990	98	0	5.5	3.2	2	0.62
Ruby-2 -300--1000	West-Siberian Basin	393	38	6/800 = 0.008	3.9	2.0	5	2.5

Quartz

Rift

Ruby-1

4 Empirical PNE source scaling

4.1 Summary

The yield- m_b relationship is compared for different media (salt, sandstone/shale, clay, and limestone/dolomite) and in different shot depths from 95 well-coupled peaceful nuclear explosions (PNEs) in former Soviet Union (FSU; Sultanov et al, 1999). The yield of the explosions ranges from 1.1 to 80 kt, the m_b ranges from 4.4 to 6.0, the shot depth ranges from 161 to 2485 m and mostly between 395 and 1212 m, and the source media include salt, sandstone/shale, clay, limestone/dolomite, granite, gabbro, tuff, apatite, anhydrite, and chalk. With a modified Mueller-Murphy explosion-source model (Serenio et al., 1988), the corner frequency (f_c) of P and S source spectra of 19 PNEs is determined from the regional phases P_n and S_n , and then a linear relationship of $\log_{10} f_c$ with $\log_{10} W$ (W : yield) and with m_b is established respectively. Among the analyzed media, for a same yield, the m_b is the highest in clay, the second highest in salt, the third highest in sandstone/shale and the lowest in limestone/dolomite. The m_b generally decreases with the increase of source depth. With the source depths between 485 and 1212 m, the determined yield- m_b relationship for clay is $m_b = (5.02 \pm 0.16) + (0.45 \pm 0.14) \times \log_{10} W$, and a general linear relationship is determined for all the “hard” rocks except clay as: $m_b = (4.46 \pm 0.07) + (0.75 \pm 0.07) \times \log_{10} W$. From the 19 PNEs, the f_c of S -phase is close but lower than P -wave. The linear correlation of $\log_{10} f_c$ with m_b appears stronger than with $\log_{10} W$. For the P -wave, $\log_{10} f_c = (3.8 \pm 0.3) - (0.63 \pm 0.06) \times m_b$; for S -wave, $\log_{10} f_c = (3.4 \pm 0.3) - (0.56 \pm 0.06) \times m_b$.

4.2 Introduction

Regional phases P_n , P_g , S_n and L_g have been widely used to determine seismic-source characteristics (Molnar et al., 1973; Murphy, 1977; Der et al., 1985; Evernden et al., 1986; Xie, 1993, 1996), estimate seismic magnitude and yield (Evernden, 1970; Mueller and Murphy, 1971; Bache, 1982; Nuttli, 1986; Ringdal et al., 1992; Murphy, 1996; Murphy et al., 2001), and determine the variations of crustal structure (Rapine et al., 1997; Sandvol et al., 2001; Li et al., submitted). The regional phases also become significant for the Comprehensive Nuclear Test-Ban Treaty (CTBT) research to discriminate small-magnitude nuclear explosions from other seismic sources including earthquakes and chemical explosions (Murphy and Bennett, 1982; Pomeroy et al., 1982; Walter et al., 1995; Xie, 1999; 2002).

Magnitude determinations play a central role to estimate source yield and to discriminate nuclear explosions from earthquakes. However, the yield- m_b relationship depends on source medium and source depth. Calibration of the yield- m_b relationship in different media and different depths is necessary for better estimates of source yield. Moreover, the source characteristics of nuclear explosions should be different from

earthquakes according to the different source mechanisms (Xie, 1996). Understanding the spectral characteristics of different sources is critical to use the source parameters and regional phases for nuclear discrimination.

From Mueller and Murphy's model (1971) and the work of Hays (1969) and Bache (1982), for a same medium, the phase amplitude is proportional to W^m/h^n , while the corner frequency (f_c) is proportional to h^a/W^b . The W is yield in kt, and h is source depth in m. For a fixed depth h , the m_b is proportional to the logarithm of W ($\log W$), while the logarithm of f_c ($\log f_c$) is inversely proportional to $\log W$. Similarly, for a fixed W , the m_b is inversely proportional to the logarithm of h ($\log h$), while $\log f_c$ is proportional to $\log h$. Therefore, a linear relationship is expected between m_b and $\log f_c$.

The source medium is another important factor to affect m_b and f_c . The magnitude is higher and the f_c is lower for an explosion in soft medium such as clay than an explosion in a dense, rigid formation such as limestone (Sharpe, 1942). With the established m_b - f_c relationship, the source yield can be estimated with higher credibility by determining m_b through both phase amplitude and corner frequency.

Due to the complexity of geology in different tectonic areas, calibration of the

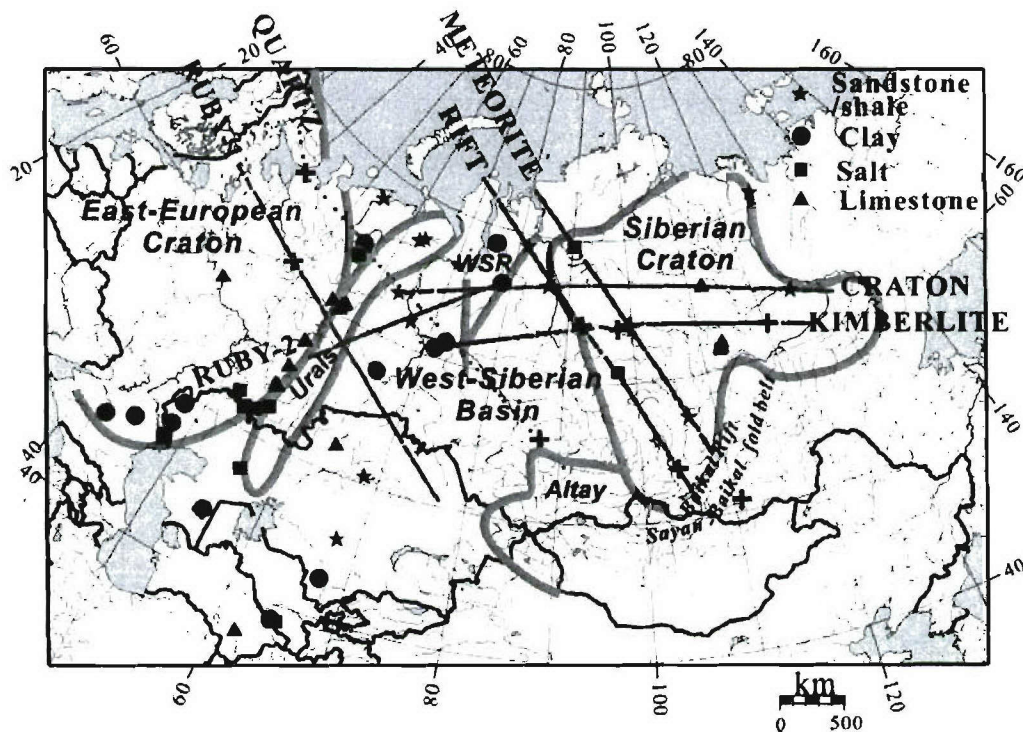


Figure 4-1. Map of northern Eurasia and the locations of PNEs carried out from 1960s to 1980s.

The shots marked by big stars were exploded in sandstone/shale, the shots marked by solid dots were exploded in clay, the shots marked by squares were exploded in salt, the shots marked by triangles were exploded in limestone/dolomite, and the shots marked by "+" were exploded in other media including 3 shots in granite, 2 in tuff, 2 in chalk, 1 in gabbro, and 1 in anhydrite. Seven PNE profiles (RUBY-1, RUBY-2, QUARTZ, CRATON, KIMBERLITE, RIFT, and METEORITE) with 19 PNEs were analyzed in this paper.

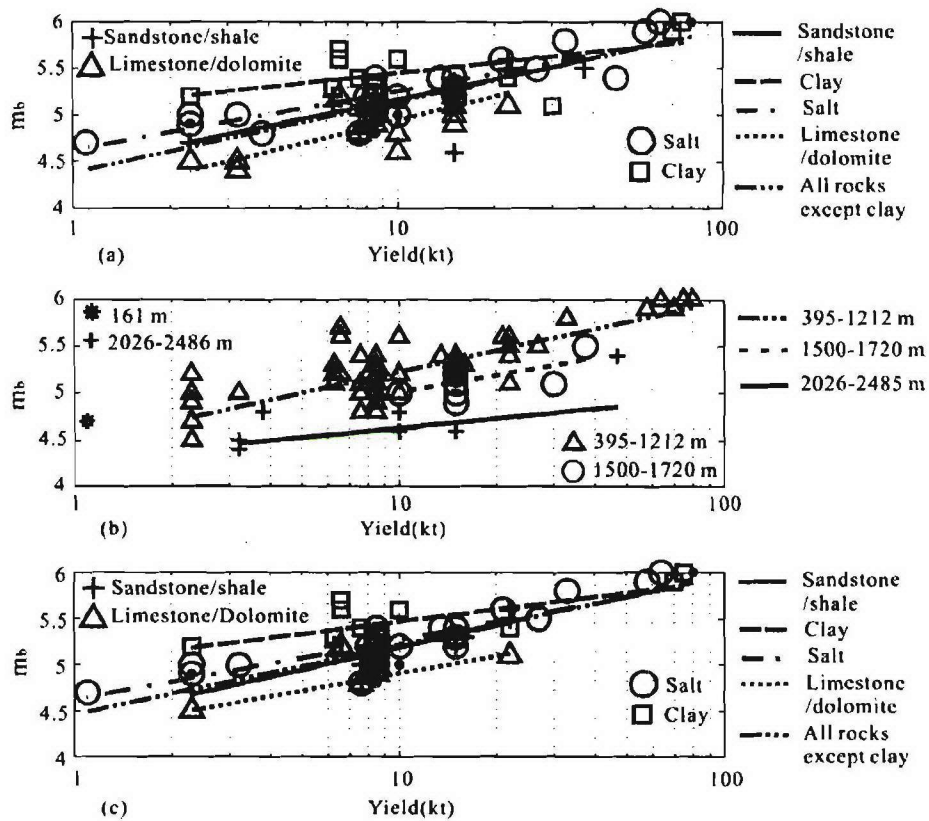


Figure 4-2. The yield- m_b relationship within different media (a), with different depths (b), and with different media with shot depths <1212 m (c). From (a) and (c), the source coupling of clay is much better than other media and the m_b is the lowest for an explosion in limestone/dolomite for a same yield. In (b), the m_b of the explosions generally decreases with the increase of shot depth. A general relationship is determined for all the “hard” rocks except clay.

yield- m_b relationship and source characteristics in a specific area is necessary for yield estimation and source calibration. From 1960s to 1980s, the former Soviet Union (FSU) conducted a number of peaceful nuclear explosion (PNE) tests (Sultanov et al, 1999) in a variety of geologic areas (Figure 4-1) and at different depths (Figure 4-2). The scientists in FSU acquired a network of dense, linear, long range, three-component profiles using the PNEs over a large area of northern Eurasia. The historic data provide unique opportunities to study the yield- m_b relationship and the source characteristics of nuclear explosions in different source conditions, and to understand the propagation characteristics of the regional phases in different tectonic areas.

By using the PNE data provided by Sultanov (1999), this study compares the yield- m_b relationship for different media and different source depths. With 19 PNEs along seven PNE profiles, this study analyses the spectral characteristics of all the regional phases. After resolving Q for Pn - and Sn -phases in different tectonic areas and estimating overshoot parameter β according to the known source medium, corner frequency f_c is

determined with a modified Mueller-Murphy explosive-source model and a wave propagation model (Mueller and Murphy, 1971; Sereno et al., 1988). Thereafter, a linear relationship of $\log f_c$ with $\log W$ and with m_b is compared for both P - and S -phases. Meanwhile, the site effect on phase spectra is estimated by the spectral ratios of horizontal over vertical components from all the regional phases, and then removed from the horizontal components.

4.3 Analysis of yield- m_b relationship from PNE data

The former USSR conducted 122 PNE tests from 1965 to 1988 (Sultanov et al, 1999), widely distributed across the territories of the FSU (Figure 4-1), including (from west to east) the East-European Craton, Ural Mountains, Kazakh massif, Altay Mountains, West-Siberian Basin, West-Siberian Rift, Sayan-Baikal fold belt, Siberian Craton, and Baikal Rift zone. These PNEs were conducted in a variety of geologic media including sandstone/shale, clay, salt, limestone, dolomite, tuff, granite, gabbro, apatite, anhydrite, and chalk with a broad range of yields and source depths. Without including excavation explosions and simultaneous detonations, 95 PNEs were used in this study. The yield ranges from 1.1 kt to 80 kt, the m_b ranges from 4.4 to 6.0, and the source depth ranges from 161 to 2485 m with 78 PNEs between 395 and 1212 m.

For a same yield, the explosion in clay usually has the highest m_b , the explosion in limestone/dolomite has the lowest m_b , and the source coupling effect of sandstone/shale is the similar as salt (Figure 4-2; Table 4-1). The values of m_b generally decrease with increasing depth and the linear relationship is clear for the explosions between shot depths 395 and 1212 m (Figure 4-2b). The uncertainty of the linear relationship for all the media becomes smaller with the smaller depth range (Table 4-1) due to the smaller effect of shot depth. A general linear relationship is determined for all the “hard” rocks (Everden, 1970; Mueller and Murphy, 1971) except clay, and the source coupling coefficients are similar with the different ranges of shot depth (Table 4-1).

The depth of the PNEs range between ~500 and 1000 m; the yield ranges from 7.6 to 22 kt; and the m_b ranges from 4.8 to 5.3. The source media include sandstone/shale, clay, tuff, granite, gabbro, dolomite, and anhydrate (Table 4-2). Different media usually have different Poisson’s ratios (Carmichael, 1982; Christensen, 1996; Mallick, 2001), and using these Poisson’s ratios, we estimated the β (S -wave velocity) for the host rocks in Table 4-2. Q_P and Q_S are determined for different tectonic areas by a two-station spectral ratio method (Chapter 3 of this report). The central frequencies f_c for the P varies were determined as explained below, and range from 2.1 to 6.2 Hz. The corresponding f_c values for S range from 1.9 to 5.5 Hz (Table 4-2).

From Table 4-1, we also estimated a linear relationship for magnitude of the form: $m_b = p(1) + p(2) \times \log_{10} W$ (Figure 4-2). The slope ($p(2)$) for clay is significantly lower than the other media, while the offset on m_b axis ($p(1)$) is higher. The errors of all the parameters become smaller for shallower detonation depths. The yield- m_b relationship of limestone demonstrates that the coupling effect decreases with the increase of burial depth (Figure 4-2).

4.4 Spectral characteristics of PNE regional phases

From the 19 PNEs, all the regional phases are usually strong (e.g., Figure 3-1). *Pn* can be observed from offsets of ~300 km on all the records; *Pg* can be observed up to an offset of ~1000 km on most of the records; *Sn* can be observed from ~300 km and up to 2000 km, and is usually strong the far except Meteorite-5 shot in the Sayan-Baikal fold belt that travels through the Baikal Rift (Figure 4-1). *Lg* phase is usually the strongest at regional distances and can be observed up to 2000 km on some records, i.e., Craton-2, Craton-3, Craton-4, and Kimberlite-4 with the travel paths in the Siberian Craton.

The PNE data were recorded on Taiga magnetic recording system (Figure 4-3, Ryaboy, 1989) with the natural frequency at 1 Hz, and later were digitized at 20-ms sampling intervals. Based on the frequency response of the recording system, the energy below 1 Hz is attenuated, the energy at 1 Hz is amplified, and the response for the frequencies higher than 1 Hz is flat. Since the seismometers are a velocity recording system, the displacement spectrum can be obtained from the velocity spectrum divided by $2\pi f$ (f : frequency).

In order to analyze the spectral characteristics of the regional phases, the phases were identified by correlating the record sections (e.g., Figure 2-1), and their onset times were picked interactively. The observed durations of the *P*-, *Pg*- and *S*-wave trains are typically 10 to 20 s, whereas the duration of *Lg* is longer, usually > 20 s (Figure 3-1). Therefore, the phase window length is chosen as 10 s for the *P*-, *Pg*-, and *S*-waves and 20 s for the *Lg*. If the time interval between *Pn* and *Pg*, *Sn* and *Lg* is smaller than 10 s, then the phase length is equal to that time interval. By comparing the phase spectra of Kimberlite-3 at different offsets (Figure 4-4), the spectra of *Pn* and *Sn* are similar with a wider frequency band and change slowly with offsets. The high-frequency energy of *Pg* decreases much faster with offset than *Pn*-phase. The *Lg*-phase spectrum is very different from the other phases, and the main energy is concentrated at low frequencies (< 3 Hz). According to the spectral

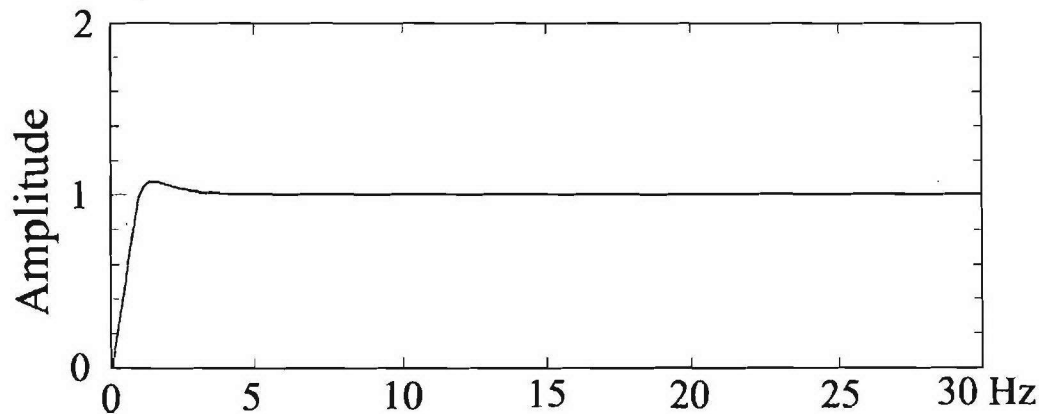


Figure 4-3. Velocity response spectrum of the seismometers on Taiga system used in PNE experiments. The natural frequency is 1 Hz (Ryaboy, 1989).

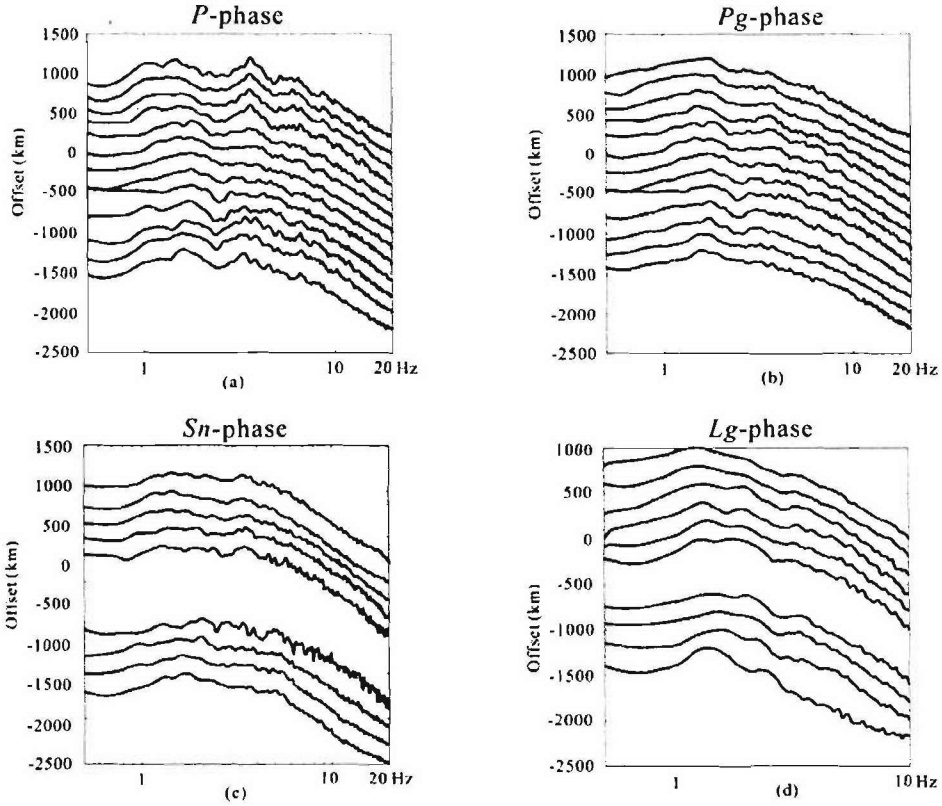


Figure 4-4. Amplitude spectra of all the regional phases *P*, *Pg*, *Sn*, and *Lg* of Kimberlite-3 at different offsets. The frequency band of *Pn* and *Sn* is much broader than *Pg* and *Lg* and change slowly with offset. The *Lg* phase has the narrowest frequency band and the main frequency is below 3 Hz.

characteristics of the regional phases, *Pn*-spectra at different offsets are used to determine the *P*-phase source spectrum, and *Sn*-spectra at different offsets are used to determine the *S*-phase source spectrum.

Before computing the spectra of the regional phases at different offsets, all the traces from all the shots were edited to remove bad traces, and then the phase and pre-phase amplitude ratios were computed for all the phases to choose high S/N (>1.1) traces (more than 30 traces for most shots) for source spectra determination.

4.5 *P* and *S*-wave source spectra

From the wave propagation model,

$$A(f, x) = S(f)G(x)R_1(f)R_2(f, x)e^{\frac{-\pi f x}{vQ}}, \quad (4.1)$$

where $S(f)$ is the source spectrum, $A(f, x)$ is the phase spectrum at offset x ; $G(x)$ is the geometrical spreading; $R_1(f)$ is the receiver response, which is known and consistent for

all the stations; $R_2(f, x)$ is the site response; Q is the average quality factor within offset x ; and v is the phase velocity. Since $G(x)$ does not affect the shape of phase spectrum and $R_1(f)$ is flat (Figure 4-3) for the frequencies above 1 Hz till 25 Hz, the shape of the phase spectrum ($A_a(f, x)$) at some offset is determined by the source spectrum, the site response, and the attenuation.

$$\frac{A_a(f, x)}{R_2(f, x)} = S(f) e^{\frac{-\pi f x}{vQ}} \quad (4.2)$$

After correcting the site response and compensating the attenuation during propagation, the source spectrum can be determined from the phase spectrum at some offset.

From previous research (Lermo and Chavez-Garcia, 1993), the characteristics of site amplification can be obtained by horizontal-to-vertical (H/V) spectral ratio of the S phase. The site effect is supposed to affect horizontal components much more than the vertical one. The spectral ratios of horizontal components (SH and SV) over vertical component (V) of all the regional phases (Pn , Pg , Sn , and Lg) from the four PNEs along METEORITE profile (Figure 4-5) show consistent variations, which should be due to the site response. An average spectral ratio trend was obtained for each station as the site response.

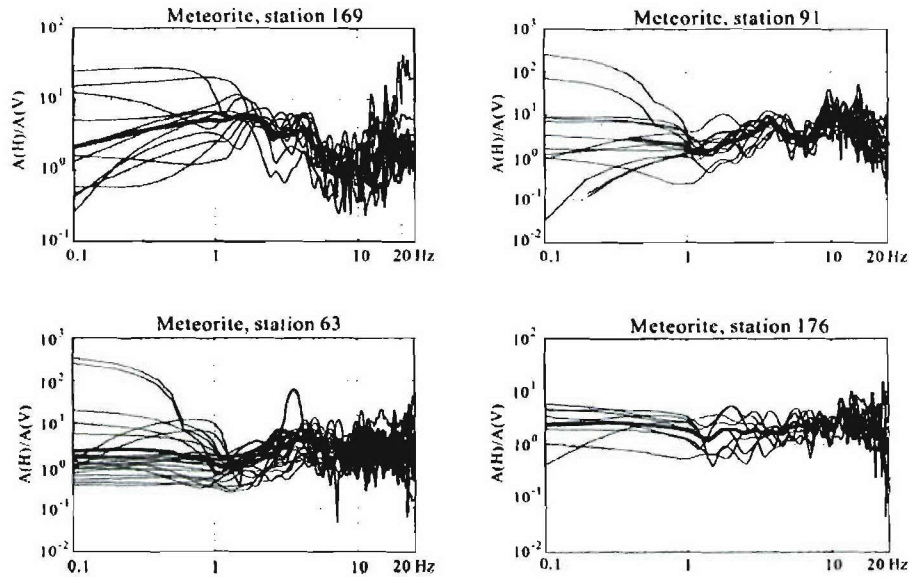


Figure 4-5. Site effect obtained from phase spectral ratios of SH and SV components over vertical component (H/V). All of the regional phases Pn , Pg , Sn , and Lg from the four PNEs along METEORITE profile. The spectral ratios from different phases and from different shots show similar trends.

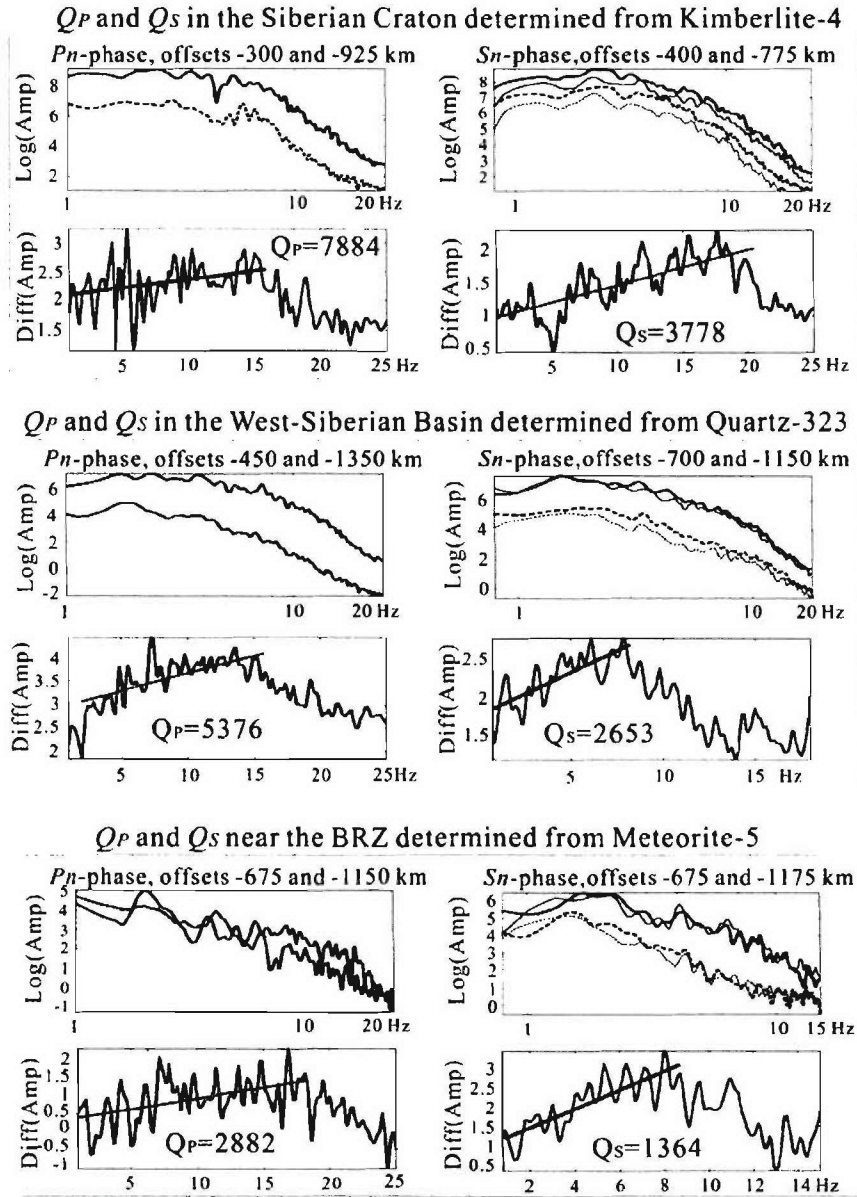


Figure 4-6. Q_P and Q_S in the Siberian Craton, the West-Siberian Basin, and near the BRZ determined by a two-station spectral ratio method. In each panel, the upper left is the P -phase spectra at two different offsets and the lower left is the logarithms of the P -phase spectral ratios from the two locations. The upper right is the S -phase spectra (thick solid and dashed lines) with the pre-phase noise spectra (thin solid and dashed lines) and the lower right is the logarithms of the S -phase spectral ratios of from two locations. Q_P and Q_S are

Unfortunately, the absolute ground motion amplitude information was deemed unrecoverable in recording for all the PNE data; therefore, constant Q by a two-station spectral ratio method (Chapter 3) is determined for both P_n - and S_n -phases. In the Siberian Craton and the East-European Craton, P_n Q is ~ 8000 and S_n Q is ~ 6000 (Figure

4-6). In the West-Siberian Basin, Pn Q is ~ 6000 and Sn Q is ~ 3000 (Figure 4-6). Pn Q and Sn Q are determined as 3500 and 1400 near the BRZ from PNE Meteorite-5 (Figure 4-6). According to the earthquake data from both FSU and the United States, Evernden et al (1986) determined the effective constant Q as ~ 9000 and ~ 4000 for Pn and Sn in stable continental areas and shields, and ~ 1000 for Pn in tectonic areas, which is consistent with this study.

From the modified Mueller-Murphy model (Sereno et al., 1988), the explosion source spectra can be modeled as

$$S(f) = \frac{M_0}{4\pi\rho v^3 [1 + (1 - 2\beta)f^2/f_c^2 + \beta^2 f^4/f_c^4]^{1/2}}, \quad (4.3)$$

where, ρ and v are source zone density and velocity, and β is overshoot

parameter, $\beta = \frac{v_p^2}{4v_s^2} = \frac{1 - \sigma}{4(0.5 - \sigma)}$, where v_p , v_s are respectively the P -wave and S -wave

velocities at the source zone, and σ is Poisson's ratio. For Poisson material, $\beta = 0.75$. According to the known source media, β is determined (Table 2) from the observed Poisson's ratios of different rock types (Carmichael, 1982; Christensen, 1996; Mallick, 2001). For a given source, the source spectrum can be rewritten as

$$S(f) = \frac{M}{[1 + (1 - 2\beta)f^2/f_c^2 + \beta^2 f^4/f_c^4]^{1/2}}, \quad (4.4)$$

and $M = \frac{M_0}{4\pi v^3}$, the apparent source moment.

The inverse procedure to determine the source parameters from regional phases is described as follows:

- 1) Calculate the spectra of all the regional phases from all the traces with offset ≤ 1200 km, and calculate the horizontal-to-vertical component spectral ratios from all the seismographs recorded at the same station and from all the regional phases, then divide the horizontal-component regional spectra by the corresponding spectral ratios to remove the site effect on the horizontal components.
- 2) Compute the average spectra of all the regional phases at offsets every 50 km until 1200 km. For each location, the spectra are the average of the traces 50 km around it to suppress noise effect. Normalize the logarithm of the spectra at all the locations to be between 0 and Max (a value).
- 3) By assuming M as between $0.8Max$ and $1.2Max$ and the increment as $0.05Max$, and assuming f_c between $fmin$ (input according to the spectra) and $fmax$ (input according to the spectra) with an increment of 0.1 Hz, with the determined β or range of β and Q for each PNE (Table 2), the modeled phase spectrum with eq. (2) and (4) at each offset is compared with the observed phase spectra to obtain a

standard error at each iteration. Therefore, the best source parameters (M , f_c , and β) are obtained from the phase spectrum at each location corresponding to the iteration with the minimal error. The final source parameters are the average of the constrained source parameters from different locations, and the corresponding std errors of these source parameters can also be obtained (Table 2).

With the inverted source parameters, the modeled source spectra are quite consistent with the observed spectra (Figure 4-7). The PNE Kimberlite-3 was shot in tuff with a yield of 8.5 kt and an m_b of 4.9. With β equal to 0.75, the f_c of P - and S -phases is determined as 5.4 ± 0.7 Hz and 4.3 ± 0.6 Hz respectively. The PNE Quartz-323 was shot in granite with a yield of 10 kt and an m_b of 5.0. With β equal to 0.75, the f_c of P - and S -phases is determined as 4.6 ± 0.4 Hz and 3.4 ± 0.4 Hz. From the given β and the calculated Q_P and Q_S in different tectonic areas, the f_c of both P - and S -phases is determined for all the 19 PNEs (Table 4-2).

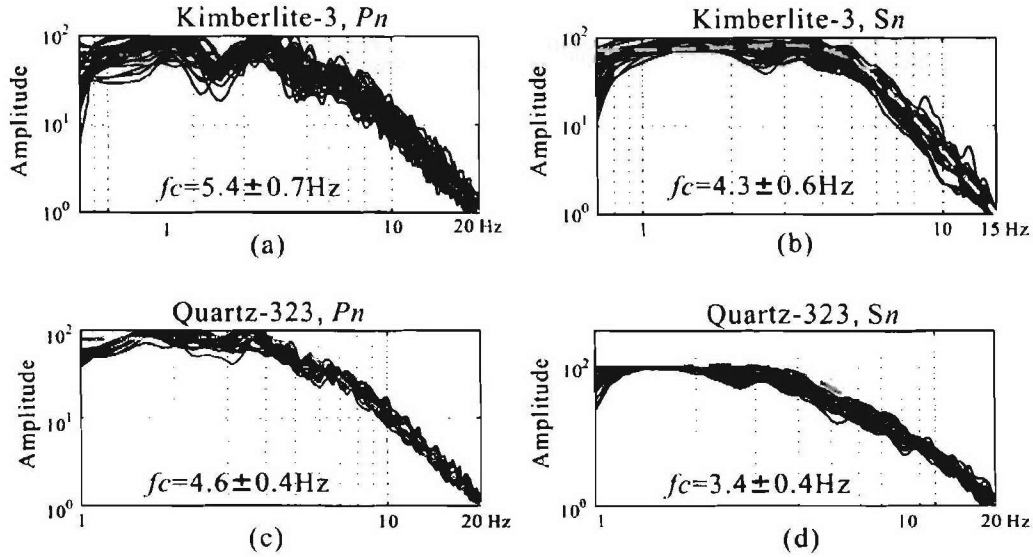


Figure 4-7. The observed phase spectra of Pn and Sn from Kimberlite-3 (a), (b) and from Quartz-323 (c), (d) at offsets every 50 km with a maximum offset of 1200 km and the determined P - and S -phase source spectra. The thick gray dashed lines are the inverted source spectra of P - and S -phases from the regional phases. The determined P -phase f_c is 5.4 ± 0.7 Hz for Kimberlite-3 and 4.6 ± 0.7 Hz for Quartz-4, and the determined S -phase f_c is 4.3 ± 0.6 Hz for Kimberlite-3 and 3.4 ± 0.4 Hz for Quartz-4.

4.6 Discussion

4.6.1 Yield- m_b -medium-depth relationship

Much work (Evernden, 1970; Mueller and Murphy, 1971; Bache, 1982; Murphy, 1996; Murphy and Baker, 2001; Stump et al, 2003) has been done to calibrate relationship

between yield and m_b in different areas and for a variety of source conditions. With 95 well-coupled nuclear explosions in FSU (Sultanov et al., 1999), the coupling effects of sandstone/shale, clay, salt, and limestone/dolomite are compared. For a same yield, the explosion in clay has the highest m_b , the explosion in salt has the similar m_b as sandstone/shale, and the explosion in limestone/dolomite has the lowest m_b . The m_b generally increases with the decrease of depth (Figure 4-2b), corresponding to the increase of rigidity of the rocks with depth (Sharpe, 1942) and the seismic signals shift to shorter periods as the burial depth increases according to Mueller-Murphy's source model (Mueller and Murphy, 1971). The linear relationship for all the media becomes more obvious with a smaller depth range (395-1212 m; Table 1):

$$m_b = (5.02 \pm 0.16) + (0.45 \pm 0.14) \log_{10} W, \quad (4.5)$$

for clay, and

$$m_b = (4.46 \pm 0.07) + (0.75 \pm 0.07) \log_{10} W, \quad (4.6)$$

for all the "hard" rocks except clay. The latter one is the same as the relationship determined from the nuclear explosions in "hard" rocks in Shagan River, Kazakhstan (Ringdal et al., 1992; Murphy, 1996; Murphy and Baker, 2001). The m_b - $\log W$ relationship for hard rocks in northern Eurasia is quite consistent, unrelated to the tectonic areas where the explosions are located, the similar observations obtained by Murphy et al (2001).

4.6.2 Spectral characteristics of the regional phases

From the 19 PNEs in northern Eurasia, the spectra of Pn and Sn are usually richer in high frequencies than Pg and Lg , which could be attributed to the lower attenuation in the upper mantle than the crust in northern Eurasia. The Lg -spectrum (Figure 4-4) is quite different from other phases, and the energy is mainly concentrated at low frequencies (<3 Hz), which could be due to the different physical mechanism of Lg formation — multiple supercritical S -wave reflections or a superposition of higher-mode surface waves trapped within the crust (Knopoff et al., 1973) or near-source scattering of explosion-generated Rg into S is the primary contributor to the low-frequency Lg from nuclear explosions (Gupta et al., 1992, 1997; He et al., 2005). The phase spectra of both Pn and Sn change slowly with offset (Figure 4-4), referring to high Q (Figure 4-6) for Pn and Sn in both the East-Siberian Craton and the West-Siberian Basin.

With the nuclear explosion data at the east Kazakh and Nevada test site, Gupta et al (1992) observed that the Lg from explosions is relatively rich in low-frequency content (< 2Hz) than corresponding earthquakes. He also observed that Lg is only rich in low frequencies, while Pn is richer in higher frequencies, the similar observations as this study.

Since the Lg energy is mainly concentrated at low frequencies, the spectrum varies much slower with yield and source conditions than Pn - and Sn -phases. Therefore, the source magnitude determined from Lg phase should have smaller error than that

determined from Pn - or Sn -phase, i.e., Lg is a promising phase to estimate source yield (Nuttli, 1986; Taylor and Dowla, 1991; Ringdal et al., 1992).

4.6.3 f_c -yield- m_b relationship

With a two-station spectral ratio method, constant Pn and Sn effective Q is determined in different tectonic areas in northern Eurasia. Pn Q is ~ 8000 in the East-European Craton and the Siberian Craton, ~ 6000 in the West-Siberian Basin, and ~ 3500 near the BRZ corresponding to higher heat flow and lower velocity in the upper mantle (Zorin et al., 2003). Sn Q is ~ 4000 in the cratons, ~ 3000 in the West-Siberian Basin, and ~ 1400 near the BRZ.

Different media usually have different values or different ranges of Poisson's ratio. According to the known source media, the overshoot parameter β in the modified Muller-Murphy explosion-source model (eq. 4) can be estimated (Table 2) from the observed Poisson's ratios of different rock types (Carmichael, 1982; Christensen, 1996; Mallick, 2001).

With the calculated Pn Q and Sn Q and the estimated β , both P - and S -phase source spectra are inverted by a wave propagation model (eq. 2) and a modified Muller-Murphy explosion-source model (Sereno et al., 1988, eq. 4). The f_c of S -phase is close but lower than P -phase. Among the 19 PNEs (Table 2), the highest P -phase f_c is 6.2 ± 1.1 Hz, from the explosion in anhydrite with a yield of 8.5 kt, an m_b of 4.8, and a shot depth of 820 m. The lowest P -phase f_c is 2.0 ± 0.2 Hz, from the explosion in clay with a yield of 22 kt, an m_b of 5.4, and a depth of 837 m.

From Mueller and Murphy's model (1971) and the work of Hays (1969) and Bache (1982), the phase amplitude is proportional to W^m/h^n , while the corner frequency (f_c) is proportional to h^a/W^b . For a same medium, a linear relationship exists between m_b and logarithm of f_c for a constant source depth or a same W . According to the elastic equation of motion, the phase amplitude is directly proportional to the area of the cavity, and inversely proportional to the rigidity of the medium; while the corner frequency is directly proportional to the velocity of the medium and inversely proportional to the radius of the cavity (Sharpe, 1942). The velocity is higher in the more rigid medium. Therefore, a linear relationship is expected between m_b and logarithm of f_c for different media.

Without considering the effect of source depths (from 550 to 982 m) on source spectrum, the linear relationship of $\log f_c$ with $\log W$ and with m_b is compared for both P - and S -phases from 19 PNEs:

For P -phase

$$\log_{10} f_c = (1.34 \pm 0.17) - (0.70 \pm 0.15) \log_{10} W, \quad (4.7a)$$

$$\log_{10} f_c = (3.8 \pm 0.3) - (0.73 \pm 0.06) m_b, \quad (4.7b)$$

and the uncertainties are 0.116 and 0.608, respectively.

For S phase,

$$\log_{10} f_c = (1.09 \pm 0.17) - (0.57 \pm 0.16) \log_{10} W, \quad (4.8a)$$

$$\log_{10} f_c = (3.4 \pm 0.3) - (0.56 \pm 0.06) m_b. \quad (4.8b)$$

The standard errors are 0.118 and 0.055, respectively.

The linear relationship is much more obvious for $\log f_c$ - m_b than $\log f_c$ - $\log W$ because the source conditions (yield, media, and depth) affect both f_c and m_b . Comparing f_c with m_b can help constrain the m_b with higher reliability, and therefore to obtain better estimates of the source yield with m_b - $\log W$ relationship.

Pn/Lg spectral ratios at frequencies above the f_c of P -phase is a promising parameter for nuclear discrimination (Xie, 1999, 2002). This could be attributed to the different source mechanisms between nuclear explosions and earthquakes (Xie et al., 1996). The amplitude of the higher frequencies near the f_c is higher for nuclear explosions than earthquakes due to the overshoot effect β . f_c can be estimated through m_b from the determined f_c - m_b relationship, and then Pn/Lg at the corner frequencies can be used for better nuclear discrimination.

4.7 Conclusions

The coupling effects in different media (clay, sandstone/shale, salt, and limestone/dolomite) and in different source depths are compared from 95 nuclear explosions in northern Eurasia (Sultanov et al., 1999). Clay has much better coupling effect than other media and the coupling effect decreases with the increase of source depth. With the source depths between 485 and 1212 m,

$$mb = (5.02 \pm 0.16) + (0.45 \pm 0.14) \log_{10} W$$

for clay, and

$$mb = (4.46 \pm 0.07) + (0.75 \pm 0.07) \log_{10} W$$

for all the “hard” rocks except clay, the same as that predicted for “hard” rocks in Shagan River, Kazakhstan (Ringdal et al., 1992; Murphy, 1996; Murphy and Baker, 2001).

According to 19 PNEs in northern Eurasia, Pn - and Sn -phases are richer in higher frequencies than Pg and Lg and the spectra change slowly with offset, which can be attributed to the low attenuation in the upper mantle. Pn and Sn are ideal phases to determine P - and S -wave source parameters. The Lg spectrum is mainly concentrated at low frequencies and therefore changes slowly with offset, and is ideal for estimating source yield.

After calculating Q_P and Q_S by a two-station spectral ratio method and estimating overshoot parameter β for different media according to Poisson's ratios, the corner frequency f_c of both P - and S - phases is obtained for 19 PNEs by the wave propagation

model and a modified Muller-Murphy explosion-source model (Serenio et al., 1988). The linear relationship of $\log_{10} f_c - m_b$ is more obvious than $\log_{10} f_c - \log_{10} W$:

$$\text{For } P\text{-phase, } \log_{10} f_c = (3.8 \pm 0.3) - (0.73 \pm 0.06) m_b \quad (\text{Figure 4-8})$$

and for S -phase (Figure 4-9):

$$\log_{10} f_c = (3.4 \pm 0.3) - (0.56 \pm 0.06) m_b.$$

Better constraint on m_b can be obtained from the $f_c - m_b$ relationship, and then better estimate on source yield. With the known m_b , f_c can be constrained from the $f_c - m_b$ relationship, and then Pn/Lg amplitude ratios of the frequencies above f_c (Xie, 1999; 2002) can be calculated for better nuclear discrimination.

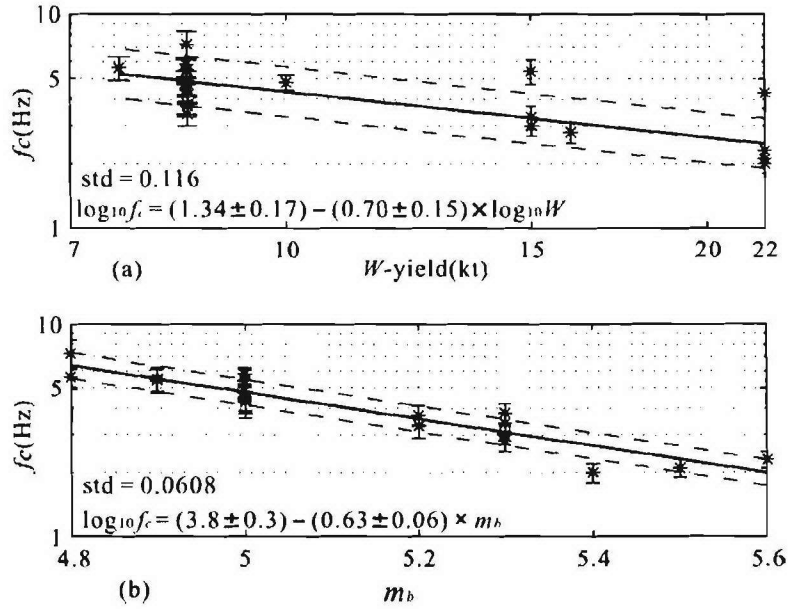


Figure 4-8. Linear relationship of the logarithms of P -phase corner frequencies (f_c) of the 19 PNEs with (a) logarithm of yield, and (b) m_b . The linear relationship between $\log f_c$ and m_b is more obvious than that between $\log f_c$ and $\log W$.

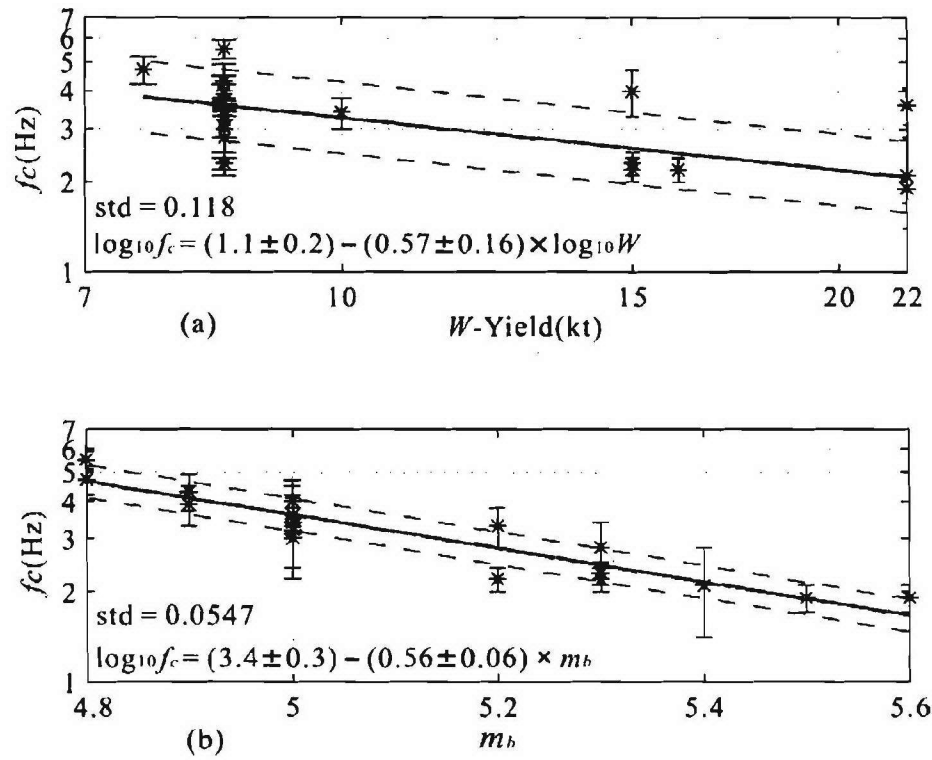


Figure 4-9. Linear relationship of the logarithms of S -phase corner frequencies (f_c) of the 19 PNEs with (a) logarithm of yield, and (b) m_b . The linear relationship between $\log f_c$ and m_b is more obvious than that between $\log f_c$ and $\log W$.

Table 4-1. Yield (W)- m_b relationship for different media in different depth ranges

Depth	395-2485 m						395-1212 m					
	No. PNE	p(1)	error	p(2)	error	σ	No. PNE	p(1)	error	p(2)	error	σ
Sandstone/shale	12	4.44	0.18	0.72	0.17	0.18	11	4.44	0.15	0.73	0.14	0.15
Clay	13	5.07	0.19	0.31	0.16	0.25	12	5.02	0.16	0.45	0.14	0.20
Salt	38	4.62	0.06	0.64	0.06	0.13	35	4.63	0.05	0.65	0.05	0.11
Limestone/dolomite	23	4.02	0.12	0.86	0.13	0.17	9	4.28	0.11	0.63	0.13	0.11
All "hard" rocks	82	4.36	0.07	0.77	0.07	0.22	63	4.46	0.07	0.75	0.07	0.18

"No. PNE" are the numbers of PNEs used in the determination of the linear relationship.

All "hard" rocks (having high rigidity modulus) include sandstone/shale, salt, limestone/dolomite, 3 PNE shots in granite, 2 in tuff, 2 in chalk, 1 in gabbro, 1 in anhydrite.

Table 4-2 Source parameters of the 19 PNEs and Q_P and Q_S along the travel paths

No.	PNE	depth(m)	Source medium	W -yield (kt)	m_b	Poisson's Ratio σ	β	Q_P	Q_S	f_c of P_n (Hz)	f_c of S_n (Hz)
1	crat-1	593	sandstone/shale	22	5.5	0.2-0.3	0.7-0.9	6000	3000	2.1±0.7	1.9±0.2
2	crat-2	886	sandstone/shale	15	5.2	0.2-0.3	0.7-0.9	8000	4000	3.3±0.4	2.2±0.2
3	crat-3	577	limestone	22	5.0	0.3	0.9	8000	4000	4.3±0.7	3.6±0.5
4	crat-4	567	sandstone/shale	22	5.6	0.2-0.3	0.7-0.9	8000	4000	2.3±0.2	1.9±0.2
5	kimb-1	837	clay	22	5.4	0.35-0.4	1.1-1.5	6000	3000	2.0±0.2	2.1±0.7
6	kimb-3	599	tuff	8.5	4.9	0.25	0.75	8000	4000	5.4±0.7	4.3±0.6
7	kimb-4	982	dolomite	8.5	4.9	0.3	0.9	8000	4000	5.5±0.7	3.9±0.6
8	meteor-2	850	salt	15	5.0	0.25	0.75	8000	4000	5.4±0.7	4.0±0.7
9	meteor-3	600	tuff	8.5	5.0	0.25	0.75	8000	4000	4.5±0.6	4.0±0.5
10	meteor-4	550	sandstone/shale	7.6	4.8	0.2-0.3	0.7-0.9	8000	4000	5.6±0.7	4.7±0.5
11	meteor-5	494	granite	8.5	5.0	0.25	0.75	3500	1400	4.4±0.6	3.0±0.6
12	rift-1	960	sandstone	16	5.3	0.2	0.7	8000	4000	2.8±0.3	2.2±0.2
13	rift-2	554	gabbro	8.5	5.2	0.3	0.9	8000	4000	3.7±0.4	3.3±0.5
14	rift-3	554	dolomite	8.5	5.0	0.3	0.9	8000	4000	5.8±0.4	3.2±0.8
15	quartz-123	759	clay	8.5	5.3	0.35-0.4	1.1-1.5	8000	4000	3.8±0.4	2.8±0.6
16	quartz-213	726	clay	8.5	5.3	0.35-0.4	1.1-1.5	6000	3000	3.4±0.4	2.3±0.2
17	quartz-323	557	granite	10	5.0	0.25	0.75	6000	3000	4.6±0.4	3.4±0.4
18	ruby-1	820	anhydrite	8.5	4.8	0.3	0.9	8000	4000	6.2±1.1	5.5±0.4
19	ruby-2	829	clay	15	5.3	0.35-0.4	1.1-1.5	6000	3000	3.0±0.3	2.3±0.2

5 Empirical model for PNE regional phase codas

5.1 Summary

Short-period, three-component recordings from peaceful nuclear explosions (PNE) of the profile QUARTZ, Russia are used to constrain the nature of the coda of PNE arrivals. In particular, we examine the unusually strong and extensive coda of the long-range P_n (interpreted as a whispering-gallery, WG) phase propagating to beyond 3000 km. Energy-balance considerations in three dimensions show that such an extensive coda is inherent not only to WG but to all other P -wave phases and can be explained by crustal scattering. The long coda is a result of excitation of short-period scattered waves (P_g , S_g , L_g , R_g) within the crust by the waves incident from the mantle, or, conversely, by generation of mantle phases from crustal guided waves within the source region. The resulting estimates of coda Q range between $Q=380$ near 2 Hz and $Q=430$ near 5 Hz and can be associated with crustal attenuation including the sediments. Our coda model also explains quantitatively the observed build-up of the arrival amplitude with time and the apparent lack of a pronounced coda of the body-wave arrivals from the mantle transition zone. These effects result from adding up the energy of the later arrivals arriving during the codas of earlier arrivals. We “deconvolve” the overlapping coda patterns and show that the true relative energies of the arrivals are significantly lower than the apparent energies measured from the raw records. A whispering-gallery interpretation of the long-range P_n and crustal scattering accounts for the entire range of observations of kinematic, spectral, and amplitude pattern of the PNE wavefield and allows the derivation of constraints on attenuation.

5.2 Introduction

Seismic studies, including deep refraction and reflection experiments using large chemical and nuclear explosions, have demonstrated strong heterogeneity of the uppermost mantle. Mantle heterogeneity is manifested in velocity contrasts and pronounced stratification of the lithosphere imaged by P/S wave conversions (e.g., Bostock, 1998), in mantle reflectivity (e.g., Pavlenkova, 1996; Morozova *et al.*, 1999), and in variations of seismic attenuation (e.g., Der *et al.*, 1986; Morozov *et al.*, 1998a, 1998b). Mantle velocity gradients and reflecting boundaries form a relatively shallow (between 100 – 150 km depth) waveguide favoring propagation of seismic energy to teleseismic distances of up to 3000 km (Figure 5-1; Mechie *et al.*, 1993; Ryberg *et al.*, 1995; Morozov *et al.*, 1998a). Such phases, known as long-range (teleseismic) P_n , were also identified in long-range profiles using large conventional explosions (Enderle *et al.*, 1997; Henstock *et al.*, 1998) and acquired critical significance for some interpretations of the fine-scale structure of the uppermost mantle (e.g., Enderle *et al.*, 1997). Since these waves are confined within the uppermost 100 - 120 km of the mantle, amplitude and coda character carry important information about the structure of this region.

Two recent interpretations of the long-range P_n sharply diverge in their interpretations of the observations and in conclusions about the uppermost mantle structure. Based on one-dimensional (1-D) modeling of coda properties using the method by Fuchs and Müller (1971), Tittgemeyer *et al.* (1996), and Ryberg and Wenzel (1999) proposed a special, “high-frequency waveguide” propagation mechanism of the long-range P_n . These authors suggested a small-scale, random sub-Moho layering with high, 5% RMS velocity fluctuations and average layer thickness of 2 km within a zone extending 75 km below the Moho (Ryberg and Wenzel, 1999). Although faced with

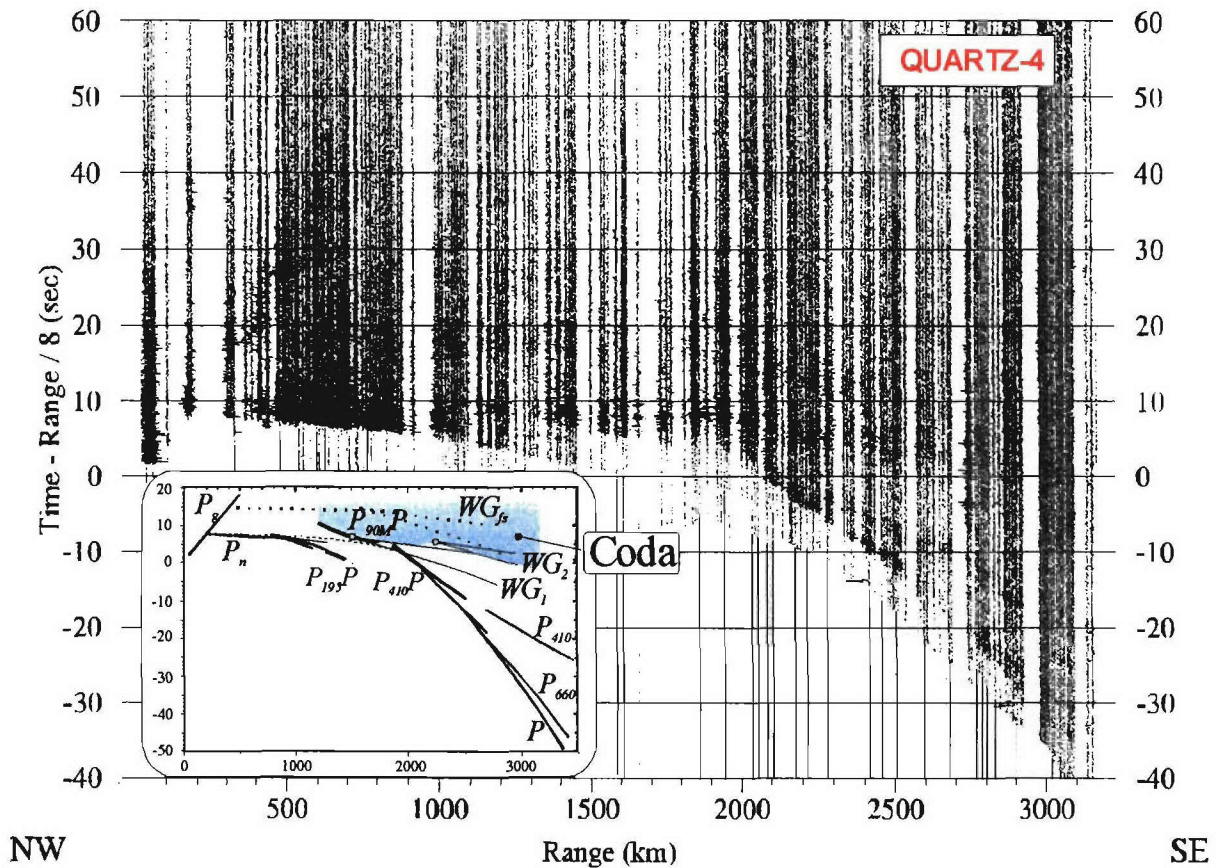


Figure 5-1. Vertical-component record from PNE QUARTZ-4 (Figure 1-1); Inset shows a sketch of refracted, reflected arrivals and their multiples identified in this complex wave pattern. The long-range P_n phase (shaded in the inset) consists of several seismic phases forming a strong band of energy propagating to 3000 km at a group velocity between 8.0 – 8.1 km/s, with a faster branch at 8.5 km/s beyond 2700 km (Morozov *et al.*, 1998a). Frequency content of this phase is close to that of the ordinary P_n (Morozov *et al.*, 1998a), and after a high-pass filtering removing the deeper mantle body waves, this phase dominates the record (Ryberg *et al.*, 1995). Note the unusually high energy of the arrivals in the primary P_n branch supporting the interpretation of the long-range P_n as a series of Moho and free-surface multiples of P_n and P_N (WG and WG_{fs}). Also note that the long-range P_n phase is strong and is followed by a coda extending beyond the ends of records shown here (Figure 5-2).

significant difficulties in petrologic interpretation of this model (e.g., Ryberg and Wenzel, 1999, p. 10,660), such strongly scattering uppermost mantle was viewed as a global phenomenon (Enderle *et al.*, 1997).

In contrast to the above model, Morozov *et al.* (1998a) argued that the observations of the long-range P_n could be better explained by multiple sub-Moho refractions (whispering-gallery modes) within the uppermost mantle. According to this interpretation, no unusual wave propagation mechanism was required in order to explain the nature of this phase and no strong

scattering within the uppermost mantle is required. At larger ranges, similar strong *PP* phases followed by extensive codas were identified in NORSAR recordings of nuclear explosions in Western Russia (Baumgardt, 1985). The enhanced high-frequency content of these phases relatively to the waves diving into the mantle transition zone was explained by increased attenuation below a depth of about 150 km (Morozov *et al.*, 1998a, b). Morozov *et al.* (1998a) and Morozov (submitted) argued that the “scattering waveguide” model was primarily based on a misinterpretation of the apparently high-frequency character of the long-range P_n by Ryberg *et al.* (1995) and by the inadequate, 1-D models of its coda employed by Tittgemeyer *et al.* (1996) and Ryberg and Wenzel (1999).

Although kinematic behavior and spectral content of the long-range P_n does not present any difficulty for the whispering-gallery model (Morozov *et al.*, 1998a), the high amplitude of this phase and particularly its extensive coda (Figure 5-1) still need to be understood. Recent studies of the decay rate of this coda resulted in surprisingly high values of coda Q between 1000 - 2000 (Ryberg and Wenzel, 1999) or even 2000 - 5000 (Ryberg *et al.*, 1995). Such high Q values can hardly be associated with crustal attenuation, and as a result, extremely strong yet horizontally coherent scattering within the mantle was suggested (Ryberg *et al.*, 1995).

Although numerical modeling of three-dimensional (3-D) scattering effects of short-period PNE wavefields still presents insurmountable difficulties, scattering is still inherently a multi-dimensional process, and only accounting for 3-D wave propagation can explain the observed coda decay rate. Fortunately, the observed coda amplitude pattern allows an explanation from simple physical considerations of energy balance; such an explanation is the focus of the present study.

For our interpretation of the long-range P_n amplitude, we extract amplitude decay curves within 200 sec of a range of seismic records from PNE QUARTZ-4 where the separation of the phases provides the best illustration of the QUARTZ PNE energy pattern (Figure 7-2). The energy in the PNE wavefield at this distance appears to build up for 20 – 30 s after the first arrivals, followed by an extensive coda that can be observed for 100 – 150 s (Figure 5-2). Both the high amplitudes of the WG phases and the coda are surprising and do not fit into conventional views. Specifically, we will seek answers to two intriguing problems of the recorded distribution of PNE energy (Figure 5-2):

- 1) What is the nature and decay character of the observed codas of PNE arrivals? Why is the coda of the free-surface multiple *PP* (WG_{fs} in our notation) much stronger than the coda of $P_{410}P$ reflections of nearly the same amplitude?
- 2) Why are the amplitudes of the WG phases so high compared to the reflections from the transition zone, whereas 1-D modeling shows much lower amplitudes (synthetic models were presented by Mechie *et al.* (1993) and Morozova *et al.*, (1999)).

These are precisely the questions put forward in support of the “scattering waveguide” interpretation by Ryberg and others; however, we emphasize that there is very little of a specific, “high-frequency” accent in these questions. Instead, these problems are more clearly posed by the low-frequency, high-amplitude pattern in Figure 5-2. Note that the “scattering waveguide” model by Ryberg *et al.* (1995) is based solely on the high-frequency coda of *WG* whereas the low-frequency coda is stronger and longer, indicating that the scattering phenomenon is broadband and cannot be attributed to a tuned, high-frequency scattering within the uppermost mantle. Also, unlike the above authors, we consider the crust, as the most structurally and compositionally

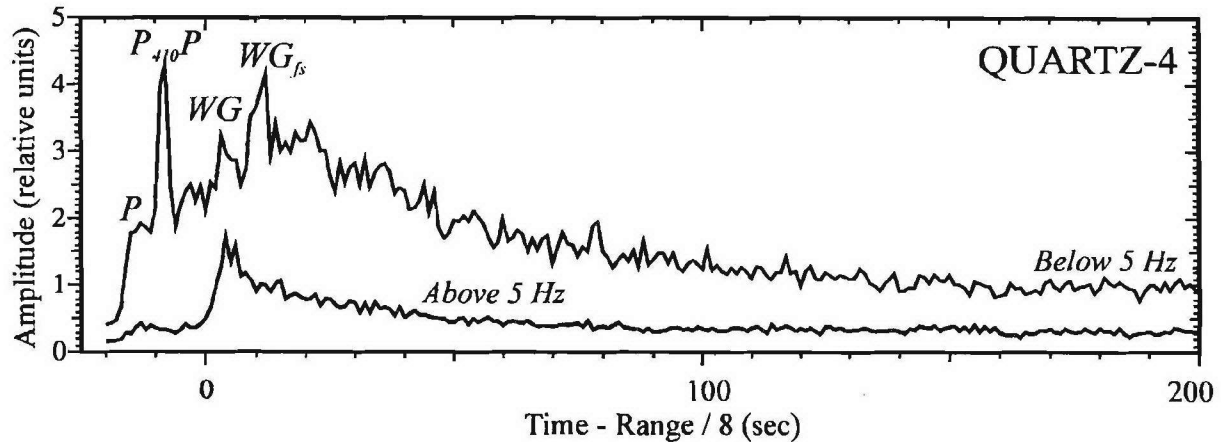


Figure 5-2. Amplitude of the high-frequency and low-frequency (filter corner frequency is 5 Hz in both cases) records within the offset range 2500 - 2600 km from PNE QUARTZ-4 (modified from Morozov *et al.*, 1998a). Time reduction is 8 km/s, and 7 three-component instantaneous trace amplitude records were averaged within a 2-s sliding time window and within the offset range (Morozov and Smithson, 1996) was used. First arrivals, a reflection from the 410-km discontinuity, and two whispering-gallery phases (WG and WG_{fs}) are indicated. Note the difference of the codas following the free-surface multiple refraction WG_{fs} at low frequencies and the Moho multiple WG at high frequencies.

complex part of the Earth, also the most likely source of seismic scattering.

As we show below, a simple physical model of the coda allows us to obtain meaningful estimates of crustal attenuation quality factor (Q) and of the relative amplitudes of the arrivals without presently impractical 3-D finite-difference modeling. Our approach follows coda models accepted in teleseismic array observations (e.g., Greenfield, 1971; Bannister *et al.*, 1990; Dainty, 1990; Gupta *et al.*, 1991) and is based on two fundamental observations. Firstly, waves propagating through the mantle and incident on the crust at high apparent velocity form a source of scattered energy different from the point-source model commonly used in coda estimates. Thus a correct coda model must take into account the distributed character of its excitation. Secondly, despite their apparent difference, we postulate that *all* the mantle arrivals could have similar coda patterns. Due to their long extent, these codas overlap creating the stepwise increase in energy seen in Figure 5-2. Decomposition of the recorded amplitude pattern allows us to obtain the true relation between the amplitudes of the onsets of the different PNE phases and their codas.

5.3 Coda decay rate of the long-range P_n arrivals

Figure 5-2 shows that the two WG multiples forming the long-range P_n are clearly distinct in the character of their codas. The first, Moho multiple labeled WG in Figure 5-2 is followed by a coda that dominates the high-frequency record (Figure 5-1). However, in the low-frequency band, the strongest phase is the free-surface P_n multiple (WG_{fs}) followed by its coda. The higher amplitude of the WG_{fs} event is consistent with higher reflectivity of the free surface compared to the Moho. Also, the longer and low-frequency coda of WG_{fs} suggests a predominance of surface waves that propagate efficiently at lower frequencies and are progressively more attenuated as the frequency

increases.

Previous measurements of coda decay rate by Ryberg *et al.* (1995) and Ryberg and Wenzel (1999) resulted in two conflicting estimates both of which suggested very high Q values over 1000 - 2000. However, values of Q might be overestimated from the use of a coda power decay rate (Aki and Chouet, 1975):

$$P(t) \propto t^{-\zeta} e^{-\omega t / Q}, \quad (5.1)$$

where t is the time after the arrival, ω is the frequency. In expression (5.1), the factor $t^{-\zeta}$ with $\zeta \geq 1$ describes the geometric spreading of the waves forming the coda, and the quality factor Q corresponds to the attenuation. Ryberg and Wenzel (1999) used a preset value of $\zeta = 2$ assuming body-wave nature of the coda waves and a point source. However, as pointed out by Morozov *et al.* (1998a) and Morozov (submitted), the energy of the coda of the long-range PNE phases is better described by a relation (5.1) with $\zeta \approx 1.0$ for the higher-frequency coda and $\zeta \approx 0.9$ for the lower-frequency coda, with $Q = \infty$. This ambiguity in the determination of the attenuation factor Q using equation (5.1) illustrates the importance of a correct model of geometrical spreading. The tendency of the geometric spreading parameter ζ to values lower than 1 when $Q = \infty$ shows that formula (5.1) may not be applicable to the coda decay rate of the long-range PNE arrivals.

Assuming predominantly crustal origin of the coda waves, coda amplitudes of PNE arrivals in Figure 5-2 can be explained readily once we take into account that seismic waves propagating through the mantle and entering the crust form a source of scattered waves that is different from a point source implied by relation (5.1). High apparent velocity of the incident waves (8 – 10 km/s) exceeds the velocity of the crustal-guided waves (3.5 – 5.5 km/s) generated through conversions on the Moho, on the basement, on surface topography, and on other velocity heterogeneities. Note that the most efficiently propagating phases within the crust (in the frequency range 0.5 - 10 Hz), post-critically reflected S waves, or L_g (Campillo, 1987), tend to the lower limit of this velocity range. High velocity of the moving source of scattered waves leads to a distributed source of coda energy.

In order to derive a phenomenological model of PNE coda excitation, we assume for simplicity that the coda of a PNE arrival consists predominantly of L_g ; however, the argument should hold for other types of waves trapped within the crust. A commonly used L_g amplitude decay relation (e.g., Campillo, 1987; McNamara *et al.*, 1996) converted to power units is:

$$P(f, D) = \frac{1}{D^{2\gamma}} R(f) S(f) e^{-2\pi f D / v Q(f)}, \quad (5.2)$$

where D is the hypocentral distance, R and S are receiver and source terms describing site effects at the recording and excitation points, respectively, f is the median frequency of the observed wave, v is the group velocity for L_g , γ is the exponent of the geometric spreading within the medium, and Q is the quality factor of L_g propagation within the crust. Since the duration of L_g increases with distance, γ is larger than the value of 0.5 used for regional surface waves (Frankel *et al.*, 1990), and a value of $\gamma = 0.83$ is generally accepted for L_g amplitude measurements in the time domain (Campillo, 1987, 1990; McNamara, 1996).

The expression (5.2) gives L_g power at distance D from the excitation point. By multiplying this expression by a time windowing function ("wavelet power") $W(t-t_0, D)$ we transform it into a

phenomenological time distribution of recorded L_g power at time t :

$$P(t, D) = \frac{W(t - t_0, D)}{D^{2\gamma}} R S e^{-2\pi D / Q}, \quad (5.3)$$

where t is the recording time, t_0 is the L_g generation time (onset of the mantle arrival at the scatterer), and we have ignored the frequency dependence for simplicity. The function $W(t - t_0, D)$ describes the broadening of the L_g wavetrain of an original duration τ at larger distances, and can be approximated as:

$$W(t - t_0, D) = \begin{cases} 1 & \text{for } \frac{D}{v} < t - t_0 < \frac{D}{v} + \tau D^{2\gamma-1}, \\ 0 & \text{otherwise.} \end{cases} \quad (5.4)$$

Relation (5.4) ensures energy balance in equation (5.3) without attenuation.

By integrating the recorded L_g power at recording point \mathbf{r} and at time t over all source (scattering point) locations, we obtain an expression for the recorded coda power:

$$P(\mathbf{r}, t) = R \int d^2 \mathbf{r}_s \frac{W\left(t - \frac{|\mathbf{r}_s|}{v_a}, D\right)}{D^{2\gamma}} S(\mathbf{r}_s) e^{-2\pi D / Q}, \quad (5.5)$$

where \mathbf{r}_s is the surface integration point, v_a is the apparent velocity of the arrival generating the coda, $D = |\mathbf{r} - \mathbf{r}_s|$, and $S(\mathbf{r}_s)$ is the scattering power proportional to the incident wave power (Figure 5-3). Note that at a given time t , the recorded coda is built up of the waves scattered from within a ring around the recording point (Figure 5-3); the area of this ring increases with time due to its increasing radius and width.

In a simple approximation corresponding to our averaged measurement of coda decay (Figure 5-2), we assume in relation (5.5) $|\mathbf{r}_s|/v_a \ll D/v$, and $S(\mathbf{r}_s) \approx \text{const}$, corresponding to a nearly simultaneous generation of scattered energy within the crust and on the Moho. The integration area in Figure 5-3 then becomes circular, and the geometric spreading and the time window factors cancel. Therefore, instead of relation (5.1), the coda of a PNE arrival is better described by a simple exponential expression (with $\omega = 2\pi f$):

$$P(t) \propto \tilde{P}(t) = e^{-\omega t / Q}. \quad (5.6)$$

A similar equation for coda energy was also derived by Dainty (1985).

The logarithmic amplitude plot (Figure 5-4) shows that the dependence (5.6) fits the observed coda amplitudes throughout 100 – 150 s of the coda. These linear trends of $\ln P(t)$ are consistent with log-RMS coda shapes of Semipalatinsk nuclear explosions presented by Baumgardt (1985). From these trends, we estimate the quality factor as $Q=320$ near 2 Hz and $Q=430$ around 5 Hz (Figure 5-4).

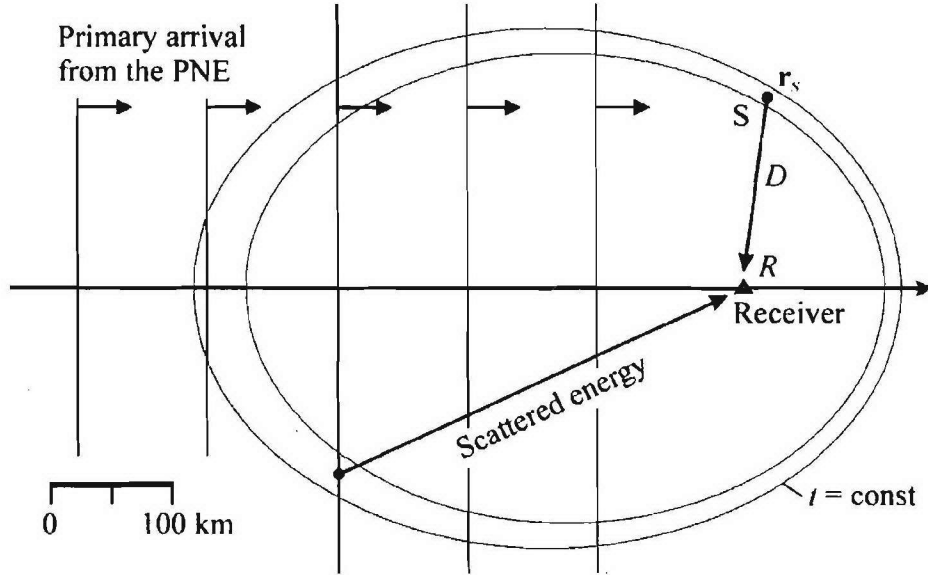


Figure 5-3. Plan view showing surface area (shaded) of the crust contributing to the coda of the long-range P_n at 50 s after the onset of this phase at the receiver. The PNE is located at 2500 km from the receiver, and the curvature of the incident wavefronts is ignored for simplicity. In this approximation, the scattering area is bounded by two ellipses $t = \text{const}$. Note that an increasing-with-time source area compensates for the geometric spreading of coda energy. For infinite velocity of the primary phase, the scattering area becomes circular, leading to cancellation of geometric spreading in the simplified equation (5.6). This plot illustrates the notation in integral (5.5).

Although we did not attempt to carry out a rigorous study of frequency-dependent attenuation, the two values above suggest a dependence of $Q \approx 270 \cdot f^{0.3}$. This moderate increase of Q with frequency agrees with values obtained for stable tectonic areas, such as the central US (Nuttli, 1982), the Canadian Shield (Hasegawa, 1985), or central France (Campillo, 1987). The resulting coda Q estimates are consistent with the values characteristic for the crust and support our association of the coda with L_g (Singh and Herrmann, 1983; Dainty, 1990). The comparatively low values of $Q \approx 270$ at 1 Hz might be related to the effect of the thick sedimentary cover of the Pechora basin sampled by the part of the profile used in this analysis (Morozova *et al.*, 1999). However, this suggestion needs to be verified by a more detailed analysis.

5.4 Decomposition of PNE energy

The second problem posed in the Introduction, that of apparently much stronger coda of WG_{fs} compared to that of $P_{410}P$ (Figure 5-2) is resolved by the observation that the whispering-gallery phases arrive on top of the extensive codas of the preceding arrivals, resulting in buildup of the recorded energy. Thus the observed, overlapping amplitude pattern in Figure 5-2 must be “deconvolved” in order to extract the actual onset and coda amplitudes of the separate arrivals.

For a simple estimate of the actual arrival amplitudes, we model each of the events as a superposition of a primary arrival and of its coda (Figure 5-5). We assume that coda power follows the time dependence (5.6) and is proportional to the total energy of the primary phase. This

approximation leads to a two-parameter amplitude decay model for each of the four arrivals labeled in Figure 5-2:

$$P(t-t^0) = \begin{cases} 0, & t < t^0, \\ \lambda P^0 \tau \tilde{P}(t-t^0), & t \geq t^0, \end{cases} \quad (5.7)$$

where t^0 is the onset time, P^0 is the squared amplitude of the onset, τ is the estimated duration of the primary phase (so that $P^0 \tau$ measures its total energy), and λ is the relative coda amplitude parameter. Since we assume that the mechanism of scattering is common for all arrivals, λ is the same for P , P_{410P} , WG , and WG_{fs} . Thus the cumulative coda power at time t after the onset of WG_{fs} is:

$$P_{coda}(t) = P_P(t-t_P^0) + P_{P_{410P}}(t-t_{P_{410P}}^0) + P_{WG}(t-t_{WG}^0) + P_{WG_{fs}}(t-t_{WG_{fs}}^0) + P_{instr}. \quad (5.8)$$

In expression (5.8), we include an additive term P_{instr} describing the noise level of the instrument and of the recording site. We estimated this term from measurements of signal amplitude between 300 – 350 s after the onset of the long-range P_n (the coda practically dissipates after about 150 - 200 s – see Figure 5-2).

Figure 5-2 shows that the P_{410P} onset is sharper than those of the two WG modes. This comparative sharpness is expected since the WG modes enter the crust at larger angles, undergo additional reflections from the free surface and from the Moho, propagate within (most likely) a more complex lithospheric structure and thus should be more subject to perturbations. In our amplitude modeling, we reflect this sharpness by setting the duration of the P and P_{410P} onsets equal to half of the duration of the WG and WG_{fs} modes. Note that the values τ and λ enter relations (5.7) only through their product, and thus the accurate absolute values of τ are not critical for coda modeling. We set $\tau=2.5$ for the two WG modes and $\tau=1.25$ for P and P_{410P} phases.

By varying the remaining parameters corresponding to the four amplitudes and λ in relations (5.7) and (5.8) in order to match the observed amplitude variations, we obtained in the amplitude units of Figure 5-2: $A_P \approx 1.7$, $A_{P_{410P}} \approx 4.1$, $A_{WG} \approx 2.1$, $A_{WG_{fs}} \approx 2.9$, $\lambda \approx 0.22$. During this inversion, we also found that a value of $Q=380$ better describes the observed pattern of overlapping codas than the value of $Q=320$ estimated from the cumulative linear trend in Figure 5-4.

Figure 5-6 shows that the simple model (5.7)-(5.8) describes the observed amplitude pattern satisfactorily throughout the entire recording time range. As expected, the strongest phase in the “deconvolved” amplitude pattern in the bottom of Figure 5-6 is the reflection from the 410-km discontinuity. Note that because of increased attenuation below about 150-km depth (Morozov *et al.*, 1998a, b), the arrivals from the mantle transition zone are very weak in the high-pass filtered records and they do not boost the apparent WG energy (Figure 5-2). Therefore, the high-frequency coda of the WG arrival in Figure 5-2 can be directly compared to our modeled WG coda in Figure 5-6. As expected, the low-frequency component of the WG phase is still stronger than the high-frequency part, reflecting the source spectrum dominated by the energy between 1- 2.5 Hz (Morozov *et al.*, 1998b).

5.5 Energy patterns of PNE wavefield

As the argument above shows, the energies of secondary phases including the long-range P_n appear stronger than they are in reality due to their enhancement by the codas of the earlier phases. This observation helps us answer the second question posed in the Introduction. However, even

after our amplitude correction, the amplitudes of the WG modes, and in particular, their total energy (Figure 5-6, bottom) are still significantly higher than expected from 1-D modeling (Mechie *et al.*, 1993; Morozova *et al.*, 1999). At longer ranges, high amplitudes of the surface multiples of P_n in this region are also indicated by the observations of a very strong PP phase (corresponding to the first phase in the WG_{fs} group in our notation) from the Semipalatinsk nuclear explosions (Baumgardt, 1985, 1990).

As a solution to this controversy, we consider two possible factors that could cause the increased energy of the WG modes and that cannot be accounted for in 1-D simulations. First, for a PNE near 700-m depth (Sultanov *et al.*, 1999) the P -wave energy radiated at about 2-Hz frequency range (the dominant frequency of QUARTZ explosions; cf. Ryberg *et al.*, 1995; Morozov *et al.*, 1998b) is enhanced due to constructive interference with the pP reflection from the free surface (Fuchs, 1966; Greenfield, 1971). This interference would focus the energy in a downward direction increasing this energy by a factor of 10 – 13 compared to a source in an infinite medium (note that such interference might account for the 2-Hz peak frequency of the recorded energy). However, a point source is an oversimplified representation for a real explosion, and any irregularity of the source region or nonlinear effects would reduce such focusing (Greenfield, 1971). As a result, 1-D modeling tends to overestimate the downgoing energy at the expense of the modes propagating subhorizontally. For an explosion detonated within a heterogeneous crust, we expect that a larger portion of energy would propagate in the form of the lithospheric-guided waves than predicted in 1-D simulations.

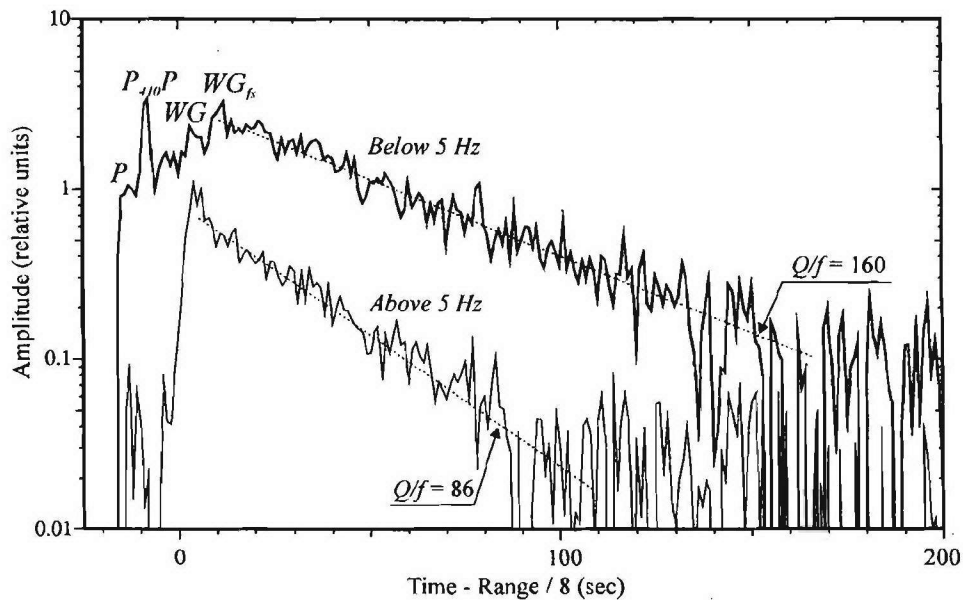


Figure 5-4. The same amplitudes as in Figure 5-2 plotted in logarithmic scale. Straight lines correspond to the relation (5.6) with $Q \approx 320$ for the low-frequency curve (at approximately 2 Hz) and $Q \approx 430$ for high frequency (at 5 Hz). Background noise estimated from a time window between 300- 350 s of the records was subtracted from both records prior to taking logarithm.

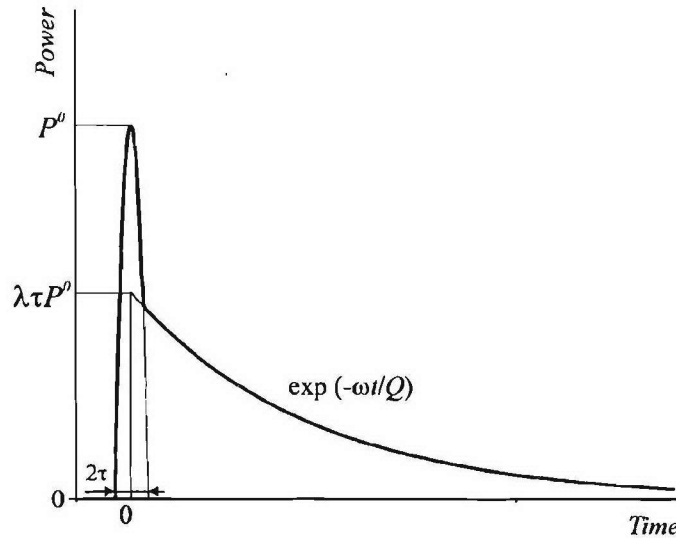


Figure 5-5. A model of intensity variation with time for a PNE event (see equations (5.7)). The energy of the primary event is approximated by a parabolic function and is characterized by its peak power P^0 and duration τ . The coda is parameterized by its coupling to the primary event λ and by its decay rate ω/Q defined in relation (5.6).

Another explanation for high amplitudes of the waves guided within the lithosphere could be their focusing under the northern part of the East European Platform. This region has a mantle structure that is distinctly different from that of the West Siberian basin (Mechie et al., 1997; Morozova et al., 1999 and personal communication). The unusually high amplitudes of the long-range P_n have been observed only on the profiles QUARTZ and RUBIN traversing the East European platform (Ryberg et al., 1995), and the strong PP phase was also identified practically along the path of the profile RUBY-1 (Figure 1-1; Baumgardt, 1985). On the contrary, our preliminary study (the Siberian PNE profiles have not been analyzed in full) suggests that the long-range P_n is much weaker and crustal attenuation is somewhat lower under the Siberian craton (Figure 5-7).

Although the above argument is only qualitative, note that not only the WG arrivals but also their primary phases P_n and P_N (the latter are refractions and reflections from regional seismic boundaries between 90 – 140 km depth; cf. Pavlenkova, 1996; Morozova et al., 1999) are very strong between the offsets of about 300 – 800 km (Figure 5-1). Such strong amplitudes should be due to high energy of the source and to the velocity gradient and reflectivity observed within the lithosphere (Morozova et al., 1999). After a reflection from the Moho and free surface, this near-critical energy could form the observed strong waveguide arrivals (Figure 5-2).

5.6 Discussion

Since our coda decay model in equation (5.6) is dictated simply by the scattering geometry and by the principle of conservation of energy, it should be applicable to other observations of scattering at teleseismic distances. Indeed, in a teleseismic study of underground nuclear explosions at Novaya Zemlya, Greenfield (1971) interpreted the observed coda as a result of near-source $R_g \rightarrow P$ scattering and pointed out that without crustal attenuation, the coda energy would have been constant. Dainty (1990) suggested that for Kazakh nuclear tests recorded at NORESS, about half

of the coda energy consisted of near-source $L_g \rightarrow P$ scattering, and another half was represented by $P \rightarrow L_g$ scattering near the seismic array, with an energy decay law similar to derived above (Dainty, 1985). Baumgardt (1985, 1990) used incoherent beams and continuous “polar scans” to identify variations in coda decay and mode content within 200 – 400 sec of the teleseismic P -wave codas.

Although the density of PNE recordings (10 - 15 km spacing) does not allow application of array methods for a detailed identification of the constituents of the coda (e.g., Bannister et al., 1990; Hedlin et al., 1994), the length of recording and the extent of coverage (Figure 5-1) allow measurements of the coda decay rate. Our model (Figure 5-6) shows that crustal-guided waves explain not only its amplitude decay but also the apparent lack of a pronounced coda of the body-wave arrivals from the mantle transition zone. Due to the slow coda amplitude decay rate, the codas of the PNE arrivals can be observed to 100 – 150 s, and therefore the codas of multiple P -wave arrivals overlap and boost the energy of the later arrivals including the long-range P_n .

The coda of the WG phases and, as we suggested above, of all the other P -wave phases are not due to anomalously low crustal attenuation and to a tuned, narrow-band, highly scattering uppermost mantle as suggested by Ryberg *et al.* (1995) or by Ryberg *et al.* (1999). The coda is neither unusually high-frequency nor long to require such an interpretation. On the contrary, we favor the traditional interpretation of the coda as a result of crustal scattering of the waves incident

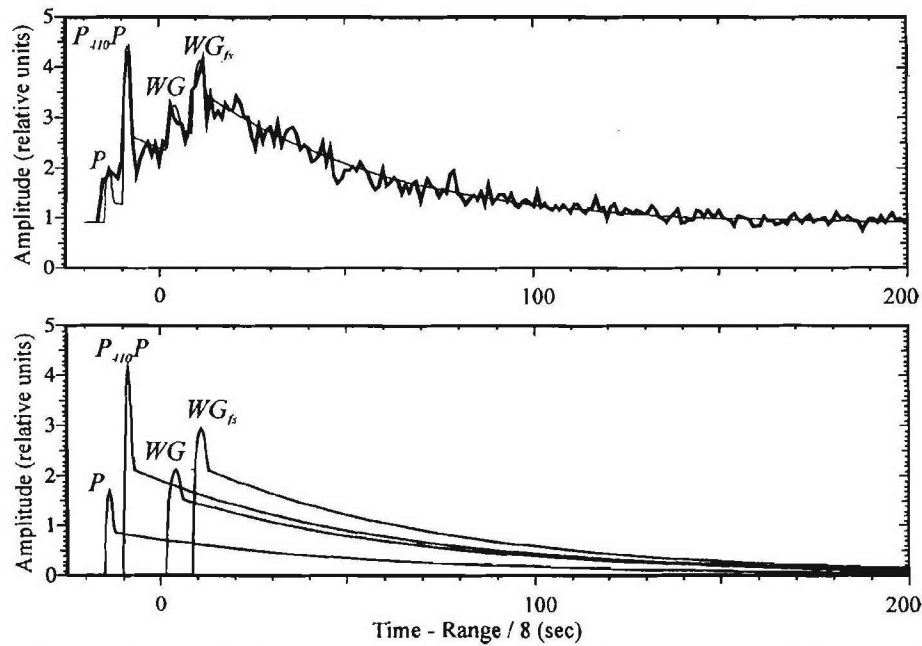


Figure 5-6. *Top*: Coda amplitude decay model for frequencies below 5 Hz (Figure 5-2). Thick line is the low-frequency amplitude from Figure 5-2, thin line shows the modeled amplitude decay described by relation (5.8). Note that crustal scattering and a simple approximation of coda power (1) explain the observed coda build-up by the subsequent P , $P_{410}P$, WG , and WG_{fs} arrivals. *Bottom*: Amplitudes and codas of the four separate arrivals forming the total coda energy (5.8). Note that this decomposed section is dominated by the reflection $P_{410}P$. Also compare the amplitude of WG in this plot to the high-frequency WG coda in Figure 5-2 and note that WG is stronger at lower frequencies, as expected.

from the mantle and propagating at high apparent velocities. The reciprocity principle complements this mechanism by its counterpart in which strong crustal-guided waves (P_g, S_g, L_g, R_g) generated by the PNE are scattered on crustal heterogeneities producing secondary phases propagating through the mantle and feeding the observed coda (Dainty, 1985, 1990).

Although our “instantaneous distributed coda source” model (5.6) above is only an approximation to the actual spreading coda source region, it is clearly more adequate than the point-source scheme (5.1) used by Ryberg *et al.* (1995) and Ryberg and Wenzel (1999). The relative velocities of the fast primary (P_n) to the slow scattered (L_g, R_g) phases lead to a distributed scattering mechanism and to the cancellation of the geometric factor in our coda decay relation (5.6). On the contrary, although the model by Ryberg *et al.* (1995) and Ryberg and Wenzel (1999) also implied distributed scattering (in their case, located within the mantle) these authors made no attempt to derive a proper coda relation for this scattering geometry. Instead, they resorted to a model of coincident coda source and receiver (Aki and Chouet, 1975) that is totally irrelevant in this case.

While attributing all scattering to the crust and Moho boundary, our argument does not eliminate the possibility of mantle scattering. Some degree of scattering should certainly be present in the uppermost mantle, yet such scattering is not required by the observations of PNE coda. At the same time, mantle scattering cannot be as high as suggested in the model by Ryberg and Wenzel (1999) in which the 75-km thick sub-Moho mantle reflects about 8-10 times more seismic energy than the Moho (as estimated by Morozov, submitted). Such strong scattering would most certainly destroy any coherent seismic waves penetrating through the uppermost mantle.

The above estimates of arrival amplitudes suggest that the dominance of the WG modes in the energy pattern of the PNE wavefield is to a certain degree apparent. Despite the high values of the observed amplitudes within the long-range P_n time window (Figure 5-2), both of the WG modes actually carry only about 75% of the power delivered to the surface by the $P_{410}P$ reflection. Since the $P_{410}P$ reflection is more coherent and shorter in duration, its coda is somewhat lower in amplitude yet it carries about 65% of the energy of both WG codas and about the same as the WG_{fs} coda alone.

Being significantly lower than it appears, the energy of the WG modes is still high compared to the predictions of 1-D simulations. As we suggested above, 1-D modeling of a PNE as a point source in a homogeneous crust could underestimate the amount of energy propagating in seismic phases guided within the crust and lithosphere. However, considering the uniqueness of the observation of high-energy long-range P_n under the East European platform and the West Siberian Basin, our preferred explanation of such high amplitudes is their being caused by focusing in these regions.

The high amplitudes of multiple refractions (PP and WG) could be qualitatively explained by the effects of crustal, Moho, and lithospheric heterogeneity favoring propagation of energy within the top 150 – 200 km of the mantle under the northern part of the East European platform and under the West Siberian basin (Figure 1-1). Among these effects are the strong velocity gradient and reflecting boundaries in the uppermost mantle (Morozova *et al.*, 1999). As demonstrated by Kennett (1987), within the ranges of PNE profiles (20° to 30°) layered structures within the mantle may act as a wave guide contributing significantly to the P -wave coda.

Baumgardt (1985) also suggested that focusing could explain the high-amplitude PP in NORSAR recordings of the Semipalatinsk nuclear explosions. In particular, near-receiver focusing

was required to account for the variations of PP amplitude across the array. In contrast to this observation, QUARTZ records show consistent and strong WG phases within the entire offset range and suggest that reflective lithosphere with vertical velocity gradient and favorable source conditions should be responsible for the overall character of the wavefield. Near-receiver scattering manifests itself in reduced coherency between the adjacent seismograms.

The unusually strong P_n and WG phases observed in QUARTZ records could support the observations of coda flattening between 310 – 450 sec after the teleseismic P -wave arrival in the recordings of Semipalatinsk explosions at NORSAR (Baumgardt, 1985, 1990). In a detailed study, Baumgardt (1990) showed that this part of the coda consisted primarily of L_g and S_n modes, with minor amounts of P_n energy and no detectable teleseismic P contribution. He interpreted this coda flattening as a result of $P_n \rightarrow L_g$ scattering under the Urals. This explanation, which appears to be the only reasonable model of the observed coda, also implies that the P_n is strong and carries enough energy to reverse the decay of the P -wave coda.

The observed difference between the amplitude dependencies of the records at lower and higher frequencies (Figure 5-4) is very significant. Similarly to the deep P -wave phases, the WG_{fs} arrival and its coda are low in their high-frequency content (Figure 5-4). Compared to WG , WG_{fs} is similar but travels two additional passes through the crust, and thus the disappearance of WG_{fs} in the high-pass filtered record should be related to crustal attenuation. Also, the increased Q at higher frequencies (Figure 5-4) and its regional variations (Figure 5-7) suggests that the low-frequency coda contains more surface waves sampling the sedimentary, lower- Q parts of the upper crust. Therefore, the difference between WG and WG_{fs} also points to a crustal nature of the coda.

An important implication of our coda model is that only a three-dimensional (3-D) analysis of scattering can yield reasonable quantitative estimates of the dynamic properties of the PNE wavefield. Although 3-D or 2-D modeling of PNE short-period records using realistic crustal and mantle models is at present not practical, it appears that interpretations of scattering based exclusively on 1-D simulations (Tittgemeyer, 1996; Ryberg and Wenzel, 1999) might be misleading. On the contrary, energy balance considerations consistent with the accepted teleseismic coda models and utilizing the true, 3-D view of the process of wave propagation allow us to explain the behavior of the coda and to unravel the amplitude relations between the observed PNE phases.

5.7 Conclusions

The work presented above focused on the observed properties of the long-range PNE phases, and particularly, on the strong amplitude and long duration of the coda of the long-range P_n . Reconsidering the available observations of this phase in the records from the PNE profile QUARTZ, we arrived at both a consistent explanation of the character of this coda as well as at a realistic estimate of its decay rate, in contrast to some of the previous results (Ryberg *et al.*, 1995; Tittgemeyer *et al.*, 1996; Ryberg and Wenzel, 1999). The key points of our coda model of PNE arrivals are:

- 1) Regardless of the accepted explanation for the nature of the long-range P_n , a long coda is not specific to this phase but it follows every PNE arrival at an offset range over 2000 km;
- 2) The 100 – 150-s long codas of the long-range arrivals are due to the generation of these codas within the crust by PNE phases propagating at high apparent velocities thus leading to distributed coda excitation and reduced geometric spreading;
- 3) The codas of the PNE arrivals build up energy within the record section leading to an increased energy within the long-range P_n time window; the amplitude pattern of the records was inverted for true amplitude relations between the arrivals.

Based on a detailed analysis of the long-range P_n , we demonstrated that this phase consists of two groups of arrivals that are clearly distinct in their frequency, amplitude, coda, and travel-time patterns. On the weight of such combined evidence, these arrivals are explained as the Moho and free-surface multiples of the refractions and reflections within the uppermost-mantle (P_n , P_N).

As a result of our PNE coda model, we obtained estimates of coda Q ranging between $Q=380$ near 2 Hz and $Q=430$ around 5 Hz. These values correspond to the values generally associated with the crust (including the sedimentary rocks) and suggest that the crust could be the source of the extensive coda pattern observed in PNE records (Figure 5-1). As our study shows, the amplitude pattern of the PNE records throughout their full length can be explained quantitatively by body- and guided waves within the upper mantle and by (predominantly) crustal scattering.

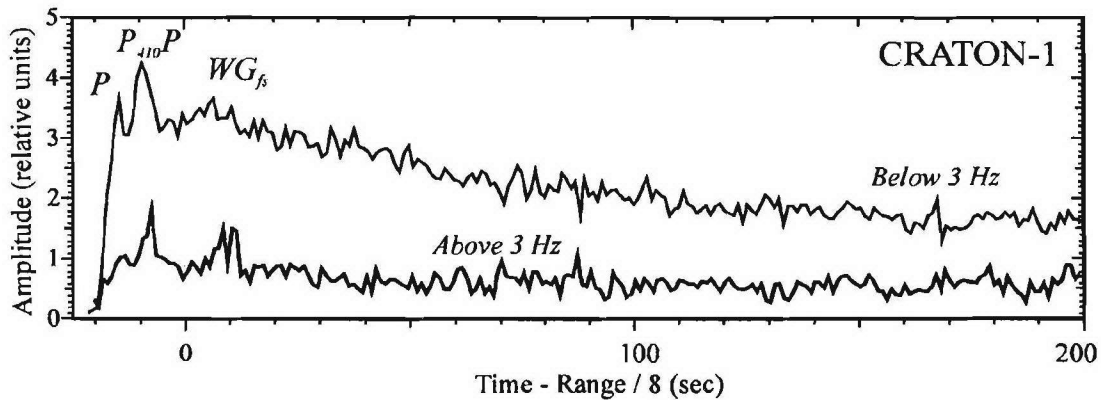


Figure 5-7. Records from PNE CRATON-1 in the West Siberian basin averaged and plotted in the same way as QUARTZ-4 records in Figure 5-2. Due to lower frequency content of these records, the frequency band separation is performed at 3 Hz instead of 5 Hz in Figure 5-2. Note that even without correcting for coda build-up, the WG_{fs} is weaker than $P_{410}P$ and also much weaker than in the records from QUARTZ-4 (Figure 5-2). Also note the longer codas and increased high-frequency content of WG_{fs} (compared to WG), in contrast to Figure 5-2. These differences suggest regional variations in WG propagation characteristics and lower crustal attenuation within the Siberian craton.

6 Anomalies in frequency-dependent Lg coda Q

6.1 Summary

A striking observation from comparative analysis of the PNEs is the difference of Lg coda decay characters across the study area. Within the East European Platform and south-west West Siberian Basin (profile QUARTZ) Lg coda amplitude decays exhibit clear frequency dependence that was previously described (Chapter 5) by frequency-dependent coda quality factor $Q \approx 350 \cdot f^{0.13}$ (f is the frequency). By contrast, within the Siberian Craton (profile KIMBERLITE), the coda exhibits a constant decay rate for all frequencies, which would correspond to Q nearly proportional to frequency. However, we argue that such a strong frequency dependence of Q could actually be due to non-frequency dependent coda attenuation process associated with geometric spreading and leakage of the energy from the crust (e.g., by refraction). The modified coda amplitude decay relation thus becomes:

$$\frac{d \log A}{dt} \approx -\gamma - \frac{\pi f}{Q},$$

where γ is the coda geometric spreading factor. Notably, when using this form, γ remains constant ($\approx 0.003 \text{ s}^{-1}$) for the entire region, and $Q \approx 470$ for QUARTZ and $Q = \infty$ for KIMBERLITE. Very low attenuation within the Siberian Craton is also indicated by Pg propagating to unusual distances of 1600-1700 km. An additional advantage of using the above expression is that Q can now be viewed as frequency-independent.

6.2 Geometrical-spreading corrected or frequency-dependent coda Q ?

Measurements of the frequency-dependent quality factor, $Q(f)$, often results in Q increasing with frequency, which is conventionally expressed as a power law:

$$Q(f) = Q_0 \left(\frac{f}{f_0} \right)^\eta, \quad (6.1)$$

where f_0 is a reference frequency often taken equal 1 Hz. Both Q_0 and exponent η are assumed constant within the frequency range of interest, and thus relation (6.1) essentially represents fitting a two-parameter dependence to the observations of Q made at a set of selected frequencies. The power-law dependence appears to be generally dictated by convenience and represents a suitable parameterization in most cases. From several Lg Q and Lg coda Q studies, the frequency-dependence parameters η typically range from ~ 0.1 to near 1.0 (e.g., Nuttli, 1973; Mitchell, 1975; Frankel, 1991; Benz et al., 1997; Mitchell et al., 1997, 1998; McNamara, 2001; Erickson et al., 2004). General correlation to tectonics appears to suggest that active tectonic regions are characterized by low Q_0 and high η , while stable cratons – by higher Q_0 and lower η (Erickson et al., 2004).

An initial attempt for application of the conclusion above to the region and frequency band of DSS profiles led to similar observations (Morozov and Smithson, 2000). Measurements of Lg coda Q at frequencies ~ 2 and 5 Hz from PNE QUARTZ-4 in the Mezenskaya Depression (near the position of PNE QUARTZ-2 in Figure 1-1) resulted in the values of $Q_1 = 350$ (at $f_0 = 1$ Hz) and $\eta = 0.13$ in relation (6.1) (Chapter 5). The somewhat low Q_0 value was explained by the influence of thick

sediments within the depression, and low η appears in agreement with the stable East European Platform.

Similar measurements using the records from profiles KIMBERLITE and METEORITE in Siberia lead to strikingly different results. From the unusual efficiency of Pg propagation within the Siberian Craton, crustal Q was expected to be relatively high (Figure 6-1). In addition, travel-time modeling of QUARTZ profile (Figure 1-1) also suggested a simpler, layered crustal structure with little Moho topography within the West Siberian Basin as compared to the northern parts of the East European Platform (Shueller et al., 1997; Morozova et al., 1999). However, the logarithm of Lg coda amplitude measured from PNE Kimberlite-3 at a station within Siberian craton shows an approximately frequency-independent decay (Figure 6-2). When interpreted in terms of the usual assumption of correctly compensated geometrical spreading of the coda (Morozov and Smithson, 2000), this decay is entirely due to the coda Q :

$$\log A_{coda}(f, t) = const - \frac{\pi f}{Q(f)} t = const - \frac{\pi}{Q_0} f^{1-\eta} t. \quad (6.2)$$

To account for the frequency-independent decay rate in relation (6.2), $Q(f)$ should be proportional to the frequency, corresponding to $\eta \approx 1$ in power law (6.1). Q_0 can be estimated as ~ 200 for Lg coda and 400 for the S -wave coda, both values appearing surprisingly low for this cratonic area and in disagreement with other observations.

The observations above suggest that the interpretation of the frequency dependence of Q could be reconsidered, at least for strong ($\eta \approx 1$) frequency dependences, in the DSS frequency band (~ 1 -10 Hz), or within the area of this study. Note that the strong frequency dependence of Q arising from formula (6.2) is observed for the entire KIMBERLITE profile (Figure 6-3), and not only at the location presented in Figure 6-2.

High $\eta \approx 1$ values in relation (6.1) imply that attenuation is quickly reduced with frequency. Liu et al. (1976) showed that linear visco-elastic rheology based on a “generalized standard linear solid” could explain frequency-dependent intrinsic attenuation observed during wave propagation through Earth materials. However, laboratory measurements are carried out at significantly higher frequencies and shorter wavelengths than those of the seismic waves considered here. At short-period seismic scales (100-10000 m), pervasive crustal and upper-mantle heterogeneity creates a complex interplay of numerous rheologies and could result in completely different properties. In particular, presence of attenuating component, such as water, would reduce the inferred high Q at higher frequencies. Moreover, for coda waves bouncing within the crustal waveguide, scattering should be the primary contributor to their attenuation. For scattering, attenuation decreasing with frequency would mean that the total volume of scatterers drops nearly linearly at smaller scale lengths. Although this could be possible, it still appears unlikely that heterogeneities within the West Siberian Basin and Siberian Craton become progressively less abundant as their sizes reduce. Typically, scaling laws suggest increasing representation of heterogeneities (e.g., faults and topographic features) at smaller scales.

Accepting the above conjecture that high η could in fact be observed where Q is very high, we note that the frequency-independent amplitude decay should not be related to the attenuation defined as an energy dissipation process proportional to the number of wave cycles (that is, to $f \cdot t$). Instead, if coda amplitude decay with time includes a purely geometrical component, it could be approximated by the following relation:

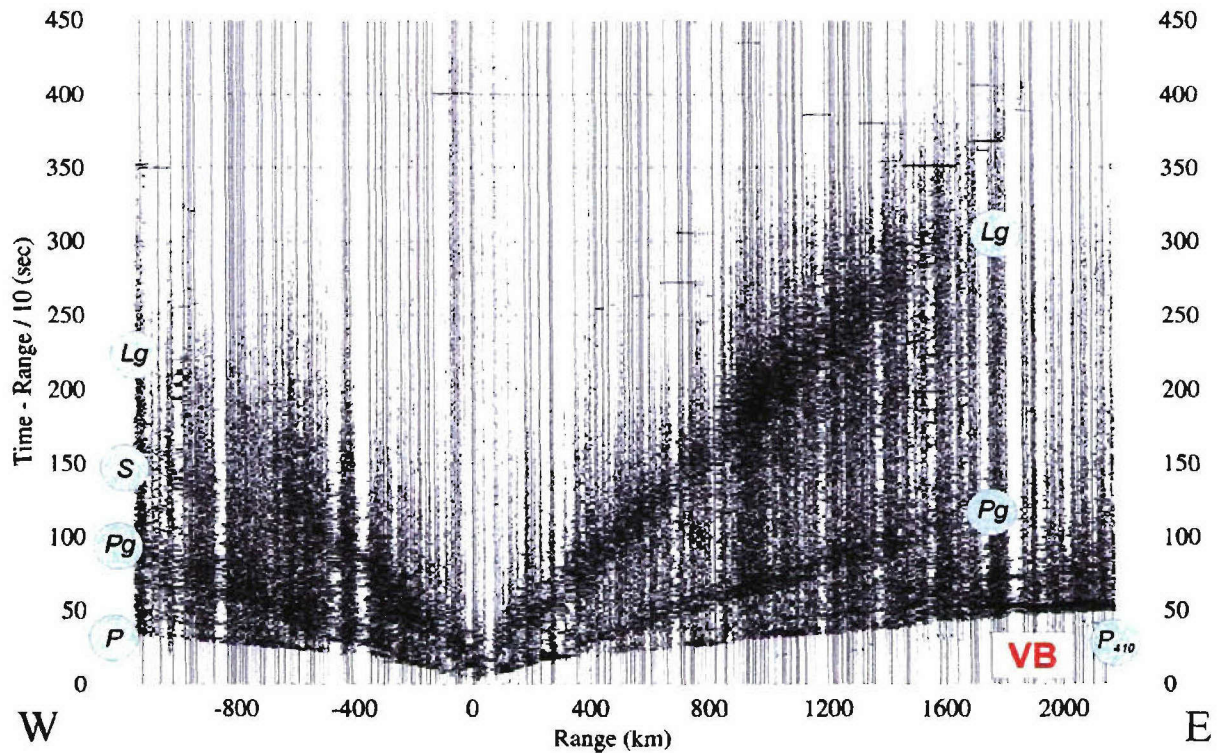


Figure 6-1. Vertical-component records from PNE CRATON-2 (Figure 1-1). Note the unusually strong propagation of Pg to ~1700 km from the shot, quickly attenuating within the Viluy basin (VB). Such high propagation efficiency suggests high crustal Q , at least in the eastern part of the profile.

$$\log A_{\text{coda}}(f, t) = \text{const} - \left(\gamma + \frac{\pi f}{Q} \right) t. \quad (6.3)$$

Here, γ describes an effective geometrical spreading process. Amplitude decaying with scattering time and independent of the frequency could correspond, for example, to leaking of the wave energy out of the Pg/Lg waveguide as the multiple-reflected waves bounce within it (Gutenberg, 1955). Note that the exponential relation for $A_{\text{coda}} \propto \exp(-\eta t)$ is primarily dictated by the convenience of working in the $(t, \log A)$ plane. With significant measurement errors inherent in attenuation measurements, other frequency-independent expressions could be defined yet in practice, they could hardly be distinguished from form (6.3).

With a single constant Q , expression (6.3) represents another two-parameter relation for $\log A_{\text{coda}}(f, t)$ which is an alternative to (6.2). Although Q could also be theoretically considered as frequency-dependent in formula (6.3), distinguishing this dependence from the effect of γ appears highly problematic with the available data. Thus, in an Ockham razor approach, we view the form (6.3) with a single and constant Q as a viable alternative to frequency-dependent $Q(f)$ for the DSS PNE data. Potential extrapolation of this conjecture to other situations will still need to be examined in the future.

Within the accuracy of fitting relations (6.2) or (6.3) to the typical data, both of them apparently could be used interchangeably. Thus, the dependence (6.3) with $Q = \tilde{Q}$, when recast in the form (6.2), would lead to frequency-dependent attenuation with:

$$\eta = -\log_f \left(\frac{\gamma}{f_{\text{ref}}} + \frac{\pi}{\tilde{Q}} \right), \quad (6.4)$$

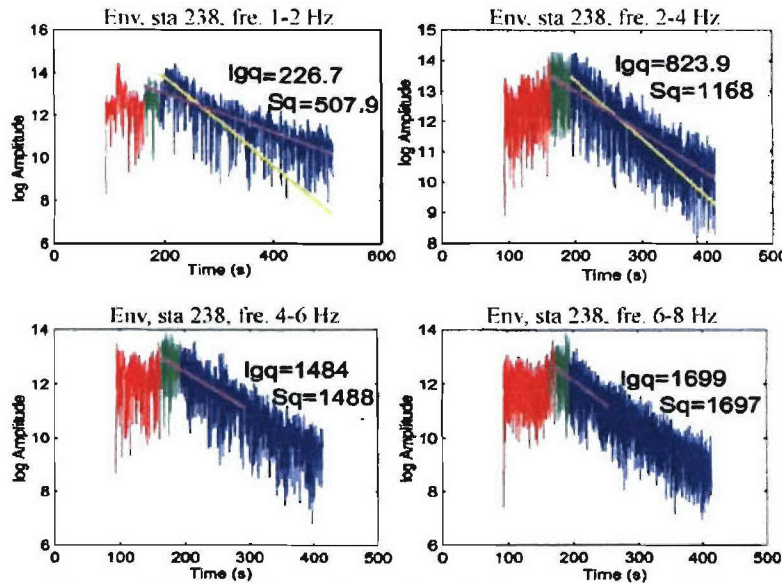


Figure 6-2 Amplitude envelope of vertical-component record from station 238 from PNE Kimberlie-3 filtered within 1-2, 2-4, 4-6, and 6-8 Hz frequency bands (labeled). Estimated coda Q for the S -wave and Lg coda windows are indicated. Note that these Q values quickly increase with frequency. Also note that at the same time, temporal slopes of $\log(\text{amplitudes})$ appear to be independent on the frequency bands.

where the reference frequency f_{ref} could be selected within the frequency band. This shows that $\eta=0$ for $\gamma=0$ and $\eta \rightarrow 1$ when $Q \rightarrow \infty$. A high γ (steep geometric coda amplitude decay, as possibly caused by strong crustal folding and rough Moho) would thus explain the low Q_0 and high η observed in active tectonic areas.

Using the dependence (6.3) instead of (6.2) to fit QUARTZ-4 (Figure and KIMBERLITE-3 (Figure 6-2) observations reveals that for both datasets, geometrical factor is the same, $\gamma \approx 0.003 \text{ s}^{-1}$, with $Q \approx 470$ for QUARTZ and $Q = \infty$ for KIMBERLITE. In agreement with the observations of unusually efficiently propagating Pg within the Siberian Craton, its crust shows very low attenuation. Close geometrical factors both east and west of the Uralian belt (Figure 1-1) could also be expected, as crustal structure remains generally similar on both sides. As another hypothesis, it appears that crustal thickness could be the primary factor controlling the values of γ . With increasing crustal thickness, the number of reverberations required to form a crustal-guided phase at a given distance would decrease, leading to lower values of geometrical attenuation γ .

If confirmed by further analysis of the DSS PNE and other data, the above observations could have several important implications for seismic calibration and nuclear test monitoring. First, as frequency dependence of Q trades off with geometrical spreading, it is important to eliminate this uncertainty before correlating the resulting parameters with the geological structures or looking for portable attributes. Equation (6.3) removes this trade-off by defining the geometrical spreading as a frequency-independent part of signal attenuation with time (distance). This could allow local measurements of geometrical spreading by spectral analysis of coda waves. The resulting spreading parameter γ could be regionalized and correlated with geology.

The second potential advantage from using form (6.3) arises from the stability of the geometrical exponent γ suggested by the present observations. If γ is confirmed to be stable or correlated with the crustal thickness, it could be used as a useful and transportable calibration parameter. Robust regional values of geometrical spreading could be utilized to correct the observed coda Q values. Moreover, because of their frequency independence, the resultant coda Q values also may have a better chance for being transportable between different the frequency bands, types of observations, and geographic regions.

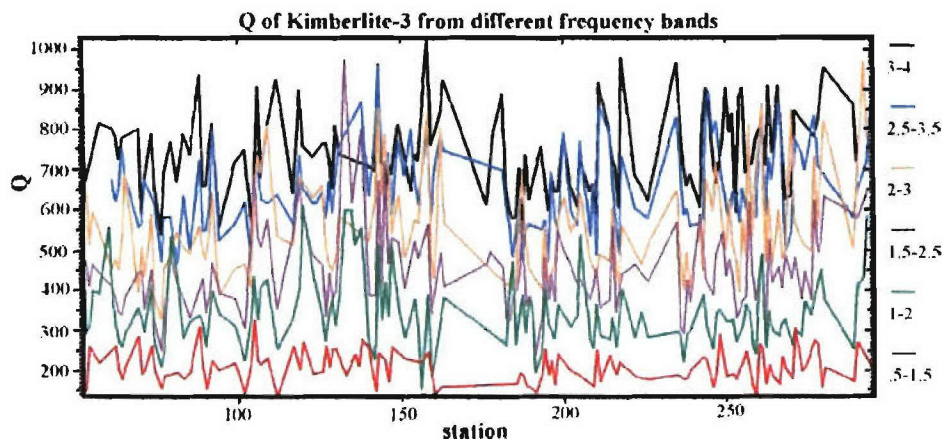


Figure 6-3. Lg coda Q of PNE Kimberlite-3 measured across the profile within several frequency bands (labeled on the right). Despite the scatter in the Lg Q values, Q consistently increases with frequency.

In most practical cases, removal of the $\gamma \leftrightarrow Q(f)$ trade-off would leave us with only frequency-independent Q in relation (6.3). The advantage of this point of view would be in freeing Q measurements from reliance on independent determinations of geometrical spreading, which are the critical part of most attenuation measurements (Benz et al., 1997). Note that because of their using band-limited data but not explicitly enforcing frequency-independence, geometrical spreading estimates may also turn out to be effectively dependent on the frequency. In addition, (γ, Q) parameterization is also closer and should be consistent with attenuation measurements using spectral ratio techniques (which eliminate the absolute amplitude effects and rely on spectral slopes, thereby typically also producing frequency-independent Q estimates insensitive to the geometrical spreading).

6.3 Conclusions

Analysis of the frequency-dependent Lg coda Q from several DSS PNE profiles in Northern Eurasia indicates significant differences in attenuation properties between the East European Platform and West Siberian Basin and Siberian Craton. A consistent interpretation arises from abandoning the traditional $Q(f) = Q_0 f^\eta$ model in favor of the model utilizing regionally-variable geometrical spreading and frequency-independent attenuation. In this model, the geometrical spreading is consistent between the two studied areas, and the attenuation appears to be very low within the Siberian Craton, in agreement with other observations

If confirmed by further analysis, these observations could have several important implications for seismic calibration and nuclear test monitoring:

- 1) it would allow more consistent and reliable measurements of geometrical spreading and Q ;
- 2) the geometrical exponent γ is likely to be stable or correlated with the crustal thickness, in which cases it could be used as a useful and transportable calibration parameter,
- 3) because of their frequency independence, the resultant coda Q values also may also be better transportable between different the frequency bands, types of observations, and geographic regions.

7 Constraints on the crustal structure from P/S conversions in the first-arrival PNE codas

7.1 Summary

In a way similar to receiver function imaging, coda of the first arrivals can be used to constrain crustal structure along controlled-source refraction profiles with multi-component recording. Stacked cross-correlations of the radial and vertical components of recordings from three nuclear explosions (PNEs) of the 3850-km long profile QUARTZ exhibit good correlation with the depth to the basement and provide a horizontal resolution level close to recording station spacing (10-15 km). The results also suggest high (~ 0.35 -0.4) average Poisson's ratios within the sediments. When applied to other multi-component long-range refraction profiles, this approach could provide a simple and inexpensive way to constrain the structure of the upper crust that is required for interpretation of the deeper structures and that cannot be constrained by other means. Most importantly, reverberations within the sedimentary column appear to account for much of the observed complexity of the first arrival waveforms, and therefore, such reverberations should be taken into account in the interpretations of seismic scattering from within the mantle.

7.2 Introduction

Analysis of the coda of the first teleseismic arrivals using receiver function (RF) methods has become a standard technique for mapping crustal thickness (Langston, 1977; Ammon, 1991). The elegance and power of the receiver function approach is in its ability to use deconvolution of vertical and horizontal-component recordings of teleseismic arrivals at a single station to neutralize the effect of seismic source. Isolation of source effects results in a RF that is interpreted (albeit with some ambiguity - cf. Ammon *et al.*, 1990) in terms of a layered crustal velocity structure. In recent years, teleseismic receiver functions of regional seismic arrays were successfully used to image subtle variations of the lithospheric and mantle discontinuities down to the mantle transition zone (e.g., Vinnik, 1977; Bostock, 1996; Dueker and Sheehan, 1998; Chevrot *et al.*, 1999; Gurrola and Minster, 2000). However, with its broad scope of application, RF analysis is still employed exclusively in natural-source, teleseismic seismology whereas many existing controlled-source, long-range refraction profiles with 3-component recording could also benefit in imaging near-receiver structures using this technique. Among such long-range profiles with great potential for RF imaging are the Deep Probe, SAREX (Henstock *et al.*, 1998), and a number of Deep Seismic Sounding (DSS) profiles in Russia (Yegorkin, 1992).

PNE recordings resulted in extensive 3-component data sets suitable for short-period coda analysis. As in earthquake studies, recording of several PNEs at each station allows stacking for noise reduction and for further isolation of source and recording site effects. In principle, the controlled-source nature of the experiments offers an advantage over the natural-source RF, allowing examination of the records across linear arrays of hundreds of densely spaced stations from close proximity to teleseismic distances from the source. Here, we illustrate the use of the coda analysis on one of the most well known profiles of the DSS program, QUARTZ (Figure 1-1 and 7-1).

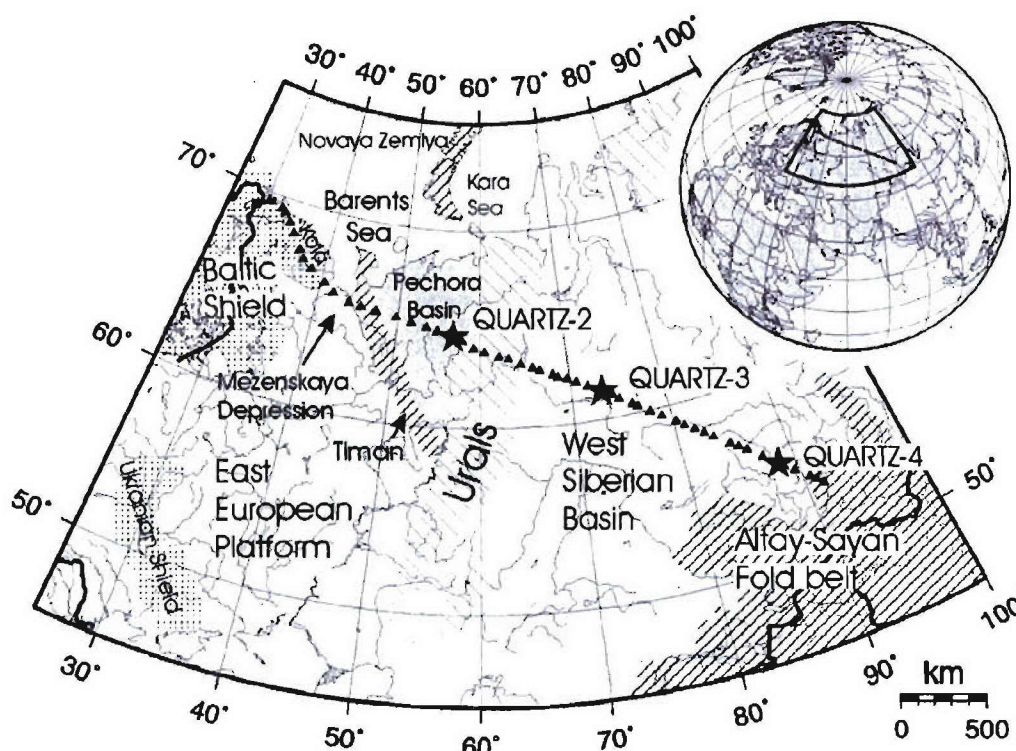


Fig 7-1. Map of the western part of the former USSR showing the profile QUARTZ. Triangles and stars indicate the locations of the chemical and nuclear explosions (PNEs) recorded by the profile, respectively. Three QUARTZ PNEs used in this study are labeled, and the major tectonic structures crossed by the profile are indicated. Inset shows the location of the map in Northern Eurasia.

Figure 7-2 shows the effect of the crustal structure on the first arrivals from PNE QUARTZ-4 between 2800 - 3100 km distances. Compared to the virtually sediment-free Baltic Shield (Kola Peninsula), the thick sedimentary rocks of the Mezenskaya depression and Pechora basin (Figure 1-1) lead to lower-frequency and more complex first arrivals, with the horizontal-component recordings becoming less synchronous with the vertical-component and exhibiting $\sim 0.3 - 0.5$ s delays after the primary onsets (Figure 7-2). A likely explanation of such delayed arrivals recorded in horizontal components is their origin in *P/S* mode conversions and/or *P*-wave reverberations within the crust, and particularly within the sedimentary cover. As our analysis below shows, this is indeed the case, and stacked cross-correlations of the radial and vertical recordings of the three QUARTZ PNEs result in a consistent image of the basement. Thus, similar to natural-source RF studies, by using the waveforms from a few distant explosions, we are able to obtain a detailed image of the sediment cover along the entire profile.

Another important implication of our results below is in emphasizing the importance of crustal reverberations for interpreting the complexity of long-range seismic arrivals. Recently, a number of authors (Ryberg et al., 1995, 2000; Thybo and Perchuc, 1997) interpreted waveform complexity and the early coda (< 10 -20 s) of the arrivals from long-range, controlled-source profiles as indicators of seismic scattering originating within the mantle. In contrast to this hypothesis, our

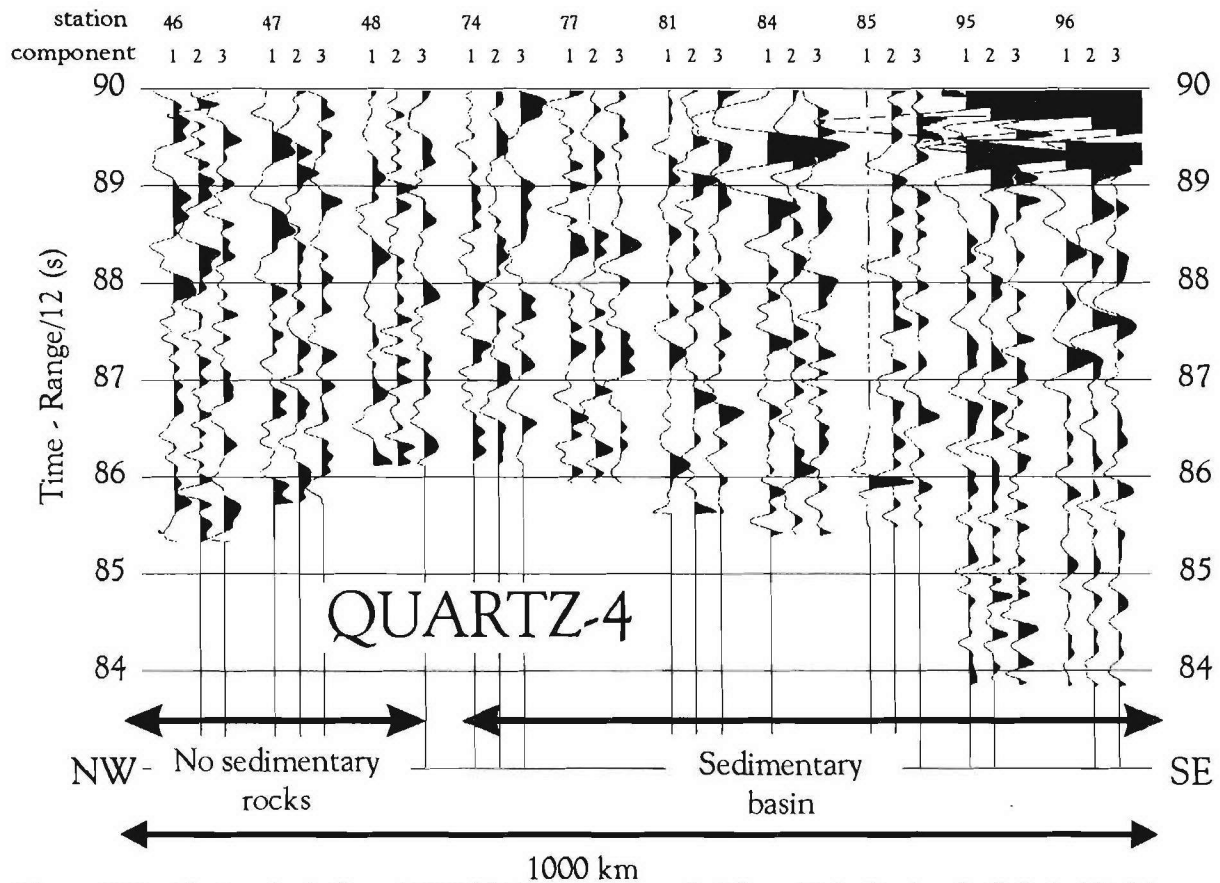


Figure 7-2. First arrivals from PNE QUARTZ-4 recorded from Kola Peninsula (labeled Baltic Shield in Figure 7-1; stations 1 - 55) to the Mezenskaya depression. Radial-component traces are labeled 1, and vertical - 3, respectively. The PNE source signature is multi-cyclic (~2-3 s long) and emergent in character, with peak energy arriving ~1 - 1.5 s after the onset. Note that the three components of recordings within the first 1-2 seconds of the records are generally more coherent within the sediment-free part of the section.

results suggest that at least the first 5-10 s of the codas of first arrivals carry a pronounced signature of the primary *P*-wave reverberations within the sedimentary column. Furthermore, Morozov and Smithson (2000; Chapter 5 here) showed that the amplitude decay patterns of 100-200-s long codas of these arrivals can also be consistently explained by crustal scattering. Therefore, as a cautionary, methodological outcome of this study, we note that waveform-based interpretations of mantle scattering without considering crustal effects may become biased toward increased mantle heterogeneity (for a detailed discussion of this subject, see Morozov, 2001).

7.3 Short-period coda of PNE arrivals

In order to emphasize the first-order effects of reverberations within the crust and to avoid potential complications of deconvolution of relatively narrow-band, short-period (0.5-10 Hz, dominated by ~2 Hz) PNE signals complicated by scattering noise, we replace deconvolution with cross-correlation of the radial (directed away from the source) and vertical components of the

records. This simplification is made for three reasons. First, we did derive RF from QUARTZ records using a traditional water-level deconvolution, with the resulting interpretation of the primary reverberations close to that arising from the cross-correlations presented below. Second, cross-correlation does not require regularization that is typical for time- or spectral-domain deconvolution and that may become problematic for noisy short-period data. At short periods (≥ 1 Hz), the crustal transfer function may no longer be close to that of a stack of planar layers (e.g., Langston and Hammer, 2002) thereby invalidating the basic assumptions of RF approach. Finally, cross-correlation also represents the first step of iterative time-domain deconvolution (e.g., Ligorria and Ammon, 1999), and thus within the context of the following discussion, it can be viewed as a (limited) proxy for RFs.

The cross-correlation functions of the recordings from the three QUARTZ PNEs are trace-normalized, corrected for a P_s travel-time delay moveout (Dueker and Sheehan, 1998; see also equation (7.1) below; also note that this correction within our range of ray parameters from 0.123 to 0.09 s/km is less than 4%), and stacked at each receiver point, resulting in an image shown in Figure 7-3. For comparison, Figure 7-3 (top) also shows a detailed QUARTZ crustal and uppermost mantle velocity model derived by Morozova et al. (1999) by travel-time inversion of the refracted and reflected seismic phases from 51 explosions of the profile. Note that even dense coverage (10-15-km station spacing) was not sufficient for detailed imaging of the upper crust, and the structure of the sediments in the top and middle of Figure 7-3 was derived from additional, detailed DSS and industry data (Morozova et al., 1999; Egorkin, personal communication).

Comparison of the cross-correlation image with the crustal velocity model shows good correlation of the main peak of the cross-correlation function with the depth to the basement (compare Figures 7-3, middle and bottom). The pattern of cross-correlation lags is correlated with the sediment thickness, which is apparent despite the strong, apparently source reverberations that are not compensated in our simple scheme (Figure 7-3, bottom). The cross-correlation peaks in our image approach zero times in the regions of the Baltic Shield, Uralian, and Altay fold belts where the sedimentary cover is thin or nearly absent, and reaches 1.5-2.5 s under the thick sedimentary covers of the Pechora and West Siberian basins. Note that the coda cross-correlation image from the PNEs allows constraining variations in the thickness of the sediments to a high degree of detail comparable to the image from detailed DSS profiling mentioned above.

Taking advantage of the known sediment thickness along the profile QUARTZ, we can distinguish between the possible types of phases causing the observed peak in our cross-correlations. The three competing hypotheses are: (1) P_s conversion on the basement, (2) P_{pp} , or (3) P_{ps} multiples within the sedimentary layers. These phases have the shortest travel-time lags after the primary P arrival, with the backscattered P_{ps} phase having been recently suggested to produce an important contribution to the early coda and used in RF imaging (Rondenay et al., 2001).

In order to evaluate the likelihood of the three possible phase interpretations above and also to constrain the values of bulk velocities within the sediments, we consider a simple time-to-depth scaling relation for the West Siberian Basin in the middle of our profile. With time delays after the P -wave onset, t_p of ~ 2.5 s in and the maximum depth of the sediments, H , of ~ 8 km (Figure 7-3) we obtain a delay per unit depth: $t_p/H \approx 0.31$ s/km. For a P_s converted mode propagating with ray parameter p , its delay after the primary P can be related to the average velocities within the sediments, V_P and V_S (e.g., Dueker and Sheehan, 1998):

$$\frac{t_D}{H} \approx \frac{1}{V_s \sqrt{1 - (pV_s)^2}} - \frac{1}{V_P \sqrt{1 - (pV_P)^2}} - p \left(\frac{pV_s}{\sqrt{1 - (pV_s)^2}} - \frac{pV_P}{\sqrt{1 - (pV_P)^2}} \right). \quad (7.1)$$

In the expression above, the first terms correspond to S - and P -wave travel times along the crustal

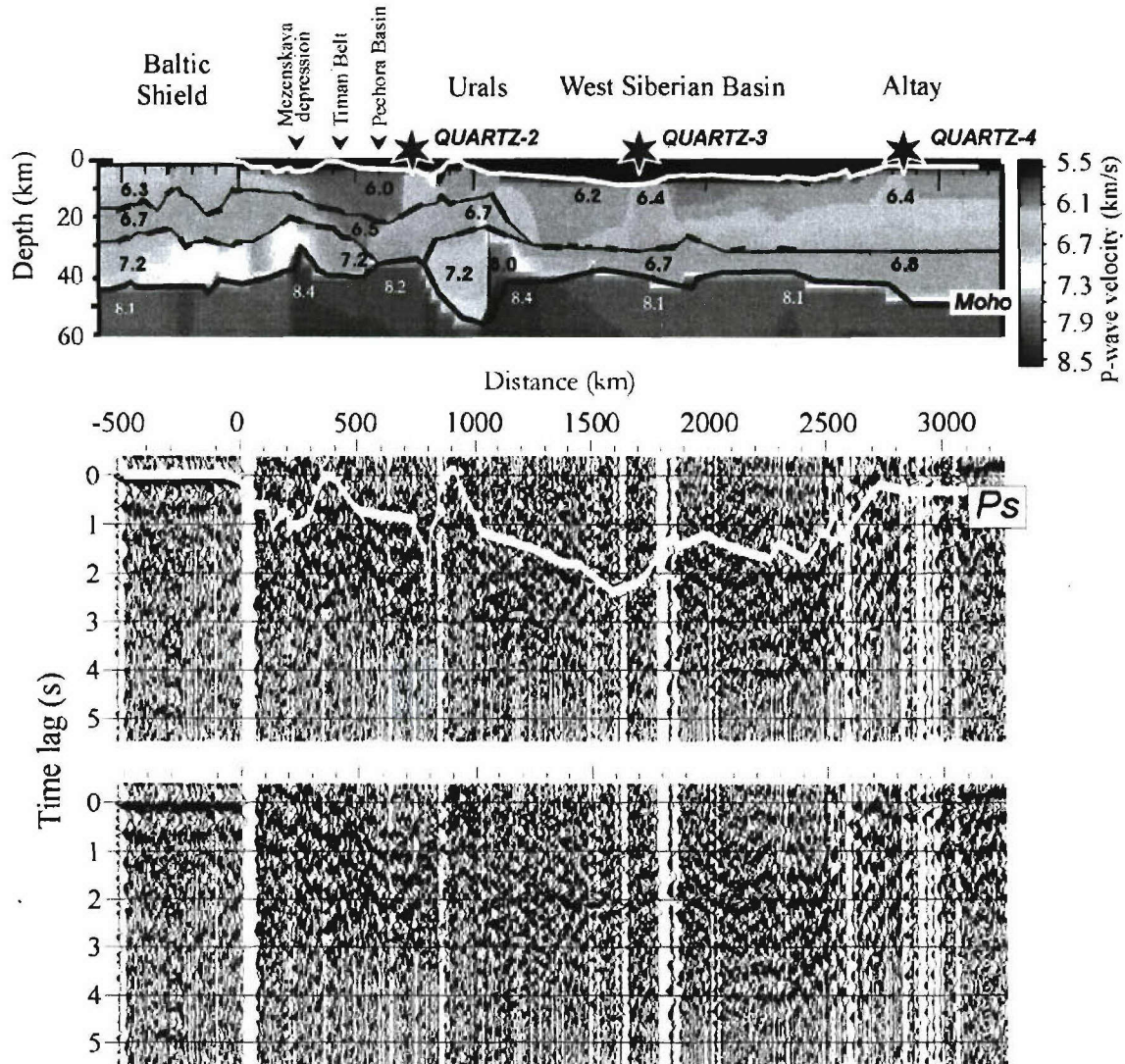


Figure 7-3. Mapping crustal reverberations using cross-correlated vertical and in-line components of QUARTZ records (Figure 7-2). *Top*: detailed crustal and uppermost mantle velocity model from profile QUARTZ (Figure 7-1). The top of the basement is highlighted with a thick white line. *Middle and bottom*: interpreted and uninterpreted stacked cross-correlation sections from the three QUARTZ PNEs, corrected for ray parameter $p=0.09$ s/km using equation (7.1). The white line in the middle plot is the profile of the basement from the crustal model (top plot) scaled to $P_s - P$ wave delay time using a factor of $time/depth = 0.31$ s/km. Note the correspondence of the basement depth with the stacked cross-correlations. Prominent reverberations at about 0.5 s period are mostly due to the source signature.

paths, respectively, and the third term is the difference of the corresponding travel times through the mantle. Similarly, assuming that the observed cross-correlation peak is due to a *Ppp* multiple (Figure 4, inset), we estimate its delay after the primary *P* wave as:

$$\frac{t_D}{H} \approx \frac{2}{V_P \sqrt{1-(pV_P)^2}} - p \frac{2pV_P}{\sqrt{1-(pV_P)^2}}. \quad (7.2)$$

For a *Pps* phase, the corresponding travel time lag per unit depth is:

$$\frac{t_D}{H} \approx \frac{1}{V_P \sqrt{1-(pV_P)^2}} + \frac{1}{V_S \sqrt{1-(pV_S)^2}} - p \left(\frac{pV_P}{\sqrt{1-(pV_P)^2}} + \frac{pV_S}{\sqrt{1-(pV_S)^2}} \right). \quad (7.3)$$

We compared the three possible interpretations above by solving equation $t_D/H = 0.31$ for V_P , with p equal 0.09 and 0.123 s/km and for a broad range of Poisson's ratios between $\sigma = 0.2$ and 0.45 (Figure 4). A *Ps*-phase interpretation would fit the observations for average Poisson's ratios of $\sigma \approx 0.4$ that are significantly higher than observed in sedimentary rocks samples in lab measurements (gray shaded area in Figure 4; Touloukian et al., 1989). An interpretation of the observed peaks as a *Ppp*

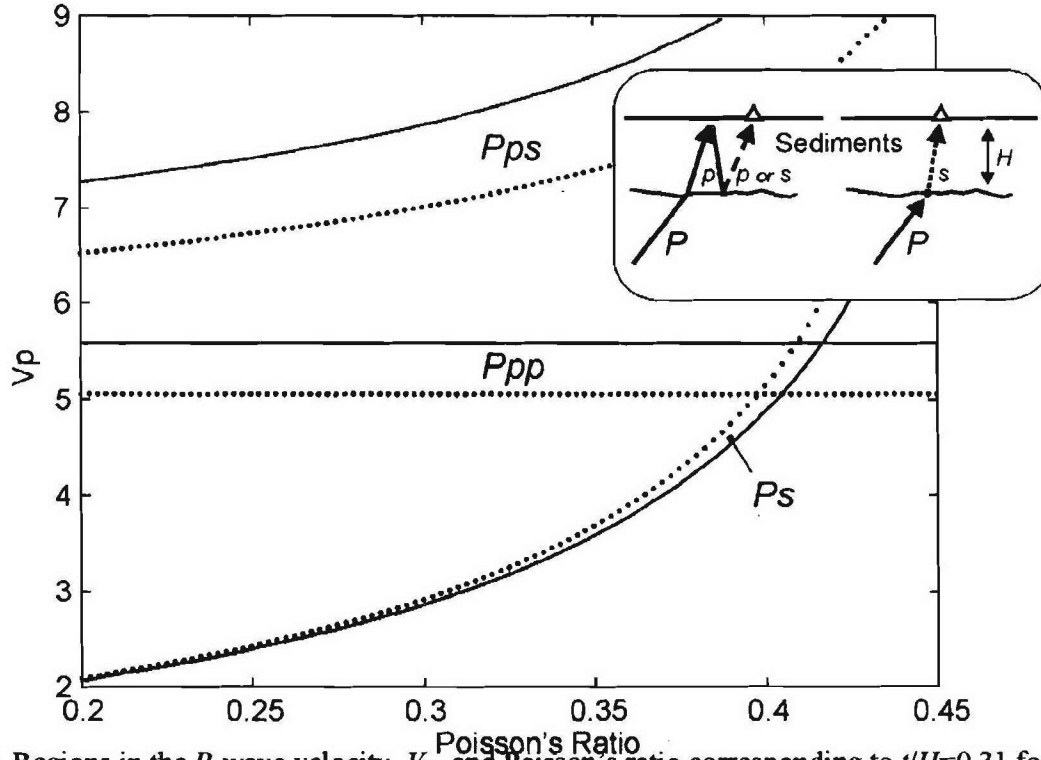


Fig 4. Regions in the *P*-wave velocity, V_P , and Poisson's ratio corresponding to $t/H=0.31$ for a *Ps* conversion at the top of the basement and for *Ppp* or *Pps* multiples within the sedimentary layers. Solid lines correspond to ray parameter values $p = 0.09$, dotted lines – to $p = 0.123$ s/km in equations (7.1-7.3). Inset shows a cartoon of the phases considered; H is the thickness of the sediments. Gray shaded area indicates the region of (V_P, σ) for typical sedimentary rocks from laboratory measurements (Touloukian et al., 1989).

multiple would also fit the observations with high but not unreasonable values of the V_P within the sediments between 5.0 – 5.5 km/s independent on the Poisson's ratios (Figure 4). By contrast, a Pps phase would produce much longer delays than Ppp , and therefore it would require very fast velocities $V_P > 7$ km/s in order to fit the observed reverberation time lags (Figure 4). Thus, based on the likelihood of required crustal velocity values, the Pps hypothesis is excluded whereas both the Ps and Ppp interpretations are possible although both are satisfied near the margins of what appears a likely sediment velocity distribution.

An additional distinction between the Ps and Ppp interpretations could potentially come from coda polarization. However, an argument based on polarization would still be inconclusive since short period (~ 2 Hz) coda in a laterally heterogeneous crust (Morozova et al., 1999) may exhibit complex polarization patterns inconsistent with the traditional flat-layer RF paradigm (Langston and Hammer, 2002). Thus we do not rely on polarization measurements; however, in general, observations of these phases on radial seismograms could also support the Ps conversion.

Our final argument in favor of the Ps conversion comes from comparison of the amplitudes of Ps converted wave within the two end-member models of sediment velocities discussed above, and a Ppp multiple within a sedimentary layer of velocity 5.0 km/s (Figure 7-5). Even within the same, high-velocity, sediments, the Ps conversion is about twice stronger in amplitude than the Ppp multiple, and with low sediment velocities inferred from our Ps interpretation of the stacked cross-correlation image, its amplitude would increase by an additional factor of ~ 2.5 (Figure 7-5). In addition, Ps conversions are also more likely to be observed in radial-component recordings.

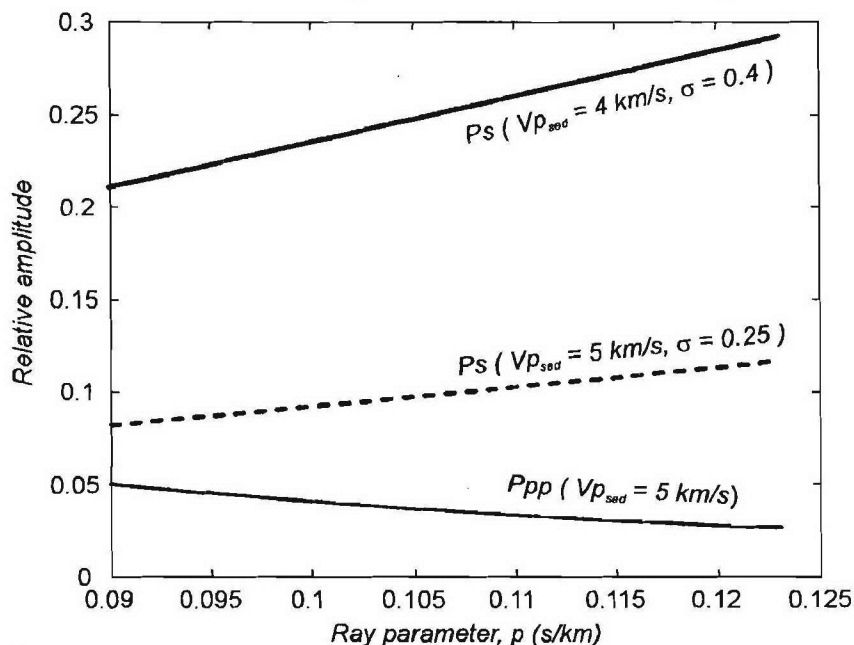


Figure 7-5. Amplitudes of the Ppp multiple and Ps converted phases for basement P -wave velocity of 6.0 km/s and Poisson's ratio $\sigma=0.25$ and the velocities within the sediments as labeled. Note that the Ps conversion is consistently higher than Ppp in amplitude, particularly for the sediments with high Poisson's ratio.

Based on the above observations, we conclude that the observed coda coherence should be due primarily to a *Ps* conversion, potentially with some interference with the *Ppp* multiple. In consequence of this conclusion, the bulk Poisson's ratio of the sediments within the West Siberian basin should be between 0.35-0.4 (Figure 4). Although such high values of the Poisson's ratio are not normally observed in laboratory measurements and appear somewhat surprising, our results suggest that they apparently could be present in large-scale sedimentary structures at seismic frequencies of ~ 2 Hz. At these frequencies, the *S* wave wavelengths are about 0.8-1.5 km, and the velocities of their propagation could be affected by large- and smaller-scale fracturing, presence of fluids, scattering and other factories leading to dispersion. These suggestions, however, are still not conclusive, and further estimates of basin-scale measurements of the Poisson's ratios at seismic frequencies are required for comparisons with our findings.

7.4 Conclusions

Coda analysis closely related to the receiver function technique could become both a useful imaging tool and a link between traditional travel-time and waveform inversion methods in controlled-source refraction seismology. The observed good correlation between the *Ps* or *Ppp* travel times and the depth to the basement in such a well-studied data set as QUARTZ suggests important generalizations that could be utilized in the interpretations of other long-range 3-component refraction surveys: (1) peaks in cross-correlations of the vertical and radial components (and therefore in receiver functions) are due to reverberations within the sedimentary layers, (2) stacked cross-correlation or RF sections could be used to constrain variations in the depth of the basement (more precisely, travel time within the sediments) to a degree of detail that might exceed the resolution of the traditional travel-time analysis, and (3) a significant part of the observed coda is due to these strong reverberations originating within the sedimentary cover. For the part of the West Siberian Basin crossed by QUARTZ profile, our results suggest high (~ 0.35 -0.4) average Poisson's ratios within the sediments.

In general, mode conversions and reverberations within the sedimentary column dominate the early coda of regional and teleseismic arrivals and could mask the details of the arrivals from the deeper crust and mantle. Therefore, such reverberations should be carefully considered in the interpretations of seismic scattering from within the lower crust and upper mantle.

8 Empirical calibration of PNE coda Q by using 1.5-D numerical modeling

8.1 Summary

Seismic codas of short-period Peaceful Nuclear Explosion (PNE) arrivals are strong and extensive in time. Some previous interpretations have described the teleseismic P_n coda as resulting from scattering in the upper 100 km of the mantle, but these interpretations have minimized effects of crustal scattering and have not addressed codas of other arrivals. Because the crust is apparently the most heterogeneous part of the Earth, it should be a key contributor to the scattered wavefields. To determine an empirical relationship between measured coda Q and crustal Q , allowing computation of crustal Q for PNE data, a surface scattering model was created in which crustal heterogeneities were described as scattering points on the Earth's surface. 1-D reflectivity synthetics based on velocity models with different crustal and upper mantle complexities governed wave propagation. The seismic response was calculated using numerical integration in time and a 2-D surface integral over uniformly-distributed, Monte-Carlo-sampled surface points. Different Q_{crust} values were used in creating the reflectivity synthetics to determine the observed Q_{coda} as a function of Q_{crust} for both teleseismic P and L_g events. Q_{crust} values were then estimated from the Quartz-4 PNE data set, collected across the Eastern European Platform, Ural Mountains, and West Siberian Basin, by measuring Q_{coda} values from selected seismic traces.

Using reflectivity synthetics based on velocity models of greater crustal complexity, like the Quartz-4 model by Morozova *et al.* (1999) and a 5-layer-crust model, led to greater coda strength in resulting receiver traces and stronger dependence of Q_{coda} on Q_{crust} . For the teleseismic P coda at 0.3 Hz, the Quartz-4 model gave a strong dependence of $Q_{coda} = 16 \cdot Q_{crust}^{0.47}$ at 0.3 Hz and $Q_{coda} = 28 \cdot Q_{crust}^{0.43}$ at 0.7 Hz. The IASP-91 model, because of its much simpler crustal structure and fewer crustal arrivals, gave a much weaker dependence of $Q_{coda} = 75 \cdot Q_{crust}^{0.06}$ at 0.3 Hz and $Q_{coda} = 75 \cdot Q_{crust}^{0.14}$ at 0.7 Hz. A model with simple IASP-91 crust and complex Quartz-4 mantle showed that the crust, not the mantle, played the most significant role in determining coda strength, since the arrivals in these synthetics were nearly identical to those in the IASP-91 model, and the relation, given by $Q_{coda} = 49 \cdot Q_{crust}^{0.14}$ at 0.3 Hz, is more similar to the IASP-91 relation than that of Quartz-4. Thus, velocity models with more complex crusts clearly result in higher-complexity seismic phase arrivals, stronger coda, and stronger Q_{coda} - Q_{crust} dependence.

The scattering potential per unit area, an empirical measure of scattering efficiency in terms of amplitude, was determined to be an average of 1.2 times greater for L_g waves than for P waves for the Quartz-4 model. For the 5-layer-crust model, the average ratio was 4. These results suggest that L_g waves are an important component of the seismic coda.

Estimates of Q_{crust} for Quartz PNE data as a function of frequency were made using relations obtained in model data, though the frequency windows of Quartz PNE data and model data differed due to modeling limitations. Teleseismic P Q_{coda} values measured from the envelope of a set of Quartz PNE traces gave Q_{crust} values of 180 at 2.5 Hz, decreasing to 50 at 5 Hz, for the East European Platform. These are crustal values commensurate with others obtained previously in other regions. The Quartz-4 L_g parameterization at 1.3 Hz gave a Q_{crust} estimate of 21 for the West Siberian Basin using the PNE Quartz L_g coda, expected to be lower since the trace was recorded in a region of thick sediments.

8.2 Introduction

In this Chapter, we examine crustal seismic attenuation by numerically modeling the teleseismic P coda and L_g coda as resulting from scattering of seismic energy from near-surface crustal heterogeneities and improve estimates of crustal attenuation for the Quartz profile (Figure 1-1 and 7-1). The L_g phase has a complex structure with no clear onset, but its maximum amplitude has a group velocity of 3.5 km/s and a coda trailing to group velocity of 2.9 km/s or less (Kennett 1986). The L_g phase may either be associated with a superposition of many higher modes of interfering surface waves trapped in the crust, or as interference of multiply-reflected S waves bouncing back and forth between the crust-mantle boundary, crustal interfaces, and the free surface (Kennett 1986). The teleseismic P_n , observed in both PNE and large conventional explosion data, propagates below the Moho to distances as great as 3000 km. It travels beneath both continents and oceans, interrupted only by major plate tectonic boundaries such as mid-ocean ridges, island arcs, and subduction zones (Molnar and Oliver 1969), with group velocity between 8.0 and 8.1 km/s and an additional branch at 8.5 km/s beyond 2700 km (Morozov *et al.* 1998a). The teleseismic P coda is composed of superposed codas of several P arrivals, including P , P_{410} , and the teleseismic P_n . This strong, extensive coda seen at offsets beyond 1500 km (Figure 5-1) is commonly thought to be due to scattering that delays the arrival of seismic energy, though the precise scattering mechanism and location remain in debate (Ryberg *et al.* 1995, 2000; Tittgemeyer *et al.* 1996, 2000; Ryberg and Wenzel 1999; Morozov *et al.* 1998a; Morozov and Smithson 2000, 2001; Morozov 2001; Nielsen *et al.* 2001). Various mechanisms have been proposed to describe teleseismic P_n propagation, including transmission of energy in a low-velocity zone beneath the Moho (Sutton and Walker 1972), guided waves in a high-velocity layer above a low-velocity layer (Mantovani *et al.* 1977), fine-scale sub-Moho layering or sub-Moho scatterers (Fuchs and Schulz 1976; Ryberg *et al.* 1995; Tittgemeyer *et al.* 1996, 2000; Ryberg and Wenzel 1999), scattering from partial-melt zones below 100 km depth (Thybo and Perchuc 1997), and whispering-gallery modes of multiple sub-Moho refractions (Stephens and Isacks 1977; Menke and Richards 1980; Morozov *et al.* 1998a).

Ryberg *et al.* (1995) proposed a velocity model containing small-scale velocity fluctuations in the upper mantle to depths of approximately 100 km to describe a scattering waveguide along which the teleseismic P_n could propagate. Tittgemeyer *et al.* (1996) and Ryberg and Wenzel (1999) performed reflectivity modeling to test similar models; Ryberg and Wenzel (1999) found that a scattering zone below the Moho of 75 km thickness with lamellae of 2 km average thickness and RMS velocity perturbation of 5% best matched the high-frequency (> 5 Hz) teleseismic P_n . These authors considered only the teleseismic P_n coda at frequencies greater than 5 Hz. This model neither describes the strong teleseismic P coda at frequencies below 5 Hz, shown by Morozov *et al.* (1998a) to be stronger than that above 5 Hz, nor explains the coda of other seismic arrivals.

Additionally, the crustal structure of the Ryberg and Wenzel (1999) and Tittgemeyer *et al.* (1996, 2000) mantle scattering models was oversimplified. Tittgemeyer *et al.* (2000) modeled the crust as a homogeneous layer with P -wave velocity (v_p) of 6.2 km/s to 30 km depth and a 5-km-thick transition zone with $v_p = 7.5$ km/s. The Moho was modeled as a first-order discontinuity with v_p contrast from 7.5 to 8.04 km/s. The simple, non-reflective crust of these models is unrealistic because the Earth's crust appears to be the most structurally and compositionally heterogeneous part of the planet. Many authors have proposed that seismic coda can be explained by scattering within the crust (Greenfield 1971; Bannister *et al.* 1990; Gupta *et al.* 1991; Morozov *et al.* 1998a; Morozov and Smithson 2000, 2001). Morozov and Smithson (2001) suggest that crustal scattering takes place both near the source and near the receiver. This scattering within the crust can produce

the necessary time delay of arrival energy to form a coda for all seismic events, not only the teleseismic P_n .

8.3 Crustal and coda attenuation

It is important to distinguish between two different Q values in this study. Intrinsic crustal attenuation describes loss of seismic energy in the crust to internal friction such as damping by fluids in cracks and pores or friction along grain boundaries. It is denoted by an intrinsic Q_{crust} value, where $Q_{crust} = \frac{2\pi E}{\Delta E}$, E is energy, and ΔE is the energy loss per cycle (Aki and Richards 1980).

Q_{coda} measures coda amplitude decay rate. It is determined by measuring the decay slope of amplitude A versus time t from a semi-log plot of the seismic trace envelope. This measurement also depends on the frequency of the signal f (Morozov and Smithson 2000):

$$A = A_0 \exp\left(\frac{-\omega t}{2Q_{coda}}\right) = A_0 \exp\left(\frac{-2\pi f t}{2Q_{coda}}\right) = A_0 \exp\left(\frac{-\pi f t}{Q_{coda}}\right)$$

Therefore, taking the natural logarithm, $\ln A = \ln A_0 + \frac{-\pi f t}{Q_{coda}}$, gives a straight line with slope

$$m = \frac{-\pi f}{Q_{coda}}. \quad \text{Thus } \frac{Q_{coda}}{f} = \frac{-\pi}{\text{slope}}, \text{ where slope is measured from the seismic trace envelope.}$$

In Chapter 5, we performed seismic trace envelope measurements on Quartz PNE data for the teleseismic P coda (Figure 5-1), finding $Q_{coda} = 430$ at 5 Hz and $Q_{coda} = 320$ at 2 Hz, and suggested the relation $Q_{coda} \approx 270 f^{0.3}$. These Q_{coda} estimates are consistent with crustal-average Q_s values and therefore support the authors' association of the coda with scattered L_g waves in the crust.

To fully address this crustal scattering problem, full 3-D modeling of crustal features, including faults, mountain ranges, basins, shorelines, and lithology would be required to account for 3-D wave propagation. However, full 3-D modeling is still not practical at this time due to limited computing resources and limited knowledge of scattering properties of the crust. We present here a heuristic simulation of teleseismic P and L_g coda amplitude decay modeled as scattering from heterogeneities near the Earth's surface, using 1-D reflectivity synthetics to describe the wavefield and the Born approximation to describe scattering behavior. Since the Rayleigh wave (R_g) decays quickly in near-surface sediments, it is not viewed as a significant factor in coda formation (Dainty 1985); R_g is not seen beyond 200 km in PNE records, so it is not examined here. As this is not a 3-D model of crustal features, it cannot provide a completely realistic picture of resultant coda decay; however, it captures the key mechanism of coda generation and provides improved estimates of crustal attenuation.

8.4 Coda model

The scattering model represents crustal heterogeneities as scatterers distributed within the Earth's crust. The resultant scattered coda energy U recorded at a receiver at time t is an integral over volume V containing all scatterers,

$$U(\vec{r}, t) = \int dt_s \iiint_V d^3\vec{r}_s \Psi(\vec{r}_s) U_{source}(\vec{r}_s, t_s) G(\vec{r}_s, t_s; \vec{r}, t), \quad (8.1)$$

where t_s is the time of the direct arrival at the scatterer, \vec{r}_s represents scatterer positions, Ψ is scattering potential, describing the amount of energy reflected at the scatterer, U_{source} is the seismic source function describing energy arriving at the scatterer from the source explosion, and G is the scattering Green's function, describing the propagation of scattered energy from scatterer to receiver. For simplicity, because the upper crust is assumed to be the primary contributor to the seismic coda, this volume integral is replaced with a surface integral (

Figure 8-1):

$$U(\vec{r}, t) = \int dt_s \iint_S d^2\vec{r}_s \Psi(\vec{r}_s) U_{source}(\vec{r}_s, t_s) G(\vec{r}_s, t_s; \vec{r}, t). \quad (8.2)$$

The Green's function is approximated as translationally invariant in time and space:

$$G(\vec{r}_s, t_s; \vec{r}, t) = G(\vec{r} - \vec{r}_s, t - t_s), \quad (8.3)$$

giving

$$U(\vec{r}, t) = \int dt_s \iint_S d^2\vec{r}_s \Psi(\vec{r}_s) U_{source}(\vec{r}_s, t_s) G(\vec{r} - \vec{r}_s, t - t_s). \quad (8.4)$$

Therefore, each scattering point acts as a secondary source for seismic waves.

For a given coda time t and velocity $v = \frac{|\vec{r} - \vec{r}_s|}{|t - t_s|}$ chosen for a particular event (e.g. scattered L_g with velocity $v = 3.5$ km/s), contributions of scattered energy originate from an elliptical ring surrounding the receiver (Morozov and Smithson 2000). The scattering area within the ring increases with time due to its increasing radius, compensating the energy decay due to geometrical spreading, since the product of the ring's area and the $1/r$ geometric spreading factor rapidly approaches a constant asymptote for increasing values of $|t - t_s|$. Therefore, for a plane of constant scattering potential and no intrinsic attenuation, coda energy would not decay. If there is attenuation, the observed Q_{coda} is indicative of Q_{crust} since the dominant contribution to coda is from crustally-propagating waves. Values of Q_{crust} and Q_{coda} may differ, however. For example, Q_{coda} less than Q_{crust} indicates that seismic energy is leaking into the mantle and does not return to the surface where it may be recorded by a receiver. Q_{coda} greater than Q_{crust} indicates mantle phases are returning to the surface and contribute to the seismic energy recorded by the receiver. These mechanisms may be frequency-dependent, causing frequency dependence of the Q_{coda} - Q_{crust} relation.

Therefore, an empirical relationship is sought:

$$\kappa_{coda} \equiv \frac{f}{Q_{coda}} = \kappa Q_{crust}^{\gamma}, \quad (8.5)$$

where f is frequency, κ_{coda} is the coda attenuation factor, and κ and γ are constants. A power law relation is used because it is general, asymptotes are well-behaved, and it has been commonly used when determining Q as a function of f in past studies.

In Chapter 5, we assumed κ values of 2 and 5 Hz and $\gamma=-1$ in Equation 5 when performing the coda measurements. In the work presented here, we perform numerical modeling to improve estimates of these parameters by using a range of Q_{crust} values in the reflectivity synthetics and filtering into different frequency bands to select f .

8.5 Synthetic PNE sections and Green's functions

Synthetic seismic sections created using the reflectivity method (Fuchs and Müller 1971) were used as source and Green's functions in the model (Figure 8-1). We used four different velocity models to compute synthetic sections (Figure 8-2). The Quartz-4 velocity model by Morozova *et al.* (1999) contains a 3-layer crust overlain by a 3-km-thick sediment layer and complex mantle with low velocity zones at 110- and 210-km depths. The IASP-91 model (Kennett 1991) contains a much simpler two-layer crust and a mantle without low-velocity zones. The IASP-Quartz model contains the IASP-91 crust and Morozova *et al.* (1999) mantle. The complex crust model has a 5-layer crust with the Morozova *et al.* (1999) mantle. Note that the Quartz-4 model and the complex crust model exhibit more complex waveforms (including crustal L_g phases in addition to the P and S phases) than the IASP-91 and IASP-Quartz models with simpler crusts (Figure 8-3).

Q_p and Q_s values, in the ratio 2:1, were specified for layers in the velocity model. Q_{crust} values, referring to Q_s values used here, range from 50 to 1000 to encompass the common range of Earth's crustal Q values. Mantle attenuation in each velocity model was specified using mantle Q_p values obtained by Morozov *et al.* (1998b) in their study of Quartz PNE data. For the Quartz-4 and complex crust models, Q_p and Q_s values of the upper 3 km were set at 10 to attenuate R_g since this phase is not seen beyond about 200 km in PNE data and is thought to be an insignificant factor in teleseismic P and L_g coda formation (Dainty 1985). A mute was applied to completely eliminate R_g from the synthetics.

8.6 Numerical modeling

The integral over time to compute the scattering model's seismic response at a receiver (Eq. 4) is performed using numerical convolution of the source function, describing the propagation of the incident wavefield of seismic energy to surface scatterers from the source explosion, and the). The 2-D spatial integral uniformly samples surface points in a Monte-Carlo fashion, simulating constant scattering potential for the entire infinite plane and allowing the quantitative dependence of Q_{coda} on Q_{crust} to be determined. To limit computing resource requirements, the region's size was limited in spatial extent but chosen to ensure that scattered energy from the region's edges would arrive after a reasonable time interval for measurement of coda slopes. Coda energy arrives from an elliptical ring, increasing in area with time, surrounding the receiver (Morozov and Smithson 2000). While this ellipse remains within the scattering region, the decay of seismic energy due to geometrical spreading will be compensated by the ellipse's increasing area. Thus, the coda is expected to ring

with attenuation dependent upon the Q_{crust} value until the ellipse begins exiting the scattering region. The teleseismic P coda was measured at 2900 km offset to allow a significant time interval in which to perform the measurement before onset of the L_g phase. Since L_g waves originating from the source (or L_g waves scattered near the source) travel too slowly to arrive within this time interval, the scattering region was assigned around the receiver only. The region size was chosen as a square 1200 km on a side, allowing 600 km from the central receiver to the nearest edges (Figure 8-4a). This allows a 3 km/s L_g wave 200 seconds before scattered energy from the edge of the region arrives at the receiver, thus giving a 200-second window in which to reliably measure coda decay. As the Q_{crust} value in the reflectivity synthetics is constant throughout the section, and crustal scattering does not depend on the source-receiver offset, the receiver's offset value should not influence Q_{coda} values measured from the output traces.

For measuring the L_g coda, both source and receiver were located within the scattering region (Figure 8-4b) to include $L_g \rightarrow P$ and $L_g \rightarrow L_g$ scattering in addition to the $P \rightarrow P$ and $P \rightarrow L_g$ scattering of the teleseismic P coda, with the resulting Q_{coda} an average of near-source and near-receiver scattering.

To obtain seismic traces at appropriate source-scatterer and scatterer-receiver offset distances for use in the numerical convolution, we coded a τ - p interpolation routine (Yilmaz 1987) for seismic traces based on a seismic section. This interpolation code is implemented as an independent tool in our SIA system and was tested separately before its use in the scattering routine. The module resamples the offset coordinate of an input seismic section to the user's specifications. Synthetic source and Green's functions were created with trace spacing of 10 km in order to conserve computer processing time and storage space.

Realizations of the numerical integration routine each produced a single output trace. This scattered response was scaled relative to the direct response at the receiver and the two were summed to form a receiver trace. In Chapter 5, we modeled coda power as a function of time by describing the primary event as a parabolic function with peak power P^0 , duration τ , and relative coda amplitude parameter λ with the product $\lambda\tau$ giving the power relative to peak. These authors determined values of $\lambda = 0.22$ for all events and $\tau = 1.25$ for the teleseismic P event. Applying these findings to data in this study gives $\lambda\tau = .275$ for the relative power; taking the square root to apply this to amplitude gives a scattered amplitude to direct amplitude ratio of 0.524, so the scattered trace should have approximately half the amplitude of the direct wave at the time of coda onset. For the L_g event, $\tau = 2.5$ was used to account for the greater width of this arrival, implying a relative amplitude for L_g events of about 0.75. The scaling factor, required to adjust the amplitude of the scattered response to the appropriate amplitude ratio of 0.5 or 0.75, was found to differ between teleseismic P and L_g codas.

From this scaling factor, the scattering potential Ψ per unit area was computed for P and L_g . Scattering potential per unit area is an effective measure of scattering efficiency in terms of the resulting amplitude; it is inversely proportional to the scaling factors computed and directly proportional to the scattering density. For the Quartz-4 model, the L_g coda was found to have an average scattering potential per unit area about 1.2 times higher than that of the teleseismic P coda. Because the teleseismic P coda is governed by $P \rightarrow P$ and $P \rightarrow L_g$ scattering but the L_g coda is also affected by $L_g \rightarrow P$ and $L_g \rightarrow L_g$ scattering, these extra scattering modes likely contribute to the greater scattering potential per unit area of L_g . For the complex crust model, the average scattering potential per unit area was found to be about 4 times greater for L_g than for P . Again, the additional

$L_g \rightarrow P$ and $L_g \rightarrow L_g$ scattering modes likely contribute to the greater scattering potential per unit area of L_g .

Approximately 15 trace realizations were computed and compiled into a data set to improve stability of the measurements, required because the surface was uniformly sampled in a Monte-Carlo fashion to avoid unnatural coherency caused by equal scatterer-receiver distances for several scattering point locations that might result if the surface were sampled as a grid. A data set was compiled for each of the 20 Q_{crust} values. Slope measurements were then performed on the trace envelopes as described in Chapter 5 to obtain a Q_{coda}/f value for each Q_{crust} set. To obtain uncertainty estimates for each value, half the traces from a set were chosen randomly and measurements performed to obtain a Q_{coda}/f value; this was repeated several times with different randomly-chosen traces to obtain a range of values. Greatest and least Q_{coda}/f values at each Q_{crust} were chosen as error bounds. Since measurement of the teleseismic P and L_g coda slopes is best accomplished by fitting the general trend of these slopes and lightly weighting short, low-amplitude drops that occur intermittently within the coda, L1 fitting is preferred because it iteratively downweights outliers. We used the L1 matrix algorithm described by Aster *et. al.* (2002).

The goal of these measurements is to parameterize the Q_{coda} - Q_{crust} relation by obtaining values of κ and γ in Equation 5:

$$\kappa_{coda} \equiv \frac{f}{Q_{coda}} = \kappa Q_{crust}^{\gamma},$$

where Q_{coda}/f is the quantity measured from coda slopes and Q_{crust} values are specified in the reflectivity synthetics. Thus κ and γ may be obtained by taking the natural logarithm of this equation,

$$\ln\left(\frac{f}{Q_{coda}}\right) = \ln(\kappa Q_{crust}^{\gamma}) = \ln \kappa + \gamma \ln Q_{crust}$$

and plotting on a log-log scale to give a straight line with slope γ and intercept $\ln \kappa$. These γ and κ values are used to compare the Q_{coda} - Q_{crust} relation obtained for the different velocity models.

8.7 Modeling results

We performed measurements on teleseismic P and L_g codas for each of the four velocity models. Traces were filtered to center frequencies of 0.3, 0.7, and 1.3 Hz to examine the codas as a function of frequency.

The data sets of numerically modeled traces for the Quartz-4 velocity model at $f = 0.3$ Hz are shown for Q_{crust} values of 50 and 1000 (Figure 8-5). A delay in onset of coda amplitude is evident between the direct teleseismic P arrival and the strong part of the coda (Figure 8-5a,b) due to the low energy of arrivals at small offset in the Green's functions before onset of the L_g phase. Just after the onset of the direct arrival, the scattering ellipse has small area; therefore, the energy of the Green's function synthetic section would need to approach infinity at zero offset to compensate for spreading at small coda times. Since the Green's function is of lower energy between 100 and 200 km, the coda builds up only after the radius of the scattering ellipse expands beyond this distance.

Measurement of coda envelope slopes for the range of Q_{crust} values gives $\gamma = -0.47$ and $\kappa = 0.019$ for the teleseismic P coda (Figure 8-5c), giving the parameterization is $Q_{coda} = 16 \cdot Q_{crust}^{0.47}$ (Eq. 5). These values will be compared with those of the other models. Lines E1 and E2 were drawn to give an estimate of stability of the values as a function of slope; γ and κ values for E1 and E2 appear on the plot.

The IASP-91 model amplitudes were examined in a similar manner (Figure 8-6). A P_g phase follows the teleseismic P phase at 500s, limiting measurement to a time interval before 500s. The slow coda amplitude rise near the onset of the direct wave is also seen for this model (Figure 8-6a,b) because the amplitude of the reflectivity synthetics is low at less than 100 km offset. Measurement of the coda envelope slope gives the relation is $Q_{coda} = 75 \cdot Q_{crust}^{0.06}$ (Table 8-1) for the teleseismic P coda, indicating a much lesser dependence of Q_{coda} on Q_{crust} (because of the smaller exponent) than for the Quartz-4 model; the relation is $Q_{coda} = 75 \cdot Q_{crust}^{0.06}$. This is expected because there is no strong crustal L_g phase in the IASP-91 synthetics as in the Quartz-4 synthetics.

The IASP-Quartz model has arrivals in the reflectivity synthetics that are similar to those of the IASP-91 model (Figure 8-3), with P_g following the teleseismic P . Measurement of the coda slope gives the relation $Q_{coda} = 49 \cdot Q_{crust}^{0.14}$ (Table 8-1) for the teleseismic P coda, indicating again a weak dependence of Q_{coda} on Q_{crust} because of the absence of the L_g arrival. Therefore, it is not the simple mantle of the IASP-91 model that causes the weak dependence; rather, the simple crust of the IASP-Quartz model is the most important factor governing the Q_{coda} - Q_{crust} dependence.

The complex crust model, with arrivals similar to the Quartz-4 model, gives the relation $Q_{coda} = 2 \cdot Q_{crust}^{0.98}$ (Table 8-1) for the teleseismic P coda, indicating a strong dependence of Q_{coda} on Q_{crust} because of the strong crustal L_g phase. This is the strongest relation of the four models.

The L_g coda gave the relation $Q_{coda} = 18 \cdot Q_{crust}^{0.40}$ for L_g coda at 0.3 Hz, quite similar to that obtained for the Quartz-4 P coda. The relation determined for the complex crust model's L_g coda at 0.3 Hz is $Q_{coda} = 6 \cdot Q_{crust}^{0.78}$, indicating a stronger Q_{coda} - Q_{crust} relation than that of the Quartz-4 model's L_g coda, consistent with the P coda parameterizations of these models.

To examine the effects of a higher frequency range, we filtered the reflectivity synthetics to a center frequency of 0.7 Hz and performed parameterizations (Table 8-1). The Q_{coda} - Q_{crust} dependence relative to that at 0.3 Hz increases slightly for the IASP-91 model and more significantly for the IASP-Quartz model, and decreases slightly for the Quartz-4 model with a more significant decrease for the complex crust model.

The synthetics at 1.3 Hz were of poor quality because their amplitude at that frequency was several orders of magnitude less than at 0.7 Hz or 0.3 Hz. Therefore, teleseismic P coda measurements were unreliable. L_g coda measurements were performed for the Quartz-4 and complex crust models; results appear in Table 8-1. The relation for the complex crust model decreases in strength while that for the Quartz-4 model increases relative to that at 0.7 Hz.

The strength of the Q_{coda} - Q_{crust} relation likely depends on the relative strengths of P and L_g as a function of frequency. To examine this frequency dependence, I compared the coefficient and exponent values obtained at 0.3, 0.7, and 1.3 Hz for the models. Only the L_g codas were examined at 1.3 Hz because of the weak signal present after synthetics had been filtered to 1.3 Hz.

Coefficient values for the Quartz-4 and complex crust models increase with frequency, but those for the simple-crust IASP-91 and IASP-Quartz models change little (Table 8-1).

The Quartz-4 P coda parameterization showed a slight decline in Q_{coda} - Q_{crust} dependence, with exponent value decreasing from 0.47 to 0.43 between 0.3 and 0.7 Hz (Table 8-1). This is likely due to the decrease in amplitude of the L_g events relative to P events from 0.3 to 0.7 Hz. The complex crust P coda dependence decreased more significantly, with exponent decreasing from 0.98 to 0.58 with increasing frequency. Amplitude was greater at 0.7 Hz than at 0.3 Hz, but energy remained comparable. For the IASP-91 model, the dependence increased slightly between 0.3 Hz and 0.7 Hz, the exponent changing from 0.06 to 0.14, in accordance with the relative increase of S/L_g amplitude relative to P amplitude with increasing frequency. The IASP-Quartz model showed a significant increase in Q_{coda} - Q_{crust} dependence, concordant with the significant relative increase of S/L_g amplitude relative to P amplitude.

The Quartz-4 model's L_g coda gave exponent values of 0.40, 0.24, and 0.50 for the increasing frequencies, indicating the strongest dependence at 1.3 Hz and weakest at 0.7 Hz. The L_g amplitude at 1.3 Hz is higher relative to P than that at 0.7 Hz, consistent with the higher Q_{coda} - Q_{crust} dependence, though the amplitude is not as great as that at 0.3 Hz. The complex crust model shows a progressive downward trend in Q_{coda} - Q_{crust} dependence as a function of frequency, consistent with the lower amplitude of L_g relative to P at 1.3 Hz than at lower frequency values.

8.8 Interpretation of observations from PNE Quartz-4

Estimates of Q_{crust} for Quartz PNE data were performed using the inverse relation of the parameterizations. The value for Q_{crust} of the Quartz data is given by:

$$Q_{crust} = \left(\frac{f}{\kappa Q_{coda}} \right)^{1/\gamma} = \left(\frac{\kappa_{coda}}{\kappa} \right)^{1/\gamma} \quad (6)$$

where values of γ and κ are from the parameterization and the inverse of coda attenuation parameter $\kappa_{coda} = \left(\frac{f}{Q_{coda}} \right)$ is measured from the coda envelope slope of Quartz data. The primary

frequencies of the Quartz data are between 1 Hz and 10 Hz, outside the strong range for the reflectivity synthetics here. Since the frequency range of the synthetics was limited by capabilities of the code used in their creation because of the tradeoff between trace length and sampling interval. Long traces, necessary when performing modeling at long offsets to achieve substantial separation between arrivals, required a greater sampling interval, and therefore the Nyquist frequency was limited to lower values than would have been possible with shorter traces.

Q_{coda} and Q_{crust} values are expected to differ based on tectonic regime. Cratons and inactive regions are expected to have the highest values, while active regions, basins, and rocks with fluid-filled cracks and pores are expected to have lower values. Thick accumulations of sediment and severe velocity gradients at the crust-mantle transition also may decrease values (Mitchell and Cong 1998); these authors also suggest that Q_{coda} values increase with time elapsed from the most recent tectonic activity because of loss of crustal fluids and permeability with time. Cong and Mitchell (1998) reported Q_{crust} values of 63 for the Turkish and Iranian Plateaus, 71 near the Black and Caspian Seas, and 201 for the Arabian Peninsula.

To obtain Q_{crust} estimates via the P coda for Quartz PNE data as a function of frequency, we stacked together seven trace envelopes between 2500 km and 2600 km offset and filtered the result

into several frequency bands between 1 Hz and 5 Hz. We then measured the trace envelope's Q_{coda}/f value for each frequency (Figure 8-7a-c). We used the Quartz-4 model parameterization because this model was obtained by travel-time modeling along the Quartz PNE line. κ was scaled to higher frequencies by performing a power law fit of the values obtained at 0.3 Hz and 0.7 Hz, giving $\kappa = \exp(0.32 \cdot \ln(f) - 3.57)$. While the Q_{crust} value obtained at 1.5 Hz may be distorted because of the 1-10 Hz dominant frequency band of Quartz data, limiting energy contribution from the low-frequency end of the 1.5 Hz frequency band, Q_{crust} values appear to generally decrease as a function of frequency (Figure 8-7d).

For an estimate from L_g coda, we selected an L_g coda segment from a Quartz trace at 650 km offset, as the L_g phase is most recognizable there (Figure 8-8). The trace was filtered to 1.3 Hz. Using the parameter values of $\gamma = -0.50$ and $\kappa = 0.020$ obtained at 1.3 Hz gives, using Eq. 5, a value of $Q_{crust} = 21$.

The Q_{crust} values we obtain for Quartz crust from the teleseismic P coda, recorded in the East European Platform, range between about 180 at 2-3 Hz to 50 at 5 Hz, commensurate with those obtained by Cong and Mitchell (1998). The L_g coda trace, recorded in the West Siberian Basin, indicates a smaller Q_{crust} value, as expected, since the Basin is overlain by a 4-5-km-thick sedimentary layer.

8.9 Discussion

The strength of the Q_{coda} - Q_{crust} relation resulting from each of the velocity models used depends on the complexity of the model and consequent seismic phases in the reflectivity synthetics. The Quartz-4 model has a 3-km-thick sediment layer overlying a 3-layer crust with velocity discontinuities at 18- and 27-km depths and Moho at 43 km (Figure 8-2a). In addition, the Quartz-4 mantle is complex, with low-velocity zones at 110- and 210-km depths. As a result of the complexity, a strong crustal L_g phase accompanies the P phases in the reflectivity synthetics (Figure 8-3a). Strong ringing and slow attenuation of both teleseismic P and L_g codas are evident, with strong dependence of $Q_{coda} = 16 \cdot Q_{crust}^{0.47}$ at 0.3 Hz for the P coda and $Q_{coda} = 18 \cdot Q_{crust}^{0.40}$ for the L_g coda (Table 8-1). The complex crust model contains a 5-layer crust with the Quartz-4 mantle (Figure 8-2d), which also produces strong L_g and P phases (Figure 8-3d) and strong relations of $Q_{coda} = 2 \cdot Q_{crust}^{0.98}$ for the P coda and $Q_{coda} = 6 \cdot Q_{crust}^{0.78}$ for the L_g coda at 0.3 Hz.

Results for these complex velocity models contrast those of the simple-crust models. The IASP-91 reflectivity synthetics, based on a simple 2-layer crust and upper-mantle velocity model without low-velocity zones (Figure 8-2b), show no strong L_g phases, indicating much less crustal propagation than for the more complex models. The teleseismic P coda is found to decay more rapidly than in the previous cases. Additionally, the Q_{coda} values are only weakly dependent on Q_{crust} , with $Q_{coda} = 75 \cdot Q_{crust}^{0.06}$ at 0.3 Hz. Evidently, simple crust, simple mantle, or both contribute to the weak dependence. The IASP-Quartz synthetics, based on a model with simple IASP-91 crust and complex Quartz-4 mantle (Figure 8-2c), show nearly identical seismic phases to the IASP-91 model, which has simple crust and mantle (Figure 8-3c). The resulting dependence appears only slightly greater than that of the IASP-91 model, with $Q_{coda} = 43 \cdot Q_{crust}^{0.14}$ at 0.3 Hz. Therefore, the simple crust of the IASP-Quartz model has a greater effect than the complex mantle. Thus, velocity models with higher-complexity crusts clearly result in more complex crustal seismic phase arrivals, stronger teleseismic P coda, and stronger Q_{coda} - Q_{crust} dependence.

To examine the Q_{coda} - Q_{crust} relation as a function of frequency, we compared the parameter

values obtained at 0.3, 0.7, and 1.3 Hz for the models. Only the L_g codas were examined at 1.3 Hz because of the weak signal present in the synthetics after filtering to 1.3 Hz.

The Quartz-4 P coda parameterization showed negligible change in the strength of the Q_{coda} - Q_{crust} relation as a function of frequency (Table 8-1). The complex crust P coda dependence decreased from an exponent value of 0.98 to 0.58 with increasing frequency. The amplitude of L_g relative to P in the synthetics was actually greater at 0.7 Hz than at 0.3 Hz, but L_g energy remained comparable between the two frequencies. For the IASP-91 model, the dependence increased slightly with frequency, in accordance with the relative increase of S/L_g amplitude relative to P amplitude between 0.3 and 0.7 Hz. The IASP-Quartz model showed a significant increase in Q_{coda} - Q_{crust} dependence with frequency, also concordant with the significant relative increase of S/L_g amplitude relative to P amplitude.

The Quartz-4 model's L_g coda gave exponent values of 0.40, 0.24, and 0.50 for increasing frequencies (Table 8-1). The L_g amplitude at 1.3 Hz is higher relative to P than that at 0.7 Hz, consistent with the stronger Q_{coda} - Q_{crust} relation, though the amplitude is not as great as that at 0.3 Hz. The complex crust model shows a progressive downward trend in strength of the Q_{coda} - Q_{crust} relation with increasing frequency, consistent with the lower amplitude of L_g relative to P at 1.3 Hz than at lower frequencies.

The stronger Q_{coda} - Q_{crust} dependence for models with higher-complexity crusts provides strong support for the argument of Morozov and Smithson (2000, 2001) that crustal scattering should be a key contributor to the scattered wavefield. A strong dependence of Q_{coda} on Q_{crust} implies that the coda wavefield is strongly influenced by crustal phases like L_g . Since the crust is thought to be the most heterogeneous part of the Earth and is known to propagate strong crustal phases, crustal scattering should contribute strongly to coda.

Other authors (Ryberg *et al.* 1995, 2000; Ryberg and Wenzel 1999; Tittgemeyer *et al.* 1996, 2000) have argued, however, that scattering occurs primarily within the upper mantle. Ryberg *et al.* (1995) argued that since the teleseismic P_n phase appears to be uninfluenced by the Ural Mountains except for systematic shifts in first arrival times due to the increased depth of the underlying orogenic root, the teleseismic P_n phase propagates in the upper mantle. These authors also estimated Q_{coda} for Quartz-4 PNE data at 10 Hz as ranging from 2000 to 5000, which are much too high to be crustal values, leading them to imply mantle scattering. These values were determined, however, assuming that coda is primarily due to body waves and a point source (Morozov and Smithson 2000). Because the crust is apparently the most heterogeneous part of the Earth and is known to propagate strong crustal seismic phases, Morozov and Smithson (2000) used a measurement technique that assumed surface waves (generated through conversions on the Moho, basement, surface, and other velocity heterogeneities in the crust) contribute most strongly to coda; resulting Q_{coda} values were typical of the crust using this technique.

Ryberg and Wenzel (1999), using the same Q_{coda} measurement technique as Ryberg *et al.* (1995), modeled the teleseismic P_n coda using reflectivity synthetics and 1-D velocity models with random velocity perturbations superimposed upon positive or negative velocity gradients. These authors found that a model with a simple 2-layer IASP-91 crust, 75-km-thick scattering zone of lamellae of 2 km average thickness and RMS velocity perturbation of 5% best represented teleseismic P_n Q_{coda} values. A model with random velocity fluctuations in the lower crust, they argued, produced a poor fit of the teleseismic P_n . But since their Q_{coda} measurement scheme assumed body waves from a point source as the primary contribution to coda, crustal phases like L_g

that likely play a significant role were minimized. Ryberg *et. al.* (2000) computed synthetic seismograms using a 2-D finite difference scheme and velocity models with random velocity fluctuations to compare with PNE data. These authors found that a 100-150-km-thick zone of scatterers below the Moho best matched PNE data. The authors found no teleseismic P_n phase at 5 Hz using lower-crustal velocity fluctuations of 5% with a constant-velocity upper crust. All of these studies focused specifically on the teleseismic P_n coda only at high frequency, neglecting codas of other arrivals and lower frequencies using oversimplified, one- or two-layer crusts in their modeling. This modeling may be consistent with the PNE data, but the Earth's crust is known to be highly heterogeneous, providing a foundation for crustal scattering; modeling that excludes crustal scattering is unrealistic.

Morozov and Smithson (2000) suggested that strong coda results from crustal scattering of seismic waves incident from the mantle as whispering-gallery phases and propagating at high apparent velocities. In addition, crustal guided waves such as P_g , L_g , S_g , and R_g likely produce secondary phases propagating through the mantle which also contribute to the observed coda (Dainty 1985, 1990). Thus, in their model, crustal scattering occurs both near the source and near the receiver. This crustal scattering mechanism addresses all frequencies and codas of all seismic arrivals. Morozov and Smithson (2000) obtained estimates for Quartz-4 PNE data (Chapter 5): $Q_{coda} = 380$ at 2 Hz and $Q_{coda} = 430$ at 5 Hz. These correspond to crustal values in Eurasia; Mitchell *et. al.* (1997) noted Q_{coda} values to range from less than 350 to greater than 800. This supports the Morozov and Smithson (2000) suggestion that this coda is primarily due to L_g energy.

Estimates of Q_{crust} were obtained for the East European Platform using the Quartz teleseismic P coda and the teleseismic P parameterization of model data. Since model data were parameterized at 0.3 Hz and 0.7 Hz, the κ value was scaled to the higher frequencies of the Quartz data (1-10 Hz) using a power law relation. Q_{coda}/f measurements, with the exception of that at 1.5 Hz, appear to generally decrease with increasing frequency (Figure 8-7b); Q_{crust} values follow the same pattern, ranging from 180 at 2.5 Hz to 50 at 5 Hz. These values are similar to those obtained by Cong and Mitchell (1998) in the Middle East. An estimate of Q_{crust} for the West Siberian Basin was obtained using the L_g parameterization, giving a value of $Q_{crust} = 21$. This value is expected to be lower since the basin contains a 4-5-km-thick sedimentary layer (Schueller *et. al.* 1997), which Cong and Mitchell (1998) suggest will lower Q values.

8.10 Conclusions

In this work, the seismic codas of teleseismic P and L_g events were simulated as seismic scattering from heterogeneities near the Earth's surface. Reflectivity synthetics based on velocity models of different crustal and upper mantle properties governed wave propagation in the model. The seismic response was calculated using numerical integration in time and a 2-D surface integral over uniformly-distributed Monte-Carlo-sampled surface points. Q_{coda} values were measured from modeled trace envelopes based on reflectivity synthetics with a range of intrinsic Q_{crust} values to determine Q_{coda} as a function of Q_{crust} . This relation was inverted to obtain Q_{crust} estimates for Quartz PNE data by measuring Q_{coda} from chosen traces.

Using reflectivity synthetics based on velocity models of greater crustal complexity, like the Quartz-4 and complex crust models, led to greater coda strength in resulting receiver traces and stronger Q_{coda} - Q_{crust} relation. For the teleseismic P coda at 0.3 Hz, the Quartz-4 model gave a strong dependence of $Q_{coda} = 16 \cdot Q_{crust}^{0.47}$ at 0.3 Hz. The IASP-91 model gave a much weaker dependence, portrayed by the much smaller exponent value, of $Q_{coda} = 75 \cdot Q_{crust}^{0.06}$ at 0.3 Hz,

because of its much simpler crustal structure and fewer crustal arrivals. The IASP-Quartz model showed that the crust, not the mantle, played the most significant role in determining coda strength, with the relation given by $Q_{coda} = 49 \cdot Q_{crust}^{0.14}$ at 0.3 Hz, since the relation is most similar to that of the IASP-91 model with simple crust and mantle. Velocity models with higher-complexity crusts clearly result in more complex crustal seismic phase arrivals, stronger coda, and stronger Q_{coda} - Q_{crust} dependence. Because the crust is apparently the most heterogeneous part of the Earth and is known to propagate strong crustal phases, crustal scattering is a viable mechanism and should contribute to the strong coda seen in PNE data.

Estimates of Q_{crust} for Quartz PNE data as a function of frequency were made using relations obtained in model data, though the frequency windows of Quartz PNE data and model data differed due to modeling limitations. Teleseismic P Q_{coda} values measured from the envelope of a set of Quartz PNE traces gave Q_{crust} values of 180 at 2.5 Hz, decreasing to 50 at 5 Hz, for the East European Platform. These are crustal values commensurate with others obtained previously in other regions. The Quartz-4 L_g parameterization at 1.3 Hz gave a Q_{crust} estimate of 21 for the West Siberian Basin using the PNE Quartz L_g coda, expected to be lower since the trace was recorded in a region of thick sediments.

8.11 Figures to this Chapter

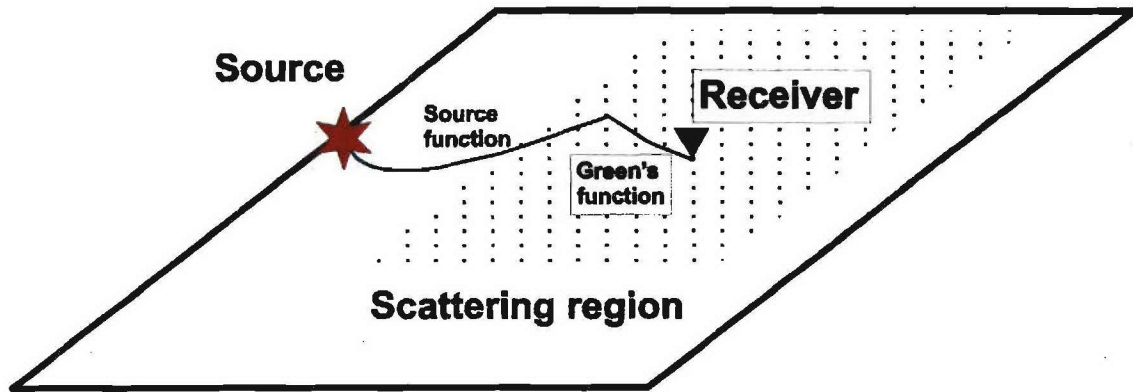


Figure 8-1. Surface scattering model. Seismic energy originates at source, scatters from uniformly-distributed Monte-Carlo-sampled surface points, and is detected at receiver. Source and Green's functions describe propagation of seismic energy.

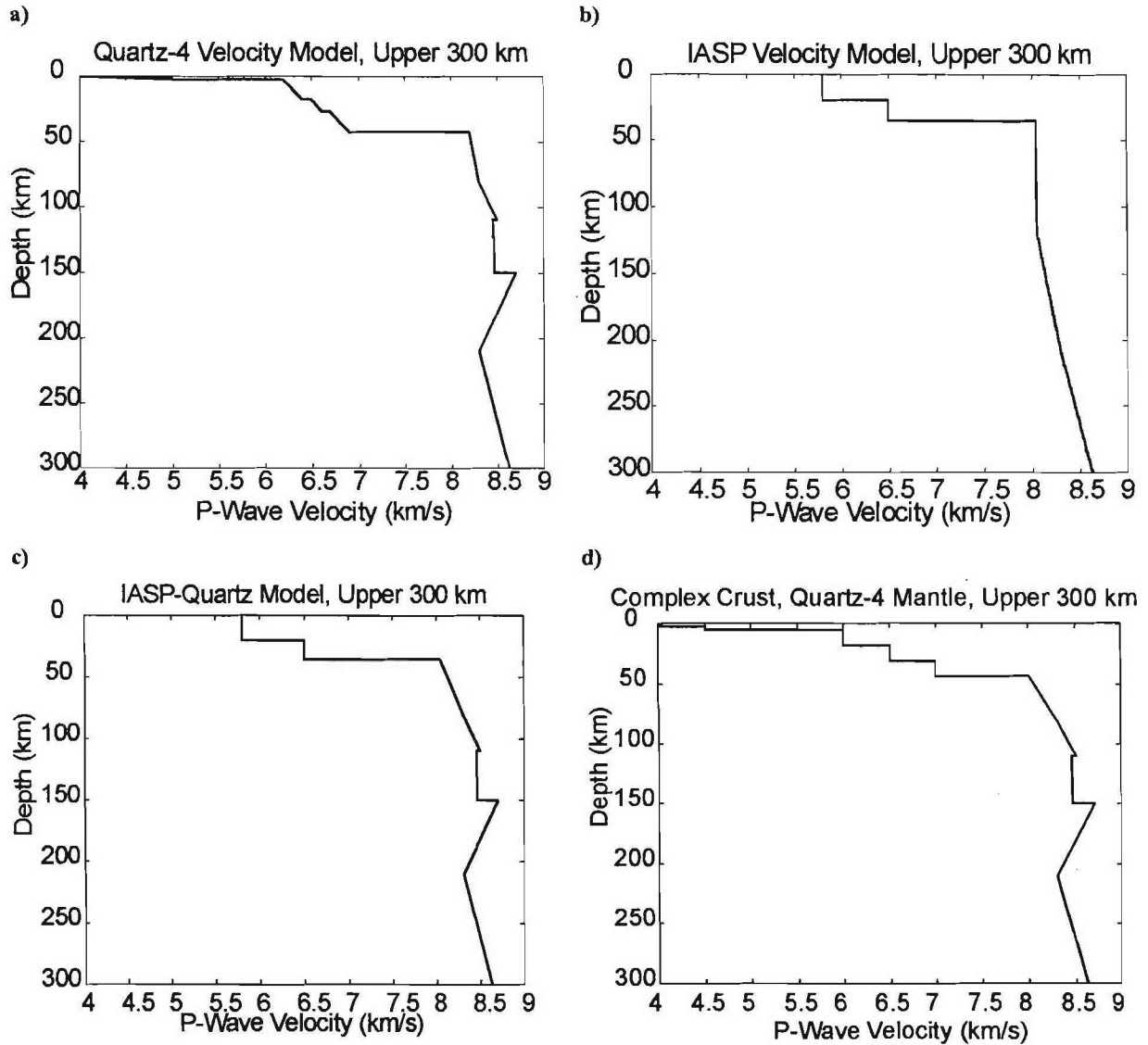


Figure 8-2. Upper 300 km of 1-D velocity models used in creation of reflection synthetic seismograms. a) PNE Quartz-4 model by Morozova et. al. (1999). b) IASP-91 model, with simpler crust and mantle than Quartz-4 model. c) IASP-Quartz model, with IASP-91 crust and Quartz-4 mantle. d) Complex 5-layer crust with Quartz-4 mantle.

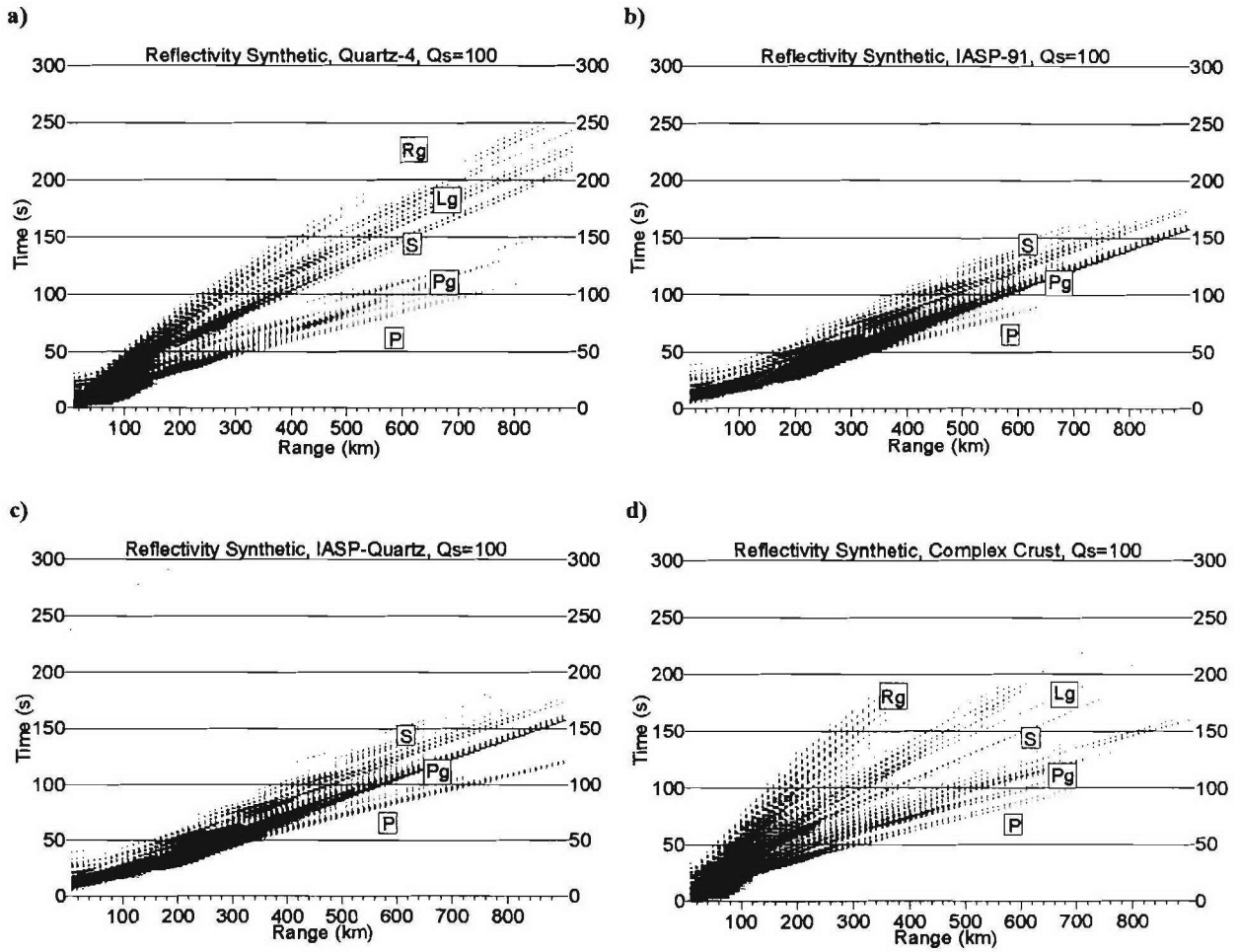
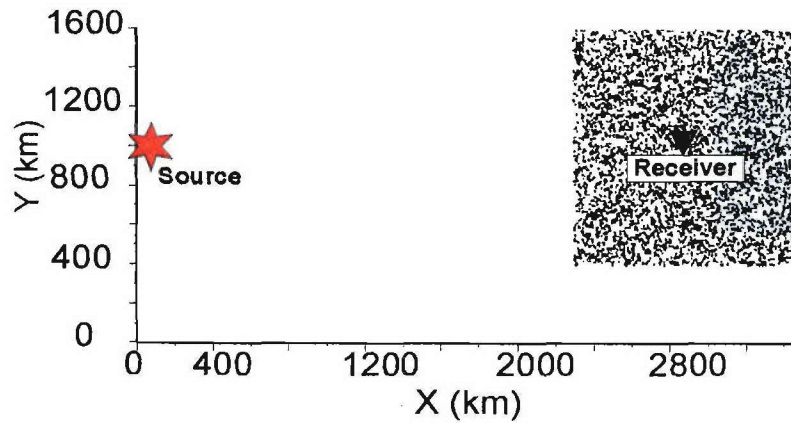


Figure 8-3. Reflection synthetic seismograms used as Green's functions, created using the four different velocity models. a) Quartz-4 model. b) IASP-91 model. c) IASP-Quartz model; note similarity to b). d) Complex crust model; note similarity to a).

a)



b)

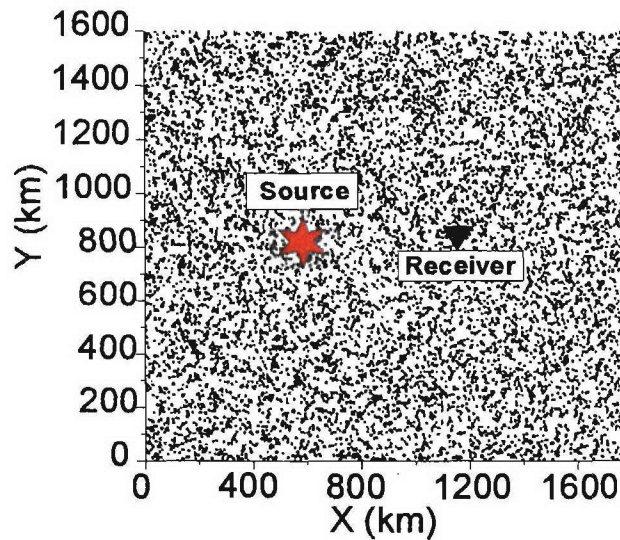


Figure 8-4. Scattering geometries. Scatterer locations within region are distributed uniformly, sampled in Monte-Carlo fashion. a) Geometry for teleseismic P coda, with long offset to achieve significant separation between teleseismic P and L_g events. Since the teleseismic P coda is being examined, the concern is with $P \rightarrow P$ and $P \rightarrow L_g$ scattering; thus the scattering region is required only around the receiver as L_g energy from the source will arrive after the measurement interval. b) Geometry for L_g coda, to include propagation of both teleseismic P and L_g source waves and all scattered waves.

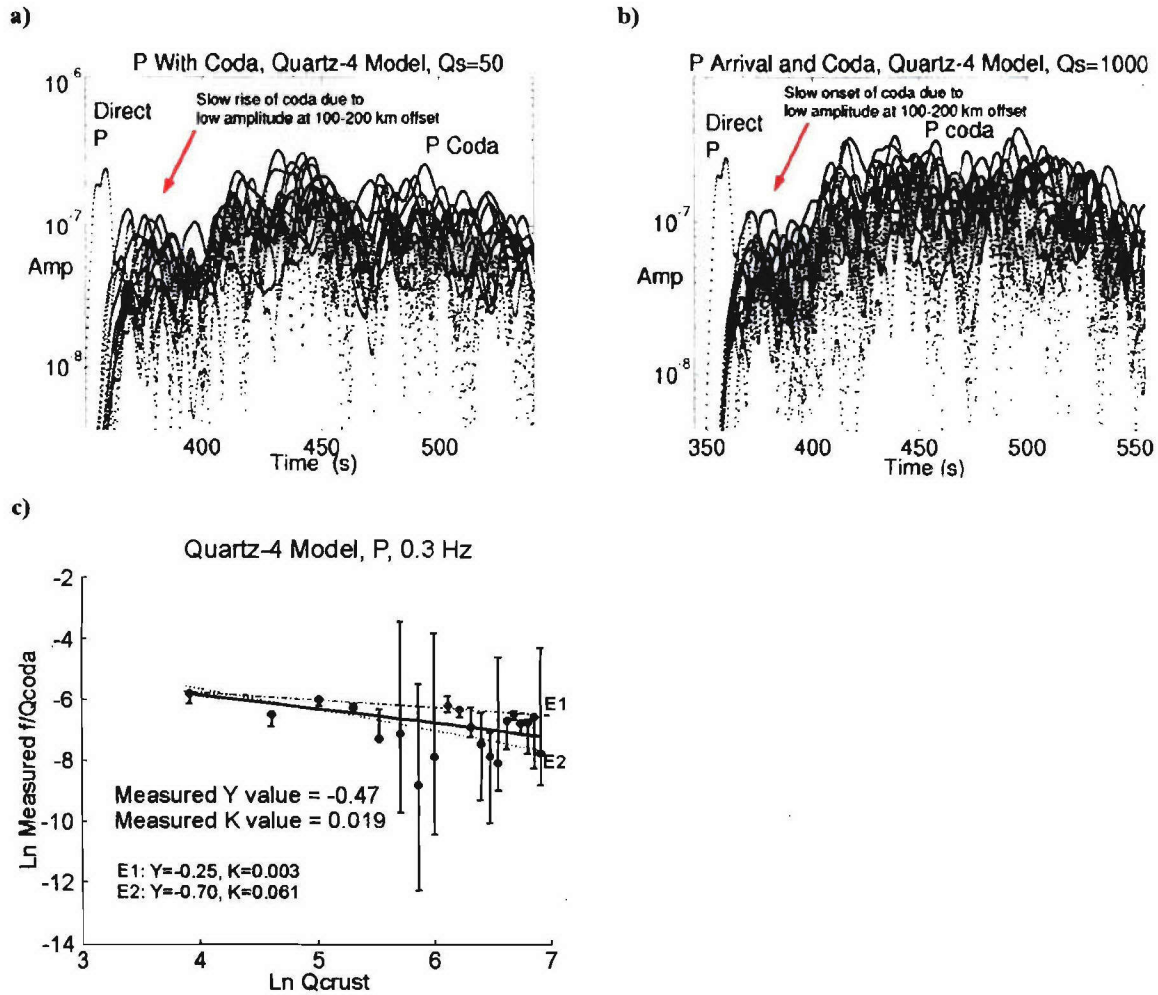


Figure 8-5. Quartz-4 model results at $f=0.3$ Hz. a) Teleseismic P direct arrival with coda for $Q_{crust}=50$. Note the slow onset of coda energy after the direct arrival. b) Teleseismic P arrival with coda for $Q_{crust}=1000$ has a noticeably flatter slope and therefore Q_{coda} shows a noticeable dependence on Q_{crust} . c) Slope fitting of $\ln(f/Q_{coda})$ vs. $\ln(Q_{crust})$ to determine parameters of Q_{coda} - Q_{crust} relation. Parameters are compared with those obtained for other models. Lines E1 and E2 give estimates of the variability of the parameters based on small changes in slope.

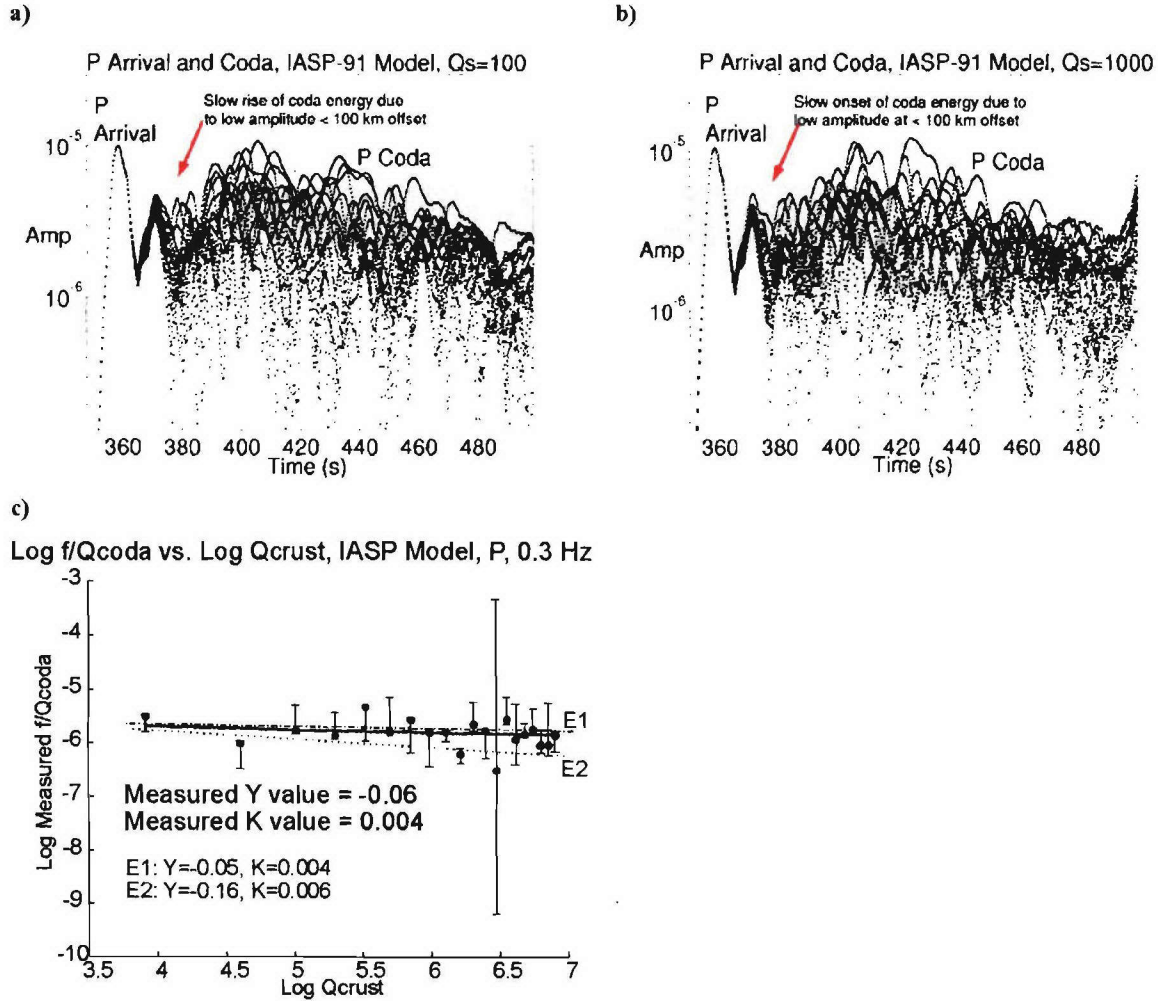


Figure 8-6. IASP-91 model results at 0.3 Hz. a) Teleseismic P direct arrival with coda at $Q_{crust}=100$; the slow rise of teleseismic P coda amplitude as seen in the Quartz-4 model is also evident here. b) Teleseismic P arrival and coda at $Q_{crust}=1000$ shows little difference in coda envelope slope from a. c) Determination of fitting parameters for Q_{coda} - Q_{crust} relation. The absolute value of γ is much lower than that obtained for the Quartz-4 model, indicating a much weaker Q_{coda} - Q_{crust} relation.

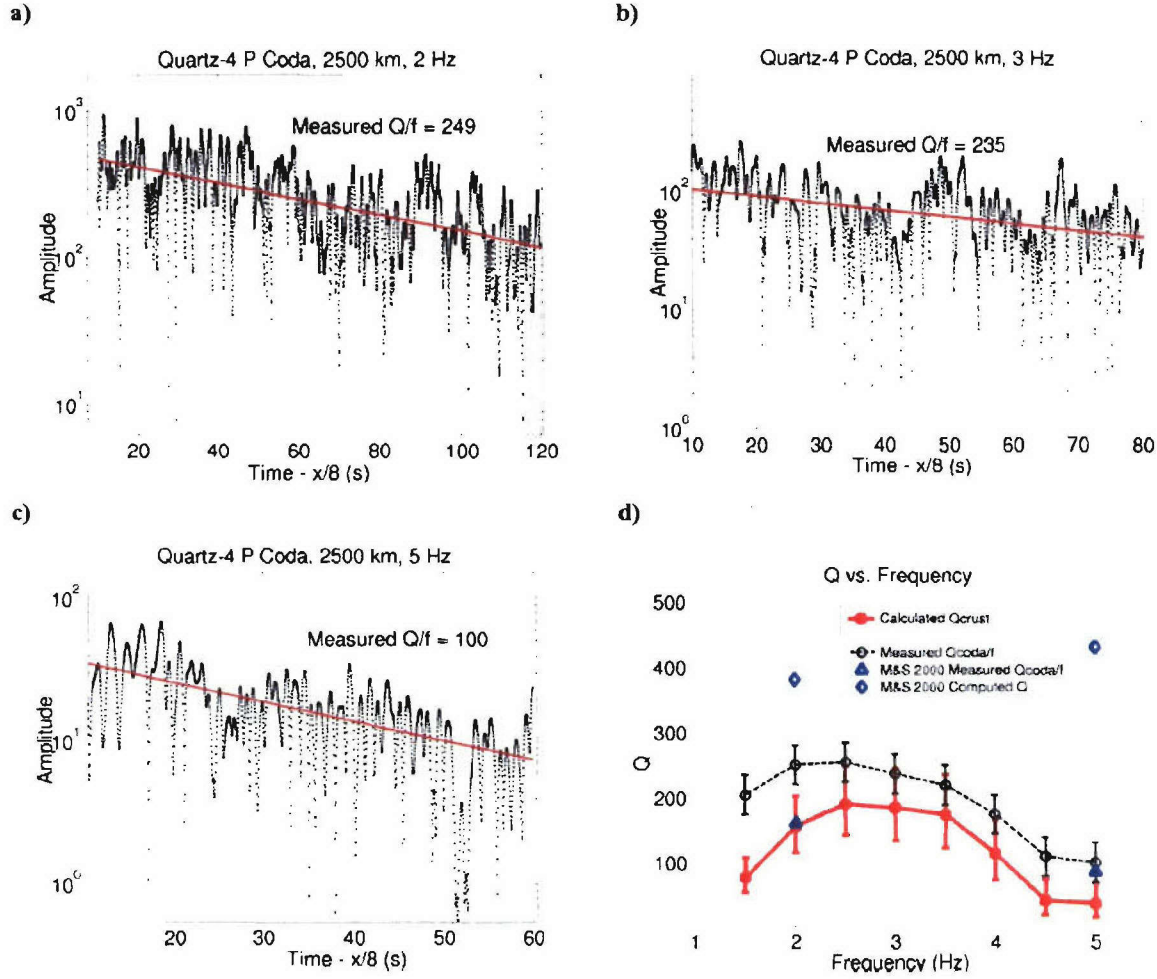


Figure 8-7. *P* coda segments from Quartz PNE data filtered to different center frequencies. Time segments used for measurement were adjusted because signal amplitude differs in the different frequency ranges. Higher frequencies had generally lower amplitudes and were therefore nearer the amplitude of noise in the data, requiring the measurement interval to be shortened. a) Data filtered to 2 Hz, measured between 10s and 120s on a 8 km/s reduced time scale. b) Data filtered to 3 Hz, measured between 10s and 80s. c) Data filtered to 5 Hz, measured between 10s and 60s. d) Q values as a function of frequency. Circles with black line are measured Q_{coda}/f values, as shown in *a*, *b*, and *c*; Squares with red line are the Q_{crust} values computed using parameterization; κ values were scaled for higher frequencies using a power law fit of values at 0.3 Hz and 0.7 Hz. Values at 1.5 Hz may be distorted by the Quartz data's dominant frequency window of 1-10 Hz, limiting energy in the lower part of the filtered band. Q_{crust} values appear to generally decrease with increasing frequency. For comparison, triangles at 2 Hz and 5 Hz represent Morozov and Smithson (2000) values of measured Q_{coda}/f , with corresponding estimates of Q represented by diamonds.

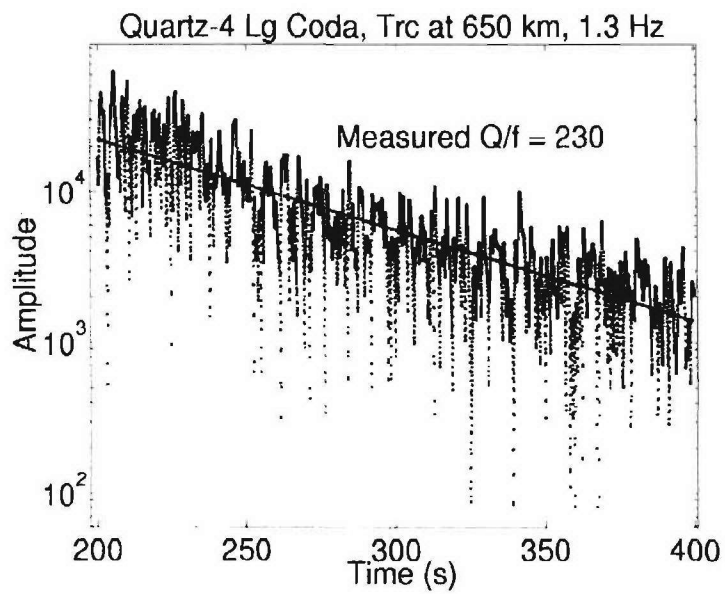


Figure 8-8. Envelope fit of L_g coda segment from Quartz PNE data, 1.3 Hz.

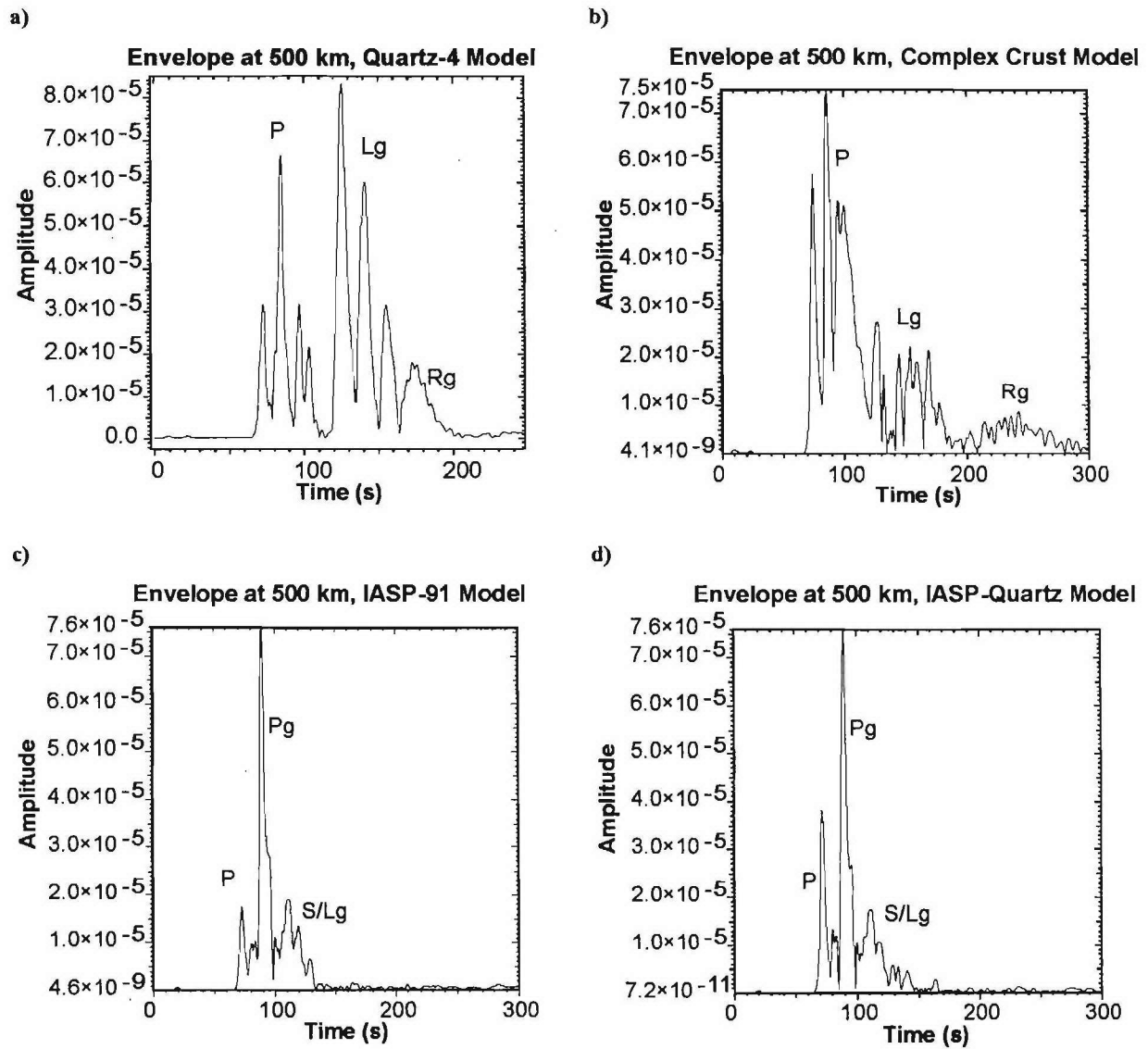


Figure 8-9. Seismic trace envelopes at 500 km offset, $Q_{crust} = 100$, 0.3 Hz. a) Quartz-4 model. b) Complex crust model. c) IASP-91 model. d) IASP-Quartz model. Lg phases are stronger for Quartz-4 and complex crust models than for the other models with simpler crusts.

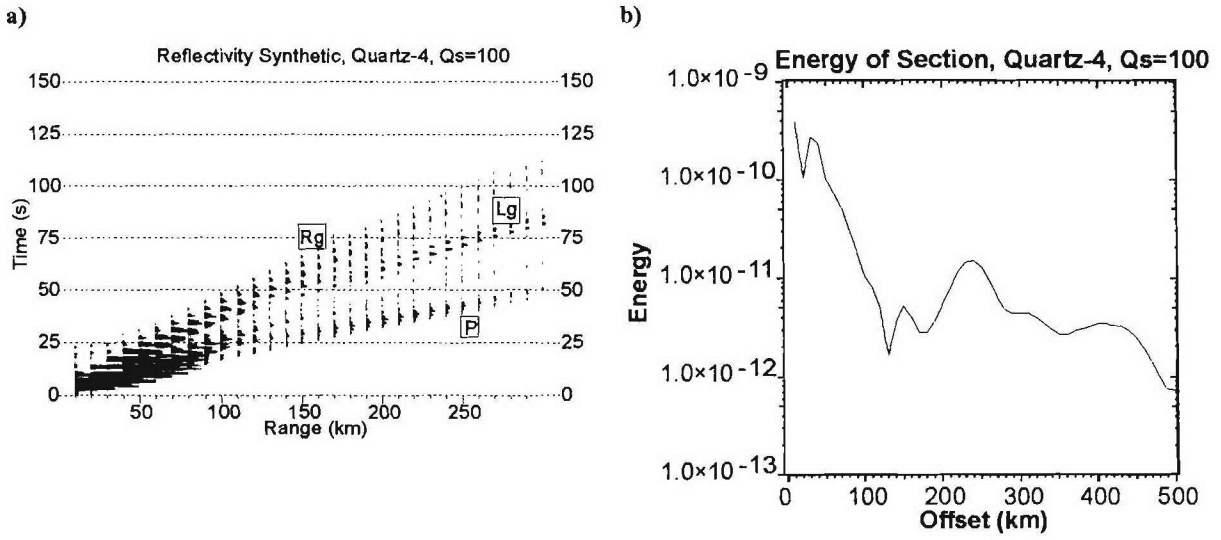


Figure 8-10. a) Arrivals in reflectivity synthetic show small P amplitude between 100 km and 175 km offset and L_g event arrival at 200 km offset at 60s, causing low energy between 100 km and 200 km, increasing past 200 km offset. b) Zoom highlighting decrease of energy at 100-200 km offset.

Table 8-1. Summary of modeling results.

Model, Coda	0.3 Hz		0.7 Hz		1.3 Hz	
	Coeff.	Exp.	Coeff.	Exp.	Coeff.	Exp.
Quartz-4, P	16	0.47	28	0.43	-	-
IASP-91, P	75	0.06	75	0.14	-	-
IASP-Quartz, P	49	0.14	37	0.42	-	-
Complex Crust, P	2	0.98	25	0.58	-	-
Quartz-4, L_g	18	0.40	63	0.24	65	0.50
Complex Crust, L_g	6	0.78	88	0.22	217	0.07

9 3-D first-arrival regional travel-time calibration model of northern Eurasia

9.1 Summary

Seismological monitoring of the Comprehensive Test Ban Treaty (CTBT) requires detailed knowledge of travel-time characteristics of seismic phases across large areas. We use first-arrival travel times from several of Russian Deep Seismic Sounding (DSS) profiles, primarily those from Peaceful Nuclear Explosions (PNEs), to construct a 3-D regional travel-time model of northern Eurasia. The method used, which can be viewed as a generalization of the existing regionalization techniques, is based on apparent-velocity-based spatial interpolation of the travel times picked from DSS records. The resulting travel-time field is described in terms of an apparent velocity model in the 3-D space of geographic coordinates and ray parameter. In the travel time calibration, this model could be used to construct approximate source-specific station correction surfaces for any location within the region, and also as a region-specific reference model to be used as a background for further calibration effort. This approach allows incremental refinement of the model as additional travel-time data become available. By converting the travel time-model into depth, a 3-D regional velocity model is obtained, providing a description of the general features of the upper mantle in northern Eurasia.

9.2 Introduction

Fast and accurate location of problem events at regional distances is among the key tasks of seismic nuclear test monitoring. In the current practice, such location is attained through construction of regional travel-time correction surfaces (source-specific station corrections; SSSC's) for the existing and proposed stations participating in seismic monitoring. SSSC corrections are obtained through prediction of the regional travel-times followed by some kind of spatial interpolation (e.g., kriging) of the travel times measured from well-located "ground truth" (GT) events (Myers and Schultz, 2000). Where recordings of regional GT events are too sparse for meaningful interpolation, travel-time calibration is performed in terms of characterization of the propagation of seismic phases within the region of interest. Such characterization is performed either by associating the types of crustal and mantle tectonics with their corresponding travel-time patterns (Tralli and Johnson, 1986) that are further combined using empirical rules (Bondár and Ryaboy, 1997; Yang et al., 2001), or by building three-dimensional velocity models (Villaseñor, 2001; Priestley et al., 2002).

In northern Eurasia, which is a focus area of seismic nuclear test monitoring, the first of the approaches above is practically impossible without special calibration explosions. This vast area is largely aseismic, very few GT events are available, and station coverage is sparse. However, owing to the extensive active-source DSS program, this area is also among the world's best-covered with refraction-reflection profiling.

In this Chapter, we present an application of DSS data to travel-time calibration of northern Eurasia by using a new seismic calibration technique inspired by the good areal coverage, density, and continuity of the datasets. Controlled source recording offered unique opportunities for characterization of the lithospheric structures across the key tectonic boundaries and also for continuous observations of seismic events propagating across 0-3000-km ranges. PNE energy ($m_b > 5$) and spatial sampling density (10-20-km) were sufficient for consistent recording of the arrivals,

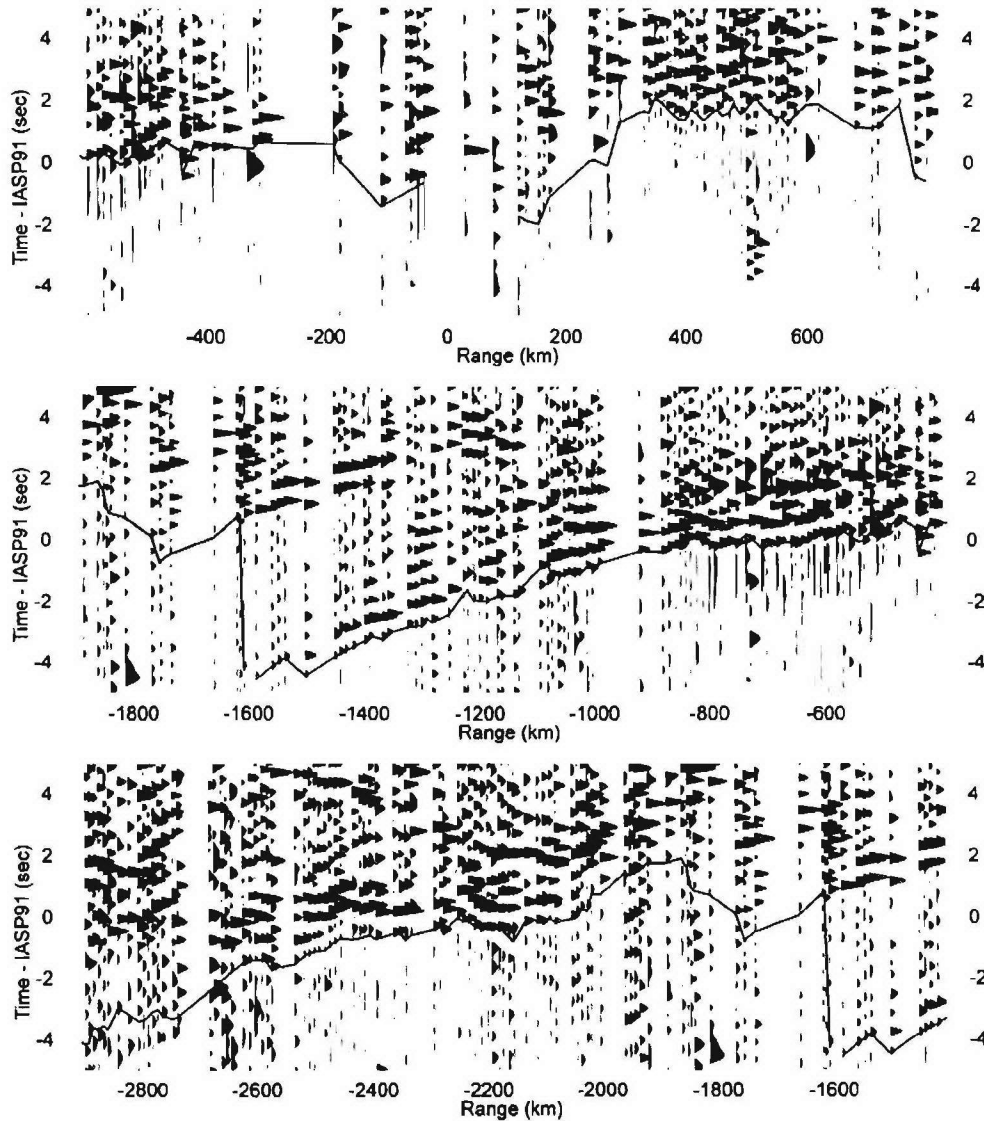


Figure 9-1. First-arrival travel-time windows from PNE QUARTZ-4 within the Altai foreland, record across the West Siberian Basin, Ural Mountains, East European Platform, and Kola Peninsula (Figure 1-1). Travel times are relative to IASP91, and the line represents our first-arrival picks. Note that the first arrivals are consistent, well-correlated, and show variations due to the variations in crustal structures and a major travel-time gap near 1500-km offset. Also note the to 4-s travel-time advance relative to the IASP91 which is typical for this region.

capturing the detailed travel-time variations caused by the regional and local crustal structures (Fig. 9-1).

Although significantly denser and more continuous than most datasets available to calibration seismology (Figure 1-1 and 9-1), DSS profiles are still far from the coverage required for a sufficiently detailed, 3-D velocity modeling. In particular, owing to the non-uniqueness of 1-D refraction travel-time inversion (e.g., Healy, 1963; Morozov, 2004), large and uncontrollable velocity-depth uncertainties would always remain in the resulting models. Fortunately, much of these uncertainties have little impact on the travel times, and therefore, in the context of seismic calibration, an appealing approach would consist in cataloguing the observed travel-time patterns directly, without attempting to mitigate the uncertainties of velocity inversion or resorting to associations of travel-time dependencies with tectonic types. Importantly, such cataloguing could incorporate the key physics of the model-based approaches and also result in 3-D velocity models (however, with the difference of their being the apparent velocity models).

The existing empirical travel-time calibration method is based on regionalization, i.e., subdividing the area of interest into a number of regions each of which is associated with the corresponding travel-time vs. offset dependence. For sources and receivers located in different regions, the regional travel-time dependencies are combined using a heuristic interpolation rule, such as (Bondár and North, 1999; Bondár et al., 2001; Yang et al., 2001):

$$t(S, R) = \frac{\sum_i L_i t_i(d_{SR})}{d_{SR}}, \quad (9.1)$$

where S and R represent the source and receiver (both assumed to be located close to the surface), L_i is the length of the great-arc segment connecting S and R and lying within the i -th region, and $d_{SR} = \sum_i L_i$ is the total source-receiver distance. The regions are outlined based on their tectonic

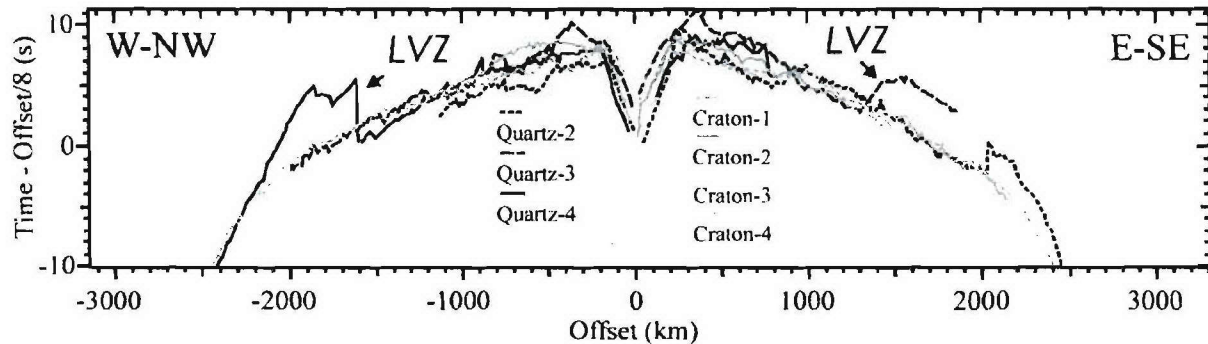


Figure 9-2. First-arrival travel times from seven QUARTZ and CRATON PNEs in northern Eurasia illustrating some of the problems of the existing travel-time interpolation approaches (Eq. 9.1). Due to the crustal and uppermost mantle variability, the travel times vary by up to 2-3 s. Note the ~5-s travel-time lags within the 1500-2000 km ranges due to the low velocities within the mantle structure under the QUARTZ profile (labeled LVZ; Morozova et al., 1999). Such variations cannot be reproduced by selecting either smaller or bigger regions in formula (9.1). Also, the local, near-source and receiver crustal structures create travel-time shifts that should not be propagated to great distances for travel-time prediction in adjacent areas.

types, and several regionalization schemes have been proposed for northern Eurasia (Kirichenko and Kraev, 2000; Conrad et al., 2001).

Although equation (9.1) is convenient for interpolation, it is not based on the physical principles of body-wave propagation through the crust and mantle. Travel times at all offsets are interpolated as if the corresponding seismic phases were propagating along the surface and at a constant velocity. Dense DSS travel times (Fig. 9-2) illustrate a typical problem of assigning fixed travel-time patterns to large areas in this method. The regions are far too large to account for the crustal variability and yet too small to allow a meaningful description of the seismic phases propagating within the mantle. Assigning a single shallow structure to large areas appears to be a conceptual limitation insurmountable in this regionalization/interpolation approach. However, crustal structures are known to both exhibit the greatest variability and to have the strongest impact on the travel times (this has also been well documented in DSS interpretations; e.g., Morozova et al., 1999). Subdividing the regions into smaller blocks does not alleviate the problem because with smaller regions, the edge effects caused by the ray paths crossing region boundaries become more pronounced.

The above scale-length disparity could be resolved by abandoning the fixed region boundaries and making the travel-time interpolation (9.1) dependent on the offsets or, equivalently, ray-parameters. Such interpolation would be based on the diving-wave kinematics and thereby reflect the vertical stratification and variable scale lengths of the lithosphere. Travel-time mapping would be more detailed at the near offsets corresponding to the shallow velocity structures where the variability is predominant. At progressively greater offsets, the model would lose detail because of decreased data coverage, greater path averaging, and also lower velocity heterogeneity within the mantle. Another desirable requirement to any travel-time calibration model is that in sparsely sampled areas, the predicted travel times should approach the nearest available regional readings rather than being controlled by some “reference” curve based on global averages (as it is commonly done with using the IASP91 model in the existing methods).

Below, we describe a practical travel-time interpolation scheme implementing the above principles. When applied to regionalized models, this approach could be viewed as a more physical (i.e., employing diving-ray kinematics) alternative to the interpolation method (9.1); at the same time, the method does not require classification of the travel-time patterns and, similarly to tomography, it could be applied to large datasets with complex spatial data distributions. By contrast to 3-D velocity modeling, this method is purely empirical, free from numerous problems related to inversion of incomplete and heterogeneous data, and focuses on the primary goal of travel-time prediction. Along with refraction travel times, generalized travel-time patterns associated with tectonic blocks could also be included into this interpolation, and thus the regionalization-based approaches (Tralli and Johnson, 1986; Bondár and Ryaboy, 1997; Bondár et al., 2001; Conrad et al., 2001) could readily be implemented as special cases of the proposed method. The approach is illustrated on several DSS PNE profiles and results in a continuous, 3-D travel-time model of northern Eurasia. Finally, from this model, the SSSC's for station BRVK are calculated and applied to 145 events recorded at this station.

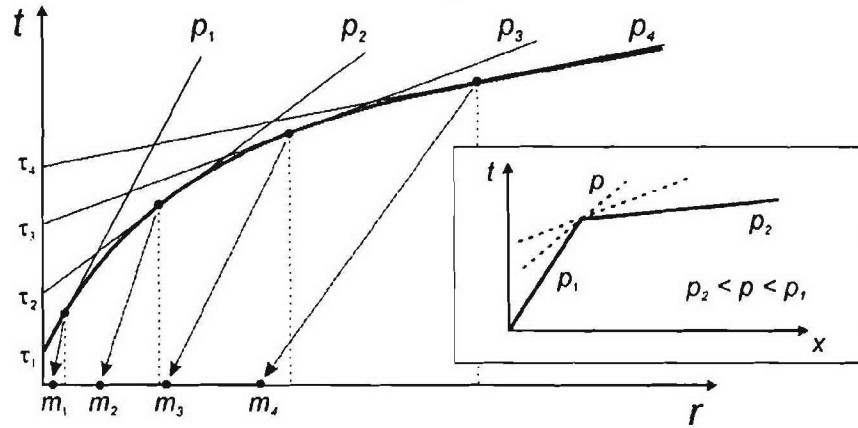


Figure 9-3. Approximation of a travel-time curve by an envelope of a suite of linear travel-time segments (head waves) $t(r) = \tau + pr$ (r is the source-receiver offset). For each value of the ray parameter p_i (which is assumed decreasing with increasing i and offset), we measure the corresponding intercept time, τ_i . The (τ, p) pair is then associated with the midpoint coordinates, m_i , in the resulting 3-D model (indicated by the arrows). Inset shows the case of a velocity discontinuity with an arbitrary set of layers with velocities $1/p$ between $1/p_1$ and $1/p_2$ (dashed lines) hidden from the first arrivals by the deeper and faster layer. In such a case, inversion (9.3) is non-unique, as we choose the smooth, Herglotz-Wiechert solution assuming that all of these layers are present in the depth model.

9.3 Method

Depending on the way travel-times patterns are parameterized and associated with surface locations, multiple interpolation schemes can be devised, and it is important to use the one reflecting the fundamental nature of the travel-time problem. Travel times vary systematically with offsets rather than with geographic coordinates of the receiver, and thus they do not readily lend themselves to spatial interpolation of the type (9.1). By contrast, velocity structures are associated with spatial coordinates and can be interpolated in a natural manner. Thus, instead of a direct interpolation of the travel times (9.1), our travel-time mapping is performed through interpolation of an effective “apparent velocity structure”. This mapping is performed in a series of three transformations:

$$t(r)|_{L_i} \xrightarrow{1) \tau-p} \tau(p)|_{L_i} \xrightarrow{2) \text{HWT}} \Delta z(p)|_{L_i} \xrightarrow{3) \text{Interpolation}} \Delta z(p)|_{(x,y)} \quad (9.2)$$

Here, $i=1 \dots N$ counts the observed travel-time curves, L_i is the great arc connecting the source and receiver, r is the range (source-receiver distance), approximated along the great arc, $t(r)$ is the observed travel time, p is the ray parameter, $\tau(p)$ is the delay (intercept) time (e.g., Buland and Chapman, 1983), x and y are the spatial (geographic) coordinates, and Δz is the layer thickness in the resulting 3-D apparent-velocity model. The Herglotz-Wiechert transform (HWT) is used to encode the $\tau(p)$ dependences into the equivalent “apparent velocity columns” $\Delta z(p)$ that are further spatially interpolated to yield a 3-D model cube, $\Delta z(p|x,y)$. Due to its combining the 2-D geographical variability with 1-D treatment of the depth dimension, we refer to this method as the 1.5-D approximation. The details of this three-step procedure are given below.

9.3.1 τ - p transformation of travel times

First, the observed travel-time curves are transformed into the τ - p domain (Bessonova et al., 1974; Buland and Chapman, 1983), thereby introducing a uniform parameterization of the resulting maps by the ray parameter, p . Note that τ is also often called the intercept time in exploration seismology (Sheriff and Geldart, 1995, Section 4.3). To obtain a $\tau(p)$ curve, we select a dense and uniform grid of ray parameters (at an increment of $2 \cdot 10^{-4}$ s/km in this study), and build an envelope of each of the travel-time curves $t(\text{offset})$ (Fig. 9-3). In order to decrease the sensitivity of the envelope to the statics (short-scale variations of the travel times caused by near-receiver velocities), the $t(r)$ travel times were smoothened using a running-average filter with length increasing from 50 km at zero offset to 150 km at 3000 km.

The τ - p parameterization of the travel times is advantageous in this problem in two ways: 1) ray parameters are related to the crustal and mantle velocities, and therefore, unlike source-receiver distances, they can be described as functions of geographic coordinates; 2) it also serves as a filter reducing the effects of receiver statics on the observed travel times. In transforming the travel times, we use a dense and uniform grid of ray parameters, and ranging within the limits carefully measured for each travel-time branch. When the travel-time moveout changes sharply across velocity discontinuities, such parameterization remains robust and results in linear $\tau(p)$ segments corresponding to sets of travel-time tangents passing through the same $t(r)$ point (Fig. 9-3, inset). In the subsequent analysis, we retain all the corresponding (τ, p) values, and thus do not impose any discontinuities in the underlying apparent-velocity models.

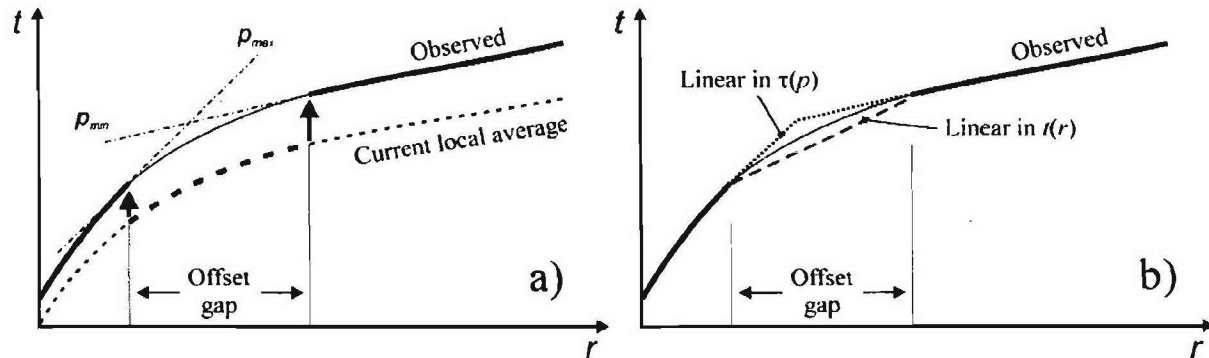


Figure 9-4. A) Treatment of gaps in the offset coverage. The heavy line represents the observed travel-time segments; the thin line is the resulting interpolated segment within the gap. A travel-time curve is derived from the current iteration of our 3-D layer-thickness model $\Delta z(p, x)$ (dashed line), its appropriate segment is extracted (heavy dash) and scaled to fill the gap (heavy arrows). Scaling is performed in the $\tau(p)$ domain, using a factor that varies linearly between the ray parameters bordering the gap (p_{min} and p_{max}). B) Comparison of this interpolation method to two other approaches: linear interpolation in the $t(x)$ (dashed line) and $\tau(p)$ (dotted line) domain. Note that our interpolation yields travel times (thin solid line) that are intermediate between the two and is also more likely to correspond to the travel-time pattern within the area.

9.3.2 Mapping of τ -p travel-times into depth

After sampled travel time curves $\{p_i, \tau_i\}$ are obtained, they are converted into the corresponding stack of layers $\Delta z_i(p)$ using a discrete form of the Herglotz-Wiechert transformation (HWT) implemented as a layer-stripping procedure (Sheriff and Geldart, 1995, eq. 4.43):

$$v_i = \frac{1}{p_i},$$

$$\Delta z_i = \frac{1}{\varphi_i(p_{i+1})} \left(\tau_{i+1} - \sum_{j=1}^{i-1} \Delta z_j \varphi_j(p_{i+1}) \right). \quad (9.3)$$

Here, Δz_i is the thickness of the i -th layer ($i \geq 0$), v_i is its velocity, and

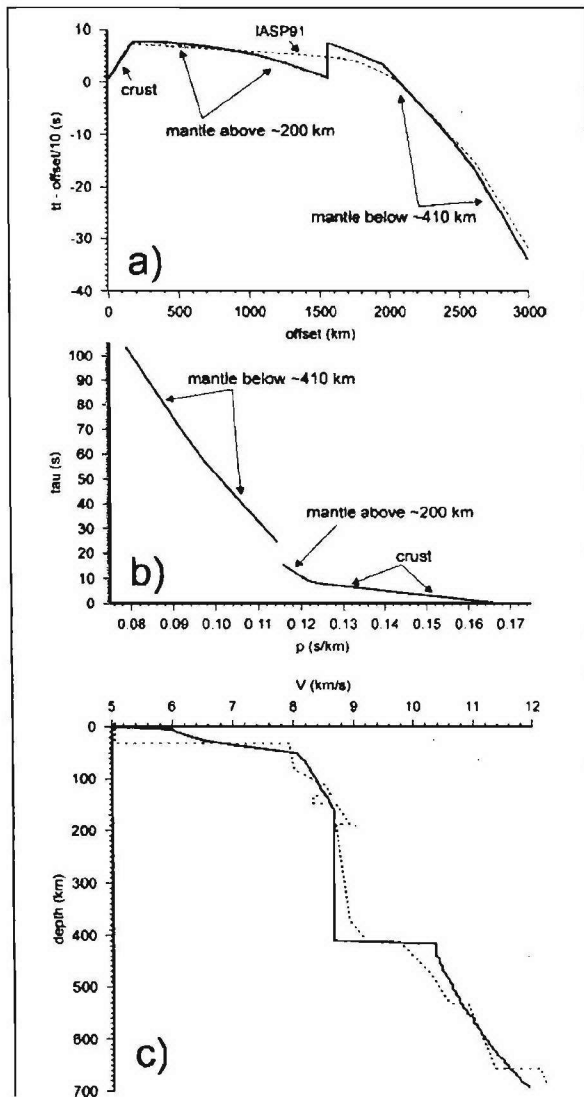


Figure 9-5. Treatment of mantle low-velocity zones, using the example of PNE QUARTZ-4: (a) The observed travel time (tt) curve is split into two segments with non-overlapping ray parameters (gray dashed lines). The IASP91 travel time curve is shown for comparison. The thick line corresponds to the travel times obtained by ray tracing in the resulting model obtained by the Herglotz-Wiechert transform (HWT; eq. 9.3). The reduction velocity is 10 km/s. (b) The $\tau(p)$ curves obtained for each of the travel-time segments, as labeled. (c) Velocity model resulting from the HWT inversion of the discontinuous $\tau(p)$ dependence. The dashed line shows the velocity cross-section across the QUARTZ 2-D model (Morozova et al., 1999). Note that the low-velocity zone below ~220 km in the model by Morozova et al. (1999) is represented by a thick, constant-velocity layer in the HWT model.

$$\varphi_i(p) = \frac{2}{v_i} \cos \theta_i = \frac{2}{v_i} \sqrt{1 - (pv_i)^2} \quad (9.4)$$

is the intercept time per unit layer depth (with θ_i being the incidence angle in the i -th layer; Sheriff and Geldart, 1995, eq. 4.42). The parameters above are computed in a single pass from the top of the model to its bottom, and the resulting model predicts all the travel times $\tau_i(p_i)$ exactly. Earth-flattening transformation can be applied if true velocities and depths are of interest; however, it is not required for the travel-time interpolation.

The resulting $\Delta z(p)$ parameterization possesses two important properties making it particularly useful for the subsequent interpolation: 1) the values of $\Delta z(p)$ can be interpreted as layer thicknesses associated with the subsurface locations; 2) as differential characteristics of the travel times [cf. the second equation (9.3)], the values of $\Delta z(p)$ are computed progressively for decreasing values of p , and the shallower layers absorb the static time shifts. Consequently, the $\Delta z(p)$ parameterization is less sensitive to the propagation of near-source time shifts (caused by the variations in the crustal structure) across the entire offset range, which is the key problem with interpolation of travel times using a direct, $t(r)$, parameterization (eq. 9.1).

The velocity model (9.3) is unique by construction, and it predicts each of the input first-arrival times $\tau(p)$ accurately. To add lateral variability to these models, we associate (somewhat arbitrarily) each value of $\Delta z(p)$ with the location of the midpoint of the great arc on the surface along which this value of p was observed (Fig. 9-3). This results in a set of $\Delta z(p|x_i, y_i)$ values of layer thicknesses at different geographical locations.

9.3.3 Spatial interpolation

In the last step of the travel-time mapping procedure, for each p , the corresponding layer thicknesses $\Delta z(p|x_i, y_i)$ are interpolated into a dense 2-D surface grid by using minimum-curvature splines (adapted after Smith and Wessel, 1990), constrained to values of $\Delta z \geq 0$. The result is a continuous, 3-D layer-thickness model $\Delta z(p, x, y)$ that reproduces the input data and is suitable for ray tracing, computation of SSSC's, plotting, and interpretation.

Thus, with complete travel-time curves from zero to the maximum recording offset available, the procedure represented by expression (9.2) results in an interpolated 3-D travel-time model in a single pass, without uncertainties or iterative inversion steps. In this mode, this procedure could provide an alternative way to interpolate the regionalized travel times $t(d_{SR})$ in equation (9.1). However, real travel-time data often have offset and travel-time gaps, and such gaps need to be accounted for in the interpolation. Clearly, there exists no ideal solution to this problem of missing data, and we resort to a reasonable heuristic approach, based again on interpolation of the $\tau(p)$ travel times.

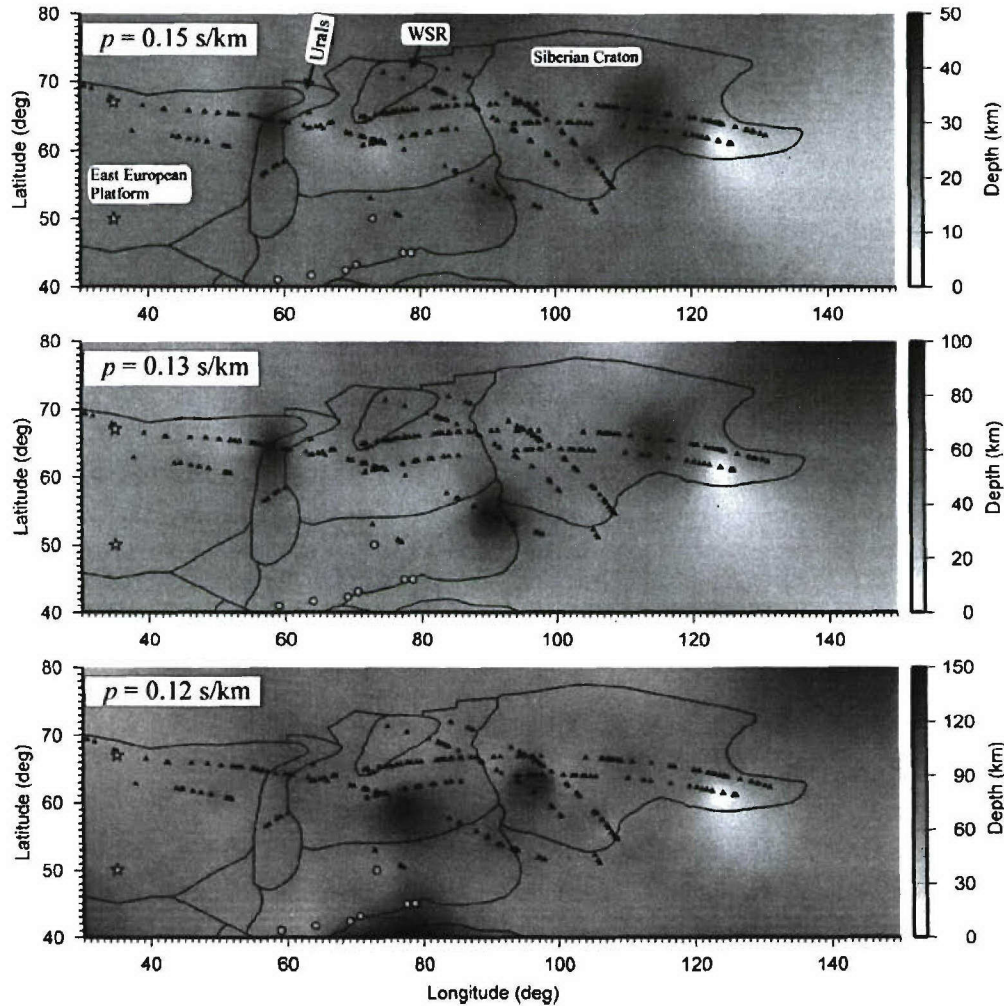


Figure 9-6. Constant-ray parameter surfaces in Northern Eurasia from interpolation of the picked first-arrival travel times. Picks from all of the PNE were used (midpoints are indicated by black dots) and complemented with picks from regional DSS investigations in Kazakhstan (gray dot) and the East European Platform (gray stars). Contours show some of the tectonic regions of Conrad et al. (2001). Note the variability of these isopach maps with ray parameter. The shallow maps appear to correspond well with some of the regions of Conrad et al. (2001) (e.g., the Ural and the West Siberian rift (WSR); labeled).

Gaps in the offset coverage. If offset gaps are present in the data, we repeat the described mapping several times. In the first pass, we initialize the $\Delta z(p)$ model using a single reference travel-time curve that could be, for example, an average $t(r)$ picked for the entire region. The exact shape of this starting dependence is not essential. Ray tracing within this model results in $\tau(p)$ curves computed at the locations of the gaps in offset coverage. For each travel-time gap, predicted reference $\tau(p)$ times are linearly scaled (also using a factor linearly varying in p) so that they fit within the gap (Fig. 9-4a). After the gaps are filled, the interpolation is performed again, and this procedure is repeated iteratively. In the case of our DSS data set, the resulting travel-time field converged in two iterations.

Other possible alternatives to the described $\tau(p)$ interpolation procedure include linear interpolation across the gap in the $t(x)$ or $\tau(p)$ domains (Fig. 9-4b). Our preferred interpolation approach leads to travel times that are intermediate between these two extremes and that also resemble the travel-time patterns recorded in the adjacent areas. Therefore, this approach appears to provide a reasonable approximation of the missing data within the offset gaps.

Gaps in the travel-time curves caused by low-velocity zones within the mantle represent another problem still not addressed in the existing regionalized travel-time models (e.g., Bondár et al., 2001) yet critical for our study area (Mechie et al., 1993; Morozova et al., 1999; Fig. 9-5). From the PNE studies, gaps of up to ~ 5 s occur near ~ 1500 km offsets (Fig. 9-2) from shots within the East European Platform and in the southern part of Western Siberia but not under the Siberian Craton (Mechie et al., 1997; Nielsen et al., 1999). To account for such gaps in the τ - p interpolation method, it is only necessary to split the $t(r)$ travel-time curves into the appropriate segments with non-overlapping ray parameters (Fig. 9-5a). This results in discontinuous $\tau(p)$ dependences (Fig. 9-5b), with the corresponding $\Delta z(p)$ models (Fig. 9-5c) reproducing the travel-time gaps (thick line in Fig. 9-5c), and the travel-time interpolation providing smooth transitions into the areas where no gaps are found.

Low-velocity zones lead to strong non-uniqueness of 1-D travel-time inversion (9.3), and additional constraints on the extents and amplitudes of the velocity anomalies are required (e.g., Bessonova et al., 1974; Morozov, 2004). In our modeling, low-velocity zones are replaced with depth intervals of zero vertical gradients (Fig. 9-5c). Reflection travel times and amplitudes could be used to improve these models, but such data are limited to only a few interpretations (e.g., Morozova et al., 1999). Nevertheless, despite the uncertainty of the mantle structure, our travel-time modeling appears to reproduce the observed regional first-arrival travel times sufficiently closely (Fig. 9-5a).

9.3.4 Prediction of travel times

The method was applied to each of the observed travel-time curves picked from 19 PNEs in northern Eurasia and from several published regional DSS investigations in Kazakhstan (Antonenko, 1984; Zunnunov, 1985; Shatsilov et al., 1993). In order to stabilize the interpolation near the edge of the model, and also to illustrate the use of generalized travel-time dependencies associated with tectonic types, additional travel-time curves were included within the Baltic Shield and East European Platform (Conrad et al., 2001). The resulting map, in the form of constant-slowness surfaces, $z(p|x,y)$, is shown in Fig. 9-6. Note that the principal objective of the ray-parameter parameterization is separation of the crustal (high values of p) and mantle ($p < \approx 0.12$ s/km, i.e., velocity above 8.3 km/s) contributions. As expected, the high- p (small-offset) maps are based on

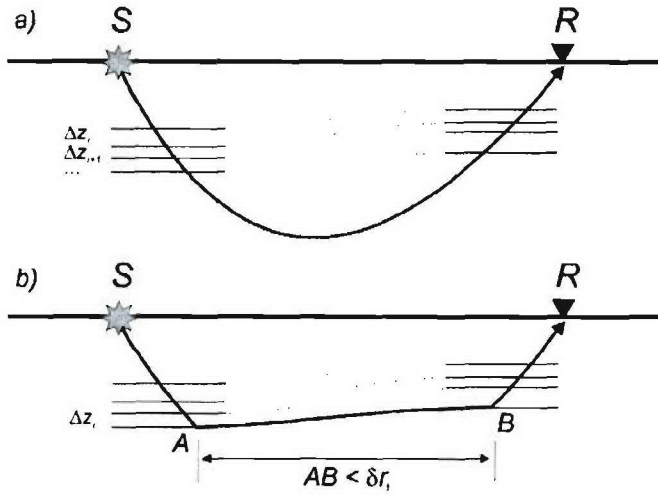


Figure 9-7. 1.5-D ray tracing: a) diving waves, b) head waves whose maximum horizontal extension is limited by an additional layer parameter δr (equation 9.6). Rays are traced from the source to the receiver assuming a locally horizontally layered velocity structure. Velocity within the i -th layer is constant and equal to $1/p_i$ (see equations (9.3)); however, the layer thicknesses and depths may vary laterally. The shape of the ray is controlled by its ray parameter, which is determined by iterative trial shootings aiming at the receiver.

denser data coverage and show more detail; at the same time, the sparsely sampled low- p readings still control the adjacent regions and no external reference model (such as the IASP91) is required. Note that for smaller regions (such as the Urals in Fig. 9-6), shallow (higher- p) structure appears to correlate with the regionalization whereas at greater depths this correlation is less apparent.

In order to predict the travel times between any two points within the region (Fig. 9-6), we trace rays through the resulting $\Delta z(p|x,y)$ maps using an approximate, 1.5-D procedure corresponding to mapping (9.2). Travel-times are computed within vertical cross-sections along the great circle paths and assuming that the $\Delta z(p)$ layers are locally horizontal along the raypath (Fig. 9-7a). With reference to the layer-stripping procedure (9.3), the predicted travel time t and offset r become:

$$\begin{aligned}
 t(p) &= \sum_{j=1}^{N(p)} \frac{\Delta z_j(x,y)}{v_j \cos \theta_i} = \sum_{j=1}^{N(p)} \frac{\Delta z_j(x,y)}{v_j \sqrt{1 - (pv_j)^2}}, \\
 r(p) &= \sum_{j=1}^{N(p)} \Delta z_j(x,y) \tan \theta_i = \sum_{j=1}^{N(p)} \frac{\Delta z_j(x,y) pv_j}{\sqrt{1 - (pv_j)^2}},
 \end{aligned} \tag{9.5}$$

and the summations are performed over all the $N(p)$ layers for which $pv_i < 1$. Because the layer thicknesses, $\Delta z_j(x,y)$, are now spatially variable, these summations are started from the source, proceed to the bottom layer, and back to the surface near the receiver. The ray parameter p in expressions (9.5) is iteratively adjusted so that the ray ends at the receiver. Unlike two-point 3-D ray tracing, this shooting method is fast and does not suffer from shadow zones caused by transitions across lateral and depth velocity contrasts.

When low-velocity zones are present, head waves from the shallow layers could mask the

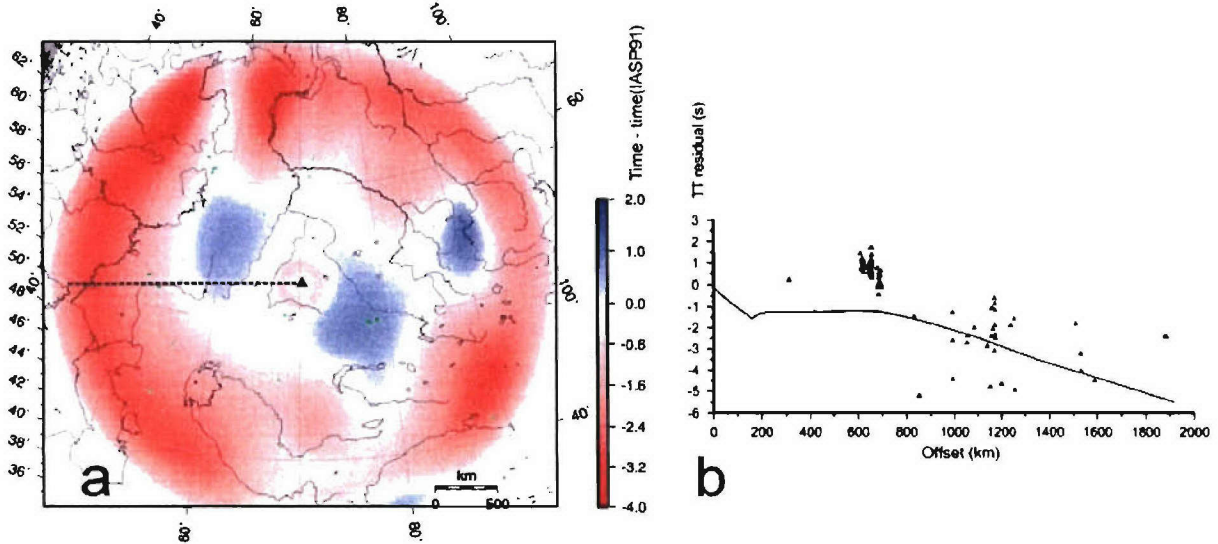


Figure 9-8. a) SSSC for a station at Borovoye, Kazakhstan (BRVK, Figure 1-1) derived by ray tracing in the 3-D apparent velocity model (Fig. 9-6) for all source locations around the station, followed by subtraction of the IASP91 travel times. b) Travel-time residuals, relative to IASP91, of 145 events recorded at BRVK (Conrad et al., 2001) (dots) and a cross-section of the SSSC (a) along a line pointing away from the station and to the west (dashed line in plot a). Note that although obtained without any of these events, the SSSC reflects their trend (advance relative to the IASP91), and the remaining misfit should be due to the local (near-source or near-BRVK) structures not captured in the model.

deeper arrivals in the first breaks (dashed line in Fig. 9-5). However, in practice, because of their low amplitudes, head waves are often not observed at large offsets, and travel-time gaps are identified in the first arrivals. To reproduce such travel-time gaps in ray tracing, head wave propagation distances need to be restricted. In our approach, this is achieved by introducing an additional model parameter, α , controlling the maximum head wave propagation distance:

$$\delta r \leq \alpha r_{crit}(p|x, y), \quad (9.6)$$

where $r_{crit}(p|x, y)$ is the critical distance for a ray with slowness p and bottoming beneath point (x, y) . This parameter is also assigned to the individual travel-time curves and spatially interpolated together with Δz . During ray tracing, the interpolated values of α are used to control the maximum extents of the head waves in each model layer (Fig. 9-7b). In Fig. 9-5a) and in the following example, α was set constant and equal 1.3 everywhere in the model.

Fig. 9-8a shows the interpolated travel times for station Borovoye in Kazakhstan (BRVK) and surface sources within a radius of ~ 2000 km around it, derived using the 3-D model in Fig. 9-6. We subtracted the IASP91 times from the interpolated travel times, so that the resulting time differences can be directly compared to the SSSC's normally used in the travel-time calibration.

9.4 Discussion

The empirical travel-time mapping scheme described by expression (9.2) should be viewed as an alternative travel-time interpolation scheme to method (9.1) rather than an attempt to invert for

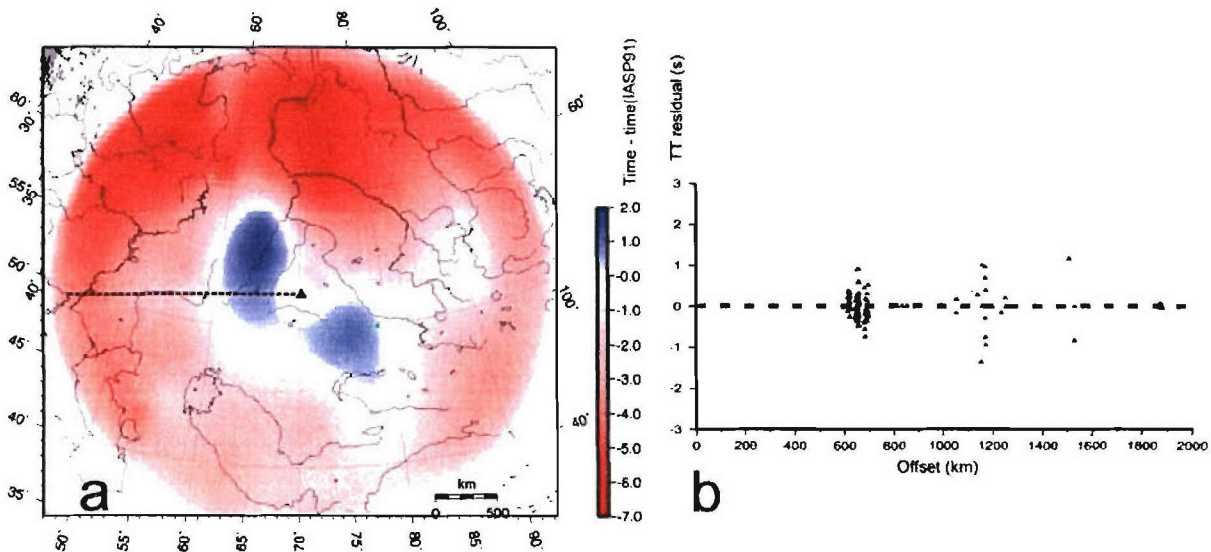


Figure 9-9. a) SSSC for a station BRVK, derived by interpolation of the travel-time residuals of the “Kitov” (Kitov et al., in review) dataset relative to the reference SSSC (Fig. 9-8). b) Final travel-time residuals, relative to the final SSSC, of 145 events recorded at BRVK (Conrad et al. 2001) (dots) and a cross-section of the SSSC along a line to the west from the station (dashed line in plot a). The remaining residuals should be due to conflicting picking errors.

the velocity structure within the region. This method still does not reflect the full complexity of the travel times (in particular, it does not account for their azimuthal dependence). Like any inversion of diving-wave travel times, the underlying model is highly non-unique (e.g., Morozov, 2004), and the choice of the HWT solution (eqs. 9.3) is dictated by its smoothness, absence of negative velocity gradients, and the ability to construct the model in a single pass of the algorithm. The only two objectives of this model are to accurately predict the observed first-arrival travel times while honoring the fundamental travel-time properties of body-wave seismic waves in the layered Earth. Note that within the context of these objectives, and because the model uncertainty above is not reflected in the first-arrival travel times, the HWT solution thus appears to be a good representative of the class of possible models.

Compared to the existing approach (eq. 9.1; Bondár and Ryaboy, 1997), this method offers significant improvements in pursuing both of these objectives, first, by utilizing significantly larger and densely spaced travel-time datasets (both raw and derived from regional generalizations), and second, by emphasizing the offset dependence in the travel-time patterns. No regionalization (i.e., subdividing the area into blocks) is needed; however, the traditional regionalized travel times (e.g., Conrad et al., 2001) or velocity models could be used in this interpolation scheme along with other data, similarly to those for the Baltic Shield and East European Platform in Fig. 9-6. Without the use of the DSS travel times and by assigning multiple sampling points and fixed travel-time curves within, e.g., Conrad’s et al. (2001) regions, interpolation should also reproduce (not exactly but within the errors caused by the regions’ edge effects in formula (9.1)) the predictions of this type of regionalization.

The resulting travel-time model of northern Eurasia (Fig. 9-6) reflects both the regional features and local variability sampled by the present datasets. The seismic velocity structure beneath this

region differs from the global average, with the regional *P* waves at 2000 km arriving by ~ 5 s earlier than in IASP91 model (e.g., Mechie et al., 1997; Fig. 9-2). Within the region, significant structural variations are apparent (Fig. 9-2), suggesting that a single, 1-D velocity model for the whole region (Ryberg et al., 1998) is hardly viable. By contrast, while retaining its character of a catalogue of the observed travel times, the 3-D model provides adequate representation of both the overall regional character of travel times and their local variability.

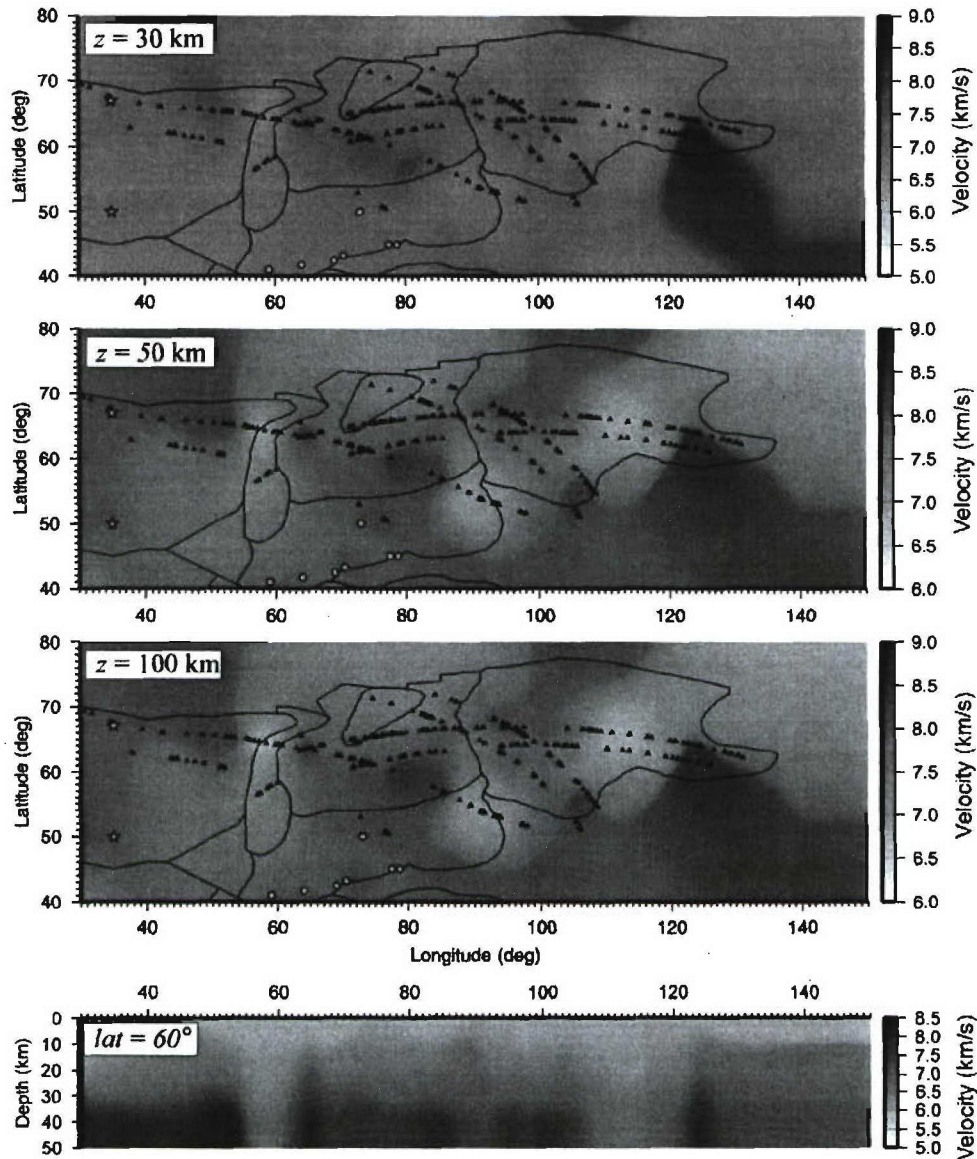


Figure 9-10. 3-D apparent *P*-wave velocity structure in Northern Eurasia derived from the ray-parametric model in Fig. 9-6. Although this model is only one (the smoothest; Morozov, 2004) of the numerous possible solutions and actually represents only a way to parameterize travel times, its velocity variations show marked correlations with the boundaries of tectonic blocks identified by Conrad (2001). Note the somewhat counter-intuitive lower velocities under the Urals and Siberi Craton.

The Source-Specific Station Correction (SSSC) surface obtained from the interpolated DSS travel times (Fig. 9-8a) illustrates the utility of the method for practical travel-time calibration. Although the number of data points used in the analysis is limited (Fig. 9-6), the SSSC reflects the key travel-time features of the region, such as the systematic *P*-wave travel-time advance relative to IASP91 (Fig. 9-8a). Note that the general pattern of the SSSC shows consistently increasing travel-time advances rather than concentric patterns typical of SSSCs derived using the IASP91 travel times as the reference model (e.g., Yang et al., 2001). Such patterns arise from the tendency of conventional algorithms to revert to a reference model (such as IASP91) when no calibration data are available. By contrast, in our method, the average travel times in northern Eurasia are automatically accepted as the reference model, and the IASP91 model is not utilized at all.

The SSSC for BRVK (Fig. 9-8a) was derived without any GT events, and also without any recordings at BRVK. Note that this SSSC correctly reproduces the regional travel-time trend, and reduces the residuals of the events observed at the station (Fig. 9-8b). Accounting for the remaining residuals would clearly require detailed knowledge of the crustal structure or travel times from reliable events. This SSSC could thus be viewed as a reference model that could be further refined by using GT events. Implementation of 1.5-D ray-tracing (Fig. 9-7) in a 3-D $\Delta z(p|x,y)$ model cube is simpler than the travel-time interpolation across the boundaries of geographic regions (Bondár and Ryaboy, 1997; Bondár and North, 1999; Conrad et al., 2001), and it could be readily incorporated into SSSC modeling procedures.

In order to test the performance of our approximate SSSC, we subtracted its predicted travel times from the first-arrival times of 145 events recorded at BRVK from 1967 to 2000 (Kitov et al., in review). Although obtained without using these events, the SSSC reflects the trend in their offset dependence (Fig. 9-8b); however, significant scatter is still present due to unresolved crustal and uppermost-mantle variations and picking uncertainties. Unlike the apparent velocity variations, these factors should be more localized in space, and kriging (Myers and Schultz, 2000) could be used to spatially average and predict these residuals. However, we utilized a simpler technique consisting of a running average followed by interpolation utilizing the minimum-curvature splines (modified program *surface* from Generic Mapping Tools; Smith and Wessel, 1990). The resulting interpolated SSSC shows a somewhat stronger time advance relative to the IASP91 (Fig. 9-9a), with remaining travel-time residuals within ± 1 s (Fig. 9-9b). These residuals cannot be explained by neither source nor receiver travel-time delays and should be due to picking inconsistencies.

By introducing ray-parameter-dependent regionalization and mapping the travel times into depth, the new method also provides a link to model-based travel-time prediction techniques. However, instead of the true crustal and mantle velocities, it utilizes a 3-D apparent velocity (ray parameter) model (Fig. 9-6) that is free from many uncertainties caused by the choice of inversion methods, regularization, and inherent ambiguity of the first-arrival inversion.

Transformation of the depth-interval model, $\Delta z(p|x,y)$, into depth:

$$z_i(p_k | x, y) = \sum_{i=k} \Delta z_i(p_k | x, y) \quad (9.7)$$

yields a 3-D model of the apparent velocity structure of northern Eurasia (Fig. 9-10). Although bearing the typical ambiguities of first-arrival inversion (e.g., Morozov, 2004), the model still reflects the variations in the structure of the mantle in the region. 3-D travel-time modeling within this model should closely reproduce the observed first-arrival travel times, and therefore this velocity model could also serve as a reference for ray-tracing-based travel time calibration and for

generation of SSSCs. Compared to 3-D travel-time tomography, the advantage of the proposed 1.5-D method is in its natural handling of sparse travel-time datasets and inherent stability. No regularization, whose effects on the resulting velocity structure might be difficult to assess, is required. Due to its smooth character, the model is not likely to create problems for 3-D ray tracing. Most importantly, in areas of poor data coverage, the resulting structure approaches a regional 1-D model, and no reference or “preferred” model is required.

The described empirical travel-time calibration method contains potential for its improvement in several ways. Bayesian kriging could replace spline interpolation in predicting the spatial distributions of layer thickness parameters $\Delta z(p|x,y)$, thereby providing statistical estimates of uncertainties in the apparent velocity models and travel times. Anisotropy parameters could be naturally incorporated in the model to account for azimuthal variations of the travel times. Owing to the depth-ray-parameter parameterization (9.3), the method can utilize depth-velocity models (e.g., CRUST 5.1; Mooney et al., 1998) that may be available for some locations in combinations with travel time curves for other places. The travel-time models could be refined by incorporating detailed maps of the basement and Moho structure known from dense DSS and industry seismic studies (Egorkin, personal communication, 1995). Most importantly, this method could also be generalized to using, along with the DSS travel-time curves, much larger datasets of all available travel times recorded in the region. With these enhancements, the 3-D apparent velocity parameterization scheme could combine the purely empirical, interpretative “regionalization”, and model-based tomographic methods into a common integrated framework required for CTBT monitoring.

9.5 Conclusions

Ray-parameter-dependent interpolation of the observed DSS first-arrival travel times results in a 3-D apparent velocity model that could be utilized in travel time calibration of northern Eurasia in several ways: 1) as a simple, purely empirical way to construct approximate SSSCs for any location within the region, 2) as a regionally variable 3-D reference model that can be used for developing SSSCs, and 3) as an alternative way to perform travel-time interpolation in the existing empirical regionalization methods, with the advantage of utilizing the principles of model-based approaches. The key advantage of this method is in its ability of using large heterogeneous (travel-time, velocity) datasets with no classification or regionalization effort required. The resulting 3D model can be used to generate approximate SSSC’s for any location, and mapping of the first-arrival travel-time patterns into depth leads to characterization of the general variability of the upper mantle velocity within the region.

Acknowledgements

Acquisition of DSS PNE data was carried out by the Center GEON, Moscow, Russia (the Special Geophysical Expedition at the time acquisition) and was made possible through the Defense Threat Reduction Agency (DTRA) grants No. DTRA01-00-C-0029, DTRA01-00-C-0031, and DTRA01-00-C-0033. Data pre-processing and analysis were supported DTRA grants DTRA01-01-C-0081 and DTRA01-01-C-0057 (this project), and also through a subcontract from Columbia University. Start-up support from the University of Saskatchewan to Igor Morozov is also acknowledged. Grants from Canada Foundation for Innovation and from the Province of Saskatchewan have contributed to building a cluster computer facility used in this project. GMT programs (Wessel and Smith, 1995) were used in the preparation of some illustrations.

10 Bibliography

- Aki, K. and B. Chouet (1975). Origin of coda waves: source, attenuation, and scattering effects, *J. Geophys. Res.*, 80, 3,322-3,342.
- Aki, K., and P. G. Richards, (2002). *Quantitative Seismology*, Second Edition, University Science Books, Sausalito, CA
- Aki, K., Richards, P., 1980. *Quantitative Seismology: Theory and Methods*, W.H. Freeman, San Francisco, CA.
- Ammon, C. J. (1991). The isolation of receiver effects from teleseismic P waveforms, *Bull. Seism. Soc. Am.*, 81, 2504-2510.
- Ammon, C. J., G. E. Randall and G. Zandt (1990). On the nonuniqueness of receiver function inversions, *J. Geophys. Res.*, 95, 15,303-15,318.
- Antonenko, A.N. (1984). The deep structure of the Kazakhstan earth crust (from seismic data). Nauka, Alma-Ata, 242 pp. (In Russian).
- Aplonov, S. V. (1995). The tectonic evolution of West Siberia: an attempt at a geophysical analysis, *Tectonophysics* 245, 61-84.
- Aster, R., Borchers, B., Thurber, C., 2002. *Parameter Estimation and Inverse Problems*, preliminary edition.
- Bache, T. C. (1982). Estimating the yield of underground nuclear explosions. *Bull. Seism. Soc. Am.* 72, s131-s168.
- Bannister, S.G., Husebye, E.S., Ruud, B.O., 1990. Teleseismic P coda analyzed by three-component and array techniques: deterministic location of topographic P-to-Rg scattering near the NORESS array, *Bull. Seis. Soc. Am.* 80, 1969-1986.
- Bassin, C., G. Laske, and G. Masters (2000). The Current Limits of Resolution for Surface Wave Tomography in North America, *EOS Trans AGU*, 81, F897.
- Baumgardt D. R. (2001). Sedimentary basins and the blockage of Lg wave propagation in the continents, *Pure Appl. Geophys.* 158, 1207-1250.
- Baumgardt, D. R. (1985). Comparative analysis of teleseismic P coda and Lg waves from underground nuclear explosions in Russia, *Bull. Seism. Soc., Am.*, 75, 1413-1433.
- Baumgardt, D. R. (1990). Investigation of teleseismic Lg blockage and scattering using regional arrays, *Bull. Seism. Soc., Am.*, 80, 2261-2281.

- Baumgardt, D. R. (2001). Sedimentary basins and the blockage of Lg wave propagation in the continents, *Pure Appl. Geophys.* 158, 1207-1250.
- Belousov, V. V., N. I. Pavlenkova, and G. N. Kvyatkovskaya (1992). Structure of the crust and upper mantle of the [Former] USSR. Part I, Integrated geophysical models of the major geostructures of the USSR, *Int. Geol. Rev.* 34, 213-343.
- Belousov, V. V., N. I. Pavlenkova, and G. N. Kvyatkovskaya (1992). Structure of the crust and upper mantle of the [Former] USSR. Part II, Generalized geophysical data on the structure of the tectonosphere of the USSR, *Int. Geol. Rev.* 34, 345-444.
- Belousov, V. V., N. I. Pavlenkova, and G. N. Kvyatkovskaya (1992). Structure of the crust and upper mantle of the [Former] USSR. Part II, Generalized geophysical data on the structure of the tectonosphere of the USSR, *Int. Geol. Rev.* 34, 345-444.
- Benz, H., A. Frankel, and D. Boore (1997). Regional Lg attenuation in the continental United States, *Bull. Seis. Soc. Am.*, 87, 600-619.
- Bessonova, E. N., V. M. Fishman, V. Z. Ryaboy, and G. A. Sitnikova (1974). The tau method for inversion of travel times, 1, Deep seismic sounding data, *Geophys. J. R. Astron. Soc.* 36, 377-398.
- Bohlen, T., (2002). Parallel 3-D viscoelastic finite difference seismic modelling, *Computers and Geosciences*, 28, 887-899.
- Bondár, I., and R. North (1999). Development of calibration techniques for potential use by the CTBT International Monitoring System, *Phys. Earth Planet. Interiors*, 113, 11-24.
- Bondár, I., and V. Ryaboy (1997). Regional travel-time tables for the Baltic Shield region, Technical report CMR-97/24.
- Bondár, I., X. Yang, R. North, and C. Romney (2001). Location calibration data for the CTBT monitoring at the Prototype International Data Center, *Pageoph Technical Volumes, Monitoring of the Comprehensive Nuclear Test-Ban Treaty: Source Location*, F. Ringdal and B. Kennett (Editors), *Pure Appl. Geophys.*, 158, 19-34.
- Bostock, M. G. (1996). Ps conversions from the upper mantle transition zone beneath the Canadian landmass, *J. Geophys. Res.*, 101, 8393-8402.
- Bostock, M.G. (1998). Mantle stratigraphy and evolution of the Slave province, *J. Geophys. Res.*, 103, 21,183-21,200.
- Buland, R., and Chapman, C. H. (1983). The computation of seismic travel times, *Bull. Seism. Soc. Am.*, 73, 1271-1302.
- Campillo, M. (1987). Lg wave propagation in a laterally varying crust and the distribution of the apparent quality factor in central France, *J. Geophys. Res.*, 92, 12604-12614.
- Campillo, M. (1990). Propagation and attenuation characteristics of the crustal phase Lg, *PAGEOPH*, 132, 1-17.
- Cao, S., and K. J. Muirhead (1993). Finite difference modeling of Lg blockage, *Geophys. J. Int.* 115, 85-96.
- Carmichael, R. S. (1982). *Handbook of physical properties of rocks*, CRC press.
- Chevrot, S., Vinnik, L. and. Montagner, J. P. (1999). Global-scale analysis of the mantle Pds phases, *J. Geophys. Res.*, 104, 20,203-20,219.
- Chubak, G., and I. B. Morozov, (in review), Integrated software framework for processing of geophysical data, *Computers & Geosciences*.

- Chun, K. Y., G. F. West, R. J. Kokoski, and C. Samson (1987). A novel technique for measuring Lg attenuation – results from eastern Canada between 1 to 10 Hz, *Bull. Seism. Soc. Am.* 77, 398-419.
- Cipar, J. J., K. Priestley, A. V. Egorkin, and N. I. Pavlenkova (1993). The Yamal Peninsula-Lake Baikal deep seismic sounding profile. *Geophys. Res. Lett.* 20, 1631-1634.
- Cipar, J., Priestley, K., 1997. Central Siberia upper mantle cross-section from Deep Seismic Sounding explosions, in *Upper Mantle Heterogeneities from Active and Passive Seismology*, Kluwer Academic Publishers, Dordrecht, The Netherlands.
- Cong, L., Mitchell, B.J., 1998. Seismic Velocity and Q Structure of the Middle Eastern Crust and Upper Mantle from Surface-Wave Dispersion and Attenuation, *Pure Appl. Geophys.* 153, 503-538.
- Conrad, C., Cormier, V., Fisk, M., Ichinose, G., Khalturin, V. I., Kim, W.-Y., Morozov, I., Morozova, E., Richards, P. G., Saikia, C., Shaff, D., Waldhauser, F., Annual Technical report: Seismic Location Calibration of 30 International Monitoring System Stations in Eastern Asia, DTRA, Contracts No. DTRA01-00-C-0029, DTRA01-00-C-0031, DTRA01-00-C-0033, October 20, 2001.
- CTBTO (Comprehensive Nuclear-Test-Ban Treaty Organisation) Preparatory Commission, Monitoring Technologies, online, accessed 29 May 2003, <<http://www.ctbto.org>>.
- Czamanske, G. K., A. B. Gurevich, V. Fedorenko, and O. Simonov (1998). Demise of the Siberian plume: paleogeographic and paleotectonic reconstruction from the prevolcanic and volcanic records, North-Central Siberia, *Int. Geol. Rev.* 40, 95-115.
- Dainty, A.M., (1985). Air Force Geophysical Laboratory Report, AFGL-TF-86-0218.
- Dainty, A.M., (1990). Studies of coda using array and three-component processing, *Pure App. Geophys.* 132, 221-244.
- Dehandschutter, B. (2001). Study of the recent structural evolution of continental basins in Altay-Sayan, Dehandschutter, B. (2001). Study of the recent structural evolution of continental basins in Altay-Sayan,
- Der, Z. A., A. C. Lees, and V. F. Cormier (1986). Frequency dependence of Q in the mantle underlying the shield region of Eurasia, Part III: The Q-model, *Geophys. J. R. Astr. Soc.*, 87, 1103-1112.
- Der, Z. A., T. W. McElfresh, R. Wagner, and J. A. Burnetti (1985). Spectral characteristics of P waves from nuclear explosions and yield estimation. *Bull. Seism. Soc. Am.* 75, 379-390.
- Dresen, L., and H. Rüter (1994). Seismic coal exploration, part B: in-seam seismics, Elsevier Science Inc.
- Dueker, K. G. and Sheehan, A. F. (1998). Mantle discontinuity structure beneath the Colorado Rocky Mountains and High Plains, *J. Geophys. Res.*, 103, 7153-7169.
- Dwyer, J. J., R. B. Herrmann, and O. Nuttli (1983). Spatial attenuation of the Lg wave in the continental United States, *Bull. Seism. Soc. Am.* 73, 781-796.
- Egorkin, A. V., and Mikhaltsev, A. V. (1990). The Results of Seismic Investigations along Geotraverses, in *Super-Deep Continental Drilling and Deep Geophysical Sounding*, K. Fuchs, Y. A. Kozlovsky, A. I. Krivtsov and M. D. Zoback (eds.), *Super-Deep Continental Drilling and Deep Geophysical Sounding*, Springer, Berlin, 111-119.
- Egorkin, A. V., S. K. Zaganov, N. A. Pavlenkova, and N. M. Chernyshev (1987). Results of lithospheric studies from long-range profiles in Siberia, *Tectonophysics* 140, 29-47.
- Egorkin, A. V., 1997. Evidence for 520-km discontinuity, in *Upper Mantle Heterogeneities from Active and Passive Seismology*, Kluwer Academic Publishers, Dordrecht, The Netherlands.
- Egorkin, A. V., 1998. Velocity structure, composition and discrimination of crustal provinces in the former Soviet Union, *Tectonophysics* 298, 395-404.

- Enderle, U., M. Titgemeyer, M. Itzin, C. Prodehl, and K. Fuchs (1997). Scales of structure in the lithosphere - Images of processes, *Tectonophysics*, 275, 165-198.
- Erickson, D., D. E. McNamara, and H. Benz (2005). Frequency-dependent Lg Q within the continental United States, *Bull. Seism. Soc. Am.*, 94, 1630-1643.
- Evernden, J. F. (1970). Magnitude versus yield of explosions. *J. Geophys. Res.* 75, 1028-1032.
- Evernden, J. F., C.B. Archambeau, and E. Cranswick (1986). An evaluation of seismic decoupling and underground nuclear test monitoring using high-frequency seismic data, *Rev. Geophys.* 24, 143-215.
- Frankel, A., A. McGarr, J. Bicknell, J. Mori, L. Seeber, and E. Cranswick (1990). Attenuation of high-frequency shear waves in the crust: measurements from New York state, South Africa, and southern California, *J. Geophys. Res.*, 95, 17441-17457.
- Fuchs, K., Müller, G., 1971. Computation of Synthetic Seismograms with the Reflectivity Method and Comparison with Observations, *Geophys. J. R. Astr. Soc.* 23, 417-433.
- Fuchs, K., Schulz, K., 1976. Tunneling of low-frequency waves through the subcrustal lithosphere, *J. Geophys.* 42, 175-190.
- Gaal, G., and R. Gorbatshev (1987). An outline of the Precambrian evolution of the Baltic shield, *Precam. Res.* 35, 15-52.
- Golmshtok, A. Y., A. D. Duchkov, D. R. Hutchinson, and S. B. Khanukaev (2000). Heat flow and gas hydrates of the Baikal Rift zone, *Int. J. Earth Sci.* 89, 193-211.
- Greenfield, R. J. (1971). Short-period P-wave generation by Rayleigh-wave scattering at Novaya Zemlya, *JGR*, 76, 7988-8002.
- Gupta, I. N., Chan, W. W., and Wagner, R. A., 1992. A comparison of regional phases from underground nuclear explosions at east Kazakh and Nevada test sites. *Bull. Seism. Soc. Am.* 82, 352-382.
- Gupta, I. N., T. R. Zhang, and R. A. Wagner (1997). Low-frequency Lg from NTS and Kazakh nuclear explosions – observations and interpretation, *Bull. Seism. Soc. Am.* 87, 1115-1125.
- Gupta, I. N., W. W. Chan, and R. A. Wagner, (1992). A comparison of regional phases from underground nuclear explosions at east Kazakh and Nevada test sites, *Bull. Seism. Soc. Am.* 82, 352-382.
- Gupta, I.N., McElfresh, T.W., Wagner, R.A., 1991. Near-source scattering of Rayleigh to P in teleseismic arrivals from Pahute Mesa (NTS) shots, in *Explosion Source Phenomenology*, Ed. S.R. Taylor, H.J. Patton, and P.G. Richards, *American Geophysical Monograph* 65, 151-160.
- Gupta, I.N., T. W. McElfresh, and R. A. Wagner (1991). Near-source scattering of Rayleigh to P in teleseismic arrivals from Pahute Mesa (NTS shots, in: Taylor, S. R., H. J. Patton, and P. G. Richards (Eds.), *Explosion Source Phenomenology*, *AGU Geophys. Monograph*, 65, 151 - 160.
- Gurrola, H. and Minster, J. B. (2000). Evidence for local variations in the depth to the 410-km discontinuity beneath Albuquerque, New Mexico, *J. Geophys. Res.* 105, 10,847-10,856.
- Gutenberg, B. (1955). Channel waves within Earth's crust, *Geophysics*, 20, 283-294.
- Hasegawa, H. S. (1985). Attenuation of Lg waves in the Canadian Shield, *Bull. Seism. Soc. Am.*, 75, 1569-1582.
- Hays, W. W. (1969). Amplitude and frequency characteristics of elastic wave types generated by the underground nuclear detonation, *Boxcar. Bull. Seism. Soc. Am.* 59, 2283-2293
- He, Y.-F., X.-F. Chen, and H.-M Zhang (2005). The excitation of Lg wave by underground nuclear explosions, *Chinese J. of Geophys.* 48, 367-372.

- Healy, J. H. (1963). Crustal structure along the coast of California from seismic-refraction measurements, *J. Geophys. Res.*, 68, 5777-5787, 1963.
- Hedlin, M. A. H., J.-B. Minster, and J. A. Orcutt (1994). Resolution of prominent crustal scatterers near the NORESS small-aperture array, *Geophys. J. Int.*, 119, 101-115.
- Henstock, T. J., A. Levander, C. M. Snelson, K. G. Miller, S. H. Harder, A. R. Gorman, R. M. Clowes, M. J. A. Burianyk, E. G. Humphreys (1998). Probing the Archean and Proterozoic lithosphere of western North America, *GSA Today*, 8, 1-5.
- Henstock, T. J., Levander, A. R., Snelson, C. M., Keller, G. R., Miller, K. C., Harder, S. H., Gorman, A. R., Clowes, R. M., Burianyk, M. J. A., Humphreys, E. D. (1998). Probing the Archean and Proterozoic lithosphere of western North America, *GSA Today*, 8, 1-5.
- <http://users.pandora.be/boris.dehandschutter/chapter-1.PDF>.
- <http://users.pandora.be/boris.dehandschutter/chapter-1.PDF>.
- Hutchinson, D. R., A. J. Golmshtok, L. P. Zonenshain, T. C. Moore, C. A. Scholz, and K. D. Klitgord (1992). Depositional and tectonic framework of the rift basins of Lake Baikal from multichannel seismic data, *Geology* 20, 589-592.
- Ionov, D. (2002). Mantle structure and rifting processes in the Baikal-Mongolia region: geophysical data and evidence from xenoliths in volcanic rocks, *Tectonophysics* 351, 41-60.
- Kennett, B. L. N. (1993). The distance dependence of regional phase discriminants, *Bull. Seism. Soc. Am.* 83, 1155-1166.
- Kennett, B. L. N. (1987). Observational and theoretical constraints on crustal and upper mantle heterogeneity, *Phys. Earth Planet. Interiors*, 47, 319-332.
- Kennett, B. L. N., 1986. Lg Waves and Structural Boundaries, *Bull. Seis. Soc. Am.* 76, 1133-1141.
- Kennett, B. L. N., 1991. IASPEI 1991 Seismological Tables, Research School of Earth Sciences, Australia National University, Canberra.
- Khain, V. E. (1985), pt.1. *Geology of the USSR*, Gebrüder Borntraeger, Berlin.
- Khain, V. E. (1994), pt.2. *Geology of northern Eurasia(ex-USSR)*, Gebrüder Borntraeger, Berlin.
- Kirichenko, V. V., and Y. A. Kraev (2000). Development of regional travel-time tables for different geotectonic provinces of Northern Eurasia. *Proceedings of 22nd Annual DoD/DOE Seismic Symposium*, New Orleans, pp.305-315.
- Kitov, I. O., G. Ekström, V. V. Adushkin, D. D. Sultanov, and Kh. D. Rubenshtein. On seismic data from Soviet underground explosions, *Bull. Seism. Soc. Am.*, in review.
- Knapp, J. H., D. N. Steer, L. D. Brown, R. Berzin, A. Suleimanov, M. Stiller, E. Lushen, R. Bulgakov, S. N. Kashubin, and A. V. Rybalka (1996). Lithospheric-scale image of the southern Urals from explosion-source reflection data, *Science* 274, 226-228.
- Knopoff, L., F. Schwab, and E. Kausel (1973). Interpretation of Lg, *Geophys. J. Roy. Astron. Soc.*, 33, 389-404.
- Knopoff, L., F. Schwab, K. Nakanishi, and F. Chang (1974). Evaluation of Lg as a discriminant among different continental crustal structures, *Geophys. J. Roy. Astron. Soc.*, 39, 41-70.
- Kozlovsky, Y. A., 1990. The USSR Integrated Program of Continental Crust Investigations and Studies of the Earth's Deep Structure under the Globus Project, in *Super-Deep Continental Drilling and Deep Geophysical Sounding*, ed. K. Fuchs, Y. A. Kozlovsky, A. I. Krivtsov, M. D. Zoback, Springer, Berlin, 90-103.

- Langston, C. A. (1977). The effect of planar dipping structure on source and receiver responses for constant ray parameter, *Bull. Seism. Soc. Am.*, 67, 1029-1050.
- Langston, C. A. and J. K. Hammer (2002). The vertical component P-wave receiver function, *Bull. Seism. Soc. Am.*, 91, 1805-1819.
- Lermo J., and F. J. Chavez-Garcia (1993). Site effect evaluation using spectral ratios with only one station, *Bull. Seism. Soc. Am.* 83, 1574-1594.
- Li, H., I. B. Morozov, and S. B. Smithson (2006). Correlation of Lg amplitude ratios from Peaceful Nuclear Explosions to crustal structure in northern Eurasia, submitted to *Bull. Seism. Soc. Am.*
- Li, H., I. B. Morozov, S. B. Smithson (2006). Characteristics of Lg phase propagation in northern Eurasia from PNE (Peaceful Nuclear Explosion) data, submitted to *Bull. Seism. Soc. Am.*
- Ligorria J. P. and Ammon, C. J. (1999). Iterative deconvolution and receiver-function estimation, *Bull. Seism. Soc. Am.*, 89, 1395-1400.
- Lindquist, S. J. (1999). The Timan-Pechora Basin province of northwest arctic Russia: Domanik-Paleozoic total petroleum system, U.S. Department of the Interior, U.S. Geological Survey Open-file report 99-50-G.
- Lindquist, S. J. (1999). The Timan-Pechora Basin province of northwest arctic Russia: Domanik-Paleozoic total petroleum system, U.S. Geological Survey Open-file report 99-50-G.
- Liu, H. P., D. L. Anderson, H. Kamamori (1976). Velocity dispersion due to anelasticity: implications for seismology and mantle composition, *Geoph. J. Roy. Astr. Soc.*, 47, 41-58.
- Logatchev, N. A., and Yu. A. Zorin (1992). Baikal Rift zone: structure and geodynamics, *Tectonophysics* 208, 273-286.
- Mallick, S. (2001). AVO and elastic impedance, the *Leading Edge* 20, 1094-1104.
- Mantovani, E., Schwab, F., Liao, H., Knopoff, L., 1977. Teleseismic Sn: a guided wave in the mantle, *Geophys. J. R. Astr. Soc.* 51, 709-726.
- McNamara, D. E. (2000). Frequency-dependent Lg attenuation in south-central Alaska, *Geophys. Res. Lett.*, 27, 3949-3952.
- McNamara, D. E., and W. R. Walter (2001). Mapping crustal heterogeneity using Lg propagation efficiency throughout the Middle East, Mediterranean, Southern Europe. *Pure Appl. Geophys.* 158, 1165-1188.
- McNamara, D. E., T. J. Owens, and W. R. Walter (1996). Propagation characteristics of Lg across the Tibetan Plateau, *Bull. Seism. Soc. Am.*, 86, 457-469.
- Mechie, J., A. V. Egorkin, K. Fuchs, T. Ryberg, L. Solodilov, and F. Wenzel (1993). P-wave velocity structure beneath northern Eurasia from long-range recordings along the profile Quartz, *Phys. Earth Planet Inter.*, 79, 269-286.
- Mechie, J., Egorkin, A.V., Solodilov, L., Fuchs, K., Lorenz, F., Wenzel, F., 1997. Major features of the mantle velocity structure beneath northern Eurasia from long-range seismic recordings of Peaceful Nuclear Explosions, in *Upper Mantle Heterogeneities from Active and Passive Seismology*, Kluwer Academic Publishers, Dordrecht, The Netherlands.
- Menke, W.H., Richards, P.G., 1980. Crust-mantle whispering gallery phases: a deterministic model of teleseismic Pn wave propagation, *J. Geophys. Res.* 85, 5416-5422.
- Mitchell, B. (1975). Regional Rayleigh wave attenuation in North America, *J. Geophys. Res.*, 80, 4904-4916.
- Mitchell, B. J., Y. Pan, J. Xie, and L. Cong (1997). Lg coda Q variations across Eurasia and its relation to crustal evolution. *J. Geophys. Res.* 102, 22767-22779.

- Mitchell, B.J., Cong, L., 1998. Lg Coda Q and its Relation to the Structure and Evolution of Continents: A Global Perspective, *Pure Appl. Geophys.* 153, 655-663.
- Molnar, P., B. E. Tucker, and J. N. Brune (1973). Corner frequencies of P and S waves and models of earthquake sources, *Bull. Seism. Soc. Am.* 63, 2091-2104.
- Molnar, P., Oliver, J., 1969. Lateral Variations of attenuation in the upper mantle and discontinuities in the lithosphere, *J. Geophys. Res.* 74, 2648-2682.
- Mooney, C. Z. and R. Duval (1993). Bootstrapping : A Nonparametric Approach to Statistical Inference, Sage University Papers Series. Quantitative Applications in the Social Sciences; No. 07-095. Newbury Park, Calif. Sage Publications.
- Mooney, W. D., G. Laske, and T. G. Masters (1998). CRIST5.1: a global crustal model at 5° S, *J. Geophys. Res.*, 103, 727-747.
- Morozov, I. B. (2001). Comment on "High-frequency wave propagation in the uppermost mantle" by T. Ryberg and F. Wenzel, *J. Geophys. Res.*, 106, 30,715-30,718.
- Morozov, I. B. (2001). Comment on "High-frequency wave propagation in the uppermost mantle" by T. Ryberg and F. Wenzel, *J. Geophys. Res.*, 106, 30,715-30,718.
- Morozov, I. B. (2004). Null-space and statistical significance of first-arrival travel-time inversion, *Geophys. J. Int.*, 156, 549-554.
- Morozov, I. B., and S. B. Smithson (1996). Instantaneous polarization attributes and directional filtering, *Geophysics*, 61, 872-881.
- Morozov, I. B., and S. B. Smithson, (1997), A new system for multicomponent seismic processing, *Computers & Geosciences*, 23, 689-696.
- Morozov, I. B., E. A. Morozova, and S. B. Smithson, (1998a). On the nature of the teleseismic Pn phase observed in the recordings from the ultra-long range profile "Quartz", Russia, *Bull. Seism. Soc. Am.*, 88 (1), 62-73.
- Morozov, I. B., E. A. Morozova, S. B. Smithson, and L. N. Solodilov. (1998b). 2-D image of seismic attenuation beneath the Deep Seismic Sounding profile "Quartz", Russia, *Pure and Applied Geoph.*, 153, 311-348.
- Morozov, I. B., Morozova, E. A., and Smithson, S. B. (1998a). On the nature of the teleseismic Pn phase observed in the recordings from the ultra-long profile "Quartz", Russia, *Bull. Seism. Soc. Am.*, 88, 62-73.
- Morozov, I. B., Morozova, E. A., Smithson, S. B., and Solodilov, L. N. (1998b). 2-D image of seismic attenuation beneath the Deep Seismic Sounding profile QUARTZ, Russia, *Pure Appl. Geophys.*, 153, 311-343.
- Morozov, I. B., S. B. Smithson, and L. N. Solodilov (2002). Imaging crustal structure along refraction profiles using multicomponent recordings of first-arrival coda, *Bull. Seism. Soc. Am.* 92, 3080-3086.
- Morozov, I. B. and Smithson, S. B. (2000). Coda of long-range arrivals from nuclear explosions, *Bull. Seism. Soc. Am.*, 90, 929-939.
- Morozov, I.B., 2001. High-frequency wave propagation in the uppermost mantle; discussion, *J. Geophys. Res.* 106, 30715-30718.
- Morozov, I.B., Smithson, S.B., 2001. Amplitude Analysis and Modeling of Regional Phases in PNE Profiles in Northern Eurasia and Seismic Regionalization, Defense Threat Reduction Agency Program Research and Development Announcement DRTA01-PRDA-01-01.

- Morozova, E. A., I. B. Morozov, S. B. Smithson, and L. N. Solodilov, (1999). Heterogeneity of the uppermost mantle beneath the ultra-long range profile "Quartz," Russian Eurasia, *J. Geophys. Res.*, 104 (B9), 20,329-20,348.
- Morozova, E. A., Morozov, I. B., Smithson, S. B., and Solodilov, L.N. (2000). Lithospheric boundaries and upper mantle heterogeneity beneath Russian Eurasia: evidence from the DSS profile QUARTZ, *Tectonophysics*, 329, 333-344.
- Mueller, R. A., and J. R. Murphy (1971). Seismic characteristics of underground nuclear detonations. Part I: seismic spectrum scaling, *Bull. Seism. Soc. Am.* 61, 1675-1692.
- Murphy, J. R. (1977). Seismic source functions and magnitude determinations for underground nuclear detonations, *Bull. Seism. Soc. Am.* 67, 135-158.
- Murphy, J. R. (1996). Types of seismic events and their source descriptions, in *Monitoring a Comprehensive Test-Ban Treaty*, Proceedings of the NATO Advanced study Institute, Kluwer Academic Publishers, 225-245.
- Murphy, J. R., and T. J. Bennett (1982). A discrimination analysis of short-period regional seismic data recorded at Tonto Forest Observatory, *Bull. Seism. Soc. Am.* 72, 1351-1366.
- Murphy, J. R., I. O. Kitov, B. W. Barker, and D. D. Sultanov (2001). Seismic source characteristics of Soviet Peaceful Nuclear Explosions, *Pure Appl. Geophys.* 158, 2077-2101.
- Myers, S. C., and Schultz, C. A. (2000). Improving sparse network seismic location with Bayesian kriging and teleseismically constrained calibration events, *Bull. Seism. Soc. Am.*, 90, 1, 199-211, 2000.
- Nielsen, L., and H. Thybo (2003). The origin of teleseismic Pn waves: Multiple crustal scattering of upper mantle whispering gallery phases, *J. Geophys. Res.*, 108 (B10), 2460, doi:10.1029/2003JB002487.
- Nielsen, L., H. Thybo, and L. Solodilov (1999). Seismic tomographic inversion of Russian PNE data along profile Kraton, *Geoph. Res. Lett.*, 26, 3413-3416.
- Nielsen, L., H. Thybo, I. B. Morozov, S. B. Smithson, and L. Solodilov (2003). Teleseismic Pn Arrivals: Influence of Mantle Velocity Gradient and Crustal Scattering, *Geophys. J. Int.*, 153, F1 –F7.
- Nielsen, L., Thybo, H., Egorkin, A. V., 2001. Constraints on reflective bodies below the 8° discontinuity from reflectivity modeling, *Geophys. J. Int.* 145, 759-770.
- Nuttli O. W. (1986). Yield estimates of Nevada Test Site explosions obtained from seismic Lg waves (USA), *J. Geophys. Res.* 91, 2137-2151.
- Nuttli, O. W. (1982). The earthquake problem in the eastern United States, *J. Struct. Div. Am. Soc. Civ. Eng.*, 108, 1302-1312.
- Nuttli, O. W. (1986). Yield estimate of Nevada Test Site explosions obtained from seismic Lg waves, *J. Geophys. Res.* 78, 876-885.
- Pavlenkova, G. A., K. Priestley, and J. Ciper (2002). 2D model of the crust and uppermost mantle along rift profile, Siberian Craton, *Tectonophysics* 355, 171-186.
- Pavlenkova, N. I. (1996). General features of the uppermost mantle stratification from long-range seismic profiles, *Tectonophysics*, 264, 261-278.
- Pavlenkova, N. I. (1996). Crust and upper mantle structure in northern Eurasia from seismic data, *Advances in Geophys.* 37, 1-133.
- Pavlenkova, N. I., (1996). General features of the uppermost mantle stratification from long-range seismic profiles, *Tectonophysics*, 264, 261-278.

- Pavlenkova, N.I., Pavlenkova, G.A., Solodilov, L.N., 1996. High velocities in the uppermost mantle of the Siberian craton, *Tectonophysics* 262, 51-65.
- Phillips, W. S., H. E. Harste, S. R. Taylor, and G. E. Randall (2000). 1 Hz Lg Q tomography in central Asia, *Geophys. Res. Lett.* 27, 3425-3428.
- Phillips, W. S., H. E. Hartse, S. R. Taylor, A. A. Velasco, and G. E. Randall (2001). Application of regional phase amplitude tomography to seismic verification, *Pure Appl. Geophys.* 158, 1189-1206.
- Pomeroy, P. W., W. J. Best, and T. V. McEvilly (1982). Test ban treaty verification with regional data – a review, *Bull. Seism. Soc. Am.* 72, S89-S129.
- Priestley, K., A. Maggi, V. K. Gaur, S. Mitra, J. L. Bonner, and J. F. Lewkowicz (2002). Broadband seismic studies in southern Asia: source and path characterization, in *Proceedings of the 24th Seismic Research Review- Nuclear Explosion Monitoring: Innovation and Integration*, September 17-19, 2002, Ponte Vedra Beach, Florida, Defense Threat Reduction Agency and National Nuclear Security Administration p. 134-143.
- Priestley, K., Cipar, J., Egorkin, A., Pavlenkova, N., 1994. Upper-mantle velocity structure beneath the Siberian platform, *Geophys. J. Int.* 118, 369-378.
- Rapine, R. R., and J. F. Ni (2003). Propagation characteristics of Sn and Lg in Northern China and Mongolia, *Bull. Seism. Soc. Am.* 93, 939-945.
- Rapine, R. R., J. F. Ni, and T. M. Hearn (1997). Regional wave propagation in China and its surrounding regions, *Bull. Seism. Soc. Am.* 87, 1622-1636.
- Reese, C. C., R. R. Rapine, and J. F. Ni (1999). Lateral variation of Pn and Lg attenuation at the CDSN station LSA, *Bull. Seism. Soc. Am.* 89, 325-330.
- Regan J, and D. G. Harkrider (1989). Numerical modelling of SH Lg waves in and near continental margins, *Geophys. J. Int.* 98, 107-130.
- Ringdal, F., P. D. Marshall, and R. W. Alewine (1992). Seismic yield determination of Soviet underground nuclear explosions at the Shagan River test site, *Geophys. J. Int.* 109, 65-77.
- Rondanay, S., Bostock, M. G., and J. Shragge, J. (2001). Multiparameter two-dimensional inversion of scattered teleseismic body waves 3. Application to the Cascadia 1993 data set, *J. Geophys. Res.*, 106, 30795-30807.
- Ryaboy, V. (1989). Upper mantle structure studies by explosion seismology in the USSR, *Delphic Associates*, 138 pp.
- Ryberg T., M. Tittgemeyer, and F. Wenzel (1999). Propagation of elastic waves in the uppermost mantle, *Suppl to EOS, Trans., Am. Geophys. Union*, 80 (46), AGU Fall Meeting, San Francisco, CA, F712.
- Ryberg, T., and F. Wenzel (1999). High-frequency wave propagation in the uppermost mantle, *J. Geophys. Res.*, 104, 10,655-10,666.
- Ryberg, T., F. Wenzel, A. Egorkin, and L. Solodilov (1998). Properties of the mantle transition zone, *J. Geophys. Res.*, 103, 811-822.
- Ryberg, T., Fuchs, K., Egorkin, A. V., and Solodilov, L. (1995). Observations of high-frequency teleseismic Pn on the long-range Quartz profile across northern Eurasia, *J. Geophys. Res.*, 100, 18,151-18,163.
- Ryberg, T., K. Fuchs, A. V. Egorkin, and L. Solodilov (1995). Observations of high-frequency teleseismic Pn on the long-range Quartz profile across northern Eurasia, *J. Geophys. Res.*, 100, 18151-18163.

- Ryberg, T., Tittgemeyer, M., and Wenzel, F. (2000). Finite difference modeling of P-wave scattering in the upper mantle, *Geophys. J. Int.*, 141, 787-800.
- Ryberg, T., Wenzel, F., Egorkin, A. V., Solodilov, L., 1998. Properties of the mantle transition zone in northern Eurasia, *J. Geophys. Res.* 103, 811-822.
- Ryberg, T., Wenzel, F., Mechie, J., Egorkin, A., Fuchs, K. and Solodilov, L. (1996). Two-dimensional velocity structure beneath Northern Eurasia derived from the super long-range seismic profile Quartz, *Bull. Seismol. Soc. Am.*, 86, 857-867.
- Sandvol, E., K. Al-Damegh, A. Calvert, D. Seber, M. Barazangi, R. Mohamad, R. Gök, N. Türkelli, and C. Gürbüz (2001). Tomographic imaging of Lg and Sn propagation in the Middle East, *Pure Appl. Geophys.* 158, 1121-1163.
- Saunders, A. D., R. V. White, R. W. England, M. K. Reichow (2005). A mantle plume origin for the Siberian traps: Uplift and extension in the West Siberian Basin, Russia, *Lithos* 79, 407-424.
- Scholz, C. A., and D. R. Hutchinson (2000). Stratigraphic and structural evolution of Selenga Delta Accommodation Zone, Lake Baikal Rift, Siberia, *Int. J. Earth Sci.* 89, 212-228.
- Schueller, W., Morozov, I. B., and Smithson, S. B. (1997). Crustal and uppermost mantle velocity structure of northern Eurasia along the profile Quartz, *Bull. Seismol. Soc. Am.*, 87, 414-426.
- Sereno, T. J., S. R. Bratt, and T. C. Bache (1988). Simultaneous inversion of regional wave spectra for attenuation and seismic moment in Scandinavia. *J. Geophys. Res.*, 93, 2019-2036.
- Sharpe, J. A. (1942). The production of elastic waves by explosion pressures. I. theory and empirical field observations, *Geophysics* 7, 144-154.
- Shatsilov V.I., P.N. Gorbunov, A.G. Fremd, O.V. Sergeev, A.M. Zusman, E.A. Razakov, Yu.E. Gribanov, O.G. Snegirev, N.P. Stepanenko, A.T. Durkin, D.M. Koylanov, G.K. Sadirova (1993). Velocity models of the Kazakhstan earth's crust, Eurasia, Almaty, 105 pp. (in Russian).
- Sheriff, R.E., and L. P. Geldart (1995). *Exploration Seismology*, 2nd Edition, Cambridge University Press, Cambridge - New York - Melbourne, 592 pages.
- Shin, T.-C., and R. B. Herrmann (1987). Lg attenuation and source studies using 1982 Miramichi data, *Bull. Seism. Soc. Am.* 77, 384-397.
- Singh, S., and R. B. Herrmann (1983). Regionalization of crustal coda Q in the Continental United States, *J. Geophys. Res.*, 88, 527-538.
- Smith, W. H. F., and P. Wessel (1990). Gridding with continuous curvature splines in tension, *Geophysics*. 55, 293-305.
- Stephens, C., Isacks, B.L., 1977. Toward an understanding of Sn: normal modes of Love waves in an oceanic structure, *Bull. Seism. Soc. Am.* 67, 69-78.
- Sultanov, D. D., J. R. Murphy, and Kh. D. Rubinstein (1999). A seismic source summary for Soviet Peaceful Nuclear Explosions, *Bull. Seism. Soc. Am.*, 89, 640-647.
- Sutton, G.H., Walker, D.A., 1972. Oceanic mantle phases recorded on seismograms in the northwestern Pacific at distances between 7° and 40°, *Bull. Seism. Soc. Am.* 62, 631-655.
- Taylor, S. R., and F. U. Dowla (1991). Spectral yield estimation of NTS explosions, *Bull. Seism. Soc. Am.* 81, 1292-1308.
- Thybo, H., and Perchuc, E. (1997). The seismic 8° discontinuity and partial melting in continental mantle, *Science*, 275, 1626-1629.

- Thybo, H., Perchuc, E. (1997). A partially molten zone beneath the global 8° discontinuity at approximately 100 km depth, in *Upper Mantle Heterogeneities from Active and Passive Seismology*, ed. Karl Fuchs, Kluwer Academic Publishers, Dordrecht, Netherlands.
- Tittgemeyer, M., Ryberg, T., Fuchs, K., Wenzel, F., 1997. Observation of teleseismic Pn/Sn on super long-range profiles in northern Eurasia and their implications for the structure of the lithosphere, in *Upper Mantle Heterogeneities from Active and Passive Seismology*, ed. Karl Fuchs, Kluwer Academic Publishers, Dordrecht, The Netherlands.
- Tittgemeyer, M., Wenzel, F., Fuchs, K., 2000. On the Nature of Pn, *J. Geophys. Res.* 105, 16173-16180.
- Tittgemeyer, M., Wenzel, F., Fuchs, K., and Ryberg, T. (1996). Wave propagation in a multiple-scattering upper mantle—observations and modeling, *Geophys. J. Int.*, 127, 492-502.
- Tittgemeyer, M., Wenzel, F., Ryberg, T., Fuchs, K., 1999. Scales of Heterogeneities in the Continental Crust and Upper Mantle, *Pure Appl. Geophys.* 156, 29-52.
- Touloukian, Y.S., Judd, W. R., and Roy, R. F. (Eds.) (1989). *Physical properties of rocks and minerals, CINDAS data series on material properties, Group II. Properties of special materials, v. II-2*, Hemisphere Publishing Co., pp. 221-256.
- Tralli, D., and L. R. Johnson (1986). Lateral variation in mantle P velocity from tectonically regionalized tau estimates, *J. R. Astr., Soc.* 86, 475-489.
- Tryggvason, A., D. Brown, and A. Perez-Estaun (2001). Crustal structure of the southern Uralides from true amplitude processing of the Urals Seismic Experiment and Integrated Studies (URSEIS) vibroseis profile, *Tectonics* 20, 1040-1052.
- Ulmishek, G. F. (2003). *Petroleum geology and resources of the West-Siberian Basin, Russia*. U.S. Geological Survey Bulletin 2201-G.
- Vernikovskiy, V. A., A. E. Vernikovskaya, A. B. Kotov, E. B. Sal'nikova, and V. P. Kovach (2003). Neoproterozoic accretionary and collisional events on the western margin of the Siberian craton: new geological and geochronological evidence from the Yenisey Ridge, *Tectonophysics* 375, 147-168.
- Villaseñor, A., M. H. Ritzwoller, A. L. Levshin, M. P. Barmin, E. R. Engdahl, W. Spakman, and J. Trampert (2001). Shear velocity structure of central Eurasia from inversion of seismic wave velocities, *Phys. Earth Planet. Interiors*, 123, 169-184.
- Vinnik, L. P. (1977). Detection of waves converted from P-to-SV in the mantle, *Phys. Earth Planet Inter.* 15, 294-303.
- Volkov V. M. (1984). *Geology of the USSR: Colloquium 01/ 27th International Geological Congress, USSR, Moscow, 4-14, August, 1984*. Publishing Office "Nauka", Moscow, 1984.
- Walter, W. R., Mayeda, K. M., and Patton, H. J., 1995. Phase and spectral ratio discrimination between NTS earthquakes and explosions. Part I: empirical observations. *Bull. Seism. Soc. Am.* 85, 1050-1067.
- Wessel P., and W. H. F. Smith, (1995). New version of the Generic Mapping Tools released, *EOS Trans. Am. Geophys. U.*, 76, p. 329.
- Wu, R. S., S. Jin, and X. B. Xie (2000). Energy partition and attenuation simulations using screen propagators, *Phys. Earth Planet. Inter.* 120, 227-243.
- Wu, R. S., S. Jin, and X. B. Xie (2000a). Seismic wave propagation and scattering in heterogeneous crustal waveguide using screen propagators: I SH waves, *Bull. Seism. Soc. Am.* 90, 401-413.
- Xie, J. (1993). Simultaneous inversion for source spectrum and path Q using Lg with application to three Semipaltinsk explosions, *Bull. Seism. Soc. Am.* 83, 1547-1562.

- Xie, J. (1999). Regional phase excitation and propagation in the Lop Nor region of central Asia and implications for P/Lg discriminants. *J. Geophys. Res.* 104, 941-954.
- Xie, J. (2002). Source scaling of Pn and Lg spectra and their ratios from explosions in central Asia: Implications for the identification of small seismic events at regional distances. *J. Geophys. Res.* 107, 10.1029/2001JB000509.
- Xie, J., L. Cong, and B. J. Mitchell (1996). Spectral characteristics of the excitation and propagation of Lg from underground nuclear explosions in central Asia, *J. Geophys. Res.* 101, 5813-5822.
- Yang, X., I. Bondár, K. McLaughlin, R. North, and W. Nagy (2001). Path-dependent regional phase travel-time corrections for the International Monitoring system in North America, *Bull. Seism. Soc. Am.*, 91, 1831-1850.
- Yegorkin, A. V. (1992). Crustal structure along seismic geotraverses, *International Geology Review*, 34, 345-362.
- Yegorkin, A. V., and N. I. Pavlenkova (1981). Studies of mantle structure in the USSR on long-range seismic profiles, *Physics of the Earth and Planetary Interiors*, 25 (1), 12-26.
- Yilmaz, O., 1987. *Seismic Data Processing*, ed. S.M. Doherty, Society of Exploration Geophysicists, Tulsa, OK.
- Zonenshain L. P., M. I. Kuzmin, and B. M. Natapov (1990). *Geology of the USSR: a plate tectonic synthesis*. American Geophysical Union, Washington, D.C.
- Zorin, Yu. A., E. Kh. Turutanov, V. V. Mordvinova, V. M. Kozhevnikov, T. B. Yanovskaya, and A. V. Treussov (2003). The Baikal rift zone: the effect of mantle plumes on older structure, *Tectonophysics* 371, 153-173.
- Zunnunov, F. (1985), *Lithosphere of the Central Asia from seismic data*. Tashkent, FAN, 208 pp.